



DISSERTATION

Micro-structure of discontinuous fibre polymer matrix composites determined by X-ray Computed Tomography

carried out for the purpose of obtaining the degree of

Doctor technicae (Dr. techn.)

submitted at TU Wien, Faculty of Mechanical and Industrial Engineering, by

Dipl.-Ing. Dietmar Salaberger

Mat. Nr.: 9630475

under the supervision of

o.Univ.Prof. Dipl.-Ing. Dr.techn. Dr.-Ing.h.c. Sabine Seidler
Institute of Materials Science and Technology

reviewed by

Prof. Andrea Bernasconi PhD
Politecnico Milano
Dipartimento di Meccanica
Campus Bovisa Sud – via La
Masa 1
20156 Milano
Italy

Prof. Dr. habil. Markus Sause
Universität Augsburg
Institute of Materials Resource
Management
Universitätsstr. 1
86159 Augsburg
Germany

Affidavit

I confirm, that going to press of this thesis needs the confirmation of the examination committee.

I declare in lieu of oath, that I wrote this thesis and performed the associated research myself, using only literature cited in this volume. If text passages from sources are used literally, they are marked as such.

I confirm that this work is original and has not been submitted elsewhere for any examination, nor is it currently under consideration for a thesis elsewhere.

Vienna, TT.MM.JJJJ

(Dipl.-Ing. Dietmar Salaberger)

i

Acknowledgements

The scientific work of this thesis has been carried out within the framework of several national research projects in cooperation of TU Wien and Upper Austria University of Applied Sciences, Wels Campus. I want to thank FH-Prof. PD DI Dr. Johann Kastner for giving me the opportunity to work in the research group Computed Tomography in Wels.

My scientific supervision was conducted by O.Univ.Prof. DI Dr. Sabine Seidler and the group of non-metallic materials at the institute of Materials Science and Technology. I want to thank her and Senior Scientist Dipl.-Ing. Dr.techn. Thomas Koch for promoting, challenging, supporting and motivating me during my research.

Several master students contributed to this thesis with their masters thesis work which are namely Bernhard Plank, Susanne Gleiss and Stefan Oberpeilsteiner. The results could only be achieved by their excellent work, which i am very grateful of. Another very important contribution is related to transfer the ideas to C++ code and user friendly software. I want to thank especially Arunachalam Kannappan, Mustafa Arikan and Christoph Heinzl for their patient implementation of the software tool iAnalyse / OpeniA.

Many thanks to my colleagues accompanying me during my work at the research group CT in Wels. My personal and scientific benefit of working in this group were tremendous. Thanks to all of you but especially Erwin Schlotthauer, Stefan Griesser, Bernhard Harrer, Richard Kicking, Bernhard Plank, Michael Reiter, Christian Gusenbauer, Christian Hanneschläger and Elena Sell. Thanks to Michael I could use Matlab in a very effective way and i learned a lot about CT basics from him and together with him.

The financial support for this research offered by the Austria Research Promotion Agency (FFG) and the regional government of Upper Austria is gratefully acknowledged.

The research projects were conducted in close cooperation with industry. I want to thank the colleagues of Borealis Linz, in particular Michael Jerabek, Harald Herbst and Thomas Lummerstorfer for the support, motivating incitement and very valuable discussions.

...

Doch Forschung strebt und ringt, ermüdend nie,
Nach dem Gesetz, dem Grund, Warum und Wie.¹

The history of Western science confirms the aphorism that the great menace to progress is not ignorance but the illusion of knowledge. ²

¹Johann Wolfgang von Goethe: Berliner Ausgabe. Poetische Werke [Band 1–16], Band 2, Berlin 1960 ff, S. 104-106.

²Daniel J. Boorstin, *Cleopatra's Nose: Essays on the Unexpected*, Edited by Ruth F. Boorstin, Chapter 1: The Age of Negative Discovery, Start Page 3, Quote Page 7, Random House, New York. 1994

Abstract

The development of novel material systems and adequate characterisation methods must go hand in hand to assure for successful implementation of innovative applications. Fibre reinforced polymer matrix composite materials have found their way to structural components already. To apply these materials more efficiently, a comprehensive determination of micro-structural features is necessary. Accurate feature values are used for material simulations that lead to more efficient safety margins, less material application and optimized light weight design. X-ray computed tomography has shown to be a powerful tool for polymer materials characterisation.

3D image processing methods were developed for the extraction of as many micro-structural features from tomographic data as possible. Very important features that influence mechanical properties of a finished part are fibre orientation distribution, length distribution, aspect ratio, local fibre content and fibre shape. The extraction of single fibres from tomographic data allows to determine all mentioned features. Two software pipeline concepts were developed, the first for short fibres with fibre content up to 30 wt.% the second one extended for long fibres and higher fibre content up to 60 wt.%. The novelty of the second concept is the medial axis extraction which is done using template matching with spherical templates.

The accuracy of both concepts was evaluated for short glass fibres in two ways: the comparison with manually determined reference data and with destructive standard methods. Reference data was generated by fitting cylinders to approx. 250 fibres at three different positions within a standard tensile test specimen produced by injection moulding. The accuracy was defined as number of cylinders, that were characterised correctly. Three levels of resolution, 1, 2 and 3 μm Voxel edge length, were compared for fibres with nominal diameter of 12.5 μm . Both methods show more than 94 % of correctly extracted fibres for 1 and 2 μm Voxel edge length. At lower resolution accuracy drops to 86 % for the second and 76 % for the first concept. The most important micro-structural features, average fibre length and fibre orientation, show differences to reference data smaller than 2 %. Fibre orientation was determined by grinding and light optical microscopy. The comparison with the developed template matching approach showed very good accordance of tensor values over sheet thickness. Fibre length distribution was determined by pyrolysis followed by light optical microscopy of the remaining fibres. Very small samples containing only ca. 300 fibres showed average deviation of

8 % for average length.

The same specimen was analysed 9 times over a period of 3 years showing very good reproducibility with variations smaller than 0.7 % for tensor elements and smaller than 1 % for average length. This method evaluation for glass fibres leads to the conclusion that a Voxel edge length of maximal $\frac{1}{6}$ of fibre diameter leads to accurate results.

As examples that show the advantages of determining orientation and length from the same data analysis, a variation of fibre content, material after compounding and after injection moulding, the skin-core layered structure and fibre degradation along injection length were analysed. All results are in good accordance with published work.

The scan volume is limited by the applied resolution together with scanner hardware like number of detector pixels. The influence of final size of evaluation volume and cutting fibres virtually at data borders was analysed leading to the conclusion that choosing a size of 5 to 6 times the average weighted fibre length in direction of main orientation guarantees for accurate results.

Long fibre materials containing glass, carbon, polyethylene terephthalate and polyvinylacetate fibres were analysed after Charpy impact testing. Free fibre length in dependence of pellet length was determined showing no trend, which fits the expectations. The big difference of shape of fracture surface between polymer and inorganic fibres can be explained by different fibre orientation underneath the surface which was analysed by visual inspection of tomographic slice images.

The developed method of single fibre characterisation was used to generate models (representative volume elements) for mechanical simulations. Models and specimens with same micro-structure were tested virtually and by interrupted in-situ experiments. Fibres showing high normal stress were broken whereas fibres with high shear stress at fibre ends were pulled out of the matrix.

Kurzfassung

Die Entwicklung neuer Materialsysteme und geeigneter Analysemethoden muss Hand in Hand erfolgen, um eine erfolgreiche Verwendung für innovative Anwendungen zu gewährleisten. Faser Kunststoff Verbundwerkstoffe werden bereits für Strukturbauteile eingesetzt. Um diese Materialien noch effizienter verwenden zu können, müssen mikrostrukturelle Parameter umfassend bestimmt werden. Materialsimulationen auf Basis von exakt bestimmten Werten werden verwendet, um weniger Material mit effizienten Sicherheitsspannen und optimiertem Leichtbaupotenzial einzusetzen. Röntgen Computertomografie hat sich zu einem leistungsfähigen Werkzeug für die Charakterisierung von Kunststoffen entwickelt.

3D Bildverarbeitungsmethoden wurden entwickelt, um so viele mikrostrukturellen Parameter wie möglich aus Tomographiedaten zu extrahieren. Wichtige Parameter, die die mechanischen Eigenschaften beeinflussen, sind Faserorientierungsverteilung, Faserlängenverteilung, Aspektverhältnis, lokaler Fasergehalt und Fasergeometrie. Die Extraktion von Einzelfasern aus Tomographiedaten erlaubt die Bestimmung aller eben genannter Parameter. Es wurden zwei Softwarekonzepte entwickelt, das erste für Kurzfasern und Fasergehalt bis zu 30 wt.%, das zweite für Langfasern und Fasergehalt bis zu 60 wt. %. Das zweite Konzept zeichnet die Extraktion der Fasermittelachsen mit Hilfe von Template Matching mit sphärischen Templates aus.

Die Genauigkeit beider Konzepte wurde für Kurzglasfasern auf zwei Arten bestimmt: der Vergleich mit manuell ermittelten Referenzdaten und mit zerstörenden Standardmethoden. Die Referenzdaten wurden mit Hilfe von Zylinderfits für ca. 250 Fasern an drei verschiedenen Positionen in einem Standardzugprüfkörper, der mittels Spritzguss hergestellt wurde, ermittelt. Die Genauigkeit wurde als Anzahl der korrekt charakterisierten Zylinder definiert. Drei verschiedene Auflösungen, 1, 2 und 3 μm Voxelkantenlänge wurden für Fasern mit nominellem Durchmesser von 12.5 μm verglichen. Beide Methoden zeigen mehr als 94 % korrekt extrahierte Fasern für 1 und 2 μm Voxelkantenlänge. Bei geringerer Auflösung sinkt die Genauigkeit auf 86 % für das zweite und auf 76 % für das erste Konzept. Die wichtigsten mikrostrukturellen Parameter Faserorientierung und Faserlänge zeigen Abweichungen zu den Referenzdaten von weniger als 2 %.

Faserorientierung wurde mittels Schliffpräparation mit optischer Mikroskopie bestimmt.

Der Vergleich mit dem entwickelten Template Matching Konzept zeigt sehr gute Übereinstimmung der Tensorwerte über die Plattendicke. Faserlängenverteilung wurde mittels Pyrolyse und optischer Mikroskopie der verbleibenden Fasern bestimmt. Ergebnisse von sehr kleinen Proben mit ca. 300 Fasern zeigten Abweichungen von 8 % für die mittlere Faserlänge.

Dieselbe Probe wurde neun Mal über einen Zeitraum von 3 Jahren analysiert. Die Reproduzierbarkeit war sehr gut mit Abweichungen kleiner als 0.7 % für Tensorwerte und kleiner als 1 % für mittlere Länge. Die Methodenevaluierung für Glasfasern zeigt, dass eine Voxelkantenlänge von höchstens $\frac{1}{6}$ des Faserdurchmessers zu sehr genauen Ergebnissen führt.

Als Beispiele, die die Vorteile der Bestimmung von Orientierung und Länge aus demselben Datensatz zeigen, wurden die Variation des Fasergehalts, der Unterschied nach Compoundieren und nach dem Spritzguss, die Skin-Core Schichtstruktur und der Faserabbau entlang des Einspritzwegs gewählt. Alle Resultate zeigen sehr gute Übereinstimmung mit publizierten Werten.

Das Messvolumen ist limitiert durch die gewählte Auflösung und die Scannerhardware wie die Anzahl an Detektorpixeln. Die Untersuchung des Einflusses von Messvolumen und virtuell geschnittenen Fasern an den Rändern des Datensatzes zeigt, dass eine Länge in Faservorzugsrichtung von 5 bis 6-facher gewichteter mittlere Faserlänge zu genauen Ergebnissen führt.

Langfasermaterialien mit Glas, Kohlenstoff, Polyethylenterephthalat und Polyvinylacetat Fasern wurden nach Charpy Kerbschlagbiegeversuchen untersucht. Die freie Faserlänge in Abhängigkeit variierender Pelletlänge zeigte wie erwartet keine Tendenz. Die Bruchfläche von Polymerfasern unterscheidet sich sehr von anorganischen Fasern. Dies kann durch die unterschiedliche Faserorientierung unter der Bruchfläche, die mittels visueller Inspektion der Tomographie Schnittbilder evaluiert wurde, erklärt werden.

Die entwickelte Methode der Einzelfasercharakterisierung wurde dazu verwendet, um Finite Elemente Modelle (repräsentatives Volumenelemente) zu erstellen. Modelle und reale Proben wurden virtuell und im realen, unterbrochenen in-situ Zugversuch belastet. Fasern, die hohe Normalspannungen zeigen, wurden gebrochen, wohingegen Fasern mit hohen Scherspannungen an den Faserenden aus der Matrix ausgezogen wurden.

Symbols and Abbreviations

Symbols

| | | |
|-------------------------|-------------------|---|
| $ZO_{\text{corrected}}$ | (mm) | Distance X-ray source to object |
| d | (μm) | Fibre diameter |
| L | (μm) | Fibre length |
| L_c | (μm) | Length correction value |
| l_n | (μm) | Average fibre length |
| l_w | (μm) | Weighted average fibre length |
| Δ | | Difference of two values |
| σ | | Deviation factor of respective feature |
| σ_D | (μm) | Deviation factor of diameter distribution |

Abbreviations

| | |
|------|---|
| C | Cluster: Voxel where medial axes touch |
| CC | Distance from one cluster to another |
| CF | Carbon fibre |
| CFD | Computational fluid dynamics |
| CFRP | Carbon fibre reinforced polymer laminate |
| CMM | Coordinate measuring machine |
| CMR | Contact micro-radiography |
| CT | X-ray computed tomography |
| FCP | Fibre Characterization Pipeline |
| FDK | Feldkamp algorithm for tomographic reconstruction |
| FEM | Finite Element Modelling |
| FLD | Fibre length distribution |
| FO | Fibre orientation |
| FOD | Fibre orientation distribution |
| GF | Glass fibre |
| GFRP | Glass fibre reinforced polymer laminate |
| I | Electric tube current |
| LOM | Light optical microscopy |
| MAE | Medial Axis Extraction |
| MIL | Mean interception length |

| | |
|------|--|
| MPS | Multi Purpose test Specimen according to DIN-EN-ISO 527-2 [89] |
| NDT | Non destructive testing |
| PET | Polyethylene terephthalate |
| PP | Polypropylene |
| PVA | Polyvinylacetate |
| PSF | Point spread function |
| ROI | Region of Interest |
| SDD | Source Detector Distance |
| SEM | Scanning electron microscopy |
| sFRP | Short fibre reinforced polymer |
| SOD | Source Object Distance |
| U | Electric tube voltage |
| VS | Voxel edge length |
| ZO | Object position on scanner Z axis |

Contents

| | |
|---|------------|
| Acknowledgements | iii |
| Abstract | vii |
| Symbols and Abbreviations | xi |
| 1 Introduction | 1 |
| 2 State of the art | 5 |
| 2.1 Fibre reinforced polymer materials processed by injection moulding | 5 |
| 2.2 Description of fibre orientation and fibre length | 6 |
| 2.3 Measuring fibre orientation distribution of short fibre reinforced polymers | 10 |
| 2.4 Measuring fibre length distribution of short fibre reinforced polymers . . . | 13 |
| 2.5 X-ray computed tomography for polymer characterisation | 14 |
| 2.6 X-ray computed tomography for characterisation of discontinuous fibre composites | 15 |
| 3 Investigated materials | 23 |
| 3.1 Fibre materials in Polypropylene | 23 |
| 3.2 Test specimens | 26 |
| 3.2.1 Material for reference data sets and reproducibility | 26 |
| 3.2.2 Specimens to consider influence factors on the measurement results | 26 |
| 3.2.3 Specimens to determine variations of fibre orientation | 26 |
| 3.2.4 Specimens for the determination of fibre length distribution | 28 |
| 3.2.5 Injection moulded A5 sheet | 28 |
| 3.2.6 Specimens for long fibre characterization | 29 |
| 4 Methods | 31 |
| 4.1 X-ray computed tomography | 31 |
| 4.1.1 Measuring technique | 31 |
| 4.1.2 Determination of real Voxel edge length | 35 |
| 4.2 CT data analysis | 37 |
| 4.2.1 Fibre characterization - Basic concept | 37 |
| 4.2.2 Fibre characterization - Concept1 (MAE) | 38 |

| | | |
|----------|---|------------|
| 4.2.3 | Fibre characterization - Concept2 (TM) | 48 |
| 4.2.4 | FCP parameters for different materials | 52 |
| 4.3 | Binary thinning | 53 |
| 4.4 | Creation of reference data sets | 53 |
| 4.5 | General pre-processing | 57 |
| 4.6 | Determination of free fibre length | 58 |
| 4.7 | CT simulation | 61 |
| 4.8 | Standard methods | 61 |
| 4.8.1 | Fibre orientation distribution | 62 |
| 4.8.2 | Fibre length distribution | 62 |
| 5 | Qualitative CT data analysis | 65 |
| 5.1 | Glass fibre composites | 65 |
| 5.2 | Polymer fibre composites | 72 |
| 6 | Evaluation of CT data analysis methods | 77 |
| 6.1 | Reference data sets | 78 |
| 6.2 | Examination of accuracy | 82 |
| 6.3 | Examination of reproducibility | 88 |
| 6.4 | Impact of evaluation volume | 92 |
| 6.5 | Impact of specimen orientation on the turntable | 94 |
| 6.6 | Comparison with standard method for FOD | 96 |
| 6.7 | Comparisons with standard methods for FLD | 102 |
| 6.7.1 | Pyrolysis comparison with CT according to ISO standard | 102 |
| 6.7.2 | Pyrolysis and comparison with CT analyses on individual fibre basis | 104 |
| 6.8 | Correction of Voxel edge length | 113 |
| 7 | Quantitative fibre characterisation | 115 |
| 7.1 | Impact of fibre content on FOD and FLD | 115 |
| 7.2 | Fibre degradation along injection moulding process | 117 |
| 7.3 | Skin-core layered micro-structure | 118 |
| 7.4 | Fibre degradation along injection length | 120 |
| 7.5 | Micro-structure of long fibres | 126 |
| 7.5.1 | Influence of analysis volume for long GF | 126 |
| 7.5.2 | Multi purpose test specimens (MPS) | 128 |
| 7.5.3 | Special features of long fibre micro-structure | 129 |
| 7.6 | Determination of free fibre length | 131 |
| 7.7 | Modelling and virtual tensile testing | 133 |
| 8 | Conclusion | 139 |
| | Bibliography | 143 |
| | Curriculum Vitae | 153 |

| | |
|-------------------|------------|
| Appendix A | 156 |
| Appendix B | 160 |
| Appendix C | 164 |
| Appendix D | 166 |
| Appendix E | 167 |

Introduction

The demands of light weight design are nowadays mainly driven by automotive and aeronautic industries. The use of novel materials or material composites and the substitution of conventional materials is one strategy to reduce weight. Another strategy is to apply less conservative design rules which allow taking full advantage of the chosen material with optimised safety margins. Polymers are eminently suitable for reducing weight but have to be enhanced in strength by adding reinforcing phases. Carbon and glass fibre reinforced polymer laminate composites (CFRP, GFRP) were developed for aeronautics and its amount within an aircraft has been increased up to 55 % per weight for a common passenger aircraft. Concept studies of CFRP cars showed the limitations which are caused by the high cycle times of CFRP laminate production. Better suitable materials for mass production are discontinuous, short fibre reinforced composites (sFRP). Especially glass fibre composites are used nowadays widely for non-structural automotive components and in other industries like leisure and construction as well.

For the use of sFRP composite materials for structural components, optimized production procedures and well known and defined micro-structural parameters of the final part are essential. These requirements can be addressed by simulation and by testing techniques. For both, novel concepts have to be developed in order to achieve accurate and meaningful results that can be used for process and design optimization. Micro-structure of composite materials is usually complex and not visible or accessible from the outside. Destructive methods are commonly used for characterisation. These are well established and lead to accurate results. For valuable prototypes or other specimens it can be very expensive and tedious to perform destructive testing. This is one reason why several non-destructive testing techniques have been developed for polymer matrix composites in the last decades. Already standardised methods are applied for ultrasonic testing which is mainly used to detect defects in CFRP laminate materials. Other methods like thermography, acoustic emission, eddy current, electron tomography

or shearography are topics of research and can be applied for very specific tasks.

All these testing methods have limitations in resolution and therefore limitations in detectability and the ability of quantitative characterisation. Industrial X-ray tomography has shown to be able to close a gap in resolution between destructive and common non-destructive methods and was used to find defects and to visualise micro-structural features like fibre bundle orientation or laminate layup. Besides higher resolution another advantage of tomographic methods, compared to other NDT methods, is the possibility to apply 3D data processing algorithms.

X-ray computed tomography was transferred from medical to industrial application in the 1990s. Novel construction concepts, which took into account the demands for industrial parts, were developed. They work according to the same principle as medical CT scanners but are equipped with high energy X-ray tubes and detectors and are built in a linear setup compared to the gantry based medical setup. Today a notable number of companies are producing industrial CT devices reaching physical resolutions down to a few 100 nm.

The trends of industrial use of discontinuous fibre composite materials are higher fibre content (up to 60 wt.%), longer fibres (LFT) and more heterogeneous combination of materials like more than one type of fibre or a combination of CFRP laminate and sFRP („organosheet“). Every material development usually demand the development of new characterisation techniques.

The work published so far indicates that the technology of laboratory X-ray computed tomography has reached a status that allows for comprehensive micro-structural characterisation. Features as fibre orientation, length and diameter were analysed, sometimes only one, sometimes all of them. The majority of work was published about individual fibre characterisation which seems to be the most comprehensive approach.

One can differentiate two objectives that micro-structural characterisation should meet: comparison of materials produced with different production parameters or material compositions and the generation of input for structural simulations. The latter case demands a certain description of micro-structural parameters. Widely used is the second order orientation tensor together with the aspect ratio to describe material properties for further processing like FE simulations. Some of the presented concepts for individual fibre characterisation like the MIL concept doesn't deliver the complete tensor information. The concepts that deliver either orientation or length are also not suitable for generating input for simulation.

All presented concepts use binarisation as basis for further image processing. The quality of the binarisation result is often not discussed but crucial, the difference of global and local thresholding is only discussed in [66]. The approaches were mostly developed for one material system without the discussion of other materials. Several approaches have similar parts but do not complete the characterisation or do not deliver all possible features or details about accuracy and limitations.

The newer concepts (published later than 2014) were not available at the beginning of

this thesis and were therefore not considered for the motivation. Since computational power and RAM size increased in the time from the first work was published and the beginning of this thesis, algorithms that were found to be too time or memory consuming could now be considered for new concepts.

The goals of this thesis are the development and application of 3D image processing tools for the determination of fibre orientation, length, diameter and content. As image acquisition device a high resolution laboratory CT device (Nanotom) was used to generate 3D data. Basic ideas of the already published concepts should be employed and improved to get accurate results in reasonable time. The quality of the developed method should be evaluated comprehensively and the applicability for different fibre composite materials should be shown.

State of the art

2.1 Fibre reinforced polymer materials processed by injection moulding

The class of polymer fibre composite materials that are addressed by this thesis are discontinuous fibre reinforced materials produced by injection moulding. A variety of polymer and fibre materials are used in industry containing short and long fibres. Over the last decades comprehensive knowledge has been acquired and published about processing, performance and applications of this group of composites. This chapter should give a compact overview of the most important issues that are relevant for this thesis. The book [1] gives all details about short fibre reinforced polymer composites. Some aspects discussed in this book will be summarized in the following.

Micro-structure is a term that is used to describe properties like fibre orientation, fibre length, aspect ratio and diameter distribution thus features on the micro-scale. Morphology on the other hand is more universally used to describe e.g. different phases within a polymer but can also be used similarly as micro-structure. For this thesis the term micro-structure was used because this is also used by the simulation and modelling community for which the determined features are most important. Micro-structure is strongly influenced by the processing method, processing parameters and material parameters. Fibres are added to the polymer to improve mechanical and physical properties. In general more fibres lead to improved properties but this might change with very high fibre contents. Well known and described effects that take place during injection moulding are alignment of fibres in injection direction, development of a layered orientation structure over wall thickness and fibre degradation.

The alignment of fibres inside the mould can lead to very complex orientation distribution which furthermore leads to orthotropic material behaviour. Processing conditions and mould geometry can strongly influence fibre orientation. Due to different melt flow

conditions inside the mould, layered orientation structure over thickness develops showing fibres in injection direction at the skin and perpendicular in the core. This effect and the change of orientation along the melt pathway are shown for example in [2]. Fibres degrade during compounding and injection moulding in form of breakage. With higher fibre content the degradation increases which can lead to decrease of tensile strength for fibre content higher than 50 wt.% [3]. Reduction of mean fibre length with increasing fibre content together with the consequences on mechanical properties for PP-GF were published [4]. The materials investigated in this thesis contain fibre with average length up to 3 mm and diameter from 7 μm up to 22 μm .

Knowledge of micro-structure and morphology of the final product is very important to take maximum advantage of fibre reinforcement. For material design and development quantitative characterisation of test specimens is crucial to understand correlations of production or material parameters with micro-structure.

There are also influences on mechanical performance that are determined by the polymer matrix or the interface between fibres and matrix but these will not be considered in this thesis.

2.2 Description of fibre orientation and fibre length

Fibre orientation distribution

For the definition of orientation of a line in 3D Cartesian coordinates, two angles are adequate. The definition of θ and ϕ can be found in almost every relevant paper and can be defined for example according to [5] or [6]. The axes can be named X, Y, Z or 1, 2, 3 where Z and 3 are usually the vertical axes (Figure 2.1).

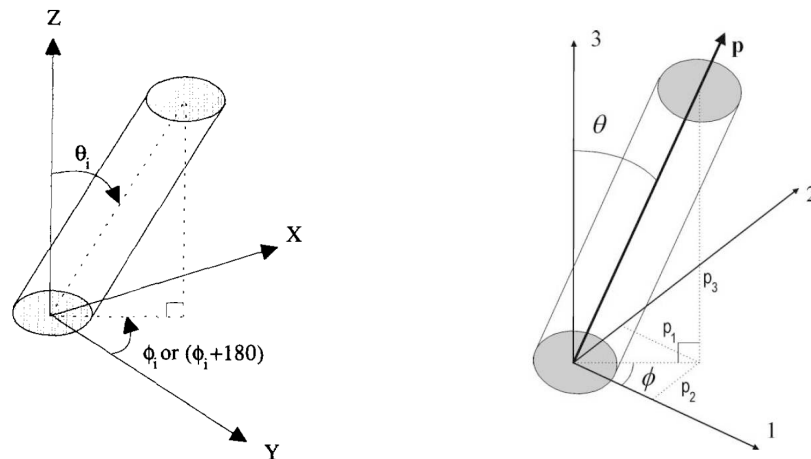


Figure 2.1: Definition of angles θ and ϕ to describe FO according to [5] and [6]

The local orientation within a Voxel data set can be determined for example by calculating the Hesse- Matrix $H_f(\mathbf{g})$. This matrix is defined as the second derivative of grey level progression in all three orthogonal, Cartesian directions according to equation 2.1.

The grey level distribution within the Voxel data set follows:

$$f(\mathbf{g}) = f(x, y, z)$$

$$H_f(\mathbf{g}) = \nabla^2 f(\mathbf{g}) = \left(\frac{\partial f(\mathbf{g})}{\partial g_i \partial g_k} \right) = \begin{pmatrix} \frac{\partial^2 f(\mathbf{g})}{\partial x \partial x} & \frac{\partial^2 f(\mathbf{g})}{\partial x \partial y} & \frac{\partial^2 f(\mathbf{g})}{\partial x \partial z} \\ \frac{\partial^2 f(\mathbf{g})}{\partial y \partial x} & \frac{\partial^2 f(\mathbf{g})}{\partial y \partial y} & \frac{\partial^2 f(\mathbf{g})}{\partial y \partial z} \\ \frac{\partial^2 f(\mathbf{g})}{\partial z \partial x} & \frac{\partial^2 f(\mathbf{g})}{\partial z \partial y} & \frac{\partial^2 f(\mathbf{g})}{\partial z \partial z} \end{pmatrix} \quad (2.1)$$

The Hesse-Matrix is symmetric which requires only six values to be calculated. This matrix is used for image processing pipelines to determine average orientation of a complete data set or as pre- processing to generate input for subsequent algorithms. By an eigenvalue analysis the local direction-vector and θ and ϕ can be calculated.

For models that are used to predict fibre orientation a description has been introduced and universally accepted using second and fourth order tensor definitions [7]. Six values are calculated since the orientation tensor \mathbf{A} is symmetric. In fact five independent values are calculated for \mathbf{A} and the sum of the main diagonal elements equals ($A_{ii} = 1$). The following equations define the second order tensor \mathbf{A} 2.2 and the fourth order tensor \mathbb{A} 2.3 as described in [8] .

$$\mathbf{A}_{ij} = \int (p_i p_j) \psi(\mathbf{p}) d\mathbf{p} = \begin{pmatrix} a_{11} & a_{12} & a_{13} \\ \dots & a_{22} & a_{23} \\ \dots & \dots & a_{33} \end{pmatrix} \quad (2.2)$$

$$\mathbb{A}_{ijkl} = \int (p_i p_j p_k p_l) \psi(\mathbf{p}) d\mathbf{p} \quad (2.3)$$

\mathbf{p} represents a unit vector with the same direction as the fibre \mathbf{p}_i and $\psi(\mathbf{p})$ is the orientation distribution function.

For a discrete number of fibres n the tensor elements can be calculated as follows:

$$a_{ij} = \frac{1}{n} \cdot \sum_{k=1}^n (p_i^k p_j^k) = \begin{pmatrix} a_{11} & a_{12} & a_{13} \\ a_{12} & a_{22} & a_{23} \\ a_{13} & a_{23} & a_{33} \end{pmatrix} \quad i, j \in 1, 2, 3 \quad (2.4)$$

The elements of the orientation tensor can be calculated from the angles ϕ and θ as follows [6]:

$$a_{11} = \sin^2 \theta \cos^2 \phi \quad (2.5)$$

$$a_{22} = \cos^2 \theta \cos^2 \phi \quad (2.6)$$

$$a_{33} = \cos^2 \theta \quad (2.7)$$

$$a_{12} = \sin^2 \theta \cos \phi \sin \phi \quad (2.8)$$

$$a_{13} = \sin \theta \cos \theta \cos \phi \quad (2.9)$$

$$a_{23} = \sin \theta \cos \theta \sin \phi \quad (2.10)$$

For individual fibre characterisation the information of ϕ and θ is available which allows to calculate tensors for every individual fibre. Representative orientation tensors are then calculated by averaging the values for all fibres or selected ones.

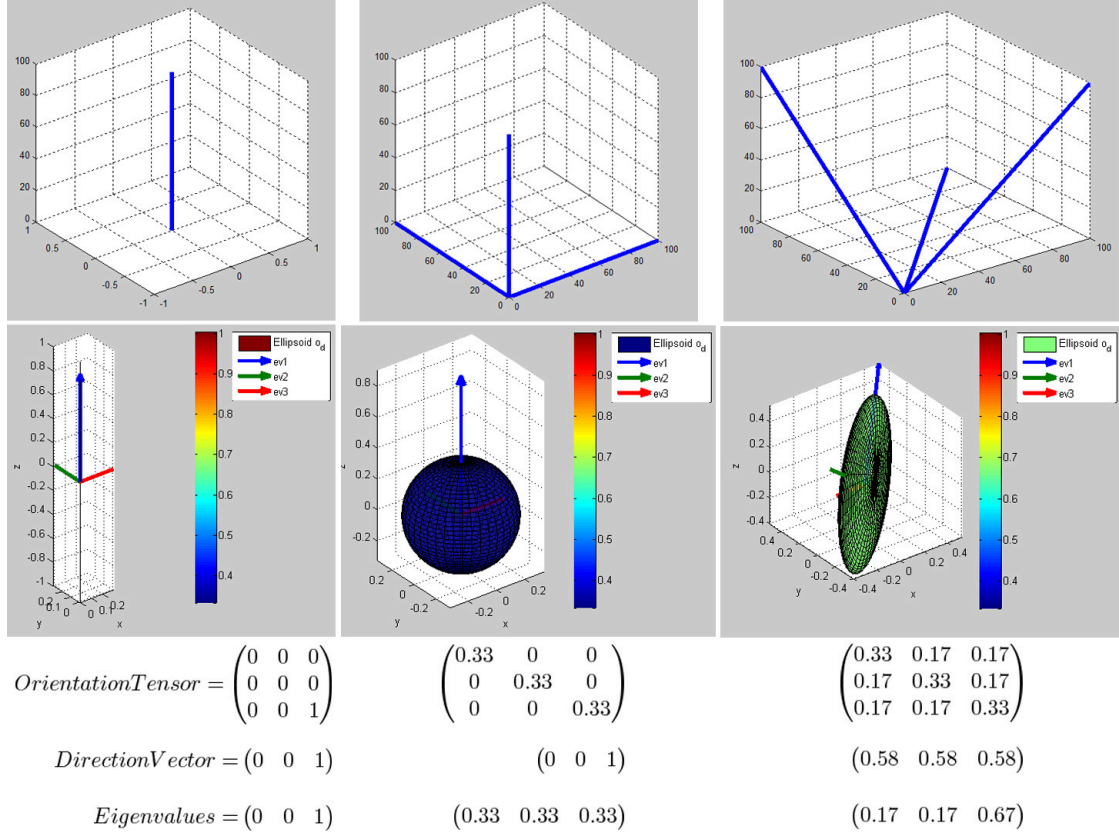


Figure 2.2: Orientation tensor values for three different fibre arrangements containing three fibres

Additional information about average fibre orientation distribution can be determined by an eigenvalue analysis. For a symmetric tensor of second order, the smallest

eigenvalue is $\lambda_{min} \geq \frac{1}{3}$. The maximum value is 1 and $trace(a_{ij}) = 1$. If all three eigenvalues are $\lambda_{1,2,3} = \frac{1}{3}$, one can conclude a random orientation, in other words no preferred orientation. If one eigenvalue is 1, the others are 0 and all fibres are oriented in the direction of corresponding eigenvector. One can draw an ellipsoid with the use of the three eigenvectors as main diagonals. The ellipsoids shape shows the average orientation.

How well the fibres are aligned can be expressed by the strength of orientation value which is usually the highest eigenvalue. Three examples are shown in Figure 2.2. The average orientations changes from perfect alignment for 1 single fibre on the left to no preferred orientation for three fibres in the middle to a preferred 3D orientation on the right. As one can see from the examples given in Figure 2.2 the analysis of the main diagonal elements alone is not enough to draw a conclusion about orientation. The values in the centre and on the right are all 0.33 but since the other elements are all 0 for one example and 0.17 in the other, the eigenvalues show differences and therefore also the average orientations differ. Non-zero minor diagonal elements represent a rotation of the ellipsoid with respect to the coordinate system. This issue is discussed for example here [6].

Fibre orientation distribution can be visualised in different ways. Polar plots (Figure 2.3) show the distribution by colour coded frequencies of subdivisions of ϕ and θ . Another way is to show the tensor values listed in tabular form or as trend over a predefined axis.

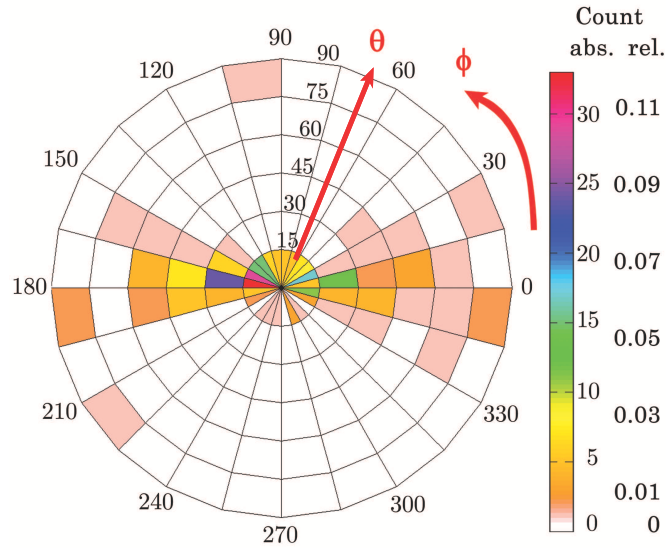


Figure 2.3: Visualisation of orientation distribution using „polar plot“. For each direction, defined by ϕ and θ in steps of 15° , the number of fibres is drawn colour coded in absolute and relative values. The colour scale is shown on the right. This figure shows an example with distinct orientation in Z-direction ($\theta < 30^\circ$).

Fibre length distribution

The standard for determination of fibre length using optical methods [9] describes how average fibre length l_n (equation 2.11) and weighted average fibre length l_w (equation 2.12) should be calculated:

$$l_n = \frac{\sum_{i=1}^n l_i}{n} \quad (2.11)$$

l_i ... length of fibre i , n ... fibre count

$$l_w = \frac{\sum_{i=1}^n (m_i \cdot l_i^2)}{\sum_{i=1}^n (m_i \cdot l_i)} \quad (2.12)$$

m_i ... count of fibres with same length

Since every individual fibre was considered for this thesis, m_i was set to 1.

An important length for the strength of the composite is the critical fibre length. It is defined as the minimum fibre length necessary to build up the axial fibre stress to the ultimate strength of the fibre [10]. Critical fibre length follows this equation:

$$l_c = \frac{r_f \cdot \sigma_F^u}{\tau} \quad (2.13)$$

where r_f is fibre radius, σ_F^u is strength of the fibre and τ is the interfacial shear stress between fibre and matrix.

Fibres which are shorter than the critical fibre length do not contribute to enhancement of strength and should not be present in the composite material.

Fibre length distribution is usually shown as histogram graph. Size and count of length classes have to be adapted to the actual length distribution.

The methods discussed in the following two sections are well established and commonly used for measuring fibre orientation and fibre length distribution. Novel methods using X-ray techniques are described in chapter 2.6.

2.3 Measuring fibre orientation distribution of short fibre reinforced polymers

Since fibre orientation is one of the most important features of a fibre reinforced polymer material, already in the 1960s several methods to measure orientation were presented and discussed. Amongst the most relevant and widely used are optical, radiographic and metallographic methods which are compared in [11] and [12].

2.3. MEASURING FIBRE ORIENTATION DISTRIBUTION OF SHORT FIBRE REINFORCED POLYMERS

Although it is possible to generate images for translucent materials via transmitted light, these methods are very limited. The more complex fibre architecture is and the more additional structures like pores are present, the more misleading the results of transmitted light methods are. Radiographic methods using X-rays and films can be divided into macro- and micro-radiography. While macro-radiography does not always respond to fibre orientation but also or solely to fibre clusters or clumps, micro-radiography is better suited to measure the orientation of the well-dispersed fibres. The method of contact micro-radiography (CMR) for fibre reinforced polymers is described in [13]. Very thin specimens in the range of 50 to 150 μm thickness are prepared by cutting. Soft X-rays together with fine grained films are used to generate high contrast and high resolution images of a considerable number of fibres. In many cases the micro-radiographs are evaluated qualitatively in order to explain mechanical properties. In [11] quantitative information in form of orientation distribution was extracted from highly magnified cut-outs. This orientation represents only in-plane orientation. Selected images that were presented in [11] are shown in 2.4. The fibres are clearly visible in micro-radiography but it is obvious that the quantitative analysis is problematic when local fibre content is high and fibre orientation is out of plane.

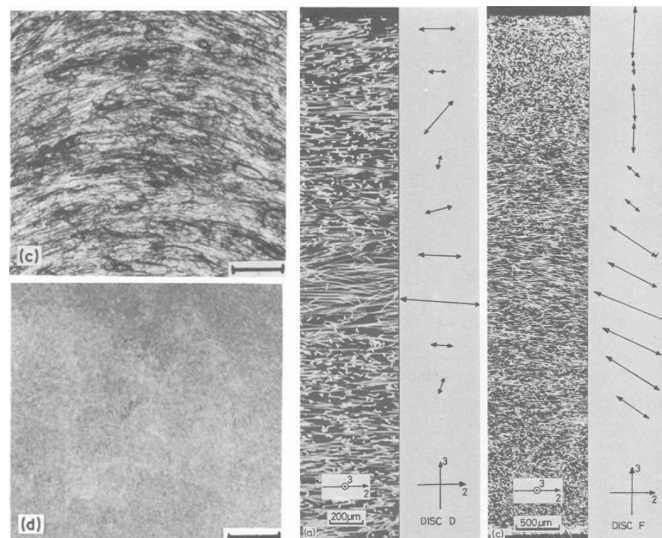


Figure 2.4: Macro-radiographic images (left) and micro-radiographic images with quantitative orientation analysis (right) taken from [11]

The other method that was used more intensively in the last decades to determine fibre orientation, is optical scanning of polished surfaces. Compared to micro-radiography it is easier to apply since no X-ray equipment is necessary and the quality of quantitative analysis is better. Image acquisition was either performed using light optical microscopy (LOM), scanning electron microscopy (SEM) or confocal laser scanning microscopy (CLSM). For LOM and SEM the specimens are prepared in a way that a cross section is polished and etched in order to increase fibre visibility. The idea is to generate

a binary image that reveals fibres as ellipses. The elliptical parameters are determined by image processing steps and used to calculate the angles ϕ and θ . Apparatus and image processing tools that follow this concept using LOM were published in [14] and [15]. One of the big challenges of these methods is the choice of sectioning angles. Cutting the fibres parallel to the fibre axes or almost perpendicular to that axes will result in big errors [16]. The other drawback is that these methods are destructive. By using only one single cross-section for orientation measurement there is an ambiguity resulting from the fact that fibres at (θ, ϕ) and $(\theta, \phi + \pi)$ lead to the same elliptical cross-section. This effect is explained for example in [6] and leads to the fact that some of the orientation tensor elements cannot be determined. In [17] some assumptions about fibre orientation are made that can reduce the problem of ambiguity.

A non-destructive method is the CLSM approach where virtual sectional images are generated by varying the focus of the CLSM apparatus which leads to so called optical sectioning. The method is described in [5] and [18] stating that information can be acquired from a depth of 150 μm , results from 50 μm and 10 μm depth are shown.

A 3D dataset consisting of Voxels generated from optical sectioning is presented in [19]. Carbon fibres are used as tracer fibres that will be detected while the glass fibres are transparent. 50 images with information of 15 μm per image was put together to form a 3D dataset. Image processing containing thinning, as shown in Figure (2.5) were applied to determine the orientation tensor. The authors report high accuracy and reproducibility of this method. Major limitations imply the necessity of transparency and additional tracer fibres.

Optical sectioning methods show the additional advantage that also fibre length distribution can be measured.



Figure 2.5: Unthinned (top) and thinned (bottom) digitized 3D fibre images taken from [19]

Further work has been published that show improvements in the quality of image analysis [20], include reports about accuracy [21] or show the definition of 3D space curves for wavy fibres [22]. Some researchers presented another method to overcome the ambiguity problem: they use the asymmetric shadow around the elliptic footprint that comes from parts of the fibre underneath the surface to determine all angles comprehensively [23], [24].

2.4 Measuring fibre length distribution of short fibre reinforced polymers

Most commonly used methods to measure fibre length are destructive methods that remove the polymer matrix by burning or digestion [12]. The remaining fibres can be analysed by sieving or by image processing. The procedure is documented in the standard ISO 22314 [9] giving guidance for burning temperature, fibre separation, image acquisition, image processing and expression of results. The scope of this standard is short glass fibres. For long fibres several groups worked on the modification of the procedure in order to achieve accurate results. Since glass fibres can degrade at higher temperatures and tend to break when taken out of the furnace to be put into the image acquisition device, the influence of the burning temperature was studied in [25]. Instead of 625 °C as mentioned in the ISO standard, a temperature of 500 °C for 1 h was suggested. The remaining fibres have to be separated as good as possible to avoid or reduce the number of clusters. Semi automatic image processing tools are available that can identify clusters and calculate fibre length for each detected fibre. Examples for available tools are the apparatus FASEP used in [25], [26] and [27], the software tools „FiVer“ (SKZ Würzburg, Germany), „FibreShape“ (IST AG Vilters, Switzerland) and „SemAfore“ [28].

Another problem that arises using this method is that fibres can be cut at the image borders if too less images are stitched together or fibres are very long. A correction method that assumes evenly and randomly distributed fibres in the imaging plane was introduced. Estimating the length of the fibres that lie across the picture and are cut at the borders is done for each defined length class. This correction allows to determine mean length and length distribution functions [28]. The limitations discussed above and a novel method are described in [26].

Another approach to estimate average fibre length is the two sectioning method [29]. The determination of number of fibres in one section, number of fibres found in both sections, fibre diameter and sectioning distance allows for the calculation of average fibre length.

2.5 X-ray computed tomography for polymer characterisation

This section will give an overview about how CT found its way into materials science having its roots in the medical field. The focus will be put on the development of CT equipment and applications for polymer characterisation.

Amongst the first work that has been published about the application of CT for materials characterisation is a paper titled „Use of computed tomography in non-destructive testing of polymeric materials“ [30] from 1984. The specimens that were analysed were reinforced tires, thick walled rubber cylinders and a reinforced thermoplastic component. A medical CT device was used since at that time no industrial CT device or applicable Synchrotrons were available. In the following years progress has been made in tube and detector technology as well as Synchrotron facilities were equipped with tomography beam lines.

An overview about the principles of X-ray tomography and in particular the differences of laboratory based and Synchrotron based CT for materials science can be found in [31], [32]. Several publications describe the method of X-ray CT and applications in detail [33], [34], [35], [36], [37], [38], [39].

First approaches to generate 3D images followed the idea to modify a SEM device by adding a target and a rotation stage [40]. Modifications of medical scanners were also tested to be used for polymer characterisation [41]. In the late 1990s the company Skyscan brought the first industrial CT device on the market [42]. At that time the main advantages of CT was described as the possibility of 3D inspection, scanning without sample preparation, scanning under special environmental conditions and the possibility of in-situ experiments.

The aspect of in-situ analysis was investigated for a cellular polymer under compression [43]. Measured X-ray attenuation coefficients were correlated with the effective density of the foam which was used to characterize certain mechanical properties.

After these initiating activities more and more applications were established for all kinds of polymer materials. CT was intensively used for the characterisation of carbon and glass fibre reinforced laminate composites (CFRP, GFRP) since the advantage of looking inside materials is especially important for these complex structures. Qualitative analyses of bundle structure and defects like pores or cracks [44], [45], [46], [47], [48], [49] as well as quantification of local fibre volume fraction and fibre orientation [50], [51], [52], [53] were conducted. Several groups presented work about using CT data to model microstructure of laminate composites [54], [55]. High resolution Synchrotron CT was used to identify and characterize damage mechanisms on the fibre scale [56], [57], [58], [59], [60]. The use of CT for discontinuous fibre composites is discussed in the next chapter 2.6.

Another application that was processed with CT was in-situ damage characterisation of unfilled polymers. Synchrotron radiation was used, once with coarse resolution but very fast and once with high resolution in moderate time. Course resolution of 15 μm Voxel edge length and 1 min scan time allowed for the meso-scale quantification of

porosity [61]. The application of higher resolution of 0.7 μm Voxel edge length revealed the micro-structure of the voids that formed during tensile testing and furthermore conclusions about the cause for the shape and size of the cavities were drawn [62], [63]. Laboratory CT devices were also used for polymer characterisation. The detection and quantification of voids in rubber under fatigue loading was investigated. A Voxel edge length of 9.2 μm allowed for segmenting pores after different number of cycles. CT helped to find the point of damage initiation [64]. Transport phenomena were studied for a polymer electrolyte membrane fuel cell material. High resolution of 1.6 μm Voxel edge length together with interrupted in-situ compression tests were used to generate knowledge about the change in micro-structure and to build up models for virtual CFD analyses [65].

2.6 X-ray computed tomography for characterisation of discontinuous fibre composites

As the capabilities of CT methods successively increased in the last decade, also the number of publications about discontinuous fibre characterisation using CT increased. Different types of fibres were analysed ranging from glass and carbon to cellulose of which glass is the most intensively studied. Polypropylene or Polyamide act as polymeric matrix.

In 2011 a paper listed the applications of „X-ray tomography to foams and fibre networks“ [66]. The entries of Table 1 that are relevant for this theses were copied and a new table with additional publications until 2018 was generated. Table 2.1 contains publications that describe CT as tool for discontinuous fibre polymer composite materials only. The papers were clustered according to the method applied to CT data as described in the list below the table.

Already the first publication followed the aim to extract quantitative data about fibre orientation and length distribution. In the beginning of 2000 the computational capacities in terms of memory and computational speed were amongst the limiting factors. CT devices brought to market in that time allowed already for the generation of data in high quality hence the quantification of thicker fibres with good contrast (like glass fibres) was possible.

Table 2.1: Publications about applications of CT for discontinuous fibre polymer composite materials extracted partly from [66] with additional recent work

| Material | CT type | CT device / facility | Voxel size (μm) | Information extracted | Year | Ref. |
|---|-------------------|-------------------------|------------------------------|-----------------------|------|------|
| Visual analysis of grey value slice images | | | | | | |
| PAGF35 | Lab. ³ | V tome x | 7.9 | Qualitative FO | 2010 | [67] |
| 2D image processing | | | | | | |
| PPGF40 | Lab. | Xradia | ¹ | Content, length | 2009 | [68] |
| PPGF20 | Lab. | Skyscan 1172 | 6 | FOD | 2015 | [69] |
| PAGF30 | Lab. | Marubun XVA160 α | ¹ | FOD | 2015 | [70] |
| Mean intercept length (MIL) | | | | | | |
| PAGF30 | SCT ² | Elettra, Syrmep | 9 | FOD, Anisotropy | 2008 | [71] |
| PACF30 | SCT | Elettra, Syrmep | 9 | FOD, Anisotropy | 2011 | [72] |
| PAGF30 | SCT | Elettra, Syrmep | 9 | FOD, angles | 2012 | [73] |
| 3D image processing | | | | | | |
| Wood fibres | SCT | Tomcat | 0.7 | Length | 2012 | [74] |
| Cellulose fibres | Lab. | Skyscan 1174 | 7 | L/d | 2016 | [75] |
| ABS10 | Lab. | Yxlon | ¹ | FOD | 2018 | [76] |
| Individual fibre characterisation | | | | | | |
| PPGF30 | Lab. | Skyscan 1072 | ¹ | FOD, FLD | 2002 | [77] |
| Foam + GF | Lab. | Skyscan 1072 | 3 | FOD, FLD | 2004 | [78] |
| PPGF | ¹ | ¹ | ¹ | FOD | 2006 | |
| GF | Lab. | ¹ | 8.7, 4 | FOD, FLD | 2010 | [79] |
| Fe Alloy fibres | Lab. | X-Tek, Nanotom | 7, 2.3 | FO, segment length | 2011 | [66] |
| PPGF1-30 | Lab. | Nanotom | 5, 2 | FOD, FLD, etc. | 2011 | [80] |
| PPGF1-60 | Lab. | Nanotom | 1-10 | FOD, FLD, etc. | 2012 | [81] |
| PPGF24 | Lab. | Nanotom | 8.1, 2 | FOD, FLD, etc. | 2013 | [82] |
| PPGF30 | Lab. | Skyscan 1072 | 1.8 | FOD, length | 2016 | [83] |
| PAGF35 | Lab. | RX Solutions | 2.53 | FOD | 2016 | [84] |

Different approaches were developed over the years to extract micro-structural information. They could be classified into 5 different groups:

- Visual analysis of grey value slice images (Orientation distribution).

¹not mentioned by authors

²SCT: Synchrotron radiation facility

³Lab.: Laboratory CT device

2.6. X-RAY COMPUTED TOMOGRAPHY FOR CHARACTERISATION OF DISCONTINUOUS FIBRE COMPOSITES

- 2D image processing on slice images (Fibre content, length, orientation)
- Mean intercept length (MIL) (Fibre orientation)
- 3D image processing using opening with structural element (Aspect ratio L/d)
- Individual fibre extraction (Complete micro-structure)

The information that can be extracted from each approach is indicated in brackets. Analysing CT slice images visually is inherent since it is the first that is done when the scan is finished. If there is no commercial tool available that could be applied to characterise micro-structure quantitatively one might use visual analysis to emphasise and confirm results acquired by other methods. [67]

The obvious approach of applying 2D image processing methods to 3D data was presented 2009 and is still used. 3D CT data is therefore represented by stacks of slice images that are processed by similar algorithms as they were used for LOM or SEM analyses. Information about fibre content and fibre length were determined semi-automatic using binarisation and eigenvalue analysis [68] [69]. A completely manual approach was presented in [70] where the main orientation tensor elements of ca. 100 fibres were determined for several slices. Making use only of a part of the comprehensive 3D information by extracting 2D cross sectional images is not efficient. Fibre length distribution is not accessible since only some fibres are visible completely in one cross sectional image.

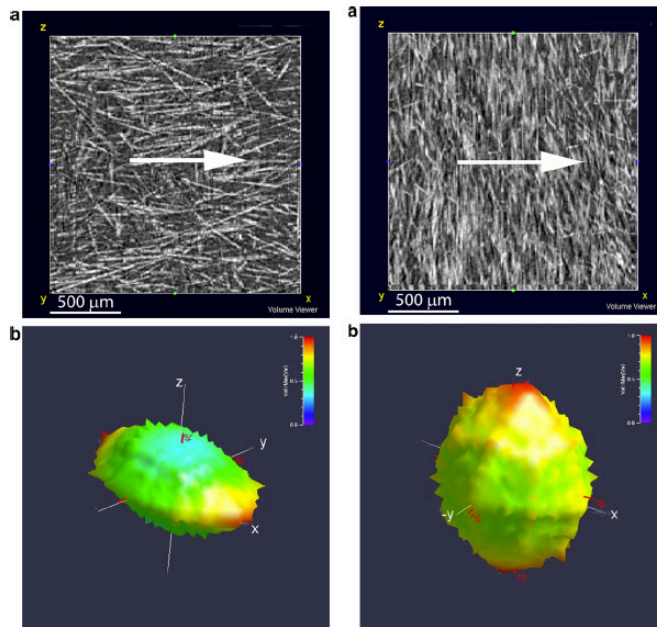


Figure 2.6: Original CT slice images (top) and MIL fabric tensor visualisation (bottom) [71]

A concept to determine information about fibre orientation was presented in 2008 using Synchrotron data and 3D image analysis applied to glass fibres in polyamide matrix [71]. The scans were performed at 9 μm Voxel edge length which was in the range of fibre diameter of 11 μm . After segmenting the fibres into a binary image a grid of lines was placed on the 3D image in different rotation angles. Mean interception length (MIL) is defined as the average distance between the two phases along a certain direction. The analysis at different angles leads to $MIL(\theta)$ values that can be visualised by polar plots (Figure 2.6). The results were shown for regions of (120 Voxels)³ in size. The MIL fabric tensor can be calculated which gives information about anisotropy. An eigenvalue analysis of this tensor leads to angles that correspond to fibre orientation. As result of this method a 3D visualisation of the MIL fabric tensor as ellipsoid, the degree of anisotropy and the angles of principle axes can be calculated. This method was also applied to carbon fibre reinforced polymers [72] and was used for a comparative study of 2D and 3D methods for orientation measurement [73]. This is the most comprehensive study published about the evaluation of a CT method by comparison with well established 2D image processing. Since both methods have in common that out of plane angle contains ambiguous information the comparison was done based on the angles θ and ϕ .

A method for the determination of fibre length and diameter forming the aspect ratio L/d was published by two groups [74], [75]. A structural element is used to apply an opening procedure on previously determined, labelled objects within a 3D dataset. Both groups developed their method for lignocellulosic fibre materials that usually show big variation in length, diameter and shape. The method was complemented by calculating the orientation efficiency factor which allows together with the aspect ratio to estimate Young's modulus [85].

Different image processing methods can be applied to determine FOD on Voxel basis. The very recent work [76] discusses methods for the determination of fibre orientation on Voxel basis. Three different image processing concepts, anisotropic Gaussian filtering, Hessian matrix calculation or structure tensor calculation are described and compared in terms of accuracy and performance. „The image is filtered by an anisotropic Gaussian filter with a certain number of discrete orientations NG to search for the best matching one.“ ([76]) The structure tensor is based on the first derivatives which are arranged in tensor form by building the dyadic products. An eigenvalue analysis leads to fibre orientation. Artificial and scanned data were used for evaluating the methods. The best results were obtained with the structure tensor method while the Hessian approach is sensitive to noise and gives wrong directions in fibre crossing regions and fibre ends.

CT data analysis methods that were tested first and are still the most powerful, since most detailed micro-structure description can be determined, are individual fibre characterisations. The aim is to extract accurate information from every single fibre within the Voxel dataset. This requires a set of image processing steps that are usually applied subsequently. It is also common that assumptions about fibre geometry and grey value distribution within the fibres are made.

2.6. X-RAY COMPUTED TOMOGRAPHY FOR CHARACTERISATION OF DISCONTINUOUS FIBRE COMPOSITES

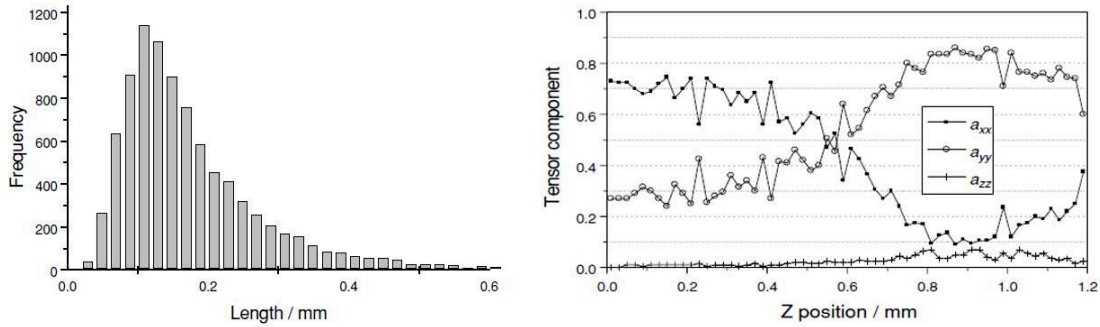


Figure 2.7: FLD and main diagonal tensor elements as results of the „vector fitting “ method for PPGF30 from [77]

The first paper about individual fibre characterisation using lab-based X-ray tomography was published in 2002 [77]. In a first step the mean intensities along chords that are rotated within the 3D dataset are analysed. The chord orientation parallel to the fibres will have higher average grey value and will therefore be saved as vector for that certain region. Taking into account the mean grey values of all saved vectors and the angles between these vectors, some vectors will be deleted resulting in remaining vectors that lie on the centre lines of the fibres. In the next step these vectors which are 10 Voxels long, are connected to form complete medial axes of single fibres. The results are shown as FLD and main tensor elements as shown in Figure 2.7. The cross sectional slice image (Figure 2.8) shows fibres in black and matrix in white. Besides some ring artefacts the fibres are not well represented in terms of sharpness and grey value distribution along the fibres. The author concludes that many fibres are not extracted (62 %) because of the presence of these artefacts.

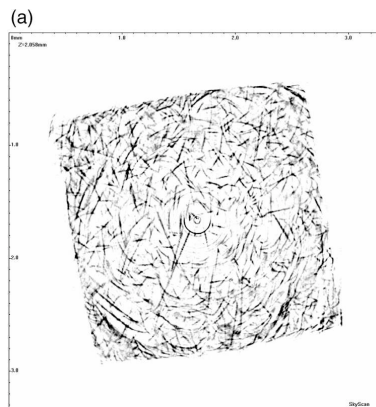


Figure 2.8: CT slice image showing glass fibres in black and matrix in white from [77]

The aim of another paper was to determine FLD and FOD of glass fibres in phenolic foam [78]. High resolution scans with 3 μm Voxel edge length were conducted leading to good contrast and reasonable image quality. The fibres were segmented and transferred to an STL model. The separation of fibres and polymer matrix was not perfectly possible since some polymer at the fibre surface was segmented too. The fibres were idealized in a way that an average shear zone diameter was defined and 300 fibres were manually modelled as perfect cylinders with 100 μm diameter which is 6 times the fibre diameter. FLD and FOD were calculated manually using a CAD tool. The authors concluded that they could determine valuable information that would not be accessible by destructive sectioning since the foam structure can only be assessed by non-destructive methods. Nevertheless there were issues with image processing and only manual measurements could be performed resulting in very time consuming analyses.

A software concept for the determination of fibre length distribution was published in [79]. Scans were performed at 8.73 μm Voxel edge length and artificial test data sets were generated. The concept is a model based approach that implies the fibres to be straight and cylindrical with the same diameter for all fibres. The idea of Eigenvalue analysis [86] of the Hesse-matrix is used to identify Voxels that are located within the cylindrical structure and use them as seed points. The fibres are reconstructed by starting from these seed points and tracing in the direction of smallest Eigenvector (Figure 2.10a). The traced line is the fibre centre line. Voxels within the predefined diameter are filled with fibre labels. Since the Hesse-matrix is not leading to correct direction at every position it is possible that two or more fibres overlap. On the other hand gaps can be produced during tracing because of noise or other CT artefacts (Figure 2.10b). Both problems are solved by the detection of critical Voxels that are processed in a subsequent step (Figure 2.10c). The length of a fibre is calculated by a multiplication of number of centre voxels and the voxel size. Artificial data sets containing up to 12 fibres lead to 98 % accuracy for fibre length. For real CT datasets the quality of the approach was visually evaluated and found to be very good. Figure 2.9 shows a cross sectional slice image on the left and the segmentation result on the right. The authors state that despite of high curvature and high overlapping rate, fibres have been segmented correctly.

The next approach of individual fibre characterisation was applied for metallic fibre mat infiltrated with resin [66]. A 3D image processing pipeline was employed in this work starting with PSF deconvolution for noise reduction followed by segmentation (binarisation by local thresholding). Local thresholding by indicator kriging showed better results than global thresholding. The binarised data (Figure 2.11) is then transferred to medial axes by skeletonisation. A problem arises when medial axes paths intersect as shown in Figure 2.12. Since the segments that are connected to the nodes were not connected, only segment lengths could be determined. Local fibre orientation was determined by the inertia tensor.

2.6. X-RAY COMPUTED TOMOGRAPHY FOR CHARACTERISATION OF DISCONTINUOUS FIBRE COMPOSITES

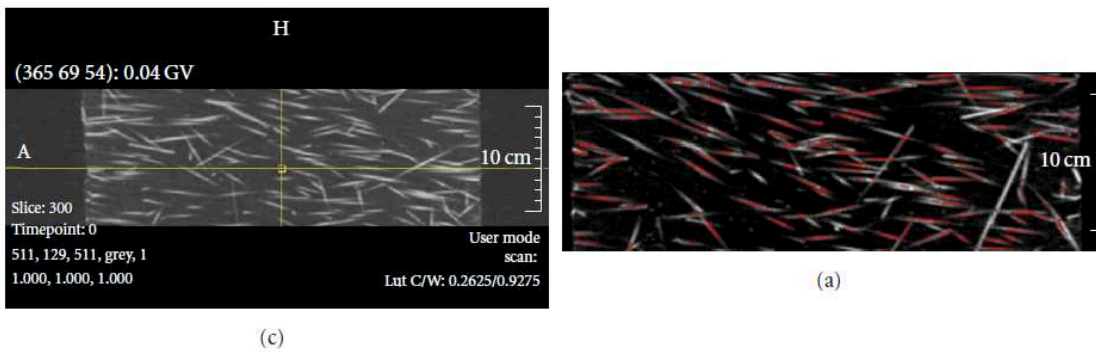


Figure 2.9: Slice image of glass fibres (left) and result of the segmentation method (right) adapted from [79]

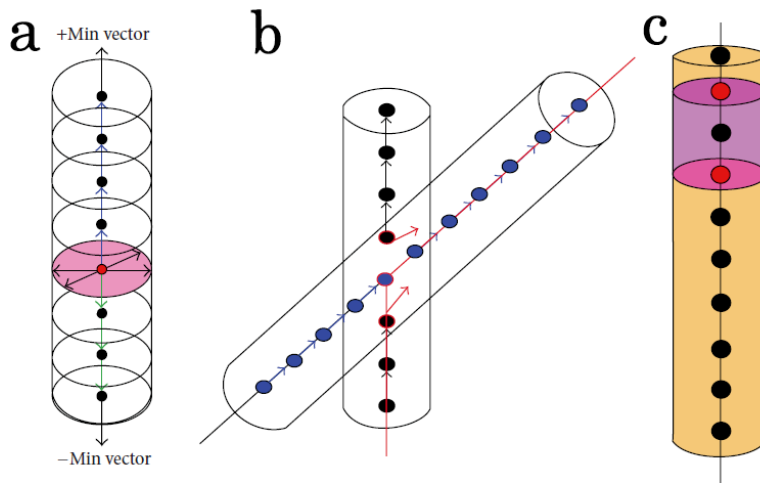


Figure 2.10: Schematic of fibres with points on medial axis (a), the intersecting problem (b) and the resulting medial axis after closing of gap (c) adapted from [79]

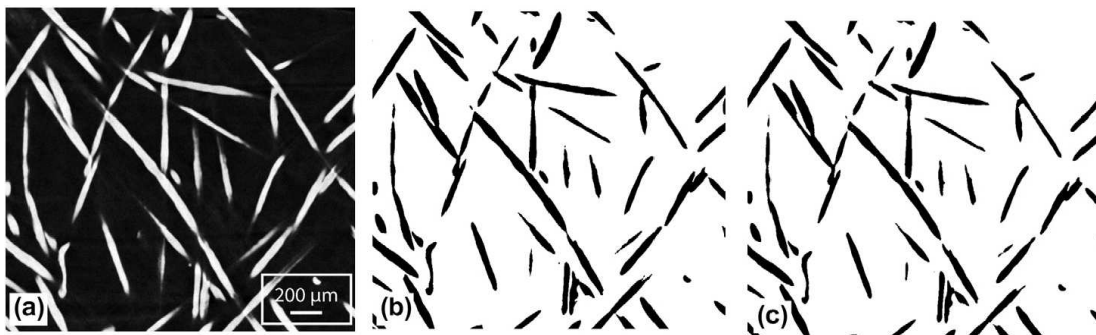


Figure 2.11: CT slice image showing metal fibres in white and matrix in black (a). Segmentation using global thresholding (b) and local thresholding (c) from [66]

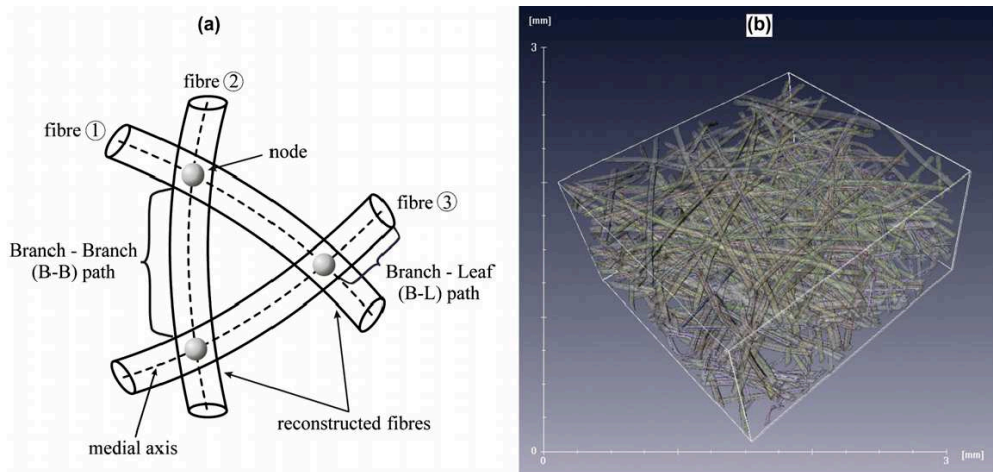


Figure 2.12: (a) A schematic illustration of the medial axes and nodes (path intersections) formed between three intersection fibres. (b) View of the medial axes and the reconstructed fibres (transparent) of the fibre network from [66]

A novel approach was published in 2016 which uses Monte-Carlo techniques to detect individual fibres [83]. A Voxel edge length of $1.8 \mu\text{m}$ was applied. The analysed material systems were glass fibre filled PA and PP with varying fibre contents. The underlying model assumes chords of cylindrical fibres with constant radii and varying length. Input for Monte-Carlo pattern matching is again filtered and binarised data. The grey value for global thresholding was chosen in a way that the fibre volume content matched the value from thermogravimetric analysis. For pattern matching the integral density functions along radial lines within randomly chosen spheres were calculated. By calculating mass and centre of gravity of all points within the sphere and the definition of a minimal deviation of these values as optimisation criterion, separate fibres could be detected. A centralised main process controls parallel distributed pattern matching routines and controls parameters that are iteratively improved. The quality of the method in terms of reproducibility and accuracy was determined using virtual fibres and comparison with 2D images from polished sections. The authors concluded that 90 % of all fibres could be detected and orientation tensor elements could be determined with high reproducibility. The evaluation of orientation of virtual data was done by comparing results with manual fibre tracking. The authors state good agreement although some tensor values differ by ca. 0.2. This method was applied in [87] to determine fibre orientation, length and diameter for feeding homogenisation models that predict Young's modulus.

Commercial software tools that allow for characterising fibres (VG Studio MAX, Avizo, GeoDict, others) can determine fibre orientation based on different methods like structure tensor or template matching. Quite recently it was made possible with Avizo to segment individual fibres and to characterise length, too. The lack of information about accuracy, performance and applicability are drawbacks of these tools. Actual scientific work is conducted with the goal to use machine learning algorithms to segment individual fibres from 3D data or even from projection images.

Investigated materials

3.1 Fibre materials in Polypropylene

The model polymer matrix material used for this thesis was Polypropylene (PP). Two grades of PP were used, a heterophasic co-polymer (PP1) and a homo-polymer (PP2). These two grades were chosen because of availability and the differences had no influence on the characterisation results since densities and attenuations were very similar.

Fibre materials investigated were glass, carbon, cellulose, Polyvinylacetate (PVA) and Polyethyleneterephthalate (PET). Short fibres were used for method development and evaluation. For long fibre composites the developed methods were applied with length specific tasks. Relevant properties of fibres and matrix are listed in Table 3.1. For an estimation of expectable radiographic contrast it is necessary to know following characteristics since the attenuation of X-rays follows the law of Lambert-Beer (Equation (3.1)):

- X-ray absorption coefficient for the respective material
- Geometry and material composition of the specimen
- Emitted energy spectrum of the X-ray tube
- Energy dependent detector sensitivity

$$I = I_0 \cdot e^{-\mu(E)d} \quad (3.1)$$

I_0 ... Intensity without attenuation

μ ... X-ray absorption coefficient

E ... X-ray energy

d ... irradiated length

Table 3.1: Chemical formulations, densities and X-ray absorption of investigated materials

| Material | Density (g/cm ³) | Chemical formula | Absorption @80 keV (1/cm) | Absorption @30 keV (1/cm) |
|-----------|---------------------------------|--|---------------------------------|---------------------------------|
| PP | 0.905 | C_3H_6 | 165 | 245 |
| PVA | 1.3 | C_2H_4O | 230 | 402 |
| PET | 1.38 | $C_{10}H_8O_4$ | 234 | 415 |
| Cellulose | 1.5 | $C_6H_{10}O_5$ | 260 | 484 |
| Carbon | 1.8 | C | 290 | 461 |
| E-Glass | 2.52 | SiO_2 (54 %) Al_2O_3 (14 %) CaO (17.5 %) B_2O_3 (10 %) MgO (4.5 %) | 3310 | 543 |

The online tool XCOM by NIST (National Institute of Standards and Technology) [88] was used to determine total X-ray absorption coefficient curves in the range of 10 to 100 keV with coherent scattering. Multiplying with density results in relative absorption $\mu(E)$ which is plotted in Figure 3.1. The values at 80 keV and 30 keV were entered into Table 3.1 since 80 kV is the voltage typically used for scanning and the average energy is at lower energy, roughly estimated with 30 keV.

One can recognize from the absorption values that all materials containing carbon, hydrogen and oxygen only show similar behaviour. The curves of Figure 3.1 for PP, PVA, PET and Cellulose run almost parallel. The only exception is the curve for carbon which shows higher absorption at higher energies and lower absorption at lower energies. Absorption can be related to density especially for higher energies. For glass the influence of energy on absorption is much higher which is related to the presence of materials with higher atomic number.

As mentioned above it is necessary to know the spectrum and the detector sensitivity to be able to predict grey values. This could be done using simulation tools. For this thesis such simulations were not performed because the relevant contrast is the one in the reconstructed data which is influenced by the reconstruction method as well as the chosen specimen geometry. The conclusion of the differences in absorption coefficients are that expectable contrast for the polymer and carbon fibres will be in similar range.

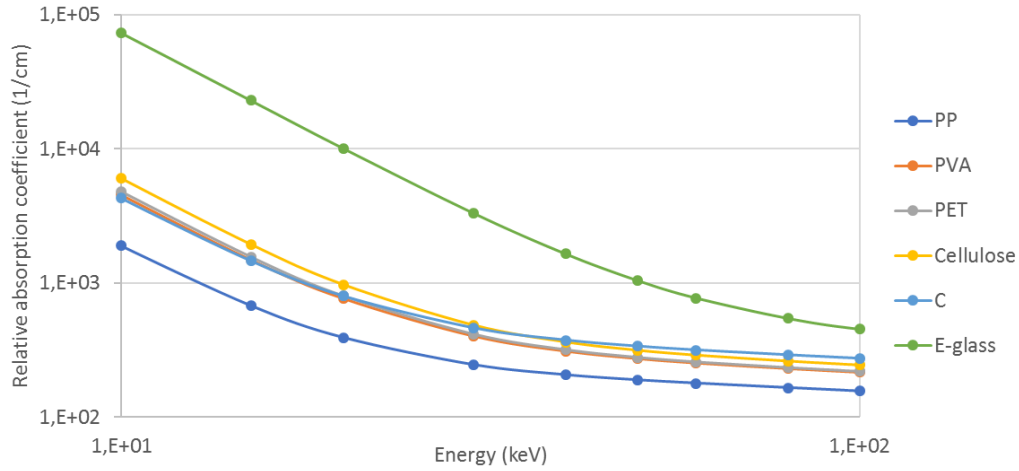


Figure 3.1: Relative absorption coefficients $\mu(E)$

From the mentioned materials, composites were produced. Short fibre composites were produced by compounding and injection moulding. The long fibres were impregnated with the matrix, chopped to pellets and injection moulded. Material compositions with fibre contents are listed in Table 3.2.

Table 3.2: Nomenclature and characteristics of investigated composite materials subdivided into short and long fibres.

| Abbreviation | Matrix | Fibres | Content per weight (wt. %) | Content per volume (vol. %) | Fibre diameter (μm) |
|-------------------------------|--------|--------|----------------------------|-----------------------------|----------------------------------|
| Short fibre composites | | | | | |
| PP-sGF-30a | PP1 | GF1 | 30 | 13.4 | 12.5 |
| PP-sGF-5 | PP2 | GF1 | 5 | 1.9 | 12.5 |
| PP-sGF-10 | PP2 | GF1 | 10 | 3.9 | 12.5 |
| PP-sGF-20 | PP2 | GF1 | 20 | 8.3 | 12.5 |
| PP-sGF-30 | PP2 | GF1 | 30 | 13.4 | 12.5 |
| PP-sPVA | PP1 | PVA1 | 20 | 14.9 | 16 |
| PP-sPET | PP1 | PET1 | 20 | 14.1 | 22 |
| PP-sCell | PP1 | Cell | 20 | 13.1 | 10.5 |
| Long fibre composites | | | | | |
| PP-IGF | PP1 | IGF3 | 23.8 | 10 | 16 |
| PP-IGF-a | PP1 | IGF3 | 40 | 19.4 | 16 |
| PP-IPVA | PP1 | IPVA2 | 13.8 | 10 | 16 |
| PP-IPET | PP1 | IPET2 | 14.5 | 10 | 22 |
| PP-ICF | PP1 | ICF2 | 18.1 | 10 | 7 |

3.2 Test specimens

Different analysis were performed using suitable test specimens. Specimens that were actually scanned, were machined from pellets, multi purpose test specimens (MPS) or sheets. Dimensions were adapted to the necessary resolution.

3.2.1 Material for reference data sets and reproducibility

For the generation of reference data sets and the determination of reproducibility the composite material PP-sGF-30 was chosen.

The repetitive scans were conducted on a specimen that was cut from an injection moulded MPS bar type 1A (according to the standard DIN-EN-ISO 527-2 [89]). A very fine notch was induced with a razor blade at one edge to be able to register all data and to ensure that the scan area is similar as possible from scan to scan.

The reference data sets were also determined from an MPS Type 1A bar. A specimen was sawed near the surface. The volumes that were taken out of the scan data were very small to contain approx. 250 fibres each. The notation was chosen according to the position of the cut-outs: *Centre_1*, *Centre_2*, *Edge*.

Another cut-out from an MPS bar type 1A made of PP-sGF-30 was used to investigate the influence of analysis volume on the fibre characterisation results.

3.2.2 Specimens to consider influence factors on the measurement results

To investigate the impact of evaluation volume cut-outs from MPS bars type 1A made of PP-sGF-5 and PP-sGF-30 were prepared. Data sets with different dimensions in Z direction were generated and analysed. Z dimensions from 0.5 mm to 3.5 mm in steps of 0.5 mm were chosen. Dimension in X and Y were 1 mm each. The Voxel edge length was set to 2 μm . Results are shown in Chapter 6.4.

The investigations of influence of specimen orientation on the turntable was performed on smaller specimens that were cut-out at the 4 positions of the Sector specimen 3.4. The size was chosen to fit the projection on the detector completely. This allows for rotating the specimen and scanning in different orientations on the turntable. These specimens were scanned at 0° and 90° orientation each (see Figure 3.4). Both data sets were registered to each other and the same region without border areas were analysed.

3.2.3 Specimens to determine variations of fibre orientation

The evaluation of fibre orientation results was conducted by comparisons with standard methods. For theses comparisons a sheet with 2 mm thickness was produced by injection moulding using PP-sGF-30a. A variation of fibre orientation was realised by using an

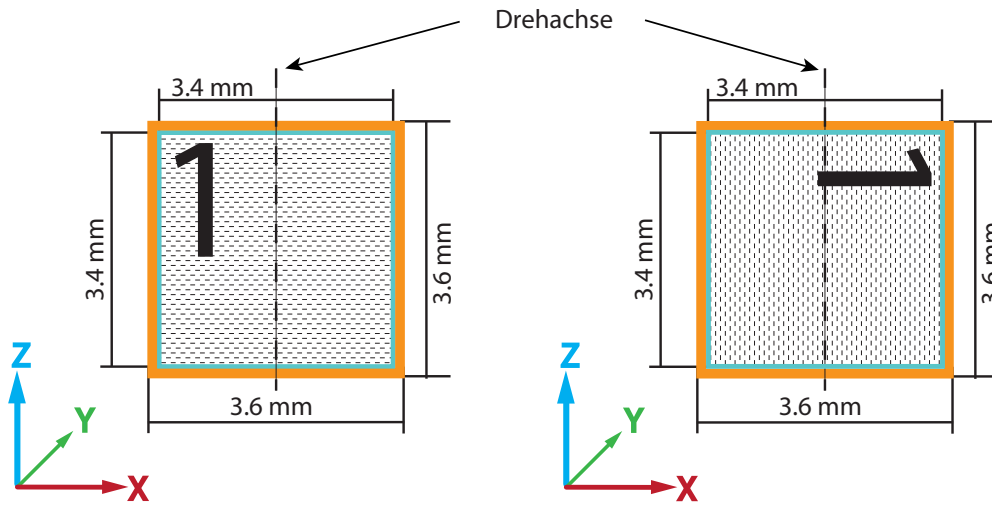


Figure 3.2: Schematic of a single specimen that was scanned at 0° and 90° orientation on the turntable. The orange area was scanned and the cyan area was analysed.

opening tool that resulted in a sector geometry.

Four positions with different distance to the gate and lateral offset were cut-out (see Figure 3.3). The size of the specimens was chosen to be able to scan at $2\ \mu\text{m}$ Voxel edge length. The size of one specimen is shown in Figure 3.4. The scan area spans $(5,3 \times 3,6)\ \text{mm}^3$ and is marked orange. Analysis area was reduced in X direction (marked cyan) to keep file size within the range of 6 GB which was limited by the used hardware (see chapter 4.2.2). The plane for grinding and optical analysis is YZ (marked red). The same specimens were used to investigate the layered orientation structure over sheet thickness.

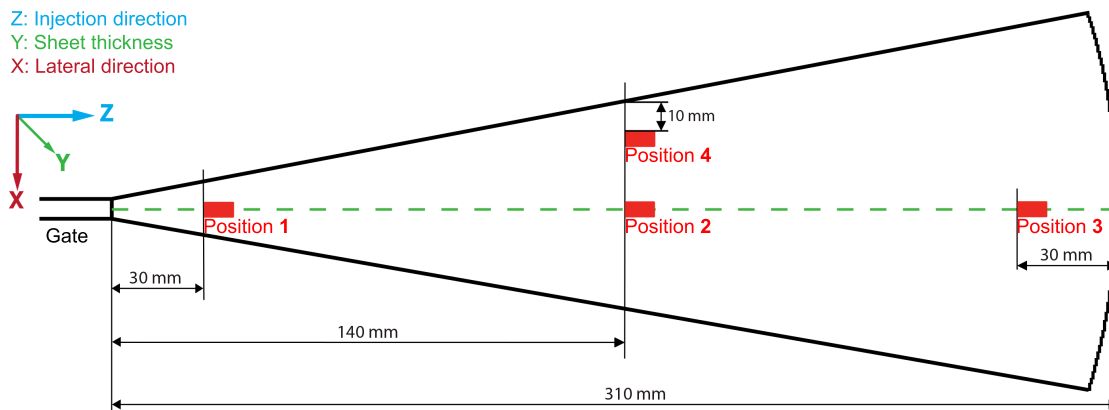


Figure 3.3: Schematic of the sheet with marks of positions (1-4) where specimens were cut out

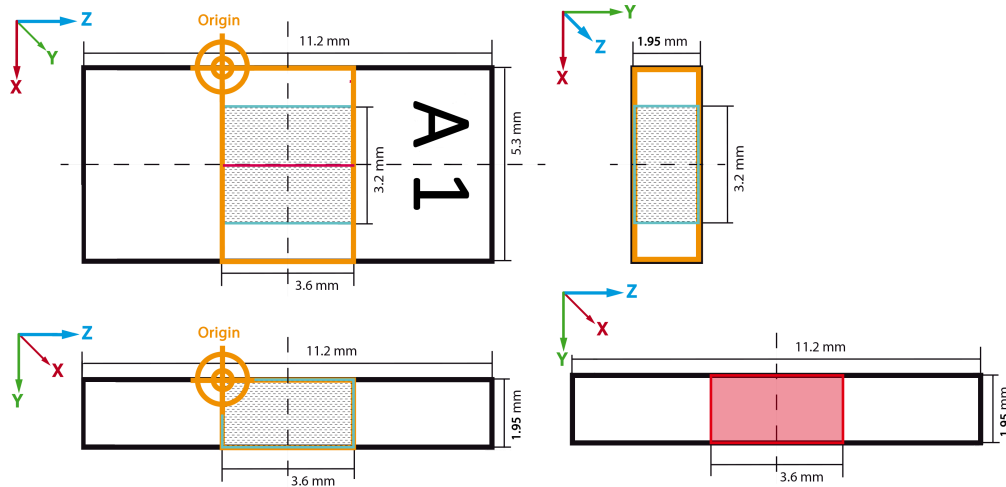


Figure 3.4: Schematic of a single specimen. The orange area was scanned. For the cyan area fibre orientation was determined by CT, the red line and rectangle mark the sectional plane for grinding.

3.2.4 Specimens for the determination of fibre length distribution

For method evaluation in terms of fibre length determination, specimens from an MPS made of PP-sGF-30 with varying fibre content were cut-out. Bigger cut-outs containing several thousand fibres were analysed by CT and by applying methods from the standard ISO 22314 [9]. Very small cut-outs were prepared that contained only a few hundred fibres. For these data every fibre was analysed by LOM and CT.

Comparison with standard method at calibration laboratory

The calibration laboratory SKZ – TeConA GmbH (Würzburg, Germany) determined fibre length distribution for PP-sGF-5, PP-sGF-10, PP-sGF-20 and PP-sGF-30 according to [9]. The size of the specimens were $2 \times 2 \times 3 \text{ mm}^3$, cut-out from MPS at longitudinal centre and near a cross sectional edge. The same specimens were scanned first and then sent to SKZ for pyrolysis.

Lab based comparison of every individual fibre

From a MPS specimen made from PP-sGF-30 very small pieces were carefully cut. The specimens were irregularly shaped with dimensions smaller than $500 \mu\text{m}$.

3.2.5 Injection moulded A5 sheet

A sheet with dimensions of A5 was injection moulded from PP-sGF-30a. A film gate in the size of the small edge was used. Specimens were cut out of 16 positions along one half of the sheet.

3.2.6 Specimens for long fibre characterization

For the determination of impact strength of long fibre materials, notched Charpy impact tests on standard Charpy specimens were conducted according to [90]. For the composite material systems PP-IGF, PP-ICF, PP-IPET and PP-IPVA free fibre length was analysed in this study.

This study also contained a variation of pellet length. In contrast to the short fibre materials the long fibre pellets were produced by impregnating continuous fibre rovings with the PP matrix. After impregnation the strand was chopped to a certain length. Pellet lengths of 4, 7, 10 and 15 mm were produced in this way. Undamaged standard MPS, produced with 7 mm long pellets, were used to characterise micro-structure additionally.

Methods

4.1 X-ray computed tomography

4.1.1 Measuring technique

The CT investigations were conducted using a Sub- μm -CT laboratory device „Nanotoms“ delivered by GE phoenix|x-ray (Wunstorf, Germany). This device was taken into operation in February 2008 at Upper Austria University of Applied Sciences, Campus Wels. A Photo of the device with mounted specimen in front of the X-ray tube is shown in Figure 4.1.

The device is equipped with an X-ray tube from GE phoenix|x-ray that can be operated at maximum 180 kV with different focal spot sizes. A cooling system for the tube housing was added on later. The detector from Hamamatsu [91] operates on the scintillation principle, has 2300 x 2300 pixels with a size of 50 μm edge length and a dynamic range of 12 bit. All components are built on a granite basis with a fixed X-ray tube position. The specimen is mounted onto a turntable that is equipped with a chuck. The turntable has an air bearing.

The target material can be changed, available materials were Tungsten and Molybdenum which are evaporated onto a beryllium window. The X-ray spectrum generated with Molybdenum fits better to lower absorbing materials since the mean energy is lower than with Tungsten. For all CT scans conducted for this thesis the target material was Molybdenum.

Parameters for acquisition of projection images

For the acquisition of projection images and setting of X-ray parameters the software tool „datos—x 2 acquisition“ (2.2.1 RTM) from GE phoenix—x-ray, which was delivered together with the CT device, was used.

Setting of acceleration voltage, current and mode has to be made for the X-ray tube. Focal spot size can be chosen by setting one of four different modi. The ideal shape of



Figure 4.1: Photo of the CT device Nanotom 180NF at Upper Austria University of Applied Sciences, Campus Wels

the focal spot would be dot-like which would lead to destruction of the target material. To avoid damage to the target, the electron beam is defocussed to spread energy discharge of the electrons over a bigger area. Modi 1 to 3 lead to fixed focal spot sizes by setting the target power to a constant value. The manufacturer gives information about the maximum power per mode in the handbook [92] with 0.6 W, 0.8 W, 1.1 W and 2.7 W. Resulting focal spot size is not mentioned, the best possible expected value is below 1 μm . The focus of the electron beam is depending on power in Mode 0 while it is constant for all other modi. At lower power values a focus adjustment is possible to optimize sharpness. Maximum possible voltage for mode 0 and target material Molybdenum is 100 kV.

The integration time („ T_i “) of the detector has to be chosen with the lower limit of 500 ms in non-binned mode. [91]

A CT setup using a flat panel detector is called „Cone beam CT“ setup which works with geometrical magnification [33]. Both distances, source to object (SOD) and source to detector (SDD) can be modified and determine together with the detector’s Pixel edge length the Voxel edge length. Equation 4.1 shows that high resolution can be achieved by either increasing SDD or decreasing SOD. At the Nanotom-s SDD can be modified between 200 mm and 500 mm. A compromise between high resolution and high grey values has to be found since high SDD leads to low intensity. Finally SOD and SDD together have to be optimized in a way that the specimen fits onto the detector image.

$$V_{xl} = \frac{SOD}{SDD} \cdot P_{xl}; P_{xl} = 50 \mu\text{m} \quad (4.1)$$

Additional parameters that have to be set before starting a CT scan are listed below. Names and abbreviations are defined by the CT manufacturer.

- Number of projection images. „NoI“

- Number of images per angular step, that are used for averaging. „Average“
This is used to reduce noise that is mainly induced by the low number of photons collected by each detector pixel because of low photon flux.
- Number of images per angular step, that are discarded at the beginning. „Skip“
After specimen rotation and especially for short integration times, 1 to 2 images should be discarded to avoid that object motion is collected by the detector.
- „Detector shift“.
Movement of the detector in horizontal direction by small random values to reduce ring artefacts.
- „Auto—Scan optimizer“.
To compensate movement of focal spot, tube or object it is possible to collect projection images at 9 angular positions, that are compared after the scan with the actual projection images. Movements in X- and Y-direction and scaling can be compensated for.
- „Binning“.
This allows to combine several pixels to one which leads to higher grey values. It can be used to reduce integration time to achieve the same grey values or to reduce noise at the same integration time. Two modi are available 2 x or 4 x 4.
- „Virtual Sensor“.
The number of pixels in horizontal direction can be doubled or tripled by moving the detector. This allows for scanning bigger specimens at the same Voxel edge length.
- „Fast—scan“.
This option reads the detector continuously during continuous rotation. Thereby it is not possible to average which leads to shorter scan times.
- „Multi—scan“.
This option allows to scan an elongated specimen with several scans one above the other in vertical direction.
- Image size X, Y.
Maximum size is 2300 x 2300 Pixel. If the application allows it, the values can be reduced. This leads to smaller memory consumption and to reduced reconstruction times.

Calibration images have to be collected before starting the scan that are used to reduce dark current of the detector (offset), inhomogeneous intensity distribution of the X-ray source and inhomogeneous detector signals (Gain). For this calibration, images with and without X-rays and without specimen are collected and saved as averaged image. The application of these calibration images is done automatically by the software. The number of images that are used for averaging can be chosen arbitrarily. Since the

signal to noise ratio of the calibration images is transferred to the projection images that will be reconstructed, a large number for averaging should be used. For all scans used for this thesis, 100 offset and 100 gain images were averaged.

Table 4.1: Optimized scan parameters for scans with different resolution for glass fibre filled composites

| VS (μm) | U (kV) | I (μA) | „ T_i “ (ms) | „NoI“ () | Tube mode () | SOD (mm) | Scan- time (min) |
|-------------------------|-----------|------------------------|-------------------|--------------|---------------------|-------------|------------------------|
| 1 | 80 | 180 | 1200 | 1900 | 1 | 6 | 270 |
| 2 | 80 | 120 | 750 | 1700 | 0 | 12 | 129 |
| 3 | 80 | 140 | 750 | 1700 | 0 | 18 | 129 |

Table 4.2: Optimized scan parameters for other fibre filled composites

| Material system () | VS (μm) | U (kV) | I (μA) | „ T_i “ (ms) | „NoI“ () | Tube mode () | SOD (mm) | Scan- time (min) |
|---------------------------|-------------------------|-----------|------------------------|-------------------|--------------|---------------------|-------------|------------------------|
| PP-sPVA | 2 | 70 | 220 | 750 | 1900 | 0 | 12 | 297 |
| PP-sPET | 3 | 50 | 250 | 1000 | 1700 | 0 | 18 | 202 |
| PP-sCell | 1,5 | 70 | 120 | 900 | 1900 | 0 | 9 | 350 |
| PP-ICF | 1 | 60 | 240 | 1000 | 1900 | 1 | 6 | 702 |

Tables 4.1 and 4.2 give selected optimized parameters for material systems and different resolutions. The same parameters were applied for different fibre content for glass fibres. Other important parameters are set as follows independent of resolution:

- „Average“ : 5
- „Skip“ : 1
- SDD : 300 mm
- „Detector-Shift“ and „Auto—Scan optimizer“: ON
- „Binning“ : OFF
- „Virtual Sensor“ and „Multi—scan“: activated only for big scan volume

CT reconstruction

For the reconstruction of projection images the software tool „datos—x 2 reconstruction“ (2.2.1 RTM) from GE phoenix—x-ray was used. The mathematical principle which is

used by the software in a modified way, is the filtered back projection according to Feldkamp. [93].

Before reconstructing the complete data set, one slice is reconstructed for the use of parameter optimization. The tool „Auto—Scan optimizer“ helps to optimize the parameters for reducing movements and for calculating the centre of rotation on the detector. The value for centre of rotation can be determined by this tool after the specimen was rotated by 360°. This value moves the projection images horizontally in order to align focal spot position at the tube, centre of rotation at the turntable and detector centre. If this is not the case, reconstruction would be blurred and double edge structures would develop.

Following parameters have to be set for reconstruction:

- Reconstruction area.
- Centre of rotation.
- Movements for optimizations („Auto—Scan optimizer“).
- Volume data type.
- Resolution adaptation (1, half or double).
- Artefact correction methods. (e.g. beam hardening correction)
- ROI filter for optimizing edge regions of the volume.
- Rotation angle of complete volume around vertical axis.

The parameters that can be standardized are given in the list, the other mentioned parameters have to set depending on the application.

- Volume data type: 32 bit float for reconstruction, unsigned 16 bit for final data set
- Resolution adaptation: 1
- Artefact correction: Beam hardening correction 8 for fibre content >30 wt.%
- ROI filter: ON

4.1.2 Determination of real Voxel edge length

For setting magnification and accordingly Voxel edge length (equation 4.1), several axes can be moved at the CT device. Positions are defined by spindle revolutions for the used Nanotom. This method is not accurate which is why the real Voxel edge length has to be determined accurately. The distances source-object and source-detector are determined

by the positions of object (ZO) and detector (ZD) along X-ray beam axis (Z) because the source position (ZS) is fixed.

For the determination of the real Voxel edge length a method described in [94] was applied. A ball bar specimen was used which consisted of two ruby spheres, glued on a CFRP rod. Sphere distance and diameter have to be adapted to the applied Voxel edge length. For this work the determination of Voxel edge length was conducted for 1 to 3 μm . The utilized spheres had a diameter of 1 mm and a distance of approx. 4 mm. Figure 4.2 shows a photo of the ball bar specimen and a 3D rendering of a CT data set with virtually fitted spheres. The spheres are arranged in an angle of 45° to cover a big part of the detector and to irradiate the spheres separately. Sphere distance was measured with tactile CMM by an accredited test laboratory and documented in an inspection report.

The desired, nominal Voxel edge length was set at the device by positioning the axes of detector and object accordingly, then the ball bar specimen was scanned. The distance of sphere centre points was measured in the CT dataset and compared to the tactile measured reference value. CT data analysis was done using VG Studio MAX by fitting virtually spheres to both spheres to determine sphere centre points. The distance is the euclidean distance between these points. The formula

$$ZO_{\text{corrected}} = ZO_{\text{nominal}} * \frac{\text{Spheredistance}_{\text{CT}}}{\text{Spheredistance}_{\text{tactile}}} \quad (4.2)$$

was used to calculate the corrected object position ZO to achieve the nominal desired Voxel edge length. A second scan of the ball bar specimen was conducted at the corrected position to give information about accuracy of the correction. Without moving the horizontal axes the actual specimen was scanned.

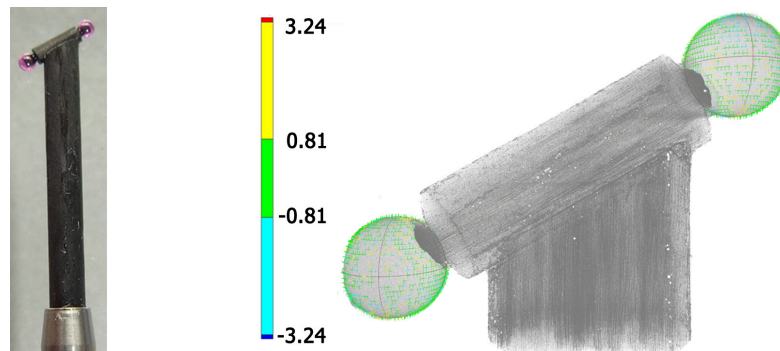


Figure 4.2: Photo of the ruby ball bar specimen on CFRP rod (left) and a 3D rendering of a CT data set with sampling points for both spheres (right). The distance from sampling point and surface of regular geometry is shown colour coded (μm).

The CT scans of the ball bar specimen were conducted using optimized parameters with choosing the most important ones same as for the actual polymer specimens. The main difference is scan time that was decreased by choosing continuous rotation without averaging („Fast Scan“). Scan parameter for the ball bar scans are shown in table 4.3. For 1 μm Voxel edge length a complete imaging of both spheres is only possible when using „Virtual Sensor“ mode (double amount of Voxels in horizontal direction). Applying this mode the continuous mode cannot be chosen because left and right image are not acquired at the same time. In addition two scans have to be performed vertically to image both spheres completely in this direction. Application of the two mentioned modes leads to higher scan time compared with the lower resolution scans.

Table 4.3: Scan parameter for scans of ball bar specimen with different resolution

| Voxel edge length (μm) | Voltage (kV) | Current (μA) | Integration- time (ms) | Number of projections | Tube mode | Scan time (min) |
|--|-----------------|------------------------------|------------------------------|--------------------------|--------------|--------------------|
| 1 | 80 | 180 | 1200 | 300 | 1 | 146 |
| 2 | 80 | 110 | 750 | 880 | 0 | 11 |
| 3 | 80 | 140 | 750 | 880 | 0 | 11 |

4.2 CT data analysis

A simple segmentation using global thresholding is not successful for real CT data for high fibre content because many fibres touch or run parallel closely nearby. Separation of such fibres in individual fibres is not possible without any further data processing. Two concepts were implemented, starting with the extraction of straight glass fibres. The application of this method to strongly curved, low contrast fibres and high fibre contents showed limitations of this concept, why an additional concept was developed. The next three chapters will explain the two concepts in detail beginning with a chapter that explains common issues for individual fibre segmentation and the basic ideas of both implementations.

4.2.1 Fibre characterization - Basic concept

A simple method to separate fibres from matrix within a 2D or 3D grey scale image is thresholding. Depending on the grey value distribution in the histogram the choice of the correct threshold can be done manually or parameter free algorithms can be used. One of these algorithms is the widely used Otsu thresholding method [95]. A bimodal grey value distribution is assumed showing two distinct peaks. The result of Otsu thresholding and labelling with connected components filter can be seen in Figure 4.3. The method leads to over-segmentation since the peak for polymer matrix is higher and the threshold value is shifted towards lower grey values. The labelled image shows a lot of

green fibres that were all connected and labelled with the same value. Lowering the threshold would lead to better results for some fibres but for others the result would be worse or same. This example shows that more sophisticated image processing is necessary to separate each individual fibre.

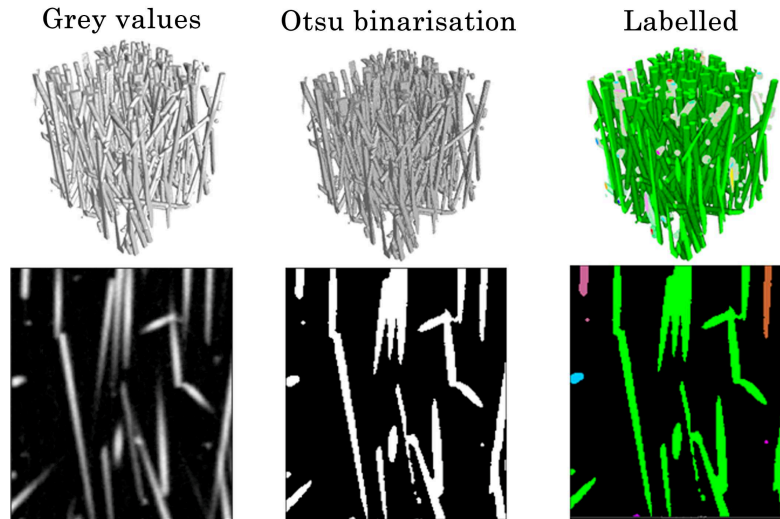


Figure 4.3: CT cross sectional image showing the original grey values, the result of Otsu thresholding and of connected components labelling

The basic concept of the methods that were developed in this thesis is a medial axes extraction followed by a cluster analysis (Figure 4.4). Scanned data have to be pre-processed to reduce noise and optimize contrast. Cluster analysis should separate false connected medial axes without separating correct and complete fibres. After separation each fibre is characterised by calculating length, orientation, diameter, volume and surface.

The output files are described in Appendix E 8.

4.2.2 Fibre characterization - Concept1 (MAE)

A pipeline of 3D data processing algorithms was implemented at FH Wels to characterize individual fibres within a fibre reinforced plastic composite material. The first concept was entitled 'Medial Axis Extraction' (MAE). For this method development, short glass fibres in PP were used.

At the beginning some assumptions and constraints were defined:

- Fibres are almost straight.
- All fibres have almost same diameter.

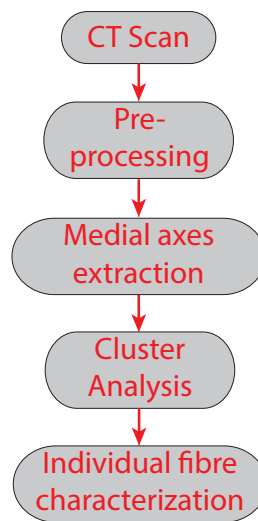


Figure 4.4: Flowchart showing the basic concept of fibre characterization pipeline FCP

- Fibre cross section is circular.
- Highest grey values are in the centre of the fibres.
- The histogram allows for a good separation of fibres and matrix.

These assumptions were based on data from the material supplier and first CT test scans. Some of them proofed wrong or changed during the research progress. For other fibre material systems these assumptions had to be adapted which lead to extension of the software pipeline. (See chapter 4.2.3)

Grey value profiles of Figure 4.5 show the grey value increase towards the centre of the fibre and the distinct maximum there. The reason for this effect is mainly the limited resolution that blurs all edges. The trend in fibre longitudinal direction is affected by noise and is also disturbed by nearby fibres. For the fibres shown, which are embedded in PP, the grey value difference between fibre centre and matrix is approx. 40000 and approx. 6000 in longitudinal direction (referred to the 16 bit range of 65535).

The development is in principle a two step process with the extraction of medial axes at first and the analysis of touching points at second.

The sequence of 3D image processing algorithms that are used after CT scanning to extract features for each and every individual fibre, is shown in Figure 4.6 schematically. At the end of this section the parameters, that have to be set for every step of the sequence, are listed. For choosing these parameters knowledge about fibre and matrix material and average fibre diameter is necessary.

In the following the single steps of the software pipeline are explained.

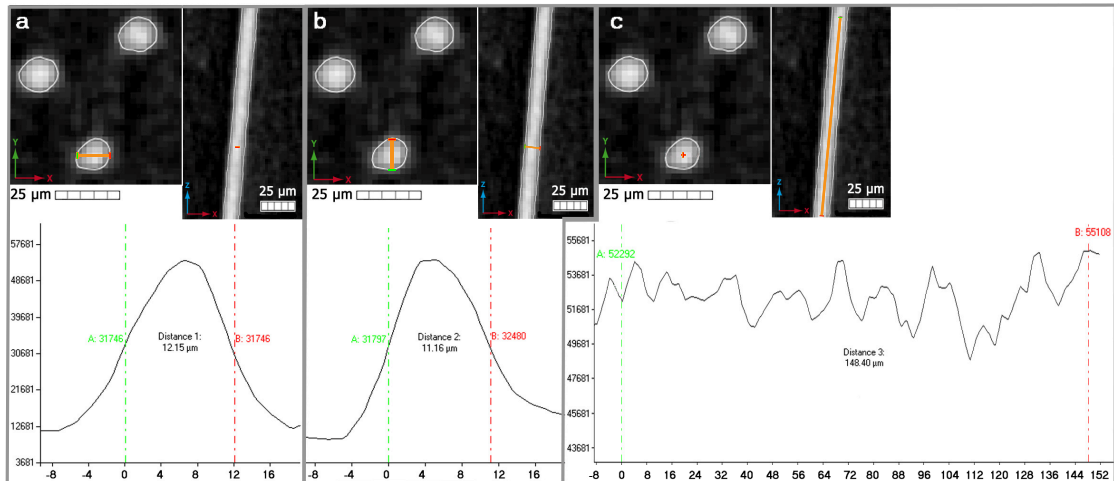


Figure 4.5: Cross sectional images and grey value profiles of one single glass fibre, transverse in 0° (a), 90° (b) and longitudinal (c). The white line at fibre borders represents the automatically determined grey value at the surface of the fibres which is the maximum grey value gradient magnitude. Voxel edge length is $2 \mu\text{m}$.

1. Data pre processing: Input data format has to be „unsigned 16bit “. Maximum file size depends on Hardware (main memory). Memory consumption is maximum 20 times the file size of the input data set as shown in Table 4.5.
2. Gaussian filtering: The first step of the automatic sequence is filtering to increase signal to noise ratio.
3. ROI: To reduce calculation time subsequent algorithms are only applied to Voxels that can be allocated to fibres. For the definition of these Voxels the Otsu method is used.
4. Gradient magnitude: The interface between foreground (fibres) and background (matrix) is emphasized by increasing the grey value.
5. Hesse Matrix: The second derivative in all three Cartesian coordinate directions are calculated for the gradient magnitude data. An eigenvalue analysis of this matrix gives information about the local fibre direction. (Formula 4.3)
6. Medial axis extraction : The information about local fibre direction, the filtered data and the ROI together are used to extract the medial axes of each individual fibre. The result are fibre segments that are not yet representing the real fibres but are partially connected to each other especially at touching points (Clusters). The principle is shown in Figure 4.7. A plane perpendicular to the local Hesse direction is generated and grey values of neighbouring Voxels within this plane are analysed. Since the medial axes after this procedure can be several Voxels broad, a thinning algorithm is applied afterwards (Chapter 4.3). After that the medial

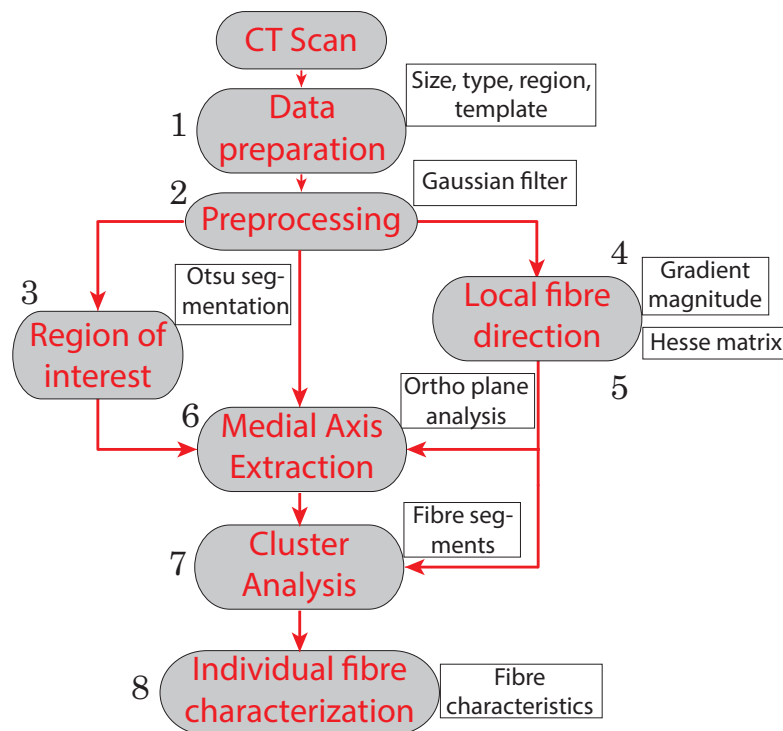


Figure 4.6: Flowchart of fibre characterization pipeline (FCP) - Concept 1.

axes are exact one voxel broad leading to fibre Voxels with maximum two fibre Voxel neighbours.

7. Cluster analysis: Connected fibre segments are transferred to individual fibres by analysing two angles. A Cluster is defined as a Voxel with more than two fibre Voxel neighbours. For the segments that are connected to one Cluster, the angle between the segments and the angle between local Hesse directions are calculated. Figure 4.9 shows a Cluster with four connected segments and the defined angles. Subsequent query of both angles assures for an optimal connection of disconnected segment. If one of the angles is below the predefined threshold, the segments are connected.
8. individual fibre characterization: At the end a length correction is applied as shown in Figure 4.10, because after medial axis extraction a part of the fibre ends is missing. After that all features of every individual fibre are calculated and written to a text file. A volume data set is generated containing medial axis with grey values same as labels in the text file.

Sorting of the eigenvalues of the Hesse matrix as follows gives the possibility to define conditions for tubular structures with high grey value (e.g. fibres) using equation 4.3 [86].

$$|\lambda_1| \leq |\lambda_2| \leq |\lambda_3|$$

$$|\lambda_1| \approx 0 ; |\lambda_1| \ll |\lambda_2| ; \lambda_2 \approx \lambda_3 ; \lambda_2 < 0 ; \lambda_3 < 0 \quad (4.3)$$

The direction at the respective Voxel corresponds to the eigenvector for λ_1 .

Almost all steps of the pipeline require the definition of parameters. Figures 4.8, 4.9 and 4.10 show, how the steps work. A list with all adjustable parameters including a short description and the standard values are listed in table 4.4. The standard values partly depend on CT data resolution, fibre properties and user requirements.

For step 2 of the pipeline the strength of smoothing can be set via the Gaussian variance. For already low-noise or smoothed data the variance value can be set to 0 which is equal to no filtering. This is generally true for low resolution data or materials with high density difference. For high resolution data or low contrast, data has to be pre filtered.

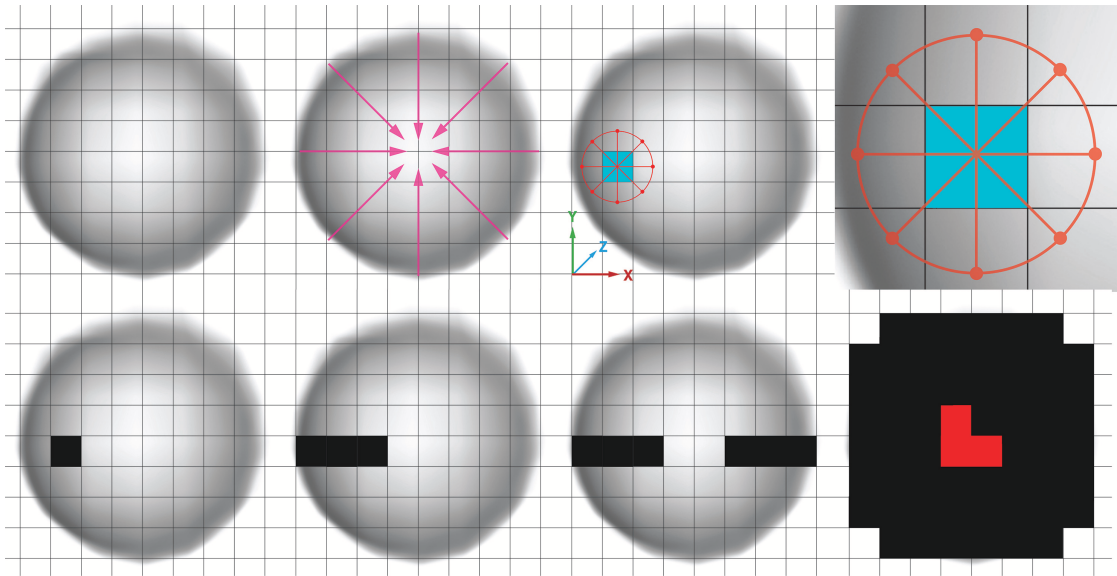


Figure 4.7: Medial axis extraction: Cross section in transverse fibre direction. The arrows show the direction of grey value gradient towards fibre centre. For every Voxel the grey values of neighbouring Voxels in equidistant distance are determined. If the grey value of the actual Voxel is biggest, the value is saved, otherwise set to zero (black). At the end of the procedure, only Voxels at the fibre centre are remaining. (red).

For step 6, „medial axis extraction“, the distance within the grey value profile can be set in Voxel. For step 7, „Cluster analysis“, several parameter can be set. If several Clusters are located nearby it makes sense to combine them to a single Cluster. If the distance is bigger than one fibre diameter, one can assume that another fibre is touching and the Cluster should not be combined. Thus the standard value can be chosen as the

fibre diameter value. For combining fibre segments, angle thresholds have to be set. In addition to a segment angle, that can lead to wrong connections especially for curved fibres, the information about local directions around the Cluster can be taken into account for connecting fibre segments. At the end of the pipeline, start and endpoint of every fibre are shifted outwards in fibre direction to compensate for shortening during „medial axis extraction “. The user can set the value that is added in sum to both ends. In the end result, fibres shorter than a defined value can be excluded.

Table 4.4 gives information how to set the parameters depending on fibre type and data quality. The standard values were determined for glass fibres in PP at different resolutions.

Table 4.4: Parameters for FCP-MAE pipeline

| Parameter | Description | Unit | Standard value |
|----------------------------|---|---------|--------------------------|
| Gaussian variance | Determined the strength of smoothing for noise reduction | () | 0 to 4 |
| Gaussian error tolerance | Parameter for the applied filter | () | 0.001 |
| MAE neighbourhood | Distance in grey value profile 4.7 | (Voxel) | 1 |
| Hesse angle ¹ | first angle for the connection of fibre segments | (°) | 31 |
| Segment angle ¹ | second angle for the connection of fibre segments | (°) | 21 |
| Cluster-Cluster-distance | Minimum distance from Cluster to Cluster . If the distance is smaller than the selected value, single Clusters will be joined together as shown in Figure 4.8 and 4.9 | (µm) | > approx. fibre diameter |
| Length correction | Correction of errors at fibre ends as shown in Figure 4.10 | (µm) | approx. fibre diameter |
| Length threshold | Minimum fibre length, that will be extracted | (µm) | user defined |

¹For both angles is considered: If the selected value is exceeded, the segments will not be connected as shown in Figure 4.9

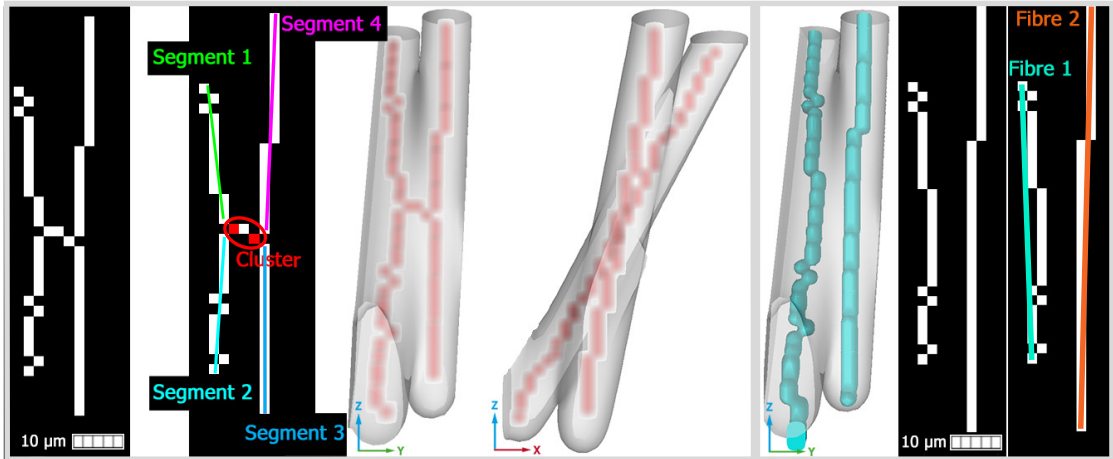


Figure 4.8: Medial axis extraction: Cross sectional images with medial axes and 3D views of CT data for 2 selected fibres that run very closely nearby. Medial axis after MAE (step 6) are shown left or red in 3D and after Cluster analysis (step 7) right or cyan in 3D.

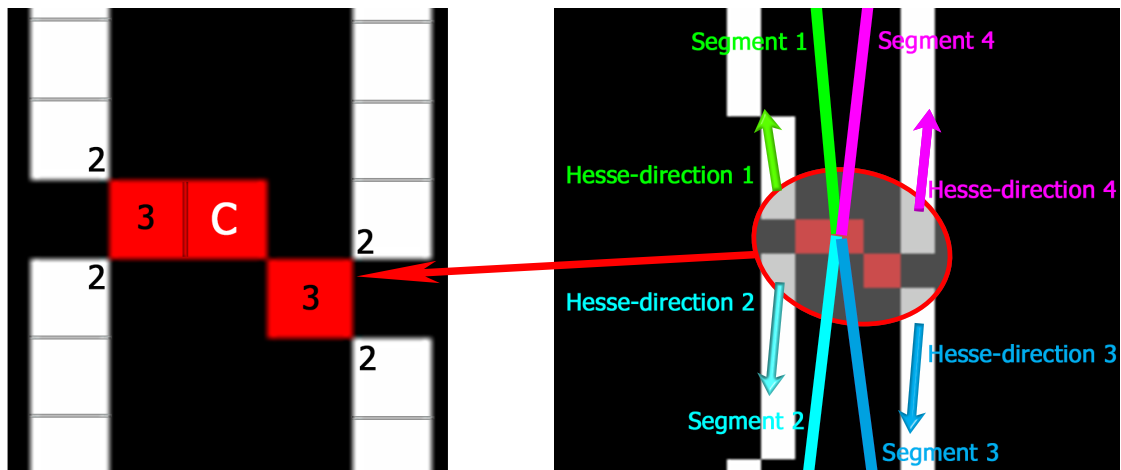


Figure 4.9: Cluster analysis: Cross section image with medial axes (white), number of neighbouring Voxels and the Cluster Voxel C. Fibre segments and local orientations (Hesse directions). All segments have a common start point, the Cluster centre Voxel. The angles between the segments and between the local directions near the Cluster are compared. The selected threshold values for Hesse angle and segment angle are used to connect the segments correctly.

One property of CT data that has to be defined before the first step of FCP- pre-processing is the size of the volumetric file. File size is determined by data type and number of Voxels. Data type during reconstruction is usually 32 bit float. For specimens consisting of only a few different materials it is usually sufficient to use 16 bit data. For this thesis all scans were converted to 16 bit after reconstruction including manual mapping for optimal utilization of the dynamic range. File size can be calculated using following formula:

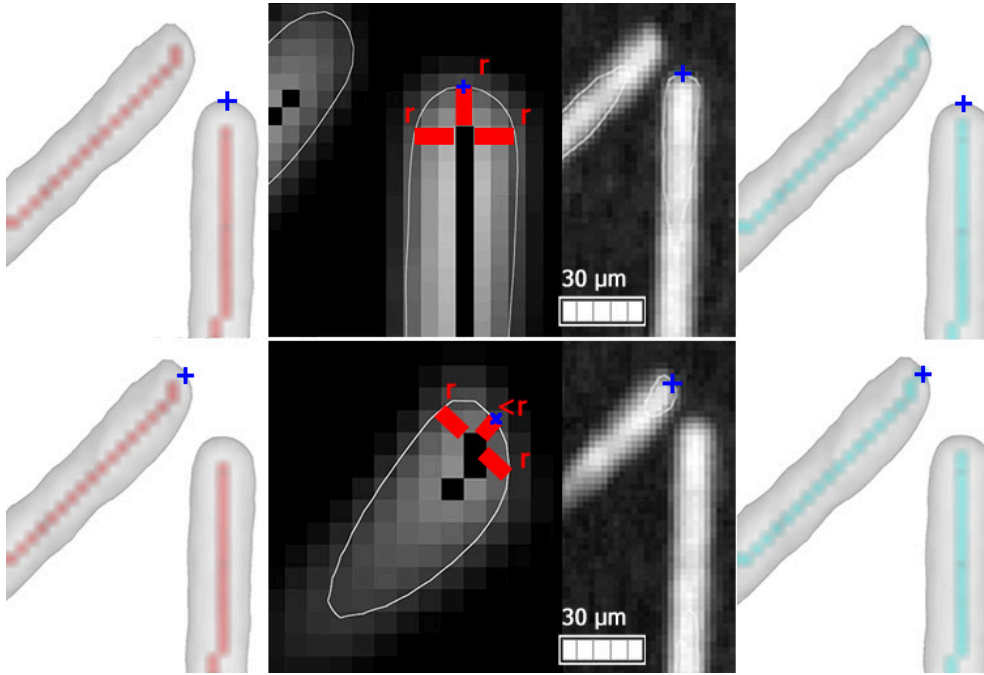


Figure 4.10: Length correction: Cross sectional images and 3D renderings of 2 selected fibre ends with medial axes. The result after MAE is shown left while Cluster analysis and length correction were applied for the right image. Blue crosses mark the real fibre ends.

$$Filesize(Byte) = Byte(datatype) * Voxel_X * Voxel_Y * Voxel_Z \quad (4.4)$$

$$Byte(Datatype) \dots 1(8bit), 2(16bit), 4(32bit)$$

Calculation of the Hesse matrix is most memory consuming from all algorithms used for the FCP pipeline. Running the pipeline implies to have several intermediate data stored to main memory in order to access it immediately when needed. Memory consumption of each step and total memory workload are shown in Table 4.5. It is obvious that during Cluster analysis most data is stored in memory. The maximum memory load can be illustrated as multiple of the input data in 16 bit format and is approx. twentyfold. Limitations in file size depend on the available hardware. For this thesis a workstation with 128 GB was available. Thus maximum file size was approx. 6 GB.

Table 4.5: Memory consumption for each step of the FCP pipeline in multiples of 16 bit input data

| Step | Abbr. | Data type (bit) | Memory consumption | | Data in memory |
|---------------------------|-------|--------------------|--------------------|--------|--------------------------------|
| | | | Step | Total | |
| CT Original | CT | 16 | 1 | 1 | CT |
| Gauss | G | 32 | 2 | 2 | G |
| Gradient magnitude | GM | 32 | 2 | 4 | G, GM |
| Hesse matrix | H | 32 | 12 | 16 | G, GM, H |
| ROI | ROI | 16 | 1 | 15 | G, H, ROI |
| Medial axis extraction | MAE | 32 | 2 | 17 | G, H, ROI, MAE |
| Cluster analysis | C | 32 | 2 | ca. 20 | G, H, ROI, MAE, FCP, csv |
| Fibre characteristic | FCP | 32 | 2 | ca. 7 | G, FCP, MAE, csv |

Causes for inaccuracies of FCP analysis (MAE)

The assumptions that were mentioned at the beginning of chapter 4.2.2 were not completely fulfilled by the investigated material systems. Structures and fibre arrangements that were not considered for software generation can lead to wrong extracted fibres. Different resolutions principally lead to differences in complexity of fibre arrangement that can be seen in CT data.

Assuming optimal choice of scan parameters and well chosen parameters for FCP, problems mainly occur at steps 5,6 and 7. The local directions that are determined using the Hesse matrix in step 5 of the pipeline do not represent real fibre orientation at every position. Reasons are limited signal to noise ratio, touching points and the grey value transition at the fibre ends. Two problems can occur at medial axis extraction (step 6): a fibre is separated in two or more single segments or several fibres are wrong connected. At low resolution, two parallel fibres that are close together could not be separated. Some possible fibre arrangements are shown in Figure 4.11.

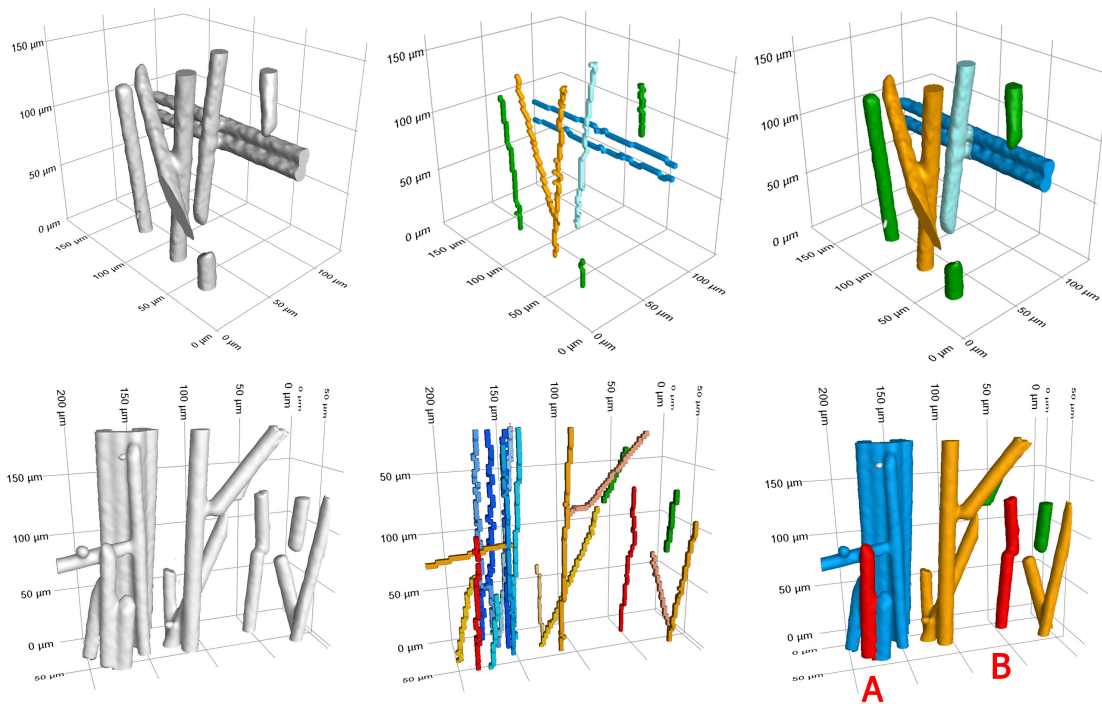


Figure 4.11: 3D renderings of two cut-outs scanned at 2 μm Voxel edge length showing different fibre arrangement. Images to the left show original CT data, medial axis are shown in the centre and right different fibre types are shown colour coded. Green are free fibres, orange are fibres, that touch in a small area, blue are parallel fibres that are close together, red are fibres that are virtually broken (A) or virtually wrong connected (B)

A virtual breakage into single segments cannot be corrected afterwards which is the reason for the extraction of larger medial axes areas in fibre centre instead of single lines. A thinning algorithm converts this region into single Voxel lines. Connected fibres are separated in the following step if necessary. Cluster analysis (step 7) can fail in terms of wrong or not connecting segments. These main problems can lead to virtual separation or wrong connection. Both leads to wrong average fibre length and wrong orientation distribution.

The determination of accuracy was conducted in a way that average fibre length and tensor values were evaluated quantitatively and it was tested how many errors (fibre breaks, wrong connections or others) occurred.

4.2.3 Fibre characterization - Concept2 (TM)

A second concept was implemented entitled „Template Matching“ (TM) to overcome limitations of the first concept and to increase accuracy. The basic principle of the MAE concept shown in Figure 4.6 is not changed but the method of step 6 „medial axis extraction“ is replaced by a template matching approach.

For this method development, long fibres in PP were used.

The assumptions and constraints that were defined for the first concept were adapted as follows:

- Fibres are almost straight → fibres can be bent.
- All fibres have almost same diameter.
- Fibre cross section is circular.
- Highest grey values are in the centre of the fibres → suitable template for grey value distribution.
- The histogram allows for a good separation of fibres and matrix → worse data quality allowed.

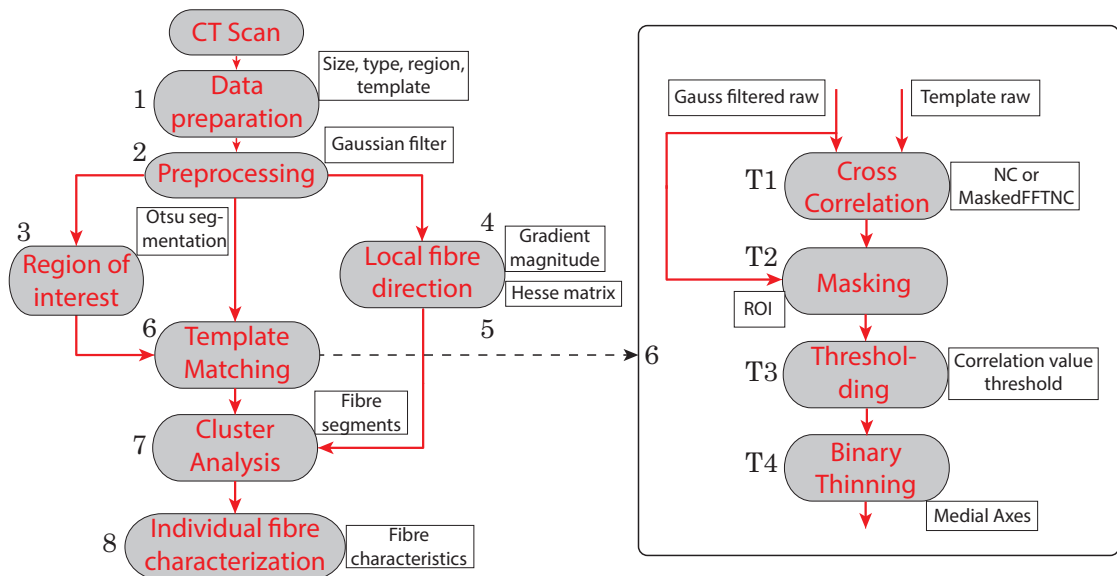


Figure 4.12: Flowchart of fibre characterization pipeline (FCP) - Concept 2.

The steps for TM shown in Figure 4.12 are described in the following: Steps 1 to 5 and 8 are not modified and are described in chapter 4.2.2.

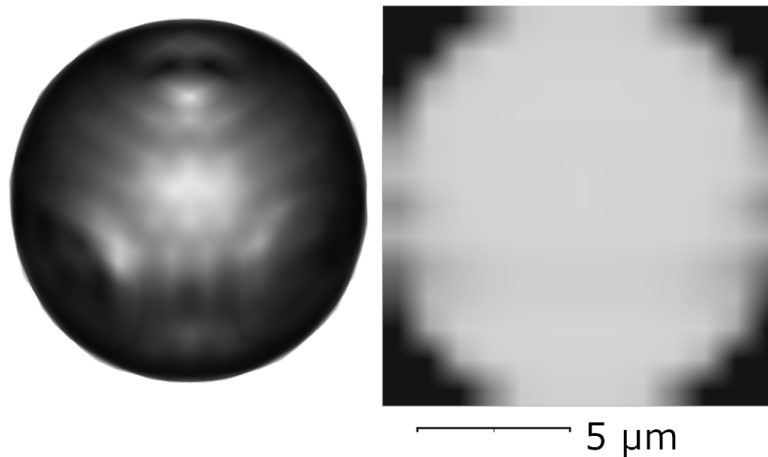


Figure 4.13: 3D rendering (left) and cross sectional image (right) of Voxel dataset of 12 μm template, 1 μm Voxel edge length

6 „Template Matching“ (TM):

- T1 Cross correlation: A normalized cross correlation of the template and the filtered input data is calculated. The result gives values between -1 and 1 where 1 implies best correlation. For cylindrical shapes the assumption is that best correlation is in the centre of the fibres. The cross correlation result should emphasize fibre centres. A CT data set that is used as template is shown in Figure 4.13.
- T2 Masking: Since the chosen correlation filter is applied to the complete dataset, the ROI is used as mask subsequently to exclude non-fibre Voxels.
- T3 Thresholding: A global threshold is applied to binarize the correlation result. Since fibre centres show higher correlation values a better separation of fibres is expected. Nevertheless a parameter study has to be conducted for every new material system and template.
- T4 Binary thinning: From the binarized medial regions the medial axes are determined same as for MAE using the binary thinning algorithm. (Chapter 4.3)
- 7 „Cluster analysis“: For analysing clusters (step 7) a method was added that can take into account curved fibres. The modification affects the way how the fibre segments that are connected to the cluster are defined. As indicated in Figure 4.9 the segments for straight fibres are defined by the cluster point and the segment end point. For curved fibres this vector is most likely not showing in fibre direction. Therefore the definition was adapted by building the segment vector from the cluster point and a point which is lying on the fibre axis and is 10 Voxels away from the cluster. The implementation allows to choose the version for straight or heavily curved fibres by a check box.

A spherical template is used since it does not have to be rotated which is computationally less effort. The correlation of a spherical template and cylindrical fibre structures will never give the maximum value of 1. Nevertheless is the correlation maximum locally in the centre of the fibre. Performing binarisation and thinning on such data leads to better representation of medial axes since the value in fibre centre was increased.

Most of the parameters and the way how to choose them is the same as for the MAE concept. The MAE neighbourhood parameter is excluded and the NCC threshold for step T3 is included. Table 4.6 shows all parameters for TM pipeline with standard values similar to Table 4.4 for MAE pipeline.

Table 4.6: Parameters for FCP-TM pipeline

| Parameter | Description | Unit | Standard value |
|----------------------------|---|-------------------|--------------------------|
| Gaussian variance | Determined the strength of smoothing for noise reduction | () | 0 to 4 |
| Gaussian error tolerance | Parameter for the applied filter | () | 0.001 |
| NCC threshold | Binarization for thinning of medial axes | () | 0.3 - 0.5 |
| Hesse angle ¹ | first angle for the connection of fibre segments | (°) | 31 |
| Segment angle ¹ | second angle for the connection of fibre segments | (°) | 21 |
| Cluster-Cluster-distance | Minimum distance from Cluster to Cluster . If the distance is smaller than the selected value, single Clusters will be joined together as shown in Figure 4.8 and 4.9 | (μm) | > approx. fibre diameter |
| Length correction | Correction of errors at fibre ends as shown in Figure 4.10 | (μm) | approx. fibre diameter |
| Length threshold | Minimum fibre length, that will be extracted | (μm) | user defined |

Generation of templates

The ideal template for straight fibres would be a cylinder. Using a cylindrical template would require iterative calculation of cross correlation for various rotation angles. To

¹For both angles is considered: If the selected value is exceeded, the segments will not be connected as shown in Figure 4.9

overcome this limitation a spherical template was tested and the results were promising. Diameter and material of the sphere should correspond to the scanned fibres. To achieve the goal of enhancement of medial grey values the grey value distribution of the sphere from centre to shell should be comparable with the grey value distribution of a fibres' cross section. Since scan quality is never perfect the grey values along fibre axes vary and especially in cluster regions grey values differ from the ideal case. Taking these facts into account it was concluded that a template without artefacts but with some blurring should be generated. The tool „Sim-CT“ with monochromatic radiation and focal spot blurring was used for generating a raw file (see Chapter 4.7). The applied ITK normalized correlation filter [96] requires odd number of Voxels in each direction which has to be considered for reconstruction. For better results, surrounding air should be removed. Unique templates have to be generated for different Voxel edge length, different fibre material and different fibre diameter.

Causes for inaccuracies of FCP analysis (TM)

The TM approach works better for fibres running parallel in close distance and for reduced data quality. Problems will still arise when fibre cross sections differ from circular shape. Fibre arrangements that will not always be extracted correctly are:

- touching fibre ends with same fibre orientation (Figure 4.11 case B)
- very high curvature 7.16
- very dense fibre packing within bundles (e.g. Figure 7.13)

4.2.4 FCP parameters for different materials

Table 4.7: FCP parameters applied for different glass fibre composite materials analysed with MAE and TM concept

| | Material Concept | PP-sGF ¹ MAE | PP-sGF ² TM | PP-sGF-30a ³ TM | PP-sGF-30a ⁴ TM |
|-------------------|----------------------|-------------------------|------------------------|----------------------------|----------------------------|
| | VS (μm) | 2 | 2 | 2 | 3 |
| Parameter | Unit | | | | |
| Gaussian variance | () | 2 | 2 | 4 | 0 |
| Length threshold | (μm) | 30 | 30 | 30 | 30 |
| Length correction | (μm) | 11.5 | 11.3 | 20 | 12.2 |
| CC fibre length | (μm) | 20 | 20 | 35 | 20 |
| NCC threshold | (μm) | – | 0.38 | 0.38 | 0.32 |
| Template diameter | (μm) | – | 12 | 12 | 12 |

Table 4.8: FCP parameters applied for different glass fibre composite materials analysed with MAE and TM concept

| | Material Concept | PP-sGF ⁵ TM | PP-sGF ⁵ TM |
|-------------------|----------------------|------------------------|------------------------|
| | VS (μm) | 1 | 2 |
| Parameter | Unit | | |
| Gaussian variance | () | 2 | 2 |
| Length threshold | (μm) | 0 | 0 |
| Length correction | (μm) | 10 | 11.3 |
| CC fibre length | (μm) | 20 | 20 |
| NCC threshold | (μm) | 0.32 | 0.42 |
| Template diameter | (μm) | 12 | 12 |

These values were always chosen the same way for all data sets:

- Gaussian error: 0.001
- ROI threshold: Otsu

¹Settings used used for the investigations of examination of reproducibility 6.3, impact of evaluation volume 6.4 and impact of fibre content on FOD and FLD 7.1

²Settings used for the investigations of fibre degradation along injection moulding process 7.2

³Settings used for the investigations of impact of specimen orientation on the turntable 6.5, comparisons with standard methods for FOD and 6.6, skin-core layered micro-structure 7.3

⁴Settings used for the investigations of fibre degradation along injection length 7.4

⁵Settings used for the investigations of Comparison with standard methods for FLD 6.7

- MAE profile neighbourhood: 1 Voxel
- Hesse angle: 31 °
- Segment angle: 21 °

For specific investigations like long fibre analyses the applied FCP parameters are given in the corresponding sections.

4.3 Binary thinning

For separating virtually connected fibres after MAE or TM it is crucial that the medial axes are exact one Voxel thick. Algorithms that fulfil this need are so called skeletonization or thinning algorithms. Since these algorithms are computation-intensive, they are mainly used in 2D but a 2D approach will not lead to the desired results for 3D CT data. For this study the ITK code „itk::BinaryThinningImageFilter“ [97] was used. This implementation showed problems for special structures like for example 3 Voxel thick lines. Another implementation in Matlab is available „Skeleton3D“ [98], a 3D skeletonization algorithm. To evaluate the two implementations, a simulated dataset containing 4 fibres was generated. Figure 4.14 shows the rendering of the 4 touching fibres. Before thinning the fibres are several Voxels thick and connected. The MAE concept introduces additionally bigger regions at the end of the fibre with 45° orientation. The original ITK algorithm deletes most of the free fibre end at the bottom of the simulated data set for both concepts. Adding the code that is included in Matlab and is missing in the ITK implementation leads to the desired result, shown in Figure 4.14 as Thinning ITK*. The modified code „itk::FHWBinaryThinningImageFilter“ is used for all further fibre analyses.

4.4 Creation of reference data sets

For the evaluation of the concepts for fibre characterization, volumetric reference data sets were created. Every individual fibre from a high resolution CT data set was measured using semi automatic cylinder fits as described in this chapter. The determined information was used as input data for CT simulation as well as reference data for comparisons. Virtual data set with different Voxel edge length and varying cylinder diameters were generated. Since reference data sets were derived from real CT data it is possible to evaluate the software results for real but also for virtual CT results.

The software VG Studio MAX allows for fitting regular geometries like spheres, cylinders, cones or others to the grey value data. Probing points have to be set on the fibre surface manually that are used as start points for fitting. The software uses up to 1000 points for a least squares error method to fit a cylinder to the grey value data. Fibre surface, which is the transition from air to material, has to be determined beforehand. A VG Studio MAX tool can be used for that which analyses the grey value histogram

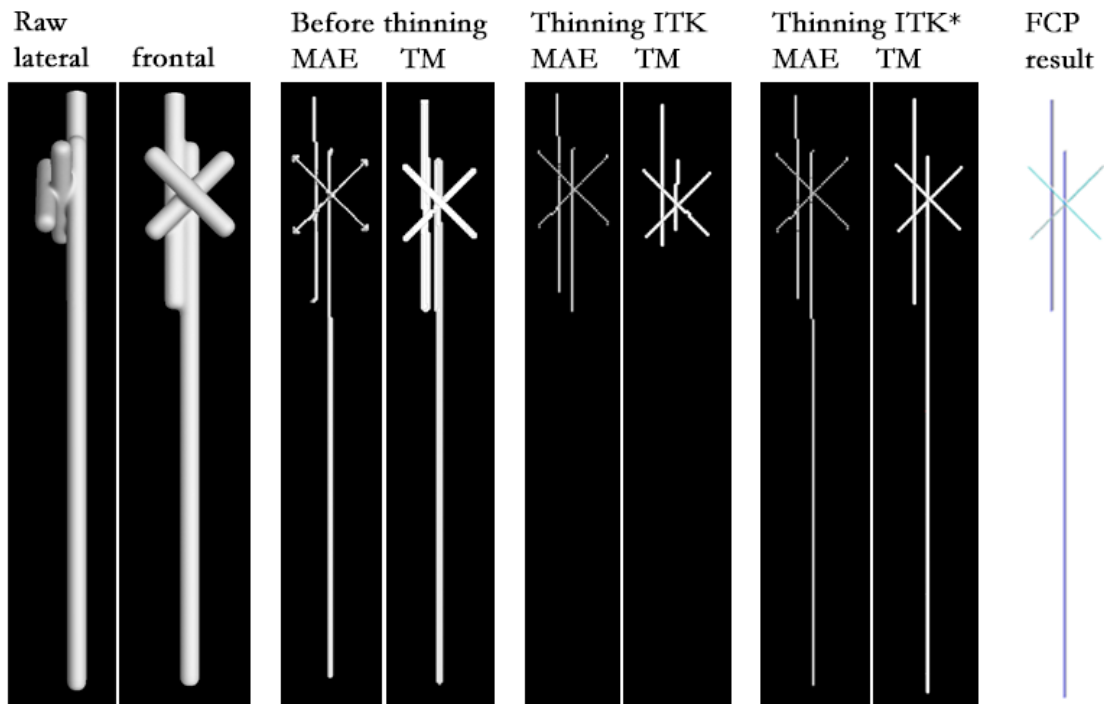


Figure 4.14: 3D rendered views of simulated data containing 4 fibres: Original grey value raw data, medial regions before thinning, after thinning with ITK original algorithm, after thinning with modified ITK* algorithm, FCP result.

and determines the surface sub Voxel accurate. Grey value distribution together with determined values for air, material and surface are shown as an example in Figure 4.15.

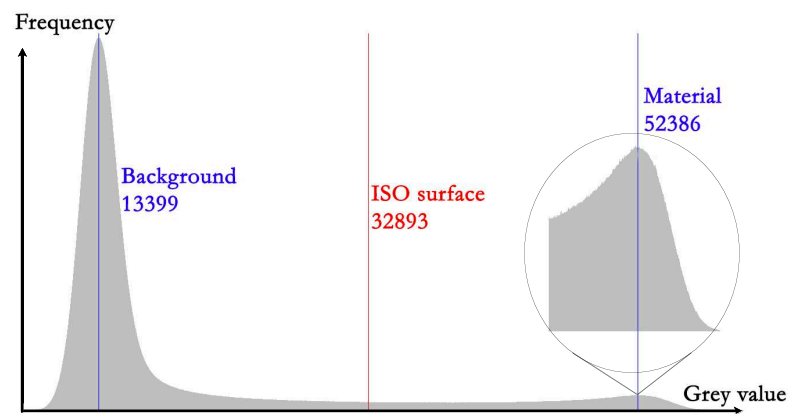


Figure 4.15: Grey value histogram of cut-out *Centre_1*, 1 μm Voxel edge length. Grey values for background (air, left) and material (glass, right) were determined automatically as local maxima. Surface grey value is exactly in the middle between air and material value.

When setting the probing points it is very important to set points at the fibre ends too to assure that the length of the cylinder represents real fibre length. Figure 4.16 shows the probing points that were used for this single fibre. 9 of these points are visible. On a regular grid the software sets a huge number of additional points automatically that are used for the fit. Deviations between regular geometry and surface are visualized colour coded. The quality of the fit depends on CT data quality, resolution, selected parameter values and the shape of the fibre. The given examples shows a quite straight fibre which results in small fit point deviations.

Quality of CT data sets can be analysed based on grey value histograms. The histogram shown in Figure 4.15 has two maxima with big grey value difference which indicates high quality. Air grey value distribution is quite small, the one of material rather broad. The broader the distribution the worse is data quality since the best possible representation of one material is one individual grey value. Since contrast between glass and polymer is very good, the standard values for the fit parameters, that were suggested by the software, were applied.

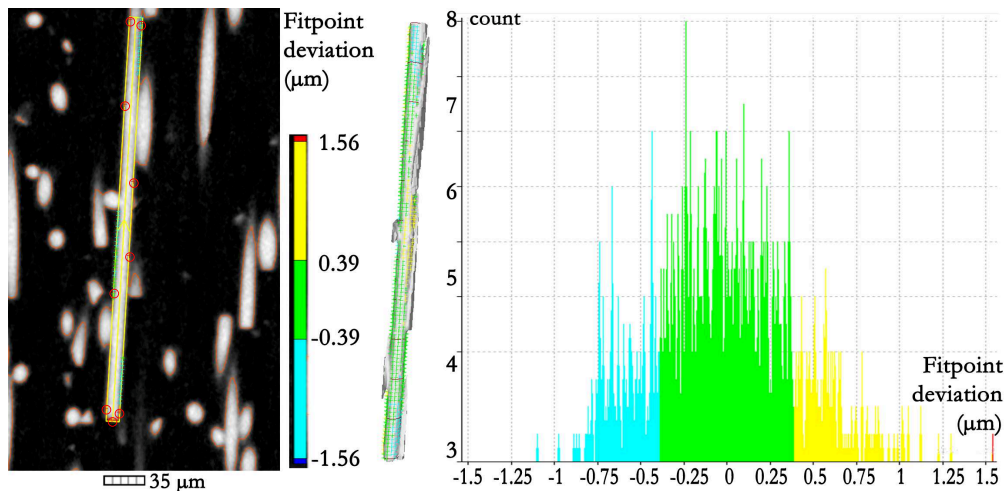


Figure 4.16: Visualization of probing points (red circles) and fitting points in a cross sectional image for an individual fibre (left). 3D rendering of the same fibre showing all fit points (centre). Deviation histogram of all fit points. (right)

Only small cut-outs of the complete data set were analysed like mentioned above since the fitting needs high manual effort. Every cut-out contains approx. 300 fibres. Three areas were selected for the generation of reference data sets which are located at different positions within the complete data set. The complete CT data set was generated for a cut-out of a 1A MPS according to DIN-EN-ISO 527-2 [89]. The material was PP-sGF-30 containing 30 wt.% short glass fibres. The Voxel edge length was 1 μm.

The reference data consists of endpoints and diameters of all fibres within the respective volume. The input for the determination is the 1 μm CT data set. This was

analysed as described above. The fibres were then modelled by cylinders using the Euclidean distance between the endpoints as length and the fitted cylinder diameter as reference diameter.

Reference data sets consist of cylinders with varying length and diameter. Since curved fibres are present at these even small cut-outs, the cylinders can have intersections. For severe intersections the cylinder of the curved fibre was not taken into account, neither as input for simulation nor for reference. Fibres at the borders of the data sets that are cut in longitudinal direction, were considered only if more than half of the fibre thickness was included in the CT data. It is obvious in Figure 4.17 that some cut fibres at the borders as well as some short fibre fragments were not modelled.

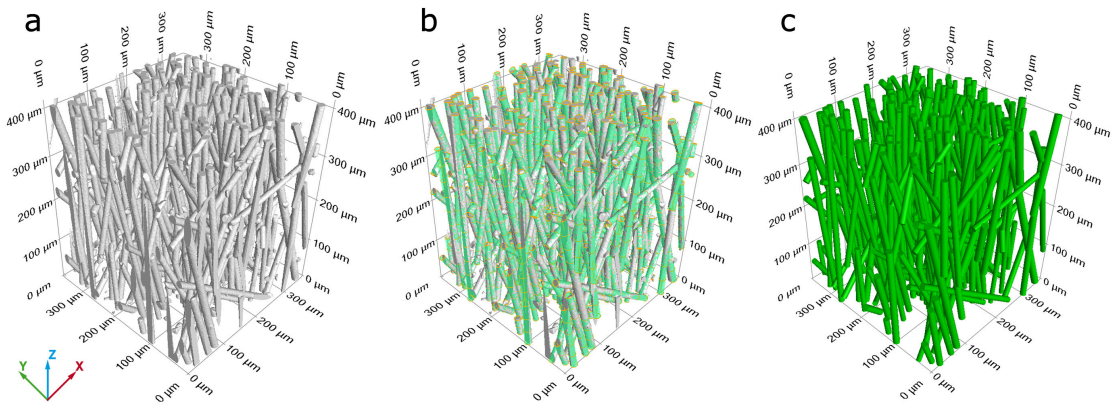


Figure 4.17: 3D rendered views of cut-out *Centre_1*, CT original data with 1 μm Voxel edge length (a), Overlay of cylinders and CT data (b) and cylinders alone (c)

CT simulation was conducted using the tool developed at FH Wels. It models all relevant components and the interaction of X-rays with matter. By defining a geometry representing the specimen, realistic projection images can be generated. Details are described in chapter 4.7. For all of the three cut-outs an input file was generated using the fitted cylinder data including real diameter variations. Additionally input files with constant diameters were generated to be able to investigate the influence of diameter variation on the FCP result. As constant value the average diameter of all fibres was chosen. Goal of the simulation study was to show the principle best possible accuracy for good quality data.

Every individual fibre of the extracted data was compared with the reference data. This comparison was conducted semi automatically using a Matlab script that tries to find corresponding fibres. As matching parameters, fibre endpoints and fibre length were selected. Errors that can occur at fibre characterization are virtual separation, wrong connection, deletion or wrong generation. The script tries to find correspondence in at least one of both fibre ends. By that it is possible to assign also wrong extracted fibres to the reference data. The rest of fibres that did not match, were tested manually by

visual inspection of CT data.

The reference specimen, made of PP-sGF-30, was scanned using different resolution (Voxel edge length: 1, 2, 3 μm) followed by the extraction of data sets from all three reference positions. A rigid registration without rotation could be performed since all scans were conducted subsequently without demounting the specimen. This approach ensures a very good geometrical conformity of all extracted regions.

Input data was additionally used for CT simulation in order to generate virtual data-sets with high quality. These were used to determine principle borders of accuracy.

For every resolution of scanned and simulated data a FCP parameter study was conducted to achieve optimal results. For first analyses length correction was deactivated. These lead to mean deviations of the mean fibre lengths that were used as length correction values for further analyses. Parameters that varied was Gaussian variance, NCC threshold and length correction. The templates for TM concept were generated using 12 μm sphere diameter. The other parameters were set as given in Table 4.9.

Applied Gaussian variance values:

- 1 μm Voxel edge length: 5 (3 for simulated data)
- 2 μm Voxel edge length: 2
- 3 μm Voxel edge length: 0

At high resolution stronger blurring is needed to assure a grey value maximum in the centre of the fibres. At lower resolution the blurring is inherently included which leads to smaller variance values. Since CT simulation leads to better image quality, blurring for 1 μm Voxel edge length was reduced from Gaussian variance 5 for scanned data to 3 for simulated data.

Applied NCC threshold values:

- 1 μm Voxel edge length: 0.32
- 2 μm Voxel edge length: 0.42
- 3 μm Voxel edge length: 0.32

4.5 General pre-processing

Starting with reconstruction, data quality is influenced by the chosen parameters. For all analyses that were performed within this thesis, some parameters or procedures were applied in the same way:

All reconstructions were initially saved in 32 bit float data format. This is the actually used format by the reconstruction software. Using this format ensures that no grey value manipulation is applied at the end of the reconstruction procedure. Since it is

Table 4.9: Parameters for FCP analyses on reference data at different Voxel edge lengths

| Parameter | Unit | Value |
|---------------------------|-------------------|-------|
| Gaussian error tolerance | () | 0.001 |
| MAE neighbourhood | (Voxel) | 1 |
| Hesse angle | (°) | 31 |
| Segment angle | (°) | 21 |
| Length threshold | (μm) | 30 |
| Cluster-Cluster- distance | (μm) | 20 |

not necessary to apply the following image processing steps on 32 bit data, a mapping to unsigned 16 bit is performed manually. This mapping is done in VG Studio MAX during data import. Care was taken that all relevant information of the grey value histogram was preserved, meaning that the contrast between matrix and fibres was optimized without cutting away relevant grey values. The histogram shown in Figure 4.15 shows the chosen region that was used mapped. Due to the presence of artefacts and the approximations used by the FDK reconstruction algorithms and sometimes due to specimen contamination with higher dense particles (metallic dust), very low and very high grey values may occur in the 32 bit data sets. These were cut away to optimize contrast between matrix and fibres. After importing and changing data type CT data was prepared in a way that surrounding air is reduced to a minimum. The data sets were aligned to specimens surfaces such that they are aligned to the coordinate axes. If a predefined size in X, Y or Z direction was required, an ROI was generated and exported to a raw file.

4.6 Determination of free fibre length

Specimens were destructively tested for fracture energy by performing the standardized Charpy impact test. One of the two remaining parts after mechanical testing was scanned at the broken end. The scan volume included the complete region around the fracture surface and all free fibres that were pulled out of the opposite part. Since the complete cross section of the MPS geometry of $10 \times 5 \text{ mm}^2$ was scanned at once, a Voxel edge length of $5 \mu\text{m}$ was feasible.

Since the diameter of carbon fibres is much smaller compared to the other fibre materials, the carbon fibre composites were scanned at $2.5 \mu\text{m}$ Voxel edge length. To achieve this resolution without destroying the specimen, the virtual sensor modality was activated. The number of detector pixels was doubled in horizontal direction.

Tube mode 0 was chosen for all scans. The complete set of parameters is listed in Table 4.10

4.6. DETERMINATION OF FREE FIBRE LENGTH

Table 4.10: Scan parameters for the characterisation of free fibre length for long fibre composite materials

| Composite | Voltage (kV) | Current (μ A) | Integration- time (ms) | Number of projections | Voxel edge length (μ m) | Scan time (min) |
|-----------|-----------------|-----------------------|------------------------------|--------------------------|------------------------------------|--------------------|
| PP-IGF | 80 | 160 | 900 | 1700 | 5 | 156 |
| PP-ICF | 70 | 160 | 1000 | 1900 | 2.5 | 404 |
| PP-IPET | 50 | 250 | 1200 | 1700 | 5 | 207 |
| PP-IPVA | 50 | 250 | 1200 | 1700 | 5 | 207 |

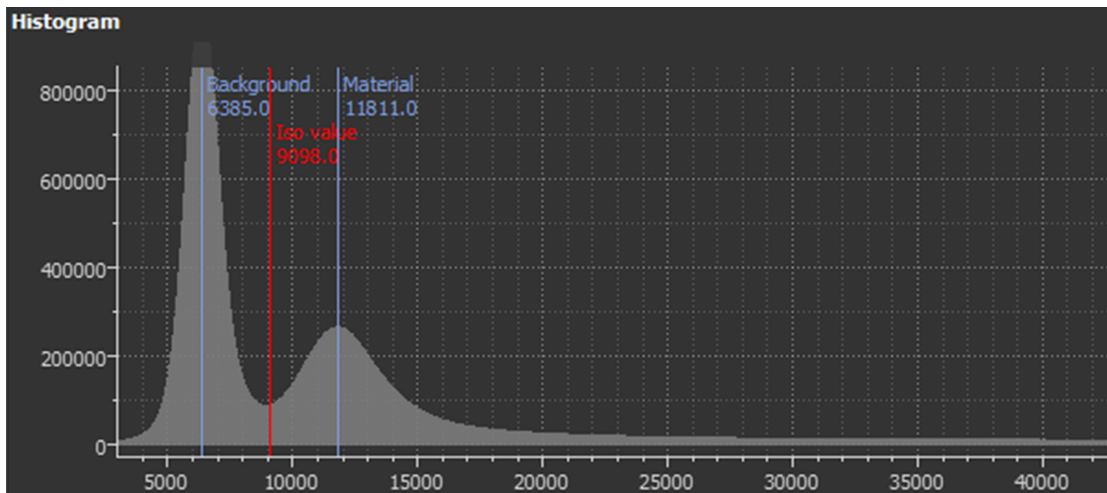


Figure 4.18: Zoomed view into the grey value histogram of a PP-IGF dataset. Grey values for Background (air) and Material (polymer) were determined by VG Studio MAX automatically. The iso value is exactly between these two and represents the transition from polymer to surrounding air (surface)

Pre-processing steps are necessary to separate free fibres from the composite. This separation is done using VG Studio MAX. The result of each step is a modified ROI which is shown in Figure 4.19. First an automatic surface determination is performed and a region at the surface is extracted. Figure 4.18 shows two peaks that were identified by the software automatically. One peak represents surrounding air (background), the other one the polymer (material), the fibre grey values are distributed over a wide range until the maximum of 65535 but with lower frequency. This also contains free fibres, pore surfaces and artefacts. An opening procedure is applied to exclude free fibres from the region. The pores can be excluded by a closing procedure. At the end the region is smoothed and inverted which leads to a region that contains only free fibres that protrude out of the fracture surface. This region is saved as a separate raw data set. For the analysis of these data sets the TM approach was applied using parameters shown in Table 4.11. Parameter studies for each material system lead to these values.

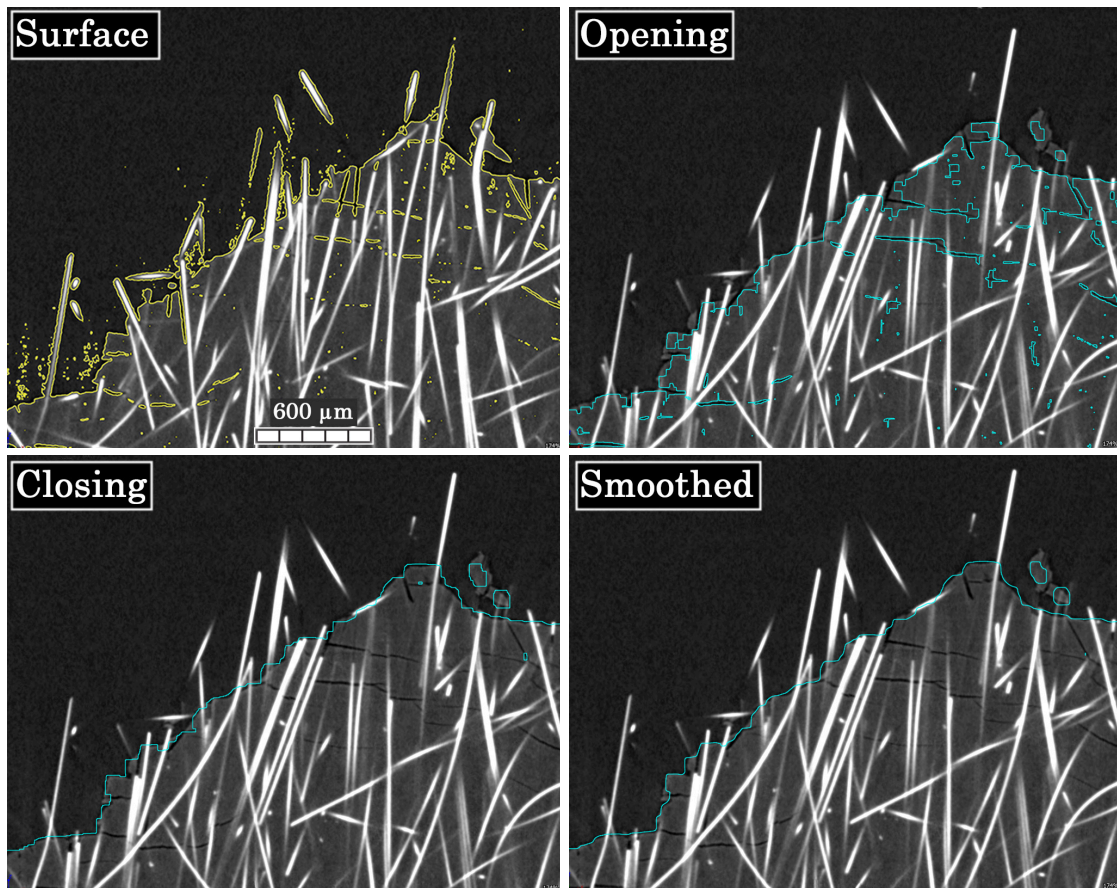


Figure 4.19: Zoomed views into slice images of a PP-IGF dataset in frontal view. The borders of the ROIs that are determined subsequently are highlighted. The smoothed ROI is the final region that is extracted into a raw data set.

For each material system and respective resolution, templates were generated and the binary threshold value optimized. For setting the parameters length threshold, length correction and CC fibre length the approach of taking fibre diameter into account, as described in chapter 4.2.2, was applied.

Table 4.11: FCP-TM parameters for the determination of free fibre length for long fibre composite materials

| Material | | PP-IGF | PP-ICF | PP-IPET | PP-IPVA |
|-------------------|-------------------|--------|--------|---------|---------|
| Parameter | Unit | | | | |
| Gaussian variance | () | 3 | 3 | 3 | 3 |
| Gaussian error | () | 0.001 | 0.001 | 0.001 | 0.001 |
| ROI threshold | () | Otsu | 39000 | 37000 | 40000 |
| Hesse angle | (°) | 31 | 31 | 31 | 31 |
| Segment angle | (°) | 21 | 21 | 21 | 21 |
| Length threshold | (μm) | 30 | 20 | 30 | 30 |
| Length correction | (μm) | 11.5 | 8 | 20 | 11.5 |
| CC fibre length | (μm) | 30 | 17 | 35 | 30 |
| Binary threshold | () | 0.38 | 0.36 | 0.38 | 0.38 |
| Template diameter | (μm) | 16 | 7 | 22 | 16 |

4.7 CT simulation

For the generation of artificial CT data sets the „Sim-CT“ tool, which was developed at University of Applied Sciences, Wels Campus, was used [99]. This simulation tool includes models for X-ray tubes, interaction of X-rays with matter and X-ray detectors. Cone beam geometries can be set up and reconstructions using an FDK algorithm can be performed.

The tool was used for two applications within this thesis: the generation of virtual data-sets for assessment of software accuracy and for the generation of templates for the TM approach. In both cases the grey value data sets should be artefact free. For that reason a monochromatic spectrum at 80 keV was chosen and noise and scatter were not considered. Since the templates should contain grey value distributions that are comparable to the scanned ones, focal spot blurring was activated for the generation of templates. All other parameters were set in a similar way as for the real scans.

The specimen geometry can be loaded into „Sim-CT“ via text-files that contain shape, size, material composition and density. For the template the sphere diameter and material properties were defined. The generation of reference data sets was conducted as described in chapter 4.4.

4.8 Standard methods

For the verification of CT results, destructive investigations were carried out to determine FOD and FLD.

4.8.1 Fibre orientation distribution

The determination of fibre orientation distribution was conducted using grinding and light optical analyses. Peter Hine of University of Leeds did the analyses applying his published methods [14], [16].

4.8.2 Fibre length distribution

The ISO standard method to determine fibre length distribution of fibres in a polymeric matrix is explained in the standard [9]. The polymeric matrix is dissolved or burnt and the fibres remain usually as network. For measuring the length of the fibres the network has to be dispersed using liquids.

Pyrolysis comparison with CT according to ISO standard

The specimens sent to the calibration laboratory SKZ – TeConA GmbH (Würzburg, Germany) were treated in a microwave oven for 30 minutes up to 400 °C and additional 180 minutes up to 600 °C. The remaining fibres were diluted in Aceton for separation. 421 fibres were evaluated for PP-sGF-5 and 1011 for the other materials with higher fibre content. Images were gathered using a digital microscope at 50-times magnification. Before destruction the specimens were scanned and fibre characteristics determined.

Pyrolysis and comparison with CT analyses on individual fibre basis

In addition to the analysis by the calibration laboratory, the topic was processed within the masters thesis of Susanne Gleiss [100]. The idea was to investigate exact the same fibres with CT and optical analysis. For this purpose very small cut-outs were prepared, scanned, pyrolysed and analysed with LOM. These cut-outs contained up to 300 fibres. Cutting the specimens was done carefully with a hot wire and hot razor blade to avoid fibre fracture. Pyrolysis and LOM analysis were performed according to [9] with modifications taken from [25] and optimized by experiments. Temperature and time for burning the matrix were optimized to assure for complete polymer removal. As specimen holder for pyrolysis and LOM likewise, a crystallizing dish was used 4.20.

The advantages of the dish were that from placing the specimen on top until LOM analysis the fibres did not have to be touched, the fibres could be dispersed on top of the ground since it was not flat, and the magnification of the microscope could be set to the necessary value of 50x. The dispersion of remaining fibres was done with distilled water and ethylalcohol and an ultrasonic device. The cup like shape of the ground prevented the fibre suspension from being moved off the top. Several images were collected and stitched together since the area covered by the fibres was rather big for the chosen magnification. Length measurement was done manually using ImageJ with plugins for saving values to text file.

Before the comparison of CT with pyrolysis was conducted, the influence of Voxel edge length was determined by scanning the specimens at 1 μm and 2 μm Voxel edge length. Worse resolution was not tested because the quality of length determination

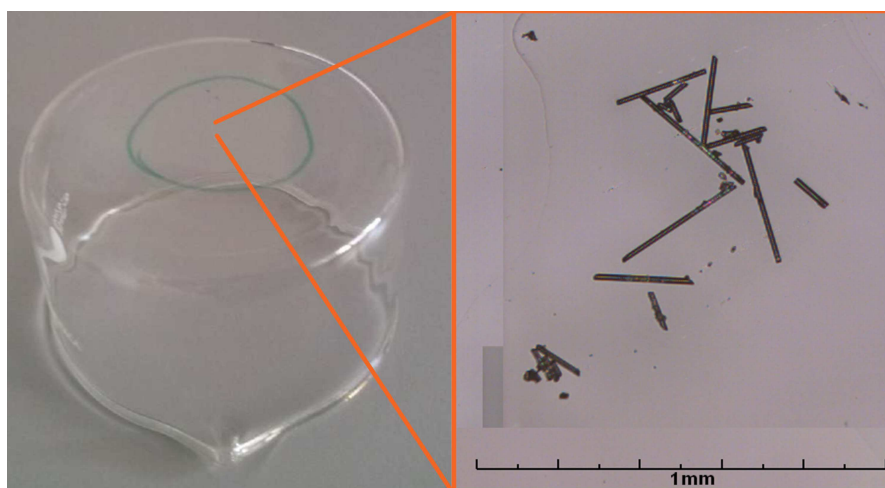


Figure 4.20: Photo of an inverted crystallization dish with dissolved fibres on top within the green mark, zoomed region of microscopy showing some fibres

should be as good as possible. 2 μm were chosen because this is the desired standard value.

Qualitative CT data analysis

The next three chapters address different aspects starting with qualitative descriptions of CT data of the investigated material systems.

The second chapter contains results in the context of the implemented CT data image processing tools. The last results chapter shows results that were acquired applying the developed methods in order to show the significance of this thesis.

Qualitative CT data analysis is performed by showing slice images and 3D rendered views. This will give an impression about scan quality, fibre morphology and microstructure of the composite material. Grey value histograms and grey value profiles will give indication about data quality with respect to potential fibre segmentation.

This chapter is divided into two sections, one for glass fibre materials, and one for polymer fibre composites.

Cross sectional slice images and a 3D rendered overview is shown for different fibre matrix composites. Grey value histograms show the complete 16 bit range from 0 to 65535 which allows for the comparison of data quality in terms of contrast and noise. Zoomed 3D rendered views show some single fibres within the composite by clipping the 3D data set which gives an impression about fibre morphology. Grey value profiles perpendicular to fibre long axis are drawn together with lines showing the nominal diameter. Line profiles plotting the grey value trend along a line through the Voxel data set can give information about image quality, too. Profiles across edges, like a fibre surface, show the blurring of the edge and also the level of noise. From the grey value difference between surrounding material and fibre, conclusions about contrast can be drawn.

5.1 Glass fibre composites

Since glass fibres are the most commonly used fibres for reinforcing polymers, some additional investigations were conducted only for this type of fibre material.

Cross sectional slice images and 3D images acquired with different Voxel edge lengths ranging from 1 μm to 5 μm are shown in Figure 5.1. Visual analysis of cross sectional slice images, especially at the best resolution of 1 μm Voxel edge length, indicates that glass fibres are straight with circular cross section and smooth surface. The axial cross section (X-Y) shows fibres with varying diameters. Fibres are touching at many positions building different structures. Fibre ends can meet in different angles, or fibres can run parallel. Since the axial cross section is showing mainly circular or elliptical structures, a distinct orientation in Z direction can be assumed. The small cut-out shows that the majority of fibres is cut on top and bottom which prevents from fibre length determination which was not the purpose of this investigation.

At 5 μm Voxel edge length it starts to get very difficult to separate fibres visually at every position. Especially the parallel running fibres tend to get merged.

Decreasing data quality starting at 3 μm Voxel edge length is also seen in the histograms in Figure 5.2. Noise level increases and contrast between polymer and glass decreases. The peak for glass at high grey values, which is visible at 1 μm Voxel edge length, disappears at lower resolution.

An overview of the influence of fibre content on image quality and composite microstructure is shown in by cross sectional images (Figure 5.3), 3D renderings (Figure 5.4) and the corresponding histograms in Figure 5.5.

The visual impression of 5 wt.% glass fibre content (equals 1.9 vol.%) is that the fibres are very homogeneously distributed and only few touching points are present. The material with 30 wt.% glass fibre content (equals 13.4 vol.%) on the contrary shows almost no free fibre and little space between the fibres. This impression is emphasised by the clipped 3D images.

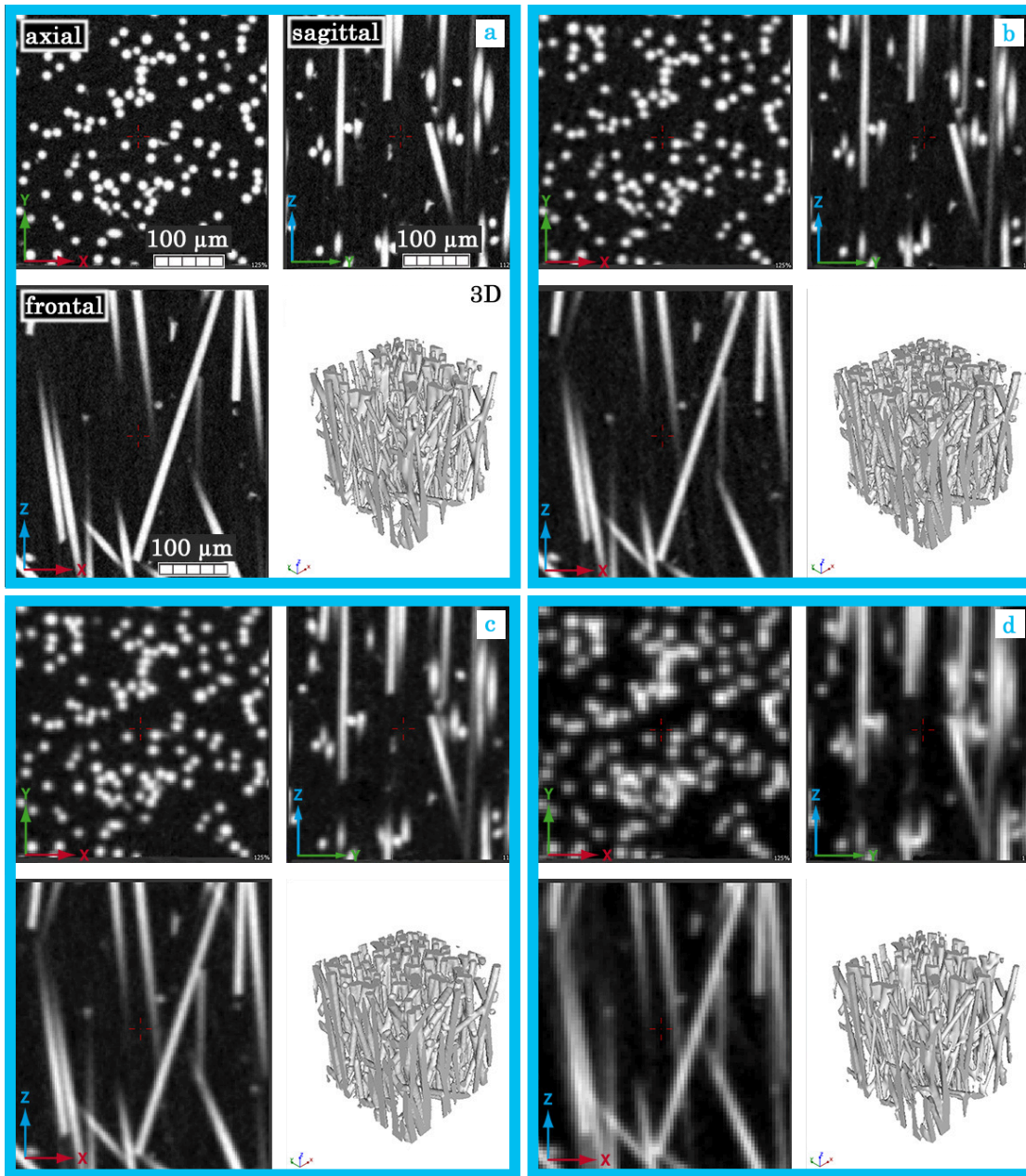


Figure 5.1: CT slice images with different resolution of PP-sGF-30 cut-out *Centre_1* scanned with different Voxel edge length: (a) 1 μm , (b) 2 μm , (c) 3 μm , (d) 5 μm

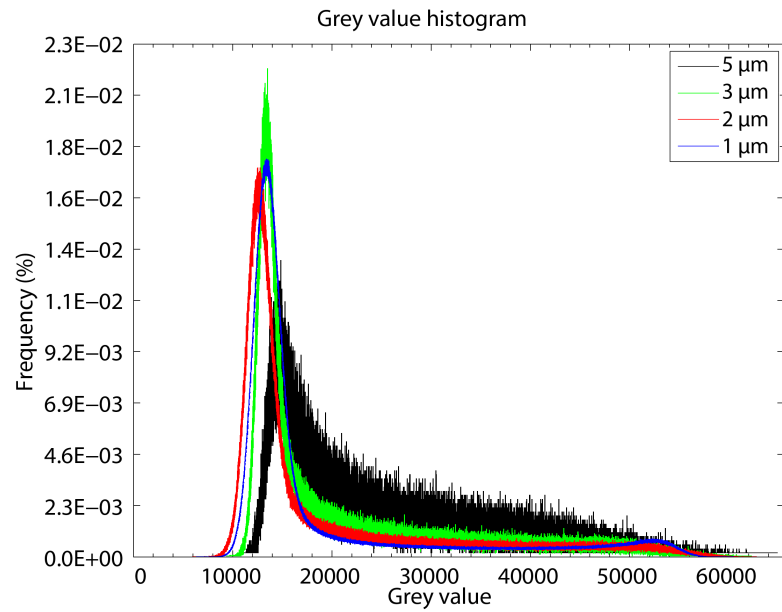


Figure 5.2: Grey value histograms of PP-sGF-30 scanned with different Voxel edge length

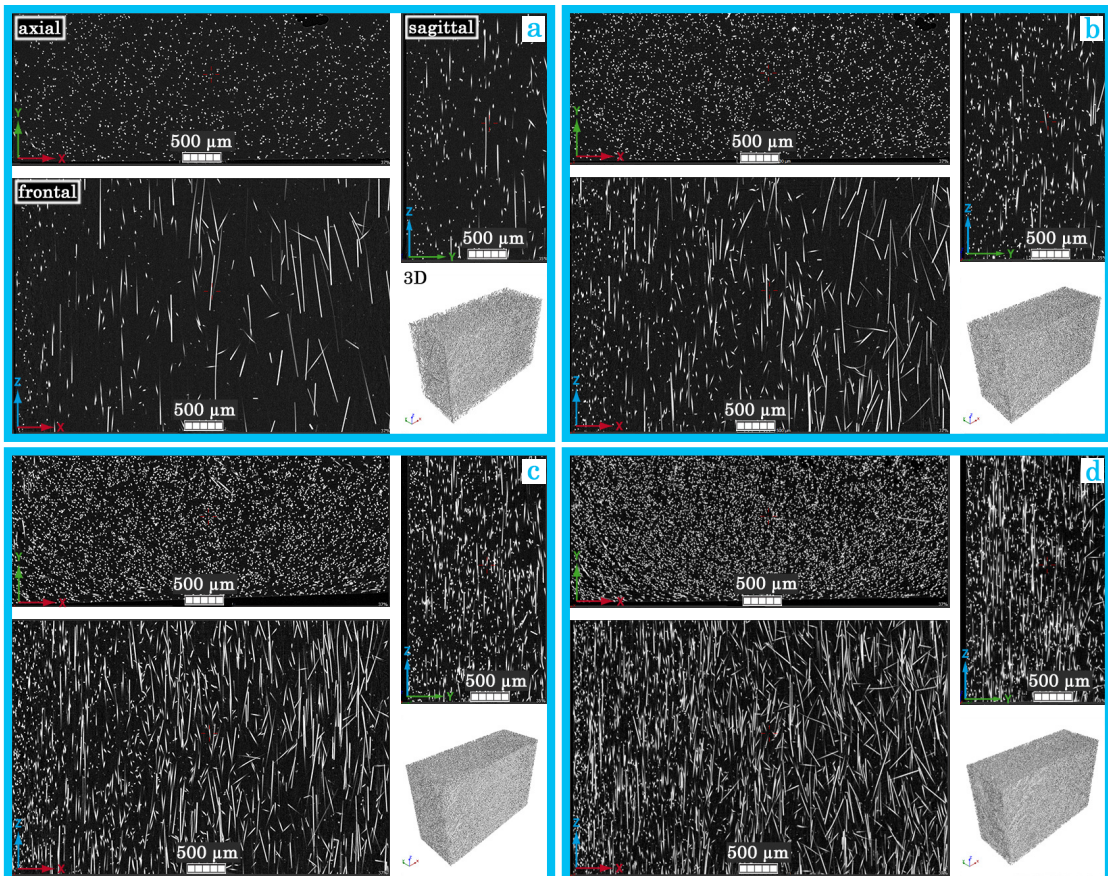


Figure 5.3: CT slice images with different fibre content of PP-sGF, quarter of an MPS scanned with 2 μm Voxel edge length: (a) 5 wt.%, (b) 10 wt.%, (c) 20 wt.%, (d) 30 wt.%

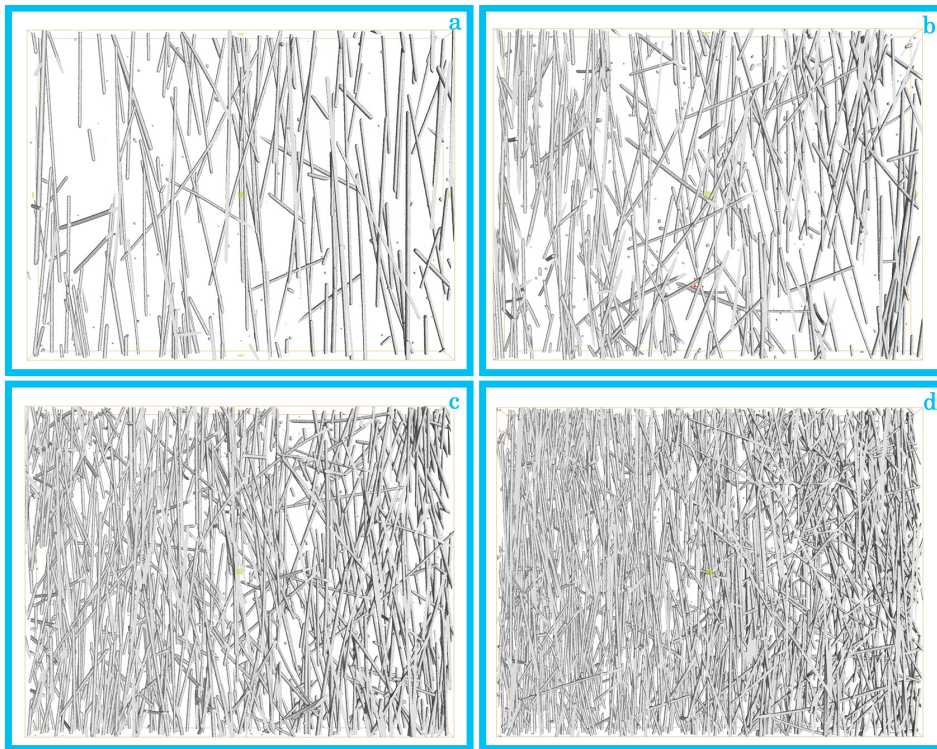


Figure 5.4: 3D rendered views of clipped regions of PP-sGF, quarter of an MPS with different fibre content scanned with 2 μm Voxel edge length: (a) 5 wt.%, (b) 10 wt.%, (c) 20 wt.%, (d) 30 wt.%

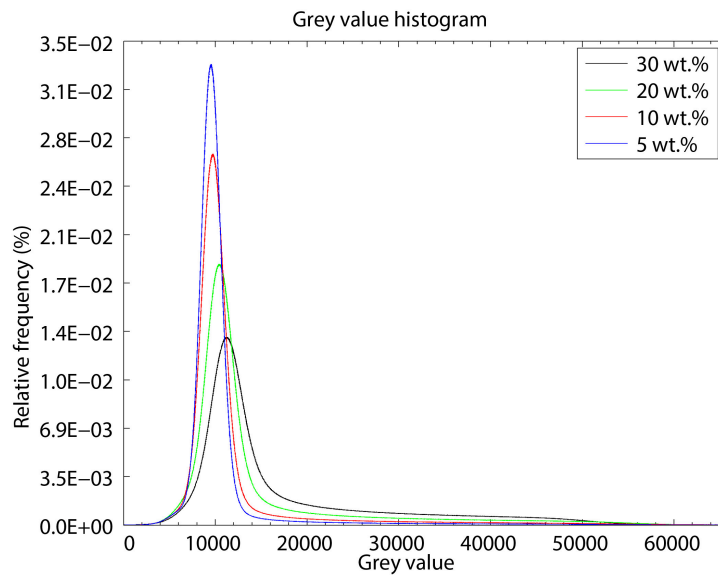


Figure 5.5: Grey value histograms of PP-sGF, quarter of an MPS with different fibre content scanned with 2 μm Voxel edge length

For individual glass fibres two positions were chosen for line profiles: a free fibre with surrounding air (5.6) and a fibre with two neighbouring fibres, a cluster region (5.7). The profiles of the free fibre in Figure 5.8 left shows the blurring at lower resolution by broadening of the peak and by reduction of contrast between surrounding polymer matrix and glass fibre. The profiles at 1 and 2 μm Voxel edge length look very similar. The right part of this Figure indicates that a separation of fibres is only possible easily at 1 and 2 μm Voxel edge length since the local grey value maxima disappear starting from 3 μm Voxel edge length.

The vertical lines in the grey value profile (Figure 5.8) indicating nominal diameter are approximately at the position of maximum of first derivative for 1 and 2 μm Voxel edge length. If the criterion of maximum of first derivative would be applied to the low resolution data, the diameters would be overestimated since the peaks are much broader.

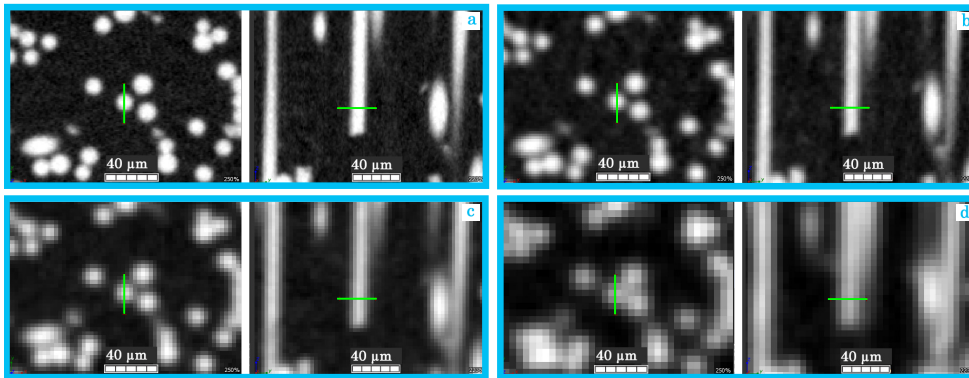


Figure 5.6: CT slice images of PP-sGF-30 scanned with different Voxel edge length showing the positions for taking the grey value profiles as green lines: 1 μm (a), 2 μm (b), 3 μm (c), 5 μm (d)

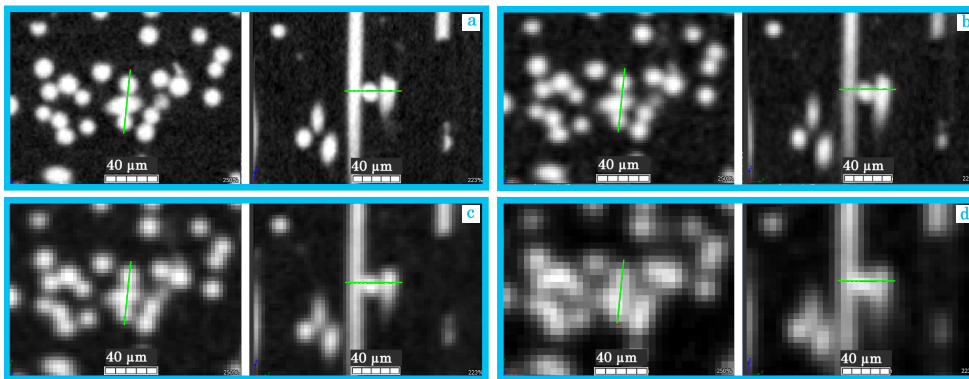


Figure 5.7: CT slice images of PP-sGF-30 scanned with different Voxel edge length showing the positions for taking the grey value profiles as green lines: 1 μm (a), 2 μm (b), 3 μm (c), 5 μm (d)

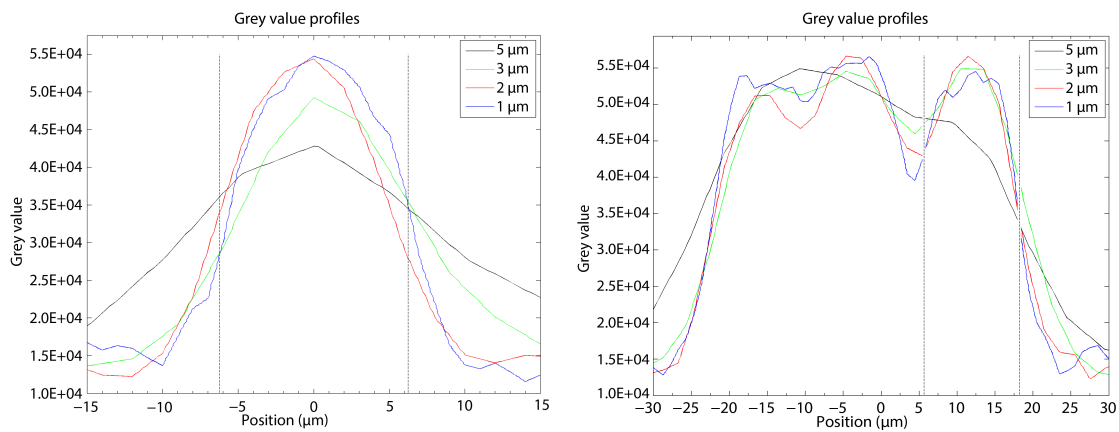


Figure 5.8: Grey value profile plots perpendicular to fibre long axis of PP-sGF-30 scanned with different Voxel edge length for free fibre (left) and cluster region (right)

5.2 Polymer fibre composites

The detection of polymer fibres within a polymer matrix is much more difficult than glass fibres since densities of fibres and matrix are similar and difference in attenuation small. This circumstance leads to worse contrast which can be seen in the histograms by broad peaks that can be separated worse. The difference in grey value between fibre and matrix is still big enough to allow for fibre segmentation. Cross sectional images and 3D images of details reveal the very complex nature of these kind of fibres (Figure 5.9). Especially PET fibres build structures with high curvature. Grey value profiles along PET fibre diameter show similar width which indicates circular shape. For PVA fibres a ribbon like structure can be concluded since width of the two orthogonal directions is different. These ribbons can be twisted along the fibre axes as seen in the 3D images like Figure 5.10.

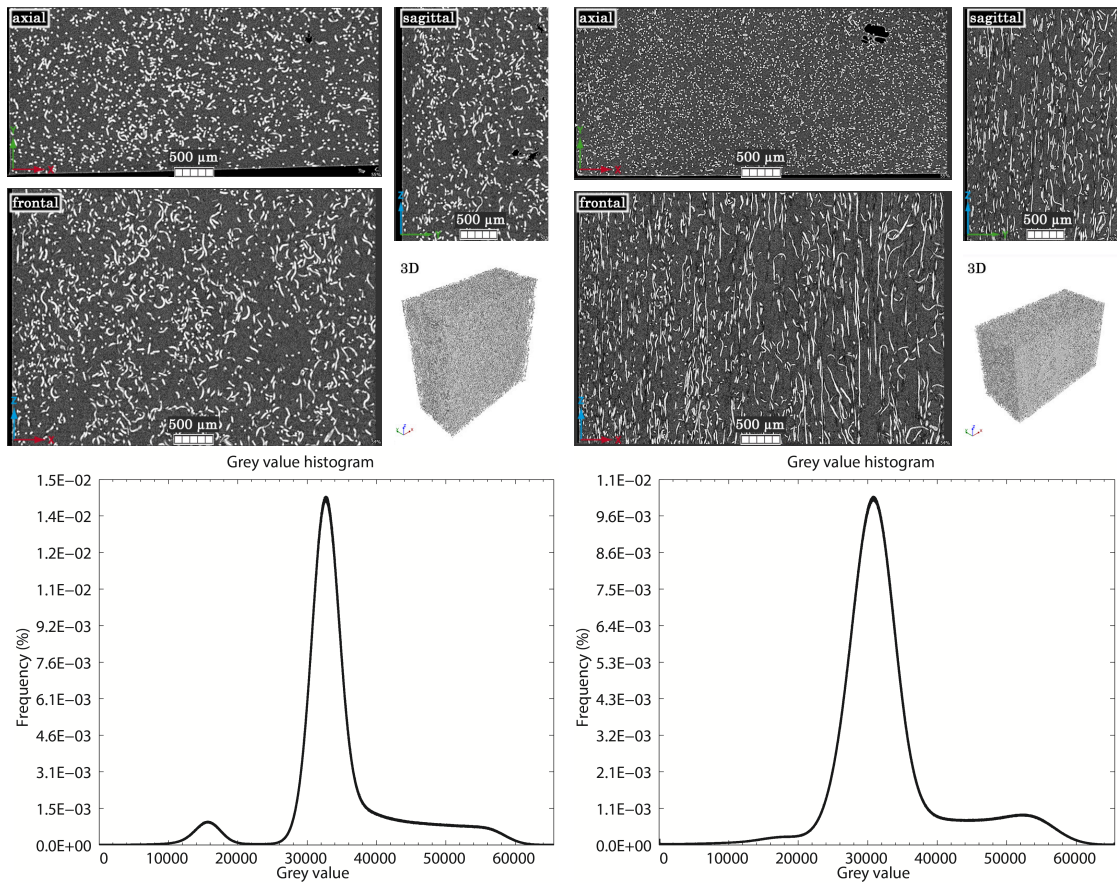


Figure 5.9: CT slice images and grey value histograms for PP-sPET (left) and PP-sPVA (right)

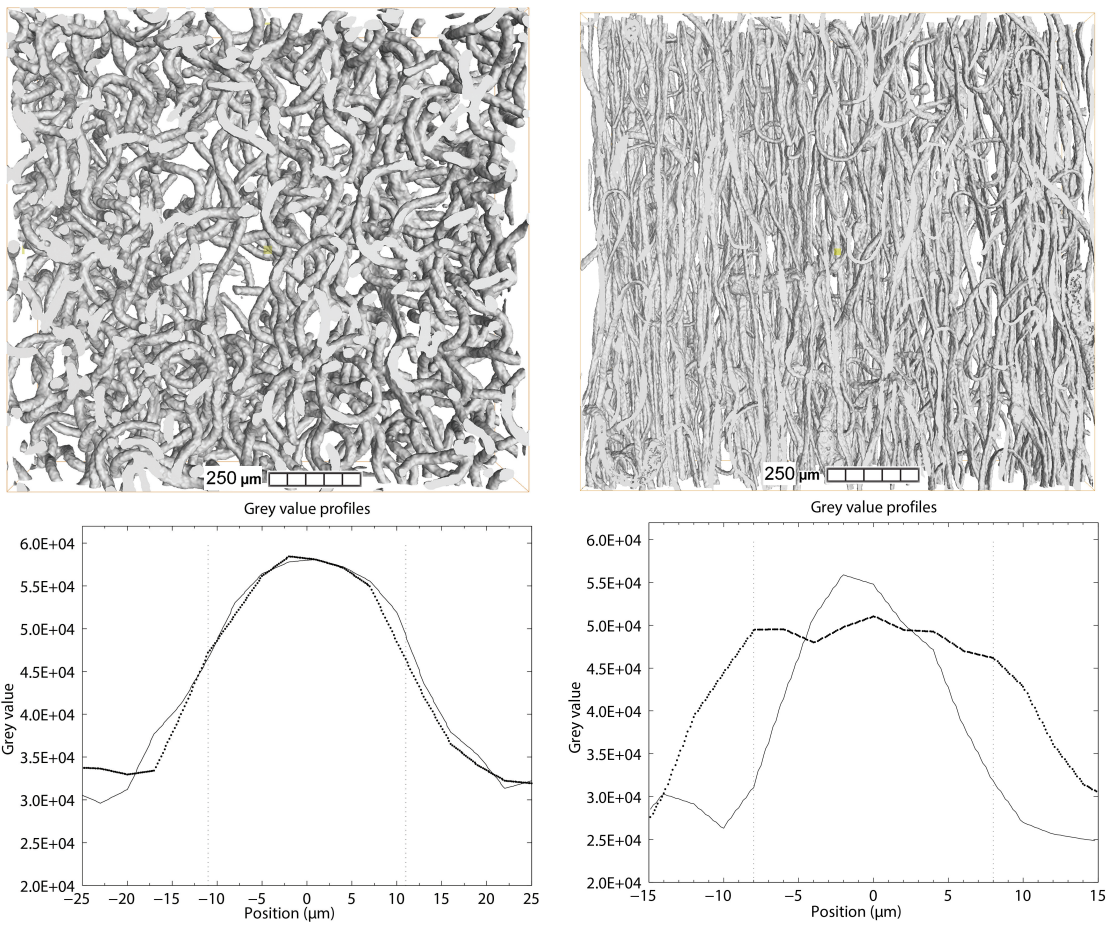


Figure 5.10: 3D rendered views of small details and grey value profiles perpendicular to a single fibre long axis for PP-sPET (left) and PP-sPVA (right). Two profiles are drawn for each material in orthogonal directions

The biggest difference of short and long polymer fibres is the stronger alignment of long fibres leading to less curvature especially in the regions of high shear within an MPS. Fibre content of short fibre materials was 20 wt.% and ca. 14 wt.% for long fibre materials. This difference additionally influences micro-structure and causes broader and higher matrix peaks in the histograms shown in Figure 5.11. The grey value profile of the selected long PET fibre (Figure 5.12) shows a local minimum near fibre core. This could be explained by scatter and refraction effects that can occur at high resolution and very stable scan conditions causing increased grey values at surfaces. This effect is seen especially for PET fibres since the ratio of diameter and Voxel edge length is highest for all investigated fibre materials.

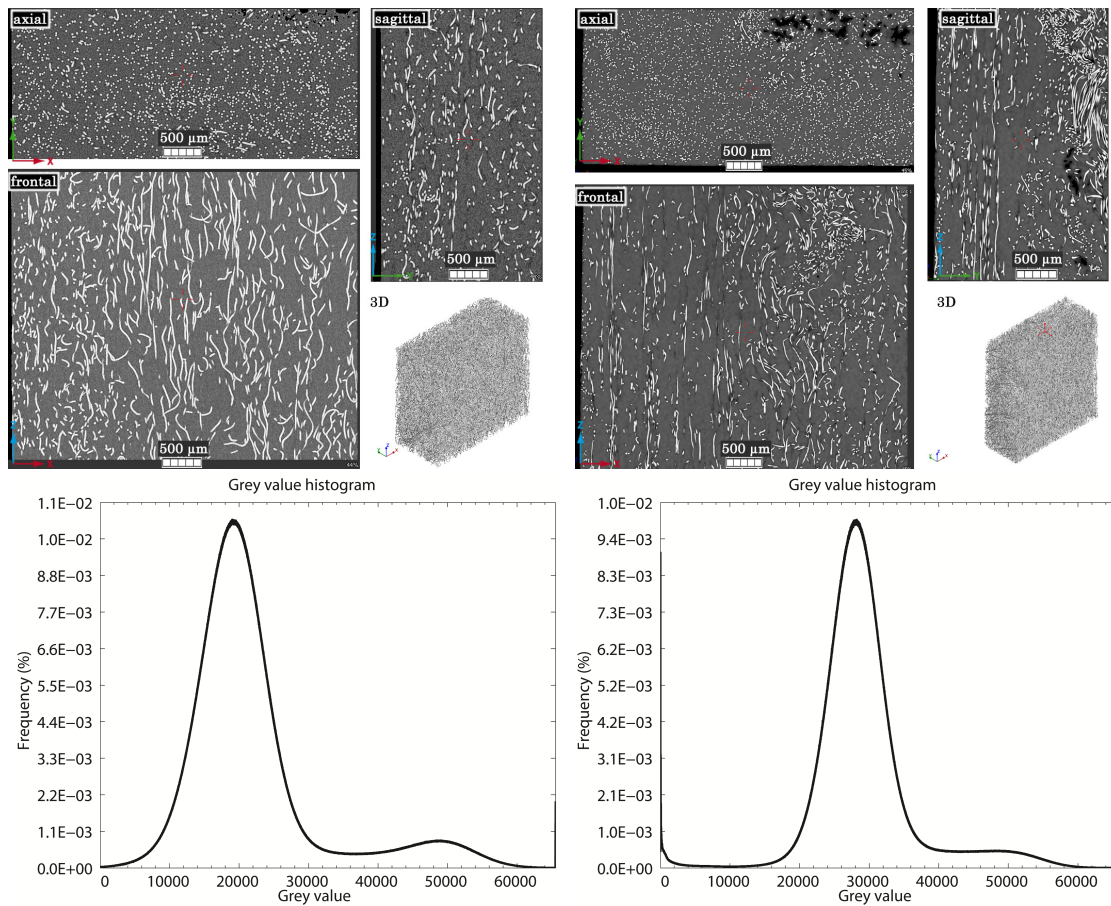


Figure 5.11: CT slice images and grey value histograms for PP-IPET (left) and PP-IPVA (right)

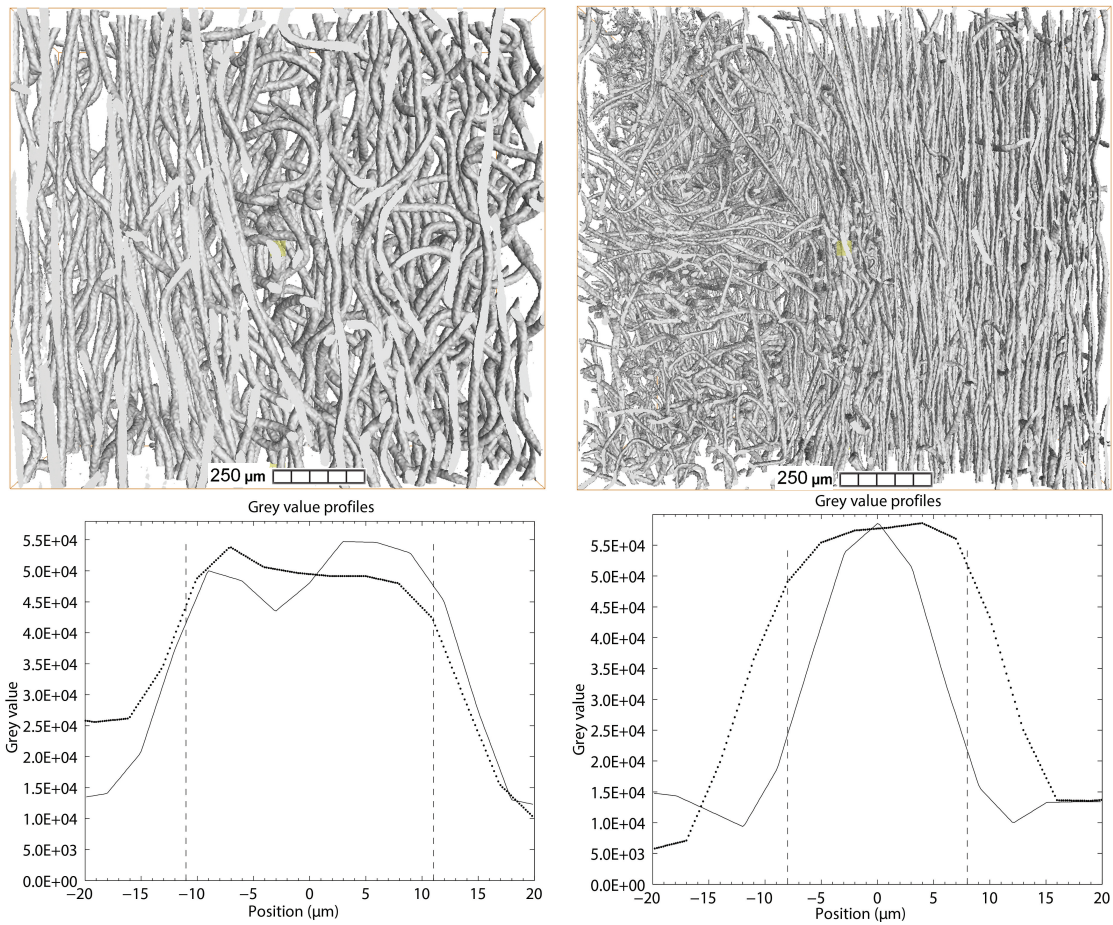


Figure 5.12: 3D rendered views of small details and grey value profiles perpendicular to a single fibre long axis for PP-IPET (left) and PP-IPVA (right). Two profiles are drawn for each material in orthogonal directions

Evaluation of CT data analysis methods

The final results of the implemented fibre characterization methods are on one hand side a Voxel dataset containing all medial axes and on the other hand a text file with all characteristic values for each individual fibre. For all fibres that are classified as curved, the intermediate coordinates along the fibre are saved to an additional text file.

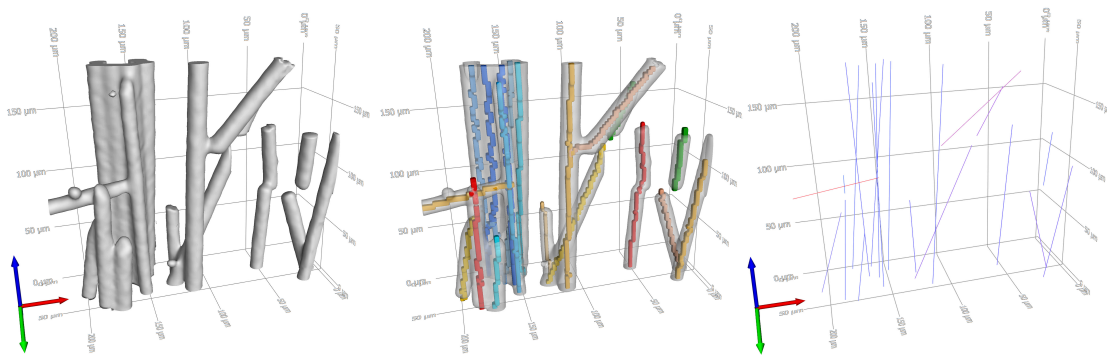


Figure 6.1: 3D visualization of raw CT data (left), colour coded medial axis with transparent CT data (middle) and extracted fibres as connected lines of endpoints with colour coded information about orientation (right)

After calculations are finished, results are visualized by connecting start and end-point of each fibre with a straight line. A colour is assigned to the line according to fibre orientation. Fibres aligned in X direction are red, in Y direction green and in Z direction blue. Intermediate directions are coloured by linear combinations in RGB space. Figure 6.1 shows exemplary some single fibres with different orientation together with the corresponding, extracted medial axes as coloured lines. Red fibres are false representation

of the real fibres since the software connected two fibres erroneously or broke one fibre into two.

The following sub chapters show results with respect to the measurement methods. In this context, measurement method is understood as the complete process chain from CT scan, reconstruction through to 3D data analysis. Investigations about measurement method comprise repeating measurements to document reproducibility, the comparison of results with reference data and the comparison with standard methods to document accuracy. Two very important influence factors to the FCP result, analysis volume and specimen orientation on the turntable, are discussed as well.

All shown results in this chapter were conducted for short glass fibre filled PP composites.

6.1 Reference data sets

Fibre arrangement, length- and orientation distribution of the three extracted data sets are different because the reference data sets were cut out of the multi purpose test specimen at different positions. Figure 6.2 shows 3D visualizations of the three data sets that indicate small difference in fibre orientation. The extent of all data sets is exactly the same.

The results of cylinder fits were used as input data for CT simulation as well as reference data for comparisons. The orientation distributions are shown in polar plots in Figure 6.3 and the length distributions are shown in Figure 6.4. Table 6.1 gives the overview of the most important features of all three data sets.

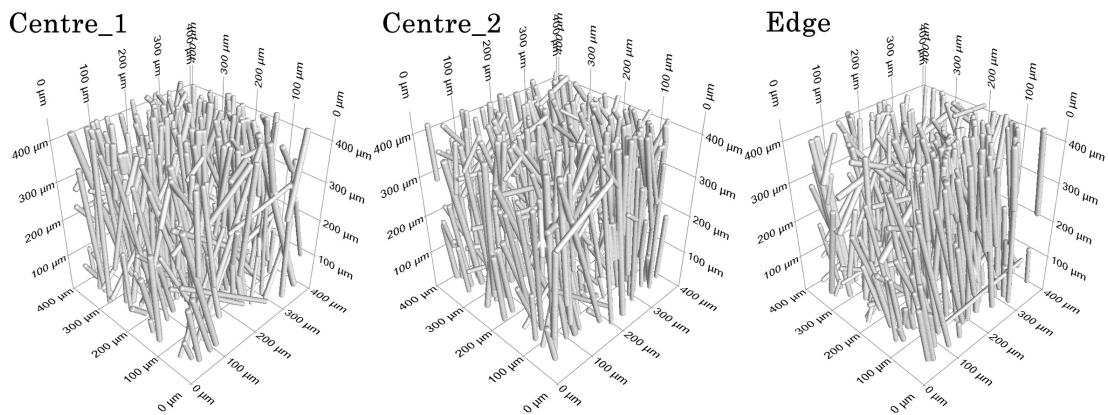


Figure 6.2: 3D Rendering of simulated data at a Voxel edge length of 2 μm .

For CT simulation all fitted cylinders were used. Thus a comparison with complete reference data is valid. At the edges of real CT data sets, problems occur for comparisons with reference data because fibres are truncated. For fibres that are truncated parallel to the long axis, CT analyses often deliver no fibres at all while fibres truncated transversal

lead to difference in length compared to reference data. For this reason problematic border fibres are excluded from comparisons by generating new reference data without border fibres. Values shown in table 6.1 are listed without border fibres for MAE concept and with border fibres for TM concept. The reason is that MAE concept cannot deal with border fibres at all while TM concepts gives acceptable results. Lower fibre volume fractions are result of deleting border fibres.

Table 6.1: Characteristics of reference data sets for MAE and TM concept used as input for comparisons

| | Input without border fibres for MAE concept | | | Input complete for TM concept | | |
|--|--|----------|-------|----------------------------------|----------|-------|
| | Centre_1 | Centre_2 | Edge | Centre_1 | Centre_2 | Edge |
| Fibre count | 237 | 232 | 223 | 255 | 246 | 228 |
| Weighted average length (μm) | 277 | 262 | 265 | 274 | 266 | 265 |
| Average length (μm) | 202 | 192 | 192 | 200 | 193 | 193 |
| Maximum length (μm) | 458 | 511 | 434 | 458 | 511 | 434 |
| Average diameter (μm) | 12.5 | 12.5 | 12.5 | 12.5 | 12.5 | 12.5 |
| σ_D (μm) | 1.4 | 1.3 | 1.4 | 1.3 | 1.3 | 1.4 |
| Fibre fraction per volume (vol.%) | 8.3 | 7.8 | 7.5 | 8.8 | 8.2 | 7.7 |
| per weight (wt.%) | 20.2 | 19.2 | 18.4 | 21.3 | 20 | 19 |
| a_{XX} | 0.124 | 0.123 | 0.144 | 0.133 | 0.132 | 0.144 |
| a_{YY} | 0.013 | 0.008 | 0.005 | 0.013 | 0.008 | 0.005 |
| a_{ZZ} | 0.863 | 0.869 | 0.851 | 0.854 | 0.859 | 0.852 |
| a_{XY} | 0 | -0.002 | 0.007 | -0.02 | -0.002 | -0.01 |
| a_{XZ} | -0.055 | -0.111 | 0.197 | -0.063 | -0.107 | -0.05 |
| a_{YZ} | 0.035 | 0.024 | 0.03 | 0.036 | 0.024 | 0.029 |
| Strength of orientation | 0.87 | 0.89 | 0.86 | 0.86 | 0.88 | 0.86 |

All three data sets show strong orientation in Z direction (injection direction). The X component is very small and the Y component practically zero. Differences can be seen in the strength of orientation where cut-out *Centre_2* shows the highest orientation. This effect can be seen in the polar plot too (Figure 6.3). *Centre_2* has the highest frequency per angular segment and shows most entirely values at $0 < \theta < 15^\circ$.

Fibre length distributions of all three data sets show only small differences. Data *Centre_1* shows highest frequency for long fibres which is also seen in mean fibre length. (Figure 6.4 and table 6.1) Although differences are small, the influence of varying fibre arrangement on the result of CT data analysis can be investigated using these data sets.

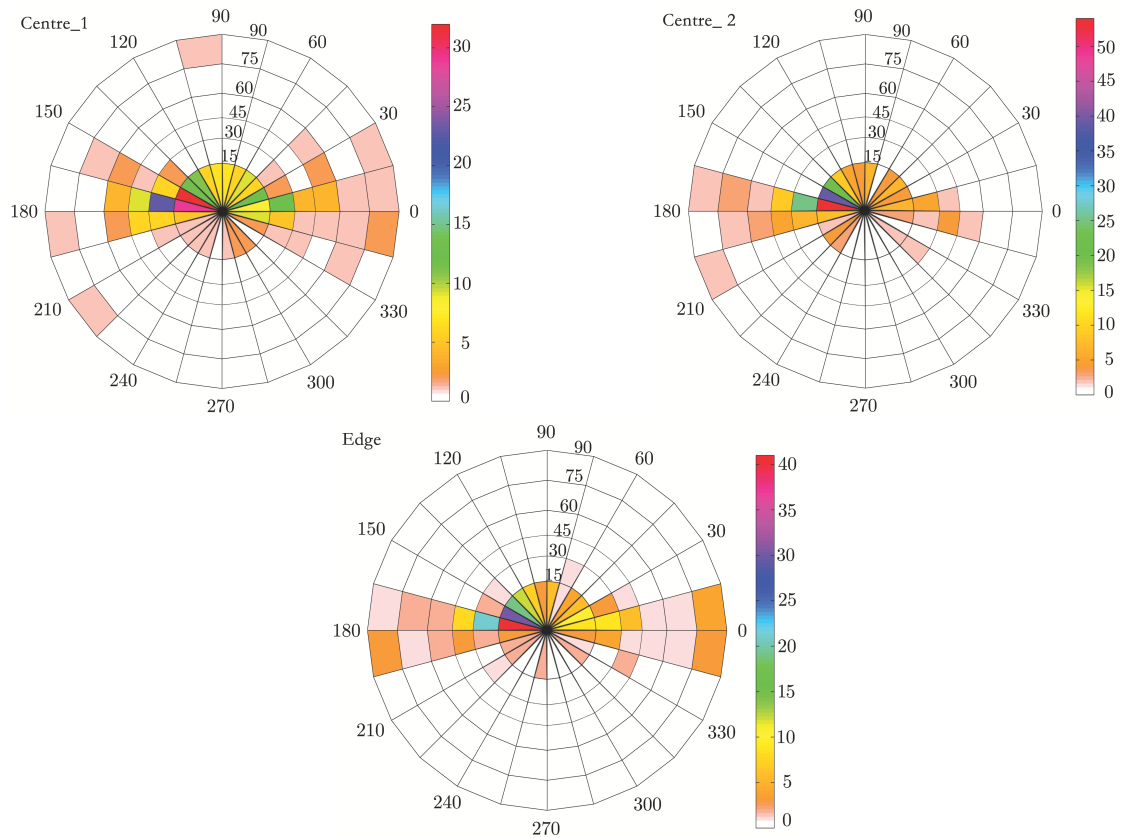


Figure 6.3: Polar plots of absolute orientation distribution for all three reference data sets *Centre_1*, *Centre_2* and *Edge*

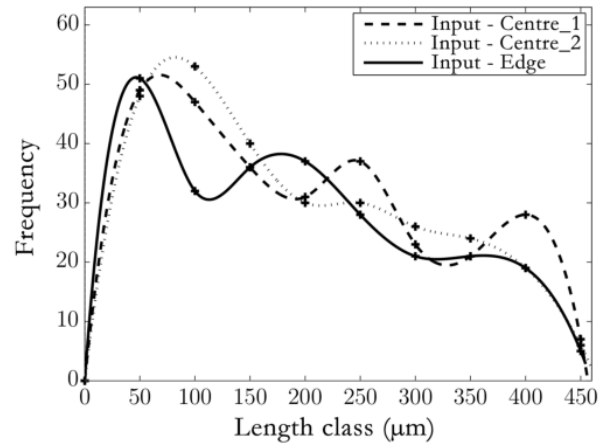


Figure 6.4: Fibre length distribution of the reference data sets *Centre_1*, *Centre_2* and *Edge*

6.2 Examination of accuracy

Accuracy of individual fibre extraction methods was determined for the three cut-out data sets. At first proper values for length correction were determined. Length correction is necessary because the medial axis extraction deletes a part of the fibre ends (Figure 4.10). The correction value is slightly depending on resolution and software method. For the determination of proper correction values, the correctly extracted fibres were determined from analyses without length correction ($l_c = 0$). A comparison with corresponding lengths of input data leads to the values for length correction at respective Voxel edge length. Since the correction values were determined with the use of only correctly extracted fibres, the value is independent from data set and only depending on Voxel edge length and software concept. For this reason a mean value for each Voxel edge length and each software concept from all three reference data sets was calculated (Table 6.2). Simulated data was evaluated only with TM concept.

Table 6.2: Length correction values for different Voxel edge length and MAE and TM analyses on scanned data and TM analysis on simulated data

| Voxel edge length (μm) | MAE | | | TM | | | TM-SIM | | |
|--|-----|-----|------|------|------|------|--------|-----|------|
| | 1 | 2 | 3 | 1 | 2 | 3 | 1 | 2 | 3 |
| $L_c(\mu\text{m})$ | 7.9 | 9.5 | 10.8 | 10.0 | 11.3 | 12.2 | 11.3 | 9.7 | 11.6 |

Data for each cut-out, resolution and software concept, that were used for averaging, are listed in Appendix A 8.

Analysing errors of individual fibre extraction on fibre basis allows to identify the most prominent reasons for errors. At higher resolution, separation and wrong connection occur in equal measure while separation tends to become the major reason at lower resolution (Figure 6.5). The effect of increase of number of errors with reduction of resolution is most prominent for the MAE concept and least pronounced for simulation with constant diameters. The same trend was found for the differences of average and weighted average length (Figure 6.6). No clear trend was found for differences of orientation tensor elements (Figure 6.7 but all differences are in a very small range.

Tables and graphs are shown as result of the examination of accuracy in the following. Graphs showing all cylinders and extracted lengths are shown for scanned data analysed with MAE and TM approach. Tables include features of length, orientation, diameter, accuracy and detected reasons for errors are given in Appendix B 8. Results are shown for all three cut-outs (*Centre_1*, *Centre_2*, *Edge*), all two software approaches (MAE, TM) and all resolutions (1 μm , 2 μm , 3 μm). Figure 6.8 contains as final result an overview of all determined accuracies (*Accuracy (Input cylinders)*).

As result of the semi-automatic comparisons of input data and CT results, all cylinders were plotted in a diagram length(cylinder ID), sorted by length. Figures 6.9 and 6.10 show diagrams for each cut-out separately. Input data is shown in green, the correct extracted fibres in blue. Cylinders that were either erroneously separated or erroneously connected are marked in red and orange. It is obvious that split fibres have shorter length than the corresponding input data. For wrong connected fibres length is most often longer than the input data. In some cases the length is even smaller which can happen for segments with opposite orientation. Start and endpoint move together and the resulting length is reduced.

Border fibres that are not extracted correctly are marked light blue. For very short fibres it can happen that these are not extracted at all because the determined length is below the length threshold. These fibres are marked purple and are denoted as *Other problems* in the graph.

Border fibres were partly excluded from analysis for quantification of accuracy. Two accuracy values were determined: the number of input cylinders with correct extracted fibre *Accuracy (Input cylinders)* and the number of extracted fibres that were correct *Accuracy (Extracted fibres)*.

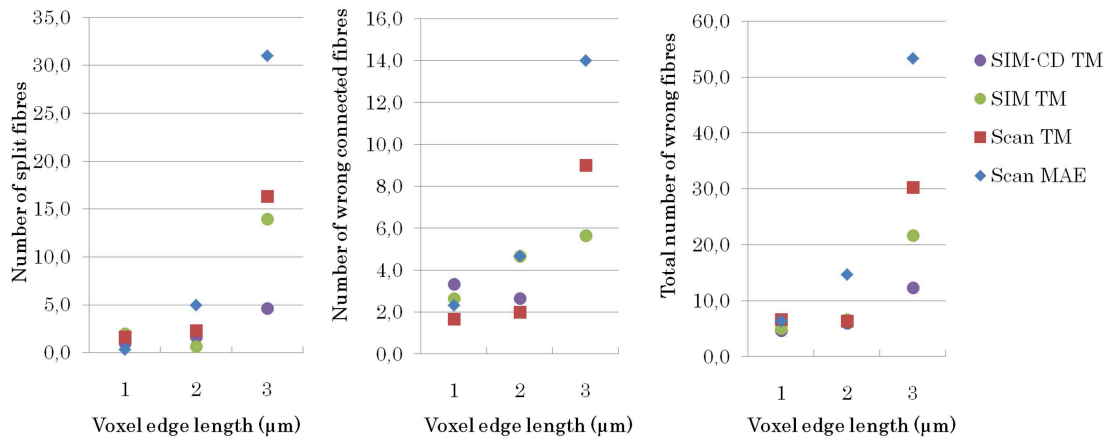


Figure 6.5: Number of erroneously extracted fibres: split fibres (left), wrong connected fibres (middle) and total number of erroneous fibres (right)

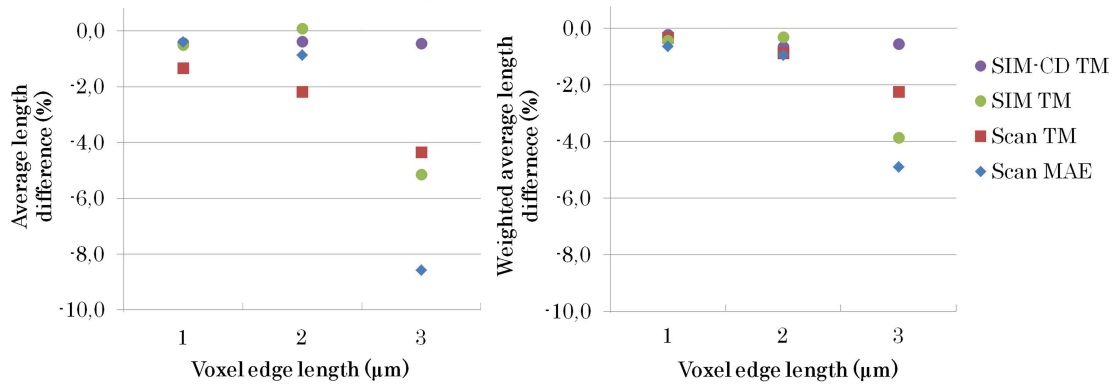


Figure 6.6: Difference of length results compared to input for different resolutions and scans analysed with MAE and TM and simulations analysed with TM

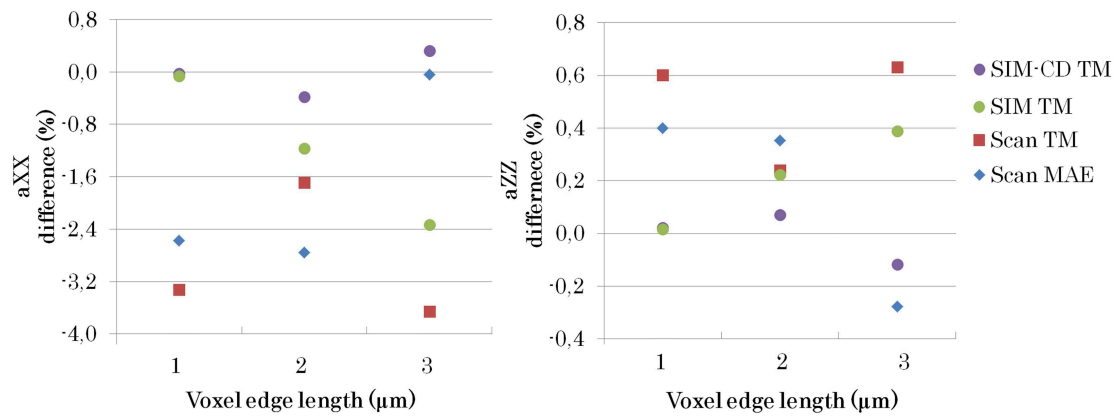


Figure 6.7: Difference of orientation results compared to input for different resolutions and scans analysed with MAE and TM and simulations analysed with TM

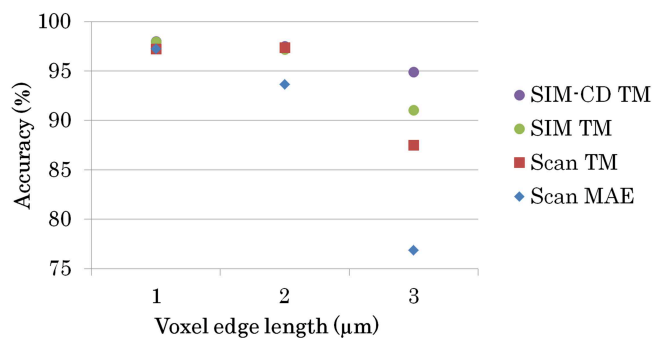


Figure 6.8: Accuracy with respect to cylinder input for different resolutions and scans analysed with MAE and TM and simulations analysed with TM

A comparison of the length over cylinder ID for MAE and TM (Figures 6.9 and 6.10) makes clear that the TM concept leads to more accurate results because much less fibres are erroneously extracted.

All results reveal the best results in terms of least differences to reference data and highest accuracy for the simulated data. Variations in diameter can lead to significant errors leading to reduced accuracy especially at lower resolution (Figure 6.8). For the scans the influence of resolution is very strong for the MAE concept and significant for the TM concept. Determination of length is affected by lower accuracy much whereas orientation is not much influenced. This is indicated by the difference in average length of ca. 5 % and only ca. 0.6 % for a_{ZZ} .

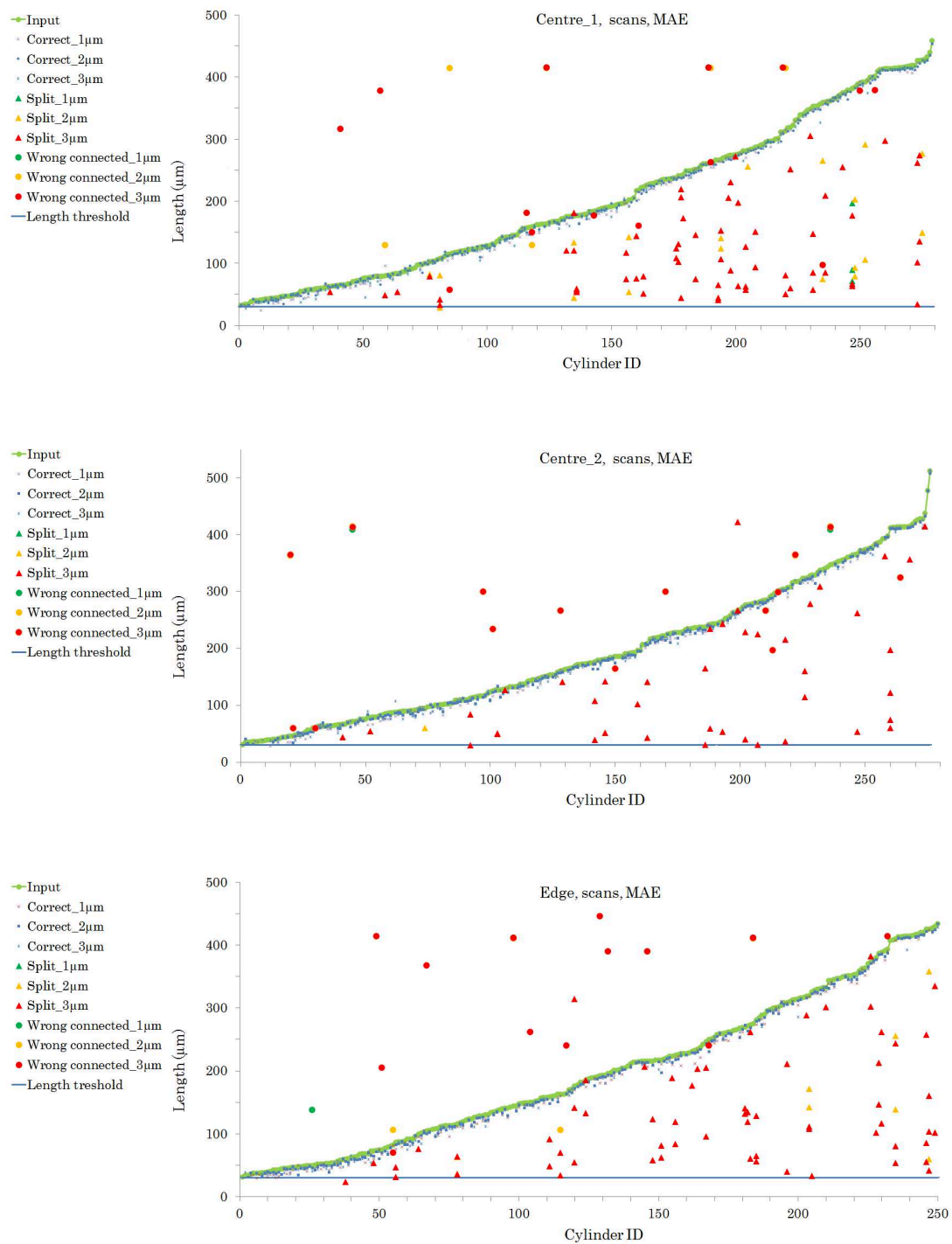


Figure 6.9: Fitted cylinder data and extracted fibre data, generated from scans with MAE concept, showing occurring problems for all three cut-outs at voxel edge length 1 μm (green markers), 2 μm (orange), 3 μm (red)

6.2. EXAMINATION OF ACCURACY

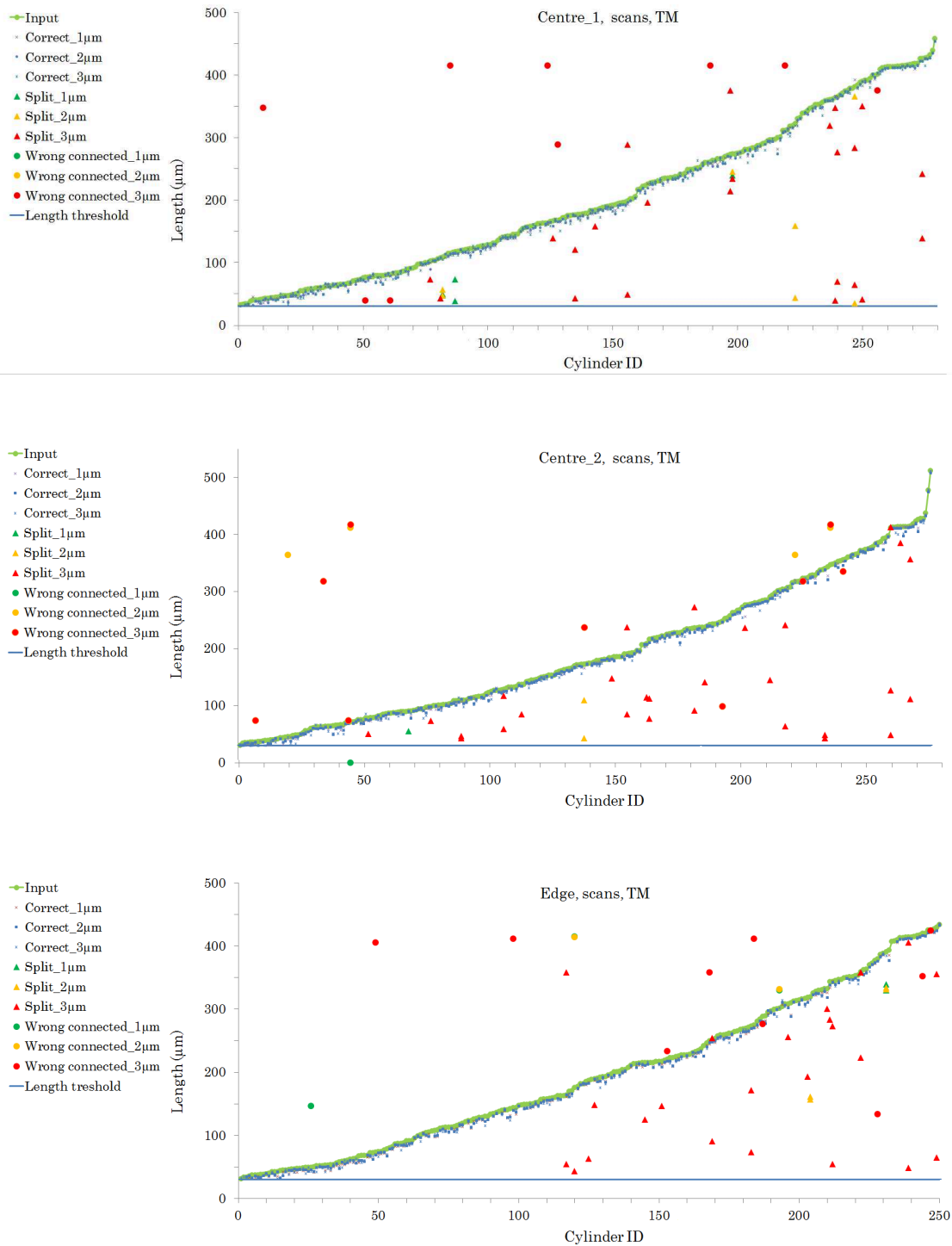


Figure 6.10: Fitted cylinder data and extracted fibre data, generated from scans with TM concept, showing occurring problems for all three cut-outs at voxel edge length 1 μm (green markers), 2 μm (orange), 3 μm (red)

The results presented in the following two sub-chapters were acquired by Bernhard Plank within his master's thesis [81]. Differences in values may occur due to the fact that the novel approach of Template Matching was used for this thesis which was not available for the master's thesis.

6.3 Examination of reproducibility

The chosen specimen (see chapter 3.2.1) was scanned several times with remounting followed by data analysis. The same specimen was repeatedly scanned over the years and analysed. Thus the shown results include variations that were induced by the scanning procedure (tube stability, axes positioning, etc.) and potential influence of software. In addition small differences in the analysed volume can exist since the complete specimen could not be analysed but a cut-out. In total 9 CT data sets were analysed.

Table 6.3: Average values and deviations of all 9 analyses

| Parameter | Unit | Average | Standard-deviation absolute | Standard-deviation (%) |
|--------------------------|-------------------|---------|-----------------------------|------------------------|
| Fibre length | | | | |
| weighted average | (μm) | 464 | 3 | 0,56 |
| average | (μm) | 310 | 3 | 0,98 |
| maximum | (μm) | 2624 | 102 | 3,89 |
| curved weighted avgerage | (μm) | 466 | 3 | 0,56 |
| curved average | (μm) | 311 | 3 | 0,98 |
| curved maximum | (μm) | 2633 | 103 | 3,90 |
| Fibre count | | 31368 | 477 | 1,52 |
| Separated fibres | | 18967 | 707 | 3,73 |
| Curved fibres | | 1796 | 132 | 7,37 |
| Maximum diameter | (μm) | 21,8 | 2,8 | 12,83 |
| Minimum diameter | (μm) | 4,7 | 1,0 | 21,27 |
| Average diameter | (μm) | 11,6 | 0,1 | 1,00 |
| Fibre volume fraction | (vol. %) | 10,8 | 0,2 | 1,89 |
| Fibre weight fraction | (wt. %) | 25,4 | 0,4 | 1,57 |
| a_{XX} | | 0,094 | 0,0006 | 0,63 |
| a_{YY} | | 0,068 | 0,0004 | 0,52 |
| a_{ZZ} | | 0,838 | 0,0007 | 0,09 |
| a_{XY} | | -0,022 | 0,0003 | 1,17 |
| a_{XZ} | | 0,200 | 0,0001 | 0,06 |
| a_{YZ} | | -0,036 | 0,0003 | 0,96 |

The result is shown as variations of orientation tensor, length distribution and diameter distribution. Table 6.3 shows relevant features of all 9 analyses with corresponding standard deviations. Figure 6.11 shows all values of main diagonal elements of the orientation tensor, Figure 6.12 shows box-plots of the same underlying data. For each element a separate graph is drawn because the range varies strongly. The axis of ordinates shows for all three graphs a range of 0.002 in steps of 0.0005.

The main element a_{ZZ} dominates whereas a_{XX} and a_{YY} are smaller than 0.1. The variation in tensor element values is very small, of main diagonal elements it is smaller than 0.7 %.

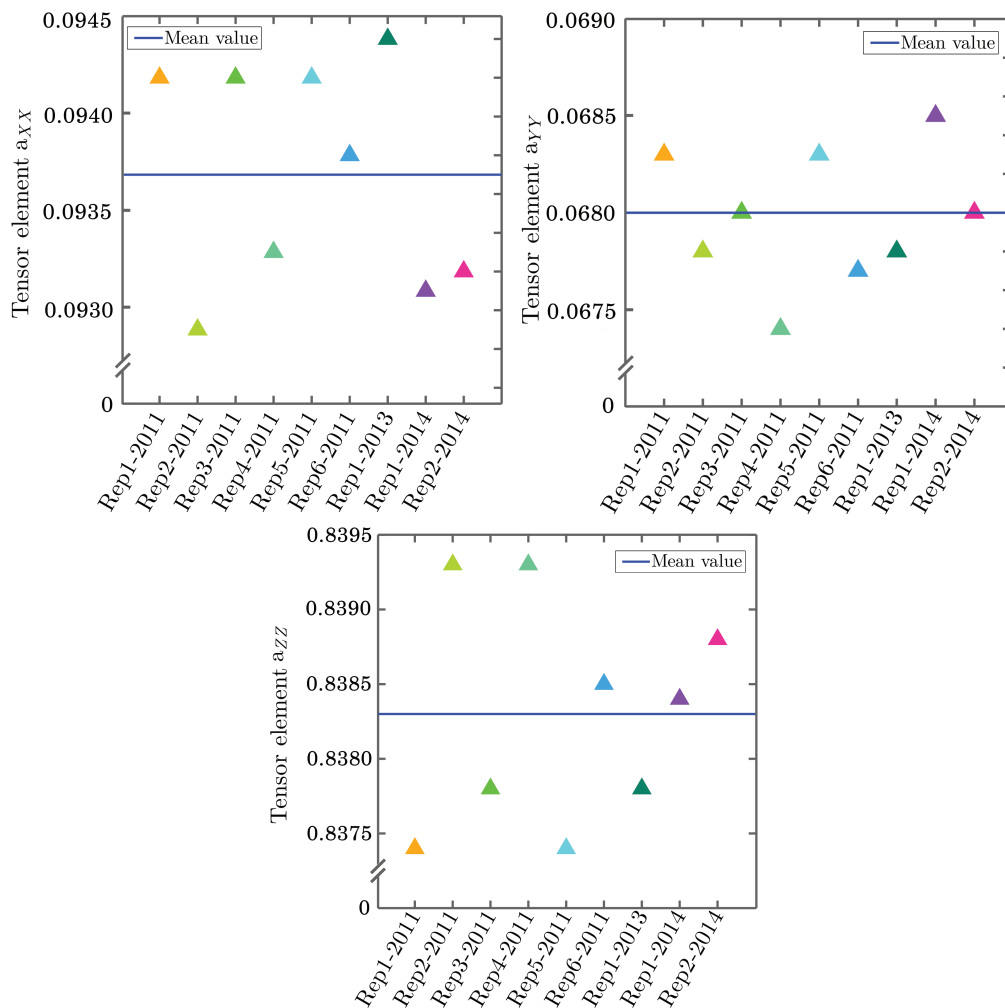


Figure 6.11: Reproducibility-FOD

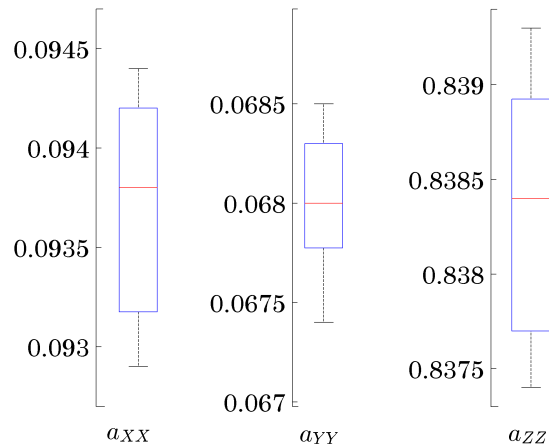


Figure 6.12: Box-plots of main diagonal element variations. Y axes of all three plots are equally scaled but in different ranges.

The absolute fibre length distributions shown in figure 6.13 indicate very small deviations at big length classes. For fibres shorter than 300 μm differences appear. Box-plot representation emphasized this finding giving clearer information about minimum, maximum and distribution of values at each length class (Figure 6.14) Deviations of average and weighted average fibre length are smaller than 1 %.

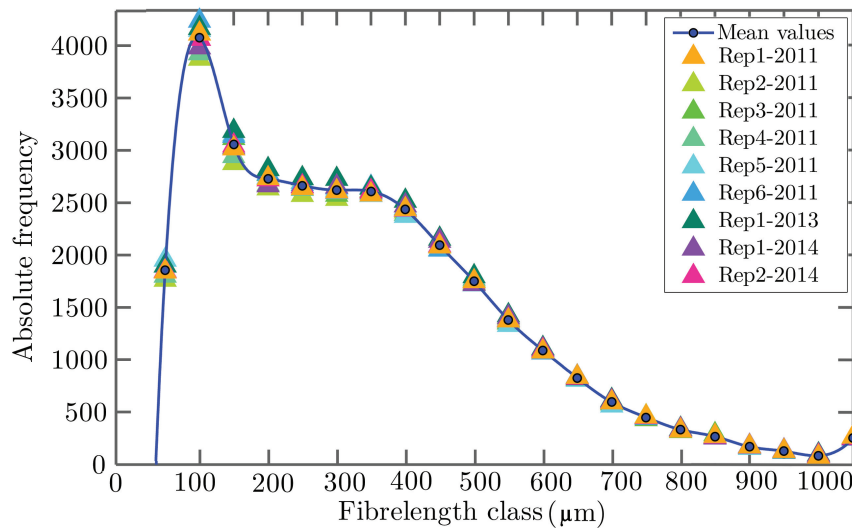


Figure 6.13: Absolute length distribution for 9 scans on the same specimen

A comparison of diameter distribution in Figure 6.15 indicates that outliers are responsible for the high values of standard deviation for minimum and maximum diameter. The average diameter is determined reproducibly with variations of 1 %. The scan of

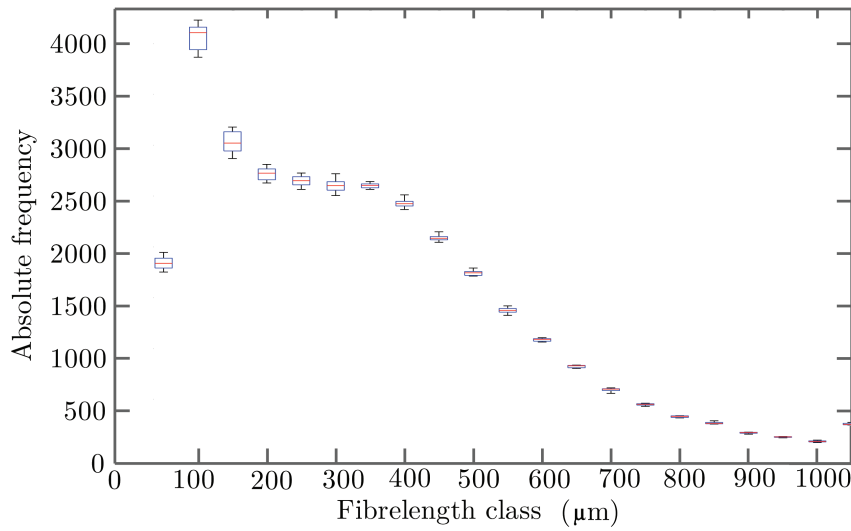


Figure 6.14: Box-plots of length distribution for 9 scans on the same specimen

2013 shows a tendency towards bigger diameters. Also the box plot representation in Figure 6.16 shows the good reproducibility and the outliers of scan Rep1-2013. The dashed blue line shows the nominal diameter of 12.5 μm . The determined average diameter of 11.6 μm is shown as dashed red line.

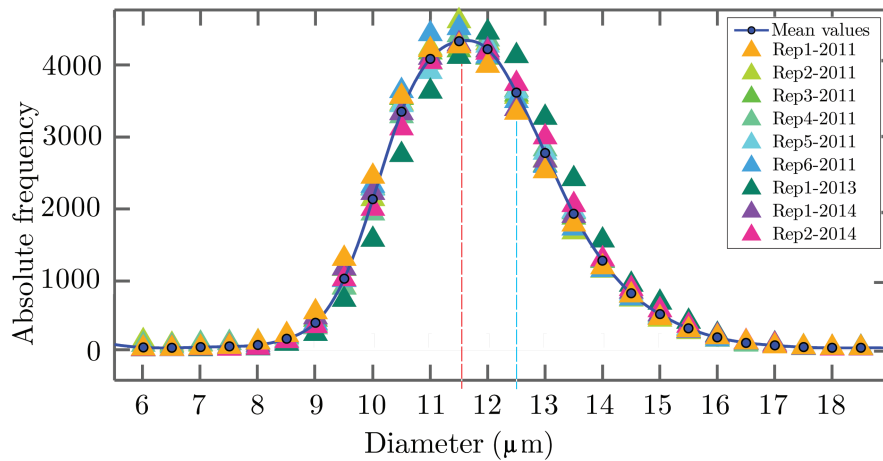


Figure 6.15: Absolute diameter distribution for 9 scans on the same specimen. Nominal diameter 12.5 μm (blue line), average result 11.6 μm (red line)

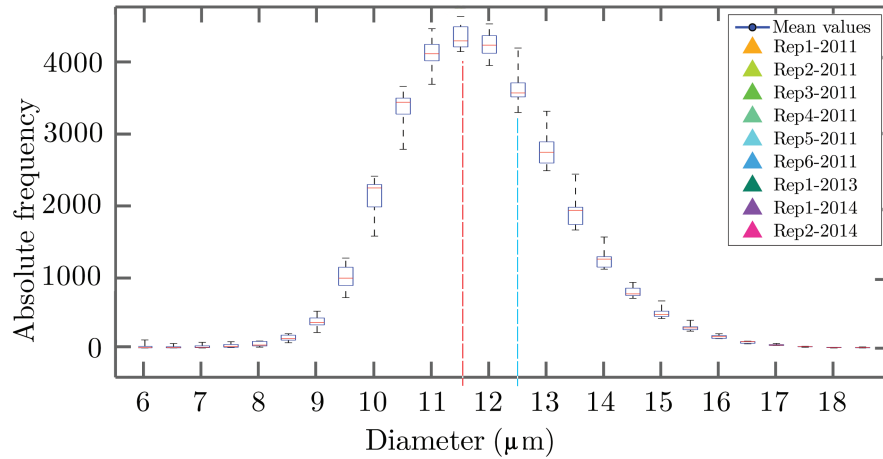


Figure 6.16: Box-plot of diameter distribution for 9 scans on the same specimen. Nominal diameter 12.5 μm (blue line), average result 11.6 μm (red line)

6.4 Impact of evaluation volume

The high resolution that is necessary for accurate fibre characterisation leads to reduced scan volume, thus fibres are cut at the borders of the data set. Determination of fibre length and orientation is influenced by this circumstance. For specimens containing 5 wt% and 30 wt% glass fibres respectively, average and weighted average fibre length and orientation tensor depending on the data set size in injection direction (direction Z) were determined.

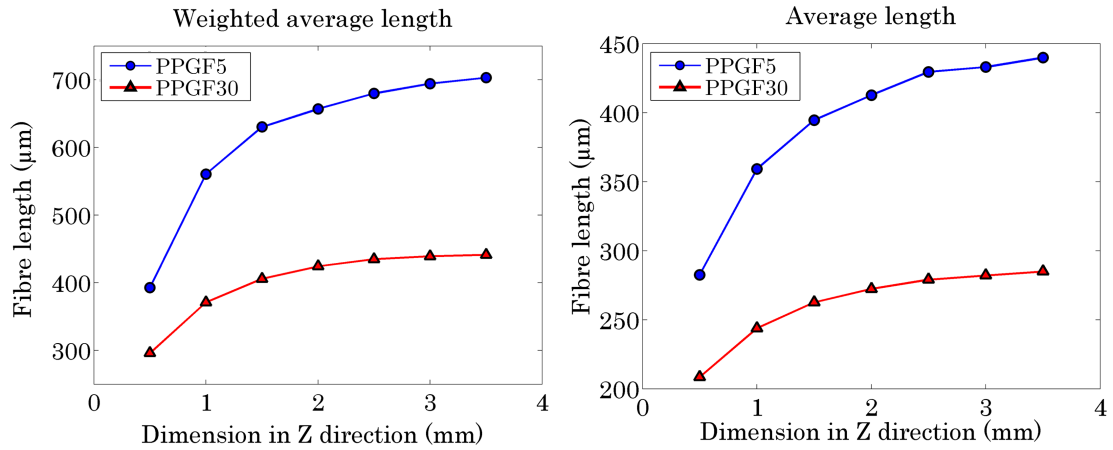


Figure 6.17: Weighted average and average fibre length for PP-sGF-5 and PP-sGF-30 at varying data set size (Z)

Change in fibre length is severe up to ca. 3 mm dimension independent of fibre

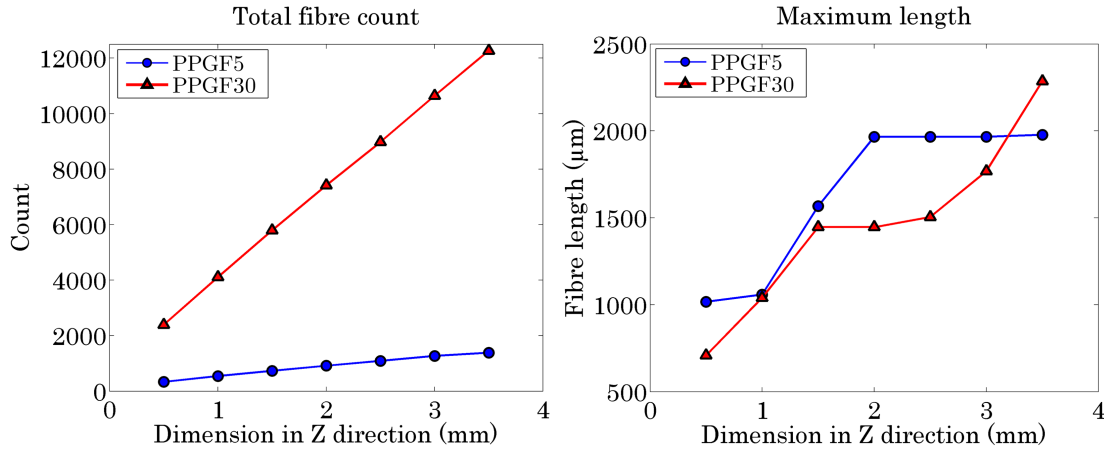


Figure 6.18: Total fibre count and maximum length for PP-sGF-5 and PP-sGF-30 at varying data set size (Z)

content (Figure 6.17). This dimension can easily be scanned at the desired standard value of $2 \mu\text{m}$ Voxel edge length. Total number of fibres increases linearly with dimension in Z which is reasonable for homogeneously distributed fibres. Maximum length changes stepwise which can be explained by the fact that only a very small number of very long fibres are present and the longest fibre might stay the same even if the dimension is increased (Figure 6.18).

Orientation tensor main diagonal elements show only small deviations but no clear stable value (Figure 6.19). Different to fibre length it is not expected that orientation should change with increasing dimension in Z unless there is a variation of orientation due to manufacturing.

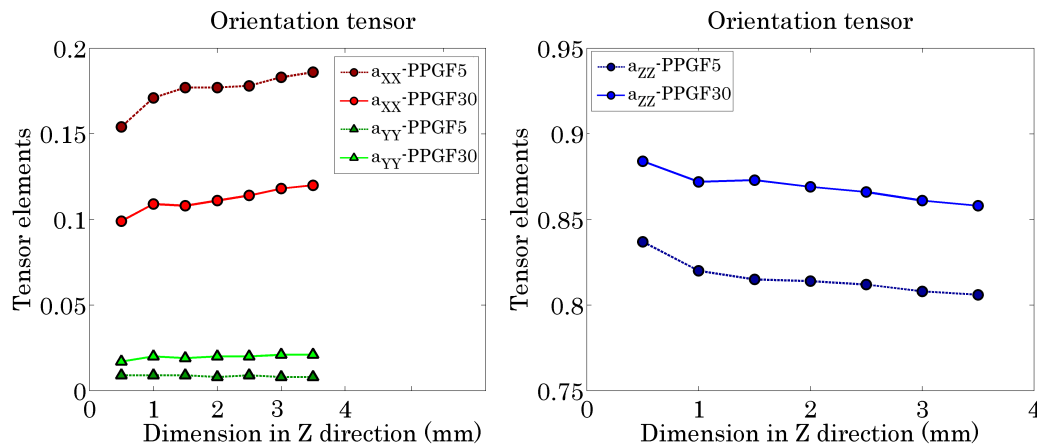


Figure 6.19: Fibre orientation tensor main elements for PP-sGF-5 and PP-sGF-30. a_{XX} and a_{YY} on the left, a_{ZZ} on the right, both images are equally scaled showing different ranges on the Y axes.

6.5 Impact of specimen orientation on the turntable

The ideal specimen for a rotational CT scan would be a cylinder that is aligned vertically onto the turntable. This would lead to the same irradiation lengths at every angular position and therefore to best possible reconstruction. For all other geometries or alignments of cylinders artefacts like streaks are induced. Some fibres in the investigated specimens are aligned vertically as desired. However most of the fibres are tilted and because of the skin core layered set up of fibre orientation, fibres in the core are tilted by ca. 90° . Horizontally aligned fibres are irradiated lengthwise and transverse once and between that in many different angles. This leads to reconstruction artefacts when using FDK algorithm.

For 4 specimens from a sector plate, 2 scans were conducted respectively: specimen alignment on turntable 0° and 90° (around Y axis) rotated. In the first case most of the fibres are aligned parallel to the rotation axis, in the latter case fibre alignment is perpendicular to rotation axis.

The average values of FCP results given in Tables 6.4 and 6.5 show only very small deviations between 0° and 90° specimen orientation on the turntable. All relevant features have a deviation below 1.4 %. The course of fibre length distributions shown in Figure 6.20 do not show any significant difference.

Table 6.4: Result of FCP analysis for specimens 1 and 2, scanned at 0° and 90° alignment

| | Position 1 | | | Position 2 | | |
|---|------------|------------|--------------|------------|------------|--------------|
| | 0° | 90° | Δ (%) | 0° | 90° | Δ (%) |
| Fibre count (x1000) | 64.81 | 65.31 | 0.8 | 68.10 | 68.29 | 0.3 |
| Weighted average length (μm) | 479 | 476 | -0.7 | 492 | 491 | -0.3 |
| Average length (μm) | 334 | 333 | -1.4 | 344 | 342 | -0.5 |
| Average diameter (μm) | 12.0 | 12.1 | 0.1 | 12.1 | 12.1 | 0.5 |
| σ_D (μm) | 1.7 | 1.6 | -5.5 | 1.7 | 1.7 | -0.1 |
| Fibre fraction per volume (vol.%) | 10.8 | 11.0 | 2.4 | 11.6 | 11.6 | 0.6 |
| per weight (wt.%) | 25.3 | 25.8 | 2.0 | 26.8 | 27.0 | 0.5 |
| a_{XX} | 0.261 | 0.262 | 0.3 | 0.253 | 0.253 | 0.1 |
| a_{YY} | 0.014 | 0.014 | -4.2 | 0.013 | 0.013 | -0.1 |
| a_{ZZ} | 0.725 | 0.725 | 0.0 | 0.734 | 0.734 | 0.0 |
| a_{XY} | 0.000 | 0.000 | 5.7 | 0.000 | 0.001 | 63.1 |
| a_{XZ} | -0.005 | -0.005 | 5.9 | 0.024 | 0.024 | 1.3 |
| a_{YZ} | 0.002 | 0.002 | 2.4 | 0.000 | -0.001 | 357.3 |
| Orientation strength | 0.73 | 0.73 | 0.00 | 0.74 | 0.74 | 0.00 |

6.5. IMPACT OF SPECIMEN ORIENTATION ON THE TURNTABLE

Table 6.5: Result of FCP analysis for specimens 3 and 4, scanned at 0° and 90° alignment

| | Position 3 | | | Position 4 | | |
|---|------------|--------|--------------|------------|-------|--------------|
| | 0° | 90° | Δ (%) | 0° | 90° | Δ (%) |
| Fibre count (x1000) | 55.88 | 55.81 | -0.1 | 67.07 | 67.64 | 0.9 |
| Weighted average length (μm) | 506 | 506 | 0.0 | 488 | 488 | -0.1 |
| Average length (μm) | 345 | 345 | 0.1 | 342 | 341 | -0.3 |
| Average diameter (μm) | 11.9 | 12.0 | 0.5 | 11.9 | 12.1 | 1.1 |
| σ_D (μm) | 1.7 | 1.7 | 0.9 | 1.7 | 1.7 | 0.7 |
| Fibre fraction per volume (vol.%) | 10.9 | 11.0 | 0.7 | 11.2 | 11.5 | 2.4 |
| Fibre fraction per weight (wt.%) | 25.5 | 25.7 | 0.6 | 26.1 | 26.7 | 2.0 |
| a_{XX} | 0.347 | 0.347 | 0.0 | 0.208 | 0.207 | -0.8 |
| a_{YY} | 0.016 | 0.016 | 1.1 | 0.014 | 0.013 | -3.6 |
| a_{ZZ} | 0.637 | 0.636 | 0.0 | 0.778 | 0.780 | 0.3 |
| a_{XY} | 0.000 | 0.000 | 22.4 | 0.000 | 0.000 | -0.5 |
| a_{XZ} | -0.024 | -0.024 | 1.3 | 0.099 | 0.099 | 0.1 |
| a_{YZ} | -0.002 | -0.002 | -6.1 | 0.000 | 0.000 | 0.7 |
| Orientation strength | 0.64 | 0.64 | -0.16 | 0.79 | 0.80 | 0.24 |

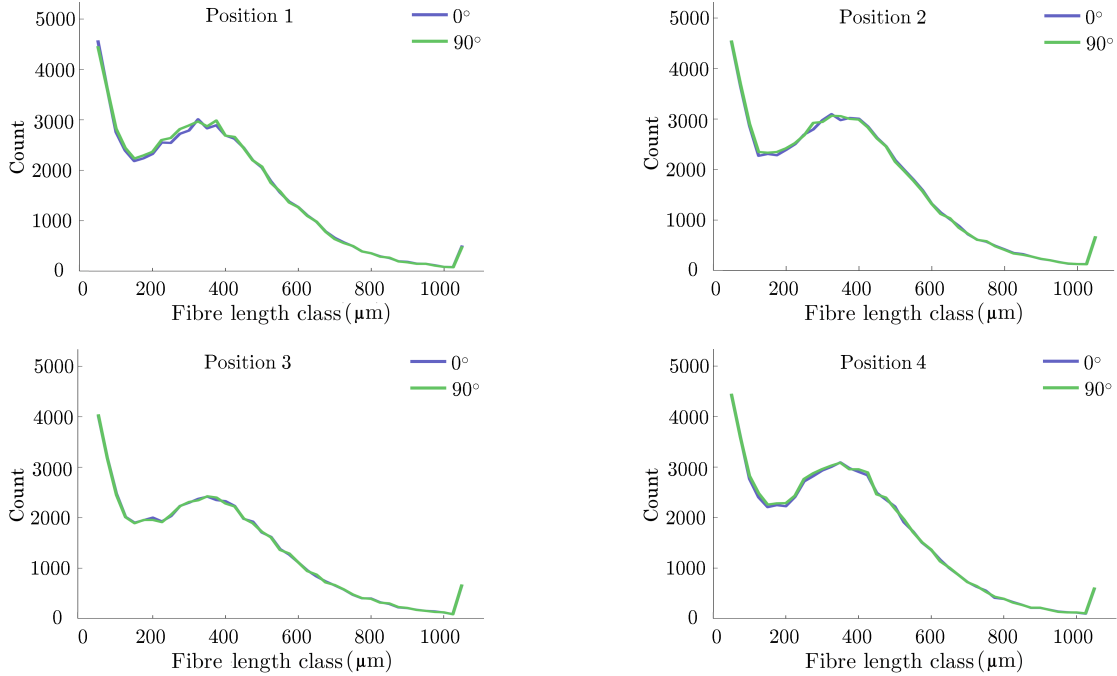


Figure 6.20: Fibre length distribution of 4 specimens at different sector positions, scanned at 0° and 90° alignment

6.6 Comparison with standard method for FOD

At first, orientation distributions of 4 positions of the sector sheet (Figure 3.3) were determined by CT analyses. Average orientation distributions from 3 specimens per position are shown in Figure 6.21 as polar plots. After the CT analyses the same specimens were prepared for grinding and were analysed with LOM.

CT analyses were conducted using the developed TM concept and a Voxel based approach. The results will be shown in the following using polar plots, tensor values and the variation of main diagonal tensor elements over sheet thickness.

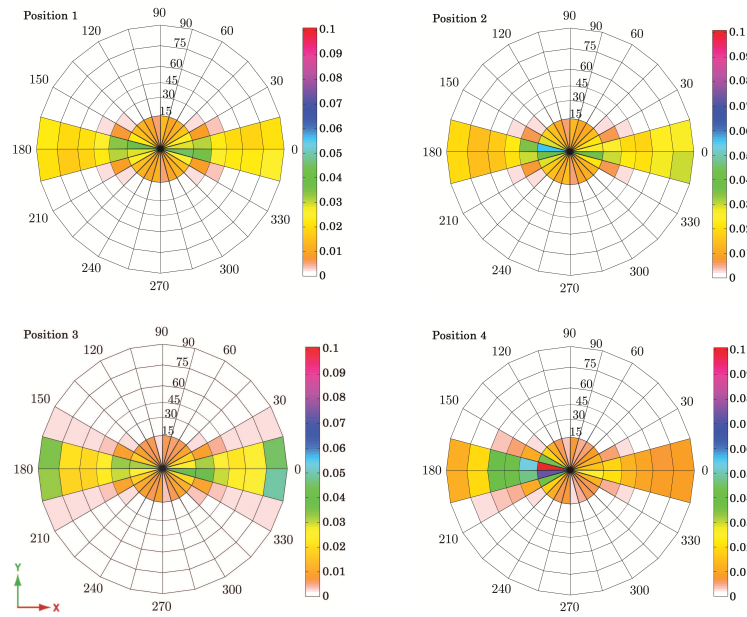


Figure 6.21: Polar plots of average values of all 4 positions scanned at $2\ \mu\text{m}$ Voxel edge length and analysed with TM concept. The colour bar shows relative values.

The polar plots for fibre orientation show a strong fibre alignment in sheet plane (ϕ in the range of 0° resp. $180^\circ \pm 15^\circ$, XZ). While fibres at position 1 and position 2 are aligned preferably in injection direction ($\theta < 15^\circ$), position 3 shows many fibres at θ ca. 90° . Position 4 showed the highest relative value of all 4 positions but the direction is tilted towards θ ca. 45° .

A comparison of averaged results from sectioning, CT concept TM and CT Voxel based concept are given in Table 6.6. In contrary to the individual fibre characterisation concept the Voxel based approach does not segment individual fibres but determines orientation for each Voxel. The underlying results of every specimen were used to calculate box plots for the main diagonal tensor elements (Figure 6.22). The TM concept gives slightly higher orientation in Z direction as compared to the other methods. The through sheet thickness component (Y) is slightly higher with the Voxel based approach

while the X component is similar for the CT methods and a bit lower than the sectioning results. Both sectioning and Voxel based CT analysis show significantly higher deviation within a set of specimens at each position. This indicates that the developed TM approach leads to more reproducible results.

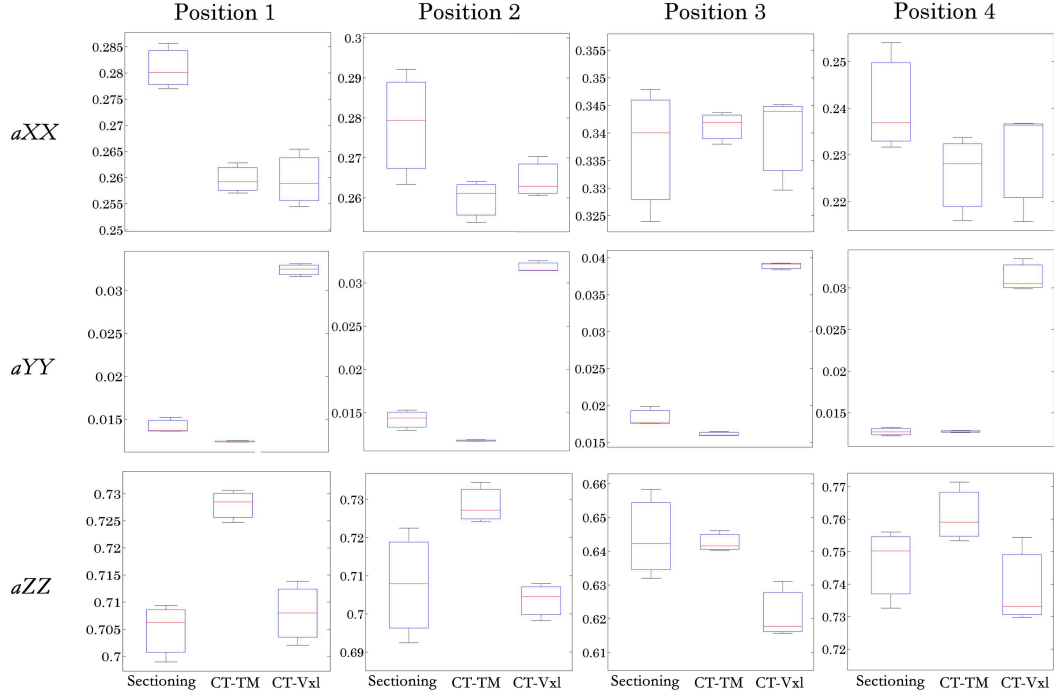


Figure 6.22: Box plots of main diagonal tensor elements a_{XX} , a_{YY} , a_{ZZ} determined by Sectioning and CT data analysed with the two concepts TM (CT-TM) and Voxel based (CT-Vxl) for each position

The variation of results at each position can be derived from the through sheet thickness results shown in Figures 6.23, 6.24 and 6.25. The min-max bars at each position over thickness conforms the conclusion that variation is less for the CT analysis using TM approach. The deviations are always small for regions with distinct fibre alignment. Near the surface and in the core region the variation is higher.

The deviations between standard method and the CT methods are small. This is indicated by averaged orientation tensor values for the complete specimens, given in Table 6.6, and by the comparison of tensor values over sheet thickness shown in Figure 6.26. The averaged tensor values for the complete specimens differ maximal by 0.029. Comparing the trend of tensor values over thickness, very good accordance at almost all distances and positions can be observed. Small deviations can be seen at the surface of the specimens and for some positions sectioning shows asymmetric distribution which is not seen with the TM approach. Minimum and maximum peaks are equal in value and position.

Table 6.6: Orientation tensors determined by Sectioning and CT data analysed with the two concepts TM (CT-TM) and Voxel based (CT-Vxl). Average values were determined from 3 specimens per position. The difference Δ is calculated from CT-TM and CT-Vxl to the sectioning results. Only the 4 tensor elements that can be determined by 2D LOM method are shown.

| | Sectioning Average | CT-TM Average | Δ | CT-Vxl Average | Δ |
|------------|-----------------------|------------------|----------|-------------------|----------|
| Position 1 | | | | | |
| a_{XX} | 0.281 | 0.260 | -0.021 | 0.260 | -0.021 |
| a_{YY} | 0.014 | 0.012 | -0.002 | 0.032 | 0.018 |
| a_{ZZ} | 0.705 | 0.728 | 0.023 | 0.708 | 0.003 |
| a_{YZ} | 0.000 | 0.000 | 0.000 | -0.001 | -0.002 |
| Position 2 | | | | | |
| a_{XX} | 0.278 | 0.260 | -0.019 | 0.265 | -0.014 |
| a_{YY} | 0.014 | 0.012 | -0.002 | 0.032 | 0.018 |
| a_{ZZ} | 0.708 | 0.729 | 0.021 | 0.704 | -0.004 |
| a_{YZ} | 0.000 | 0.000 | 0.001 | 0.001 | 0.001 |
| Position 3 | | | | | |
| a_{XX} | 0.337 | 0.341 | 0.004 | 0.340 | 0.002 |
| a_{YY} | 0.018 | 0.016 | -0.002 | 0.039 | 0.021 |
| a_{ZZ} | 0.644 | 0.674 | 0.029 | 0.621 | -0.023 |
| a_{YZ} | -0.002 | -0.001 | 0.002 | 0.003 | 0.005 |
| Position 4 | | | | | |
| a_{XX} | 0.241 | 0.226 | -0.015 | 0.230 | -0.011 |
| a_{YY} | 0.013 | 0.013 | 0.000 | 0.031 | 0.019 |
| a_{ZZ} | 0.746 | 0.761 | 0.015 | 0.739 | -0.007 |
| a_{YZ} | -0.003 | 0.000 | 0.0034 | -0.0005 | 0.0028 |

Orientation distribution over sheet thickness, shown in 6.23, 6.24 and 6.25, show the expected results for the investigated material and production process. The orientation is very strong in injection direction near the surface and changes direction towards transverse direction in the centre of the sheet. The overall orientation in thickness direction (Y) is very weak. The comparison of the positions leads to the conclusion that fibre orientation in injection direction gets weaker with increasing distance to the gate. The first two positions lead to almost same total tensor values but show slight differences in distribution over thickness. The specimen at shifted lateral position 4 shows a different behaviour in the core region and the biggest overall orientation in injection direction. Very similar values for tensor components X and Z can be caused by tilted fibre direction. This assumption is confirmed by the visual inspection of CT slice images (6.27) and is expected since position 4 is near the edge of the sector specimen where fibres should align parallel to this edge.

6.6. COMPARISON WITH STANDARD METHOD FOR FOD

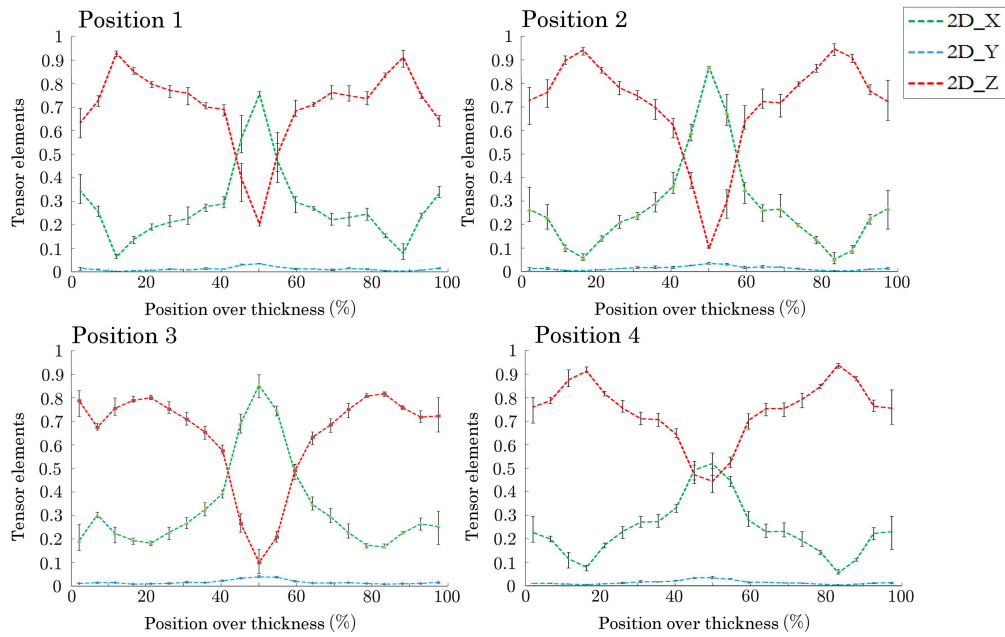


Figure 6.23: Course of average orientation distribution values over sheet thickness at all 4 positions from grinding and LOM analyses. Average of three specimens showing average values and min-max variations

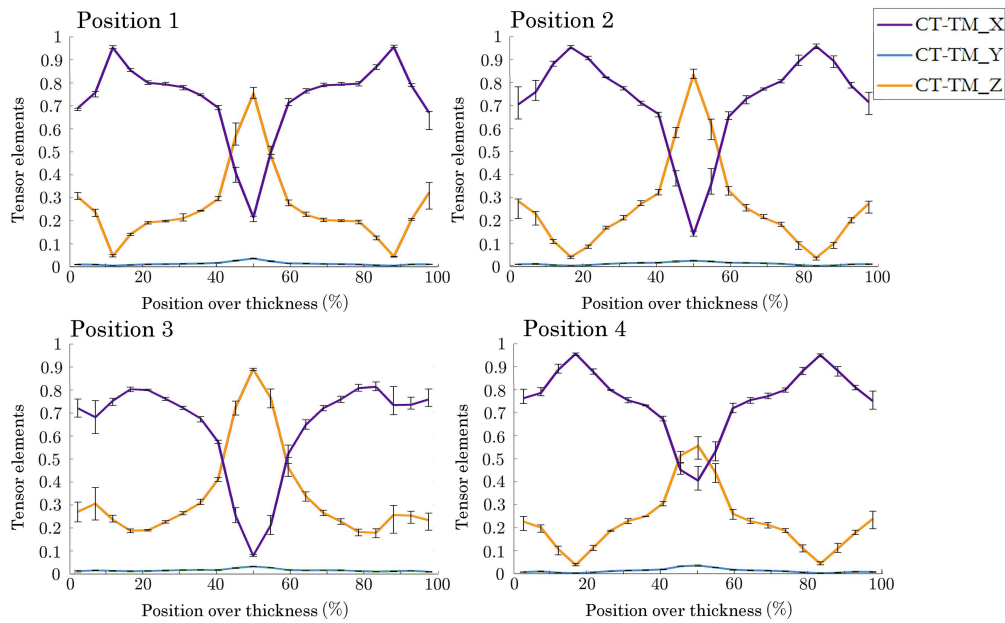


Figure 6.24: Course of average orientation distribution values over sheet thickness at all 4 positions from TM based CT analyses at 2 μm Voxel edge length. Average of three specimens showing average values and min-max variations

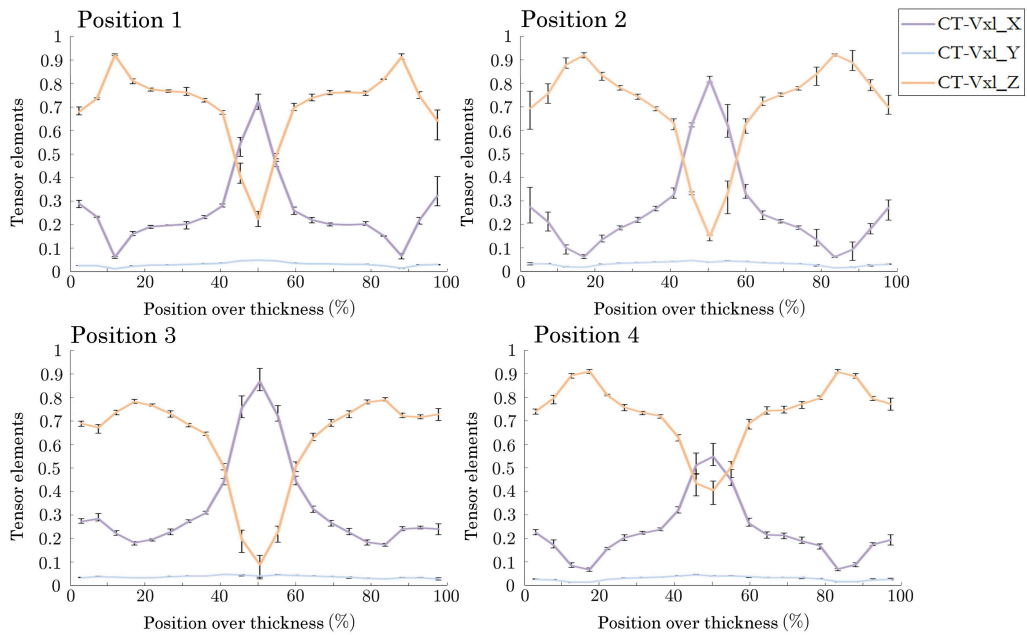


Figure 6.25: Course of average orientation distribution values over sheet thickness at all 4 positions from Voxel based CT analyses at 2 μm Voxel edge length. Average of three specimens showing average values and min-max variations

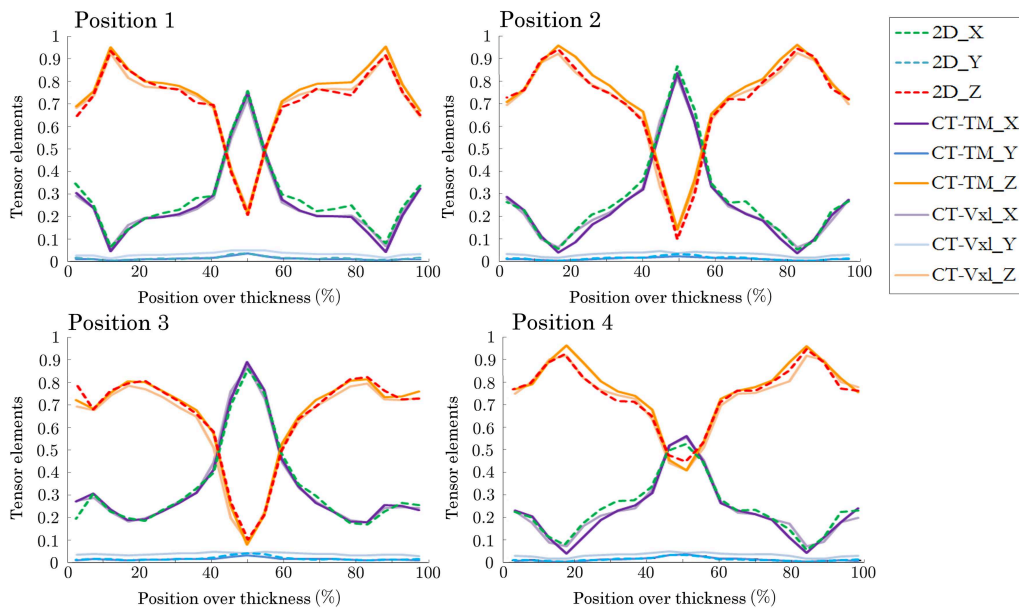


Figure 6.26: Course of average orientation distribution values over sheet thickness at all 4 positions, Comparison of average values determined by Sectioning and CT data analysed with the two concepts TM (CT-TM) and Voxel based (CT-Vxl)

6.6. COMPARISON WITH STANDARD METHOD FOR FOD

From the 21 positions over thickness, five were chosen at distinctive thickness to relate the quantitative information shown previously with visual impression. Figure 6.27 shows the first and the last position (2 % and 98 %), positions with local maxima of strength of orientation (17 % and 83 %) and the central position in XZ plane. The differences seen in the tensor values over thickness can also be found in these CT images. The remarkable weaker strength of orientation at thickness 17/83 % at position 3 is very well visible as well as the different orientation in the centre (50 %) at position 4. Near the surface fibres are distributed more randomly orientated.

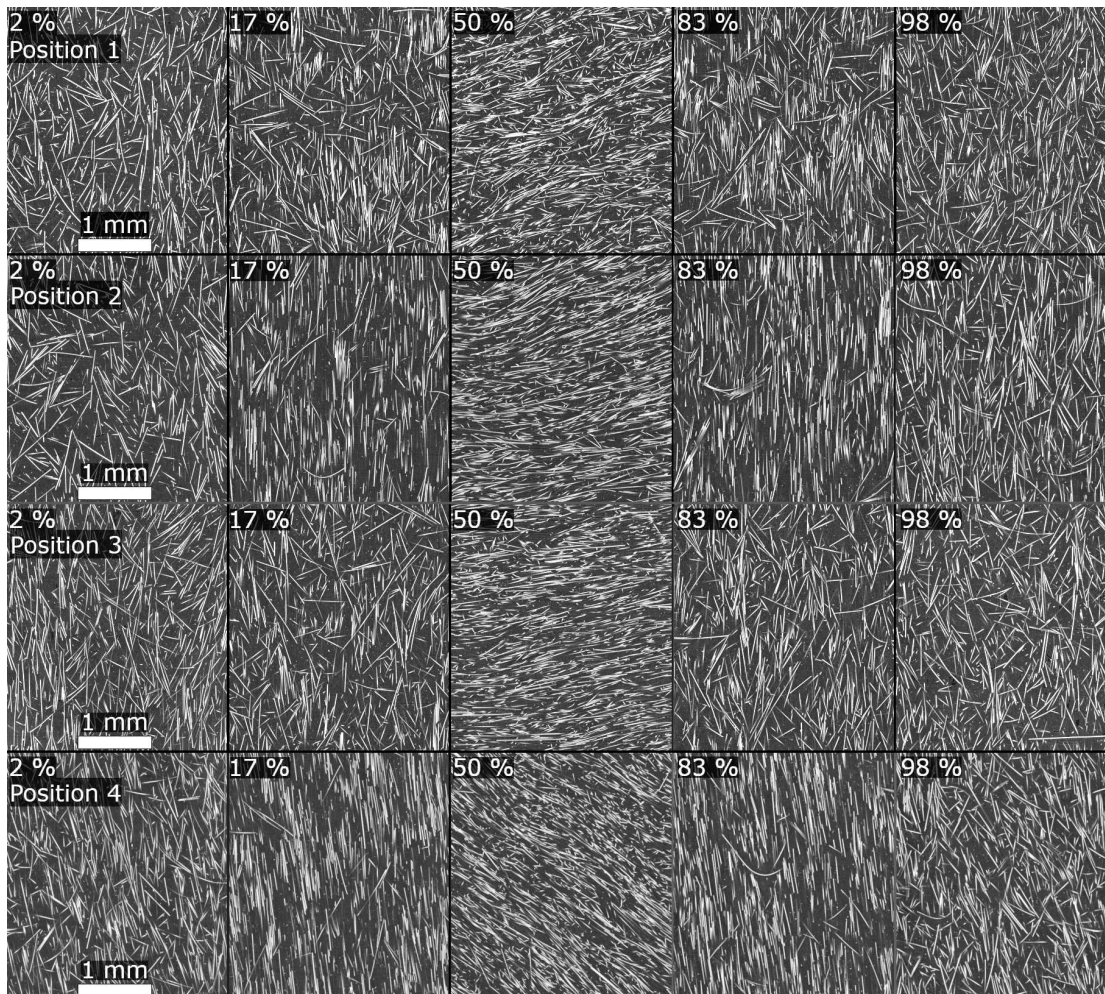


Figure 6.27: Cross sectional CT images from XZ plane at 5 depths over thickness (Y-direction: 2, 17, 50, 83, 98 %) for sector positions 1, 2, 3 and 4.

6.7 Comparisons with standard methods for FLD

This section is divided into two parts. First the method according to the ISO standard was applied to materials with varying fibre content. The second way of comparing CT and Pyrolysis was to compare every single fibre within a very small volume. These results were acquired by Susanne Gleiss during her master's thesis [100].

6.7.1 Pyrolysis comparison with CT according to ISO standard

The comparison of the two methods pyrolysis and CT were compared in terms of average length and length distribution. Images are shown to illustrate the differences in the nature of destructive and non-destructive data analysis.

While after pyrolysis only some extracted fibres were analysed with LOM, all fibres within the scanned specimen were analysed. Table 6.7 gives the respective values and Figure 6.28 shows example images for the material PP-sGF-5. Weighted average and average length for all 4 fibre contents as shown in Figure 6.29 show differences between the two methods. CT analysis tends to result in shorter length except for 5 wt. % fibre content. The length distributions shown in Figure 6.30 give more insight in the differences and the reasons for shorter average length. Specimens with 10, 20 and 30 wt. % fibre content show high relative frequency at the smallest length classes for CT analyses although the length thresholds for both methods were set to the same values.

Table 6.7: Features of destructive pyrolysis and non-destructive CT analyses for FLD determination

| | | Pyrolysis | CT | Pyrolysis | CT |
|----------------------------------|-------------------|-----------|--------|-----------|--------|
| Fibre content | (wt. %) | 5 | 5 | 10 | 10 |
| Number of fibres | | 421 | 1916 | 1011 | 5163 |
| min. length threshold | (μm) | 93 | 93 | 53 | 53 |
| Weighted average length | (μm) | 677 | 721 | 674 | 632 |
| Average length (μm) | (μm) | 509 | 506 | 514 | 416 |
| Fibre content | (wt. %) | 20 | 20 | 30 | 30 |
| Number of fibres | | 1011 | 14 912 | 1011 | 23 078 |
| min. length threshold | (μm) | 44 | 44 | 56 | 56 |
| Weighted average length | (μm) | 633 | 545 | 487 | 452 |
| Average length (μm) | (μm) | 470 | 351 | 396 | 323 |

Identified reasons that could lead to deviations between the two methods are:

- Inaccuracies of CT data analysis software.
- Inaccuracies of LOM image processing software.
- Different number of fibres taken into account.

- Lost fibres after pyrolysis and during dispersion.
- Broken fibres during dispersion.

The reason for the different results, especially for the shorter fibres, could be found within both methods. When taking the sample fibres after pyrolysis for LOM analysis some fibres could have been lost and for CT analysis the high frequency for low fibre length could have been erroneously extracted fibres. To understand the reasons better, pyrolysis and CT were performed on very small cut-outs in order to compare exactly the same fibres. These results are shown in the following chapter.

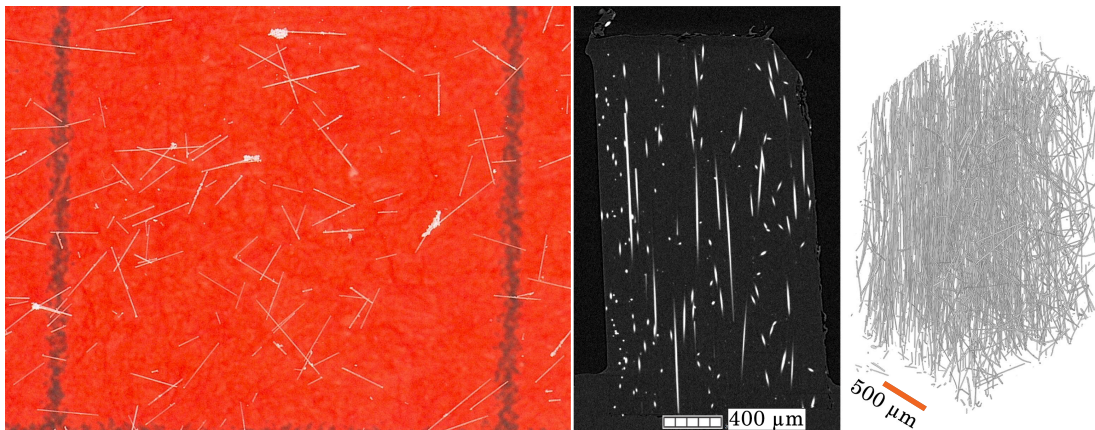


Figure 6.28: Representation of fibres in LOM image (left) and CT slice and 3D images (right) from PP-sGF-5

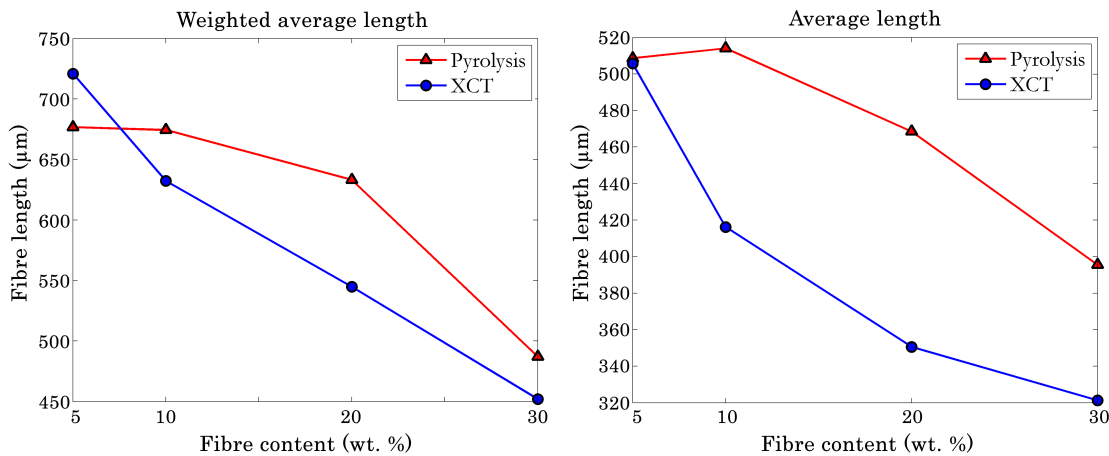


Figure 6.29: Comparison of weighted average and average length determined by destructive and CT method for different fibre contents

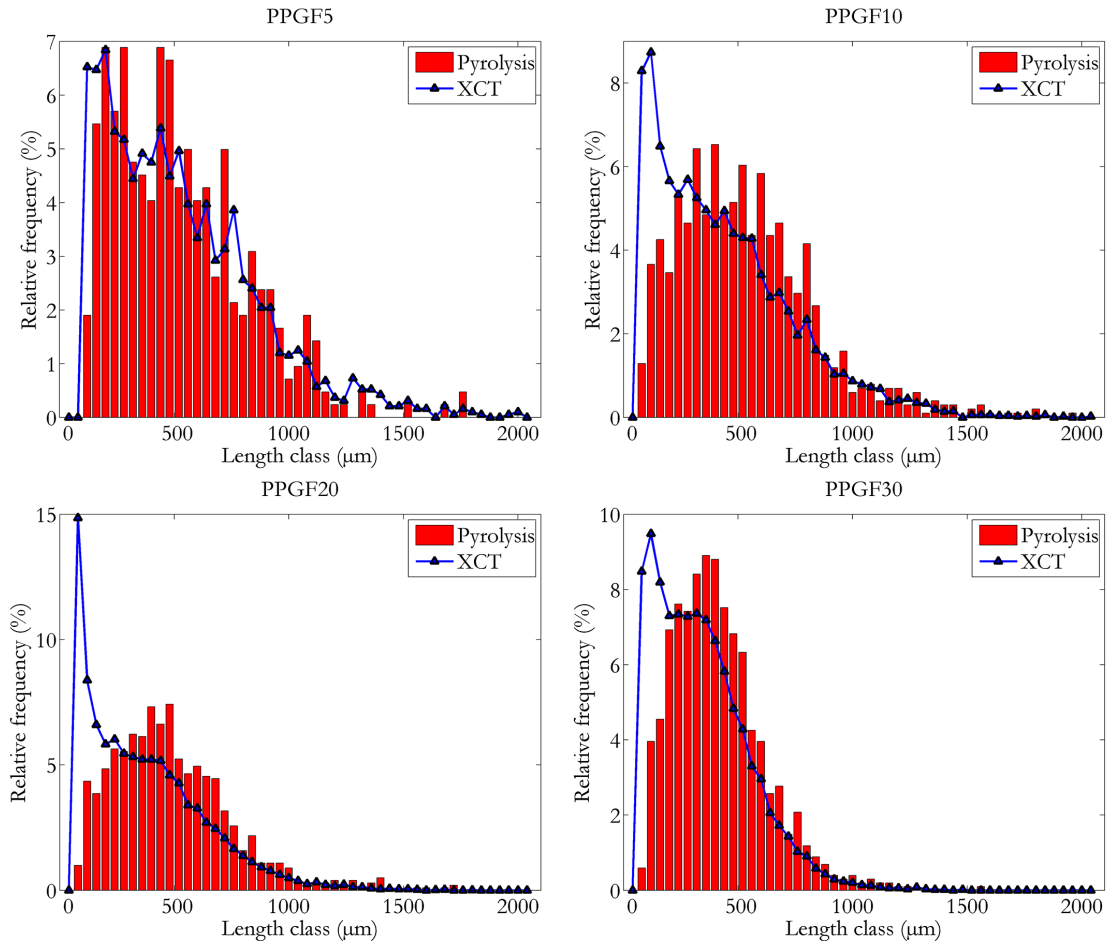


Figure 6.30: Comparison of length distribution determined by destructive and CT method for different fibre contents

6.7.2 Pyrolysis and comparison with CT analyses on individual fibre basis

CT - variation of resolution

The influence of Voxel edge length on the fibre characterisation result was tested for three different, small cut-outs. The samples contained between 200 and 340 fibres. Specimen shape and fibre arrangement of all three cut-outs can be seen in cross sectional slice images (Figure 6.31) and 3D renderings (Figure 6.37, 6.38 and 6.39) They show complex, irregular shape since the cut-outs are very small and some fibres at the outer borders are broken due to the cut-out process. There are also differences in fibre orientation, sample 3 shows highest alignment. Difference in sharpness of 1 μm and 2 μm Voxel edge length, is shown in the cross sectional CT images (Figure 6.31). The results of fibre characterisation are summed up in Table 6.8. For all three specimens,

2 μm Voxel edge length leads to slightly higher average length with deviations to 1 μm Voxel edge length smaller than 4 %. With this result it was concluded that a resolution of 2 μm Voxel edge length is sufficient for the comparison of CT results with pyrolysis.

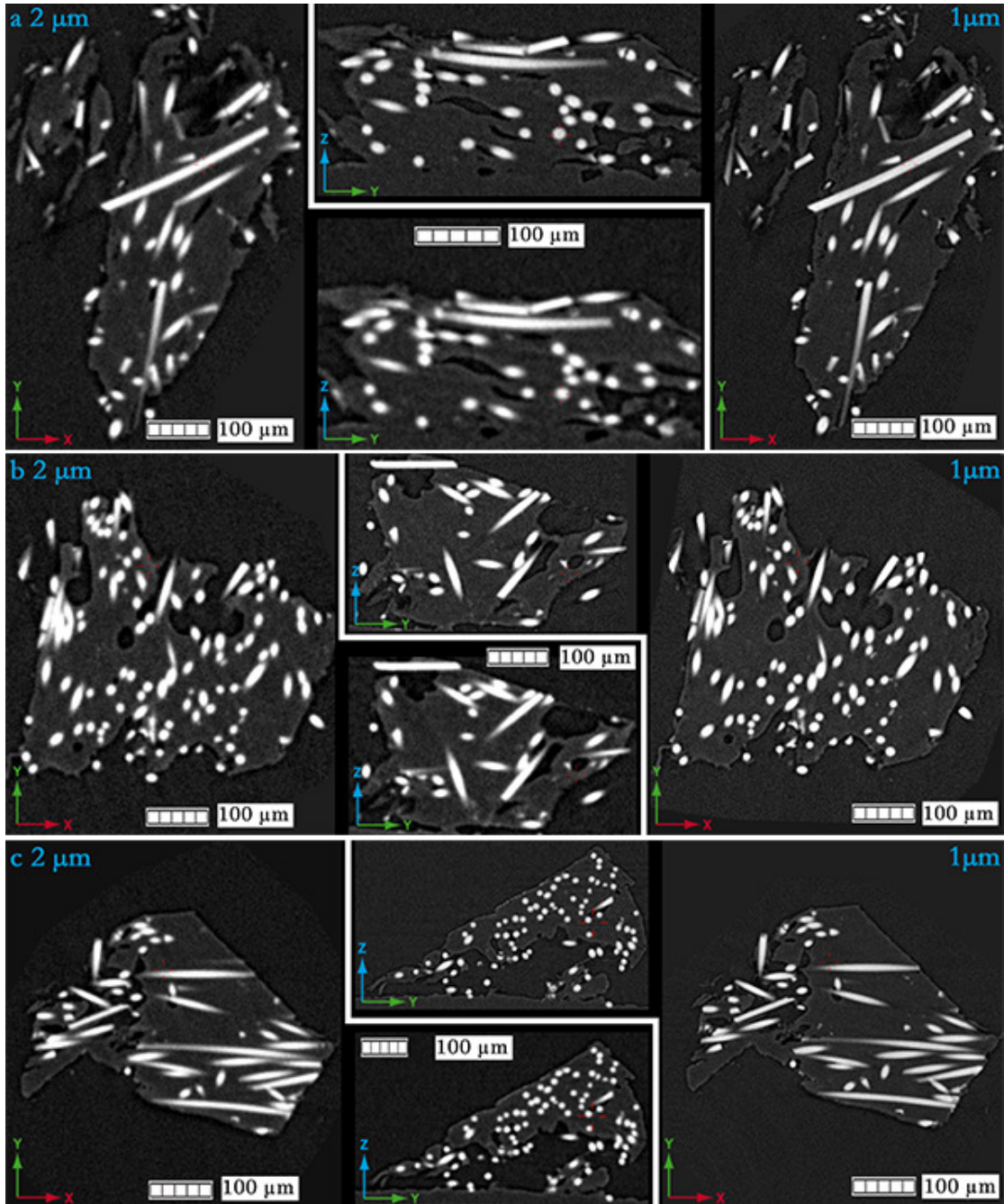


Figure 6.31: CT slice images scanned with Voxel edge length of 2 μm (left) and 1 μm (right) of sample 1 (a), sample 2 (b), sample 3 (c)

Table 6.8: Characteristics of the three small cut-outs at different resolution with deviations from 2 μm compared to 1 μm Voxel edge length

| Specimen | Voxel edge length (μm) | Average length (μm) | Deviation (μm) (%) | | Weighted average length (μm) | Deviation (μm) (%) | | Fibre count |
|-------------------|-------------------------------------|----------------------------------|---------------------------------|-----|---|---------------------------------|-----|-------------|
| 1 | 1 | 124 | | | 190 | | | 215 |
| 1 | 2 | 125 | 0.1 | 0.1 | 193 | 2.8 | 1.5 | 222 |
| 2 | 1 | 139 | | | 208 | | | 316 |
| 2 | 2 | 144 | 5.2 | 3.7 | 216 | 8.0 | 3.9 | 313 |
| 3 | 1 | 150 | | | 206 | | | 260 |
| 3 | 2 | 151 | 0.5 | 0.4 | 209 | 3.3 | 1.6 | 266 |
| Average deviation | | | 1.9 | 1.4 | | 4.7 | 2.3 | |

Comparison of Pyrolysis and CT data analyses

The stitched LOM images that were analysed with ImageJ are shown in Figures 6.32, 6.33, 6.34. For stitching single images together, the structures of the fibres as well as the unsharp structures in the background were used to align the single images manually. The complete dish was screened and images were saved for all regions where fibre were located. Marking of fibres was done in zoomed mode.

The fibres are represented by dark and bright lines depending on the reflection of light. Since all other structures in the background are blurred, the manual marking of fibres with lines works fine and all fibres were marked in that way. Examples of marked fibres are shown in Figure 6.35.

Nevertheless some structures were found where marking was more difficult. Residues of the polymer as well as contaminations as shown in Figure 6.36 required more effort in marking fibres correctly.

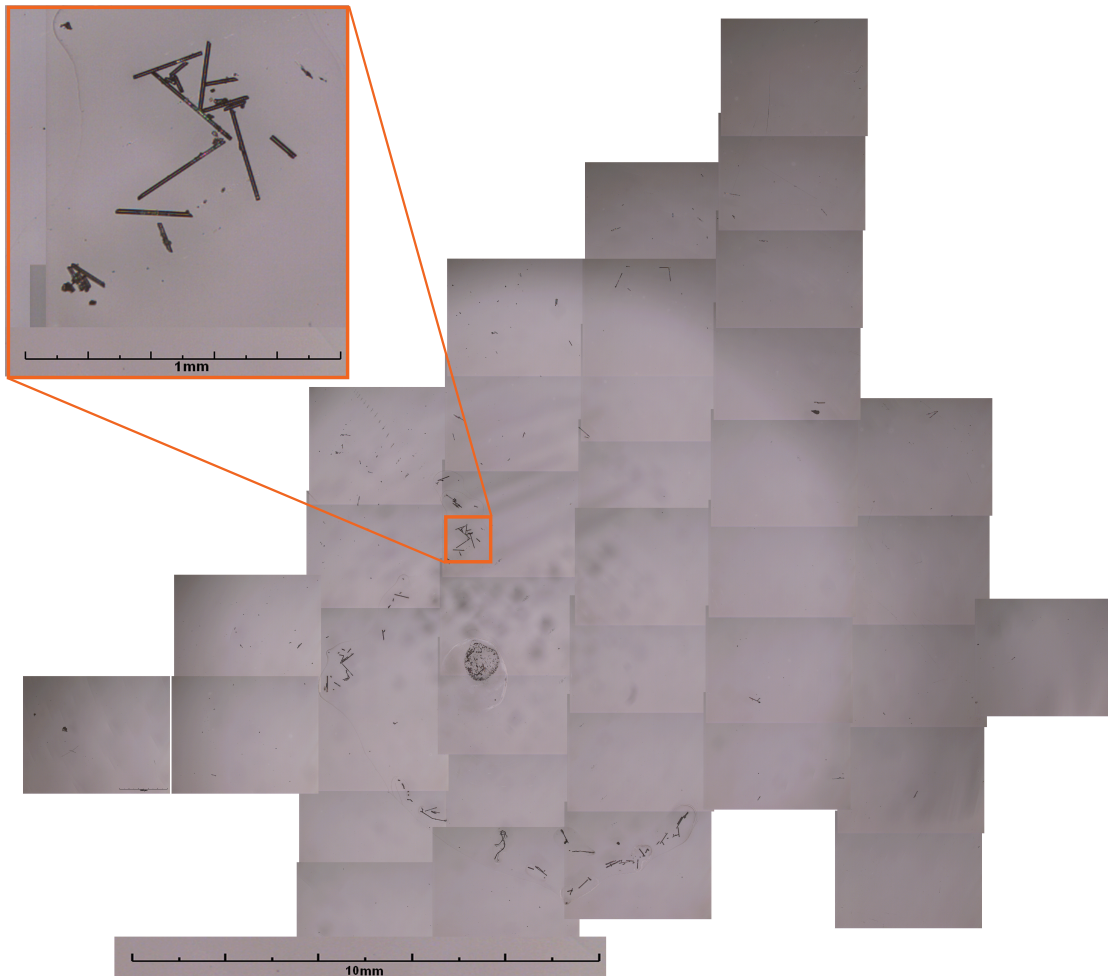


Figure 6.32: Stitched LOM image of sample 1 (PP-sGF-30) and zoomed region containing several fibres (orange square)



Figure 6.33: Stitched LOM image of sample 2 (PP-sGF-30) and zoomed region containing several fibres (orange square)

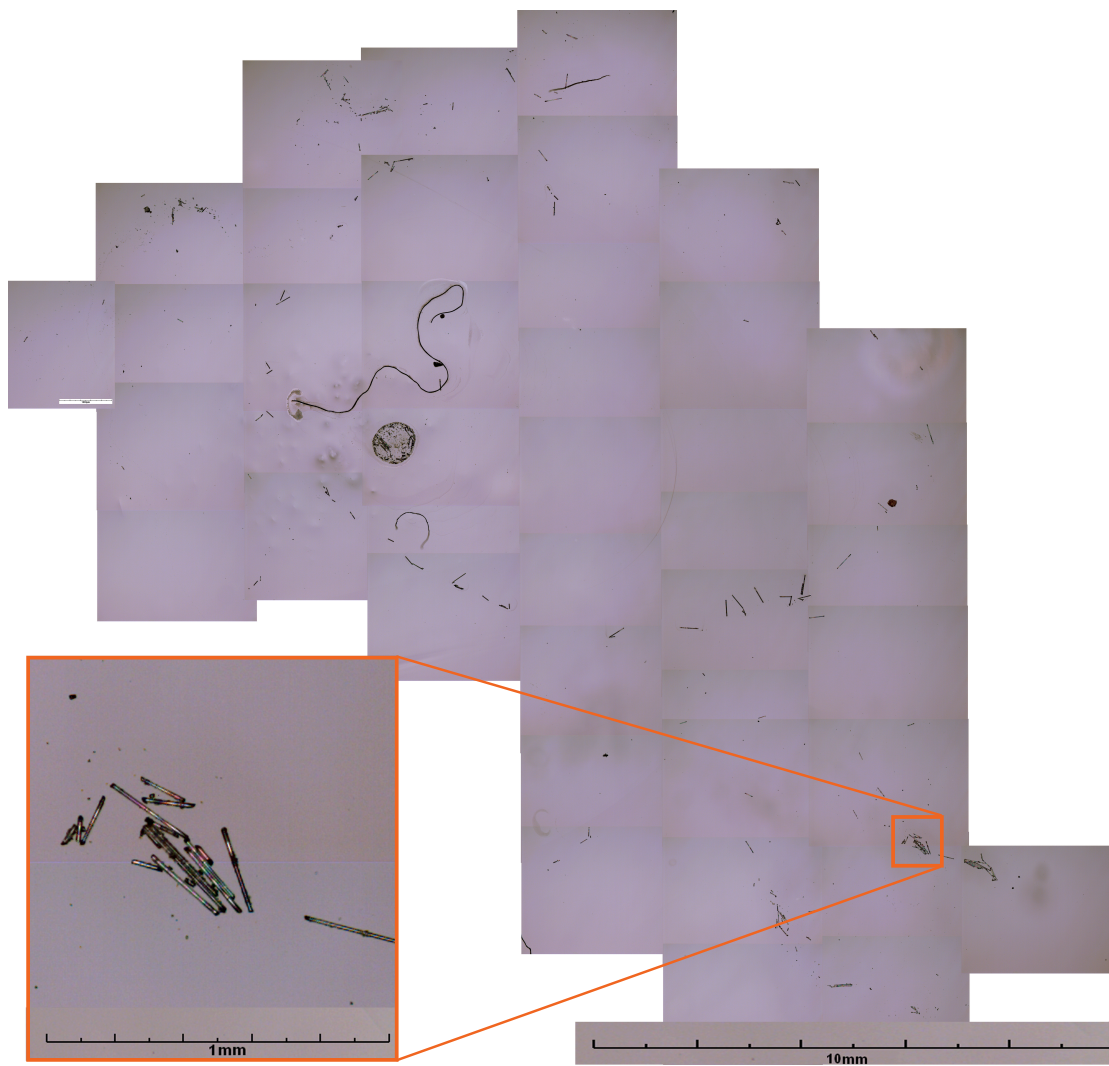


Figure 6.34: Stitched LOM image of sample 3 (PP-sGF-30) and zoomed region containing several fibres (orange square)

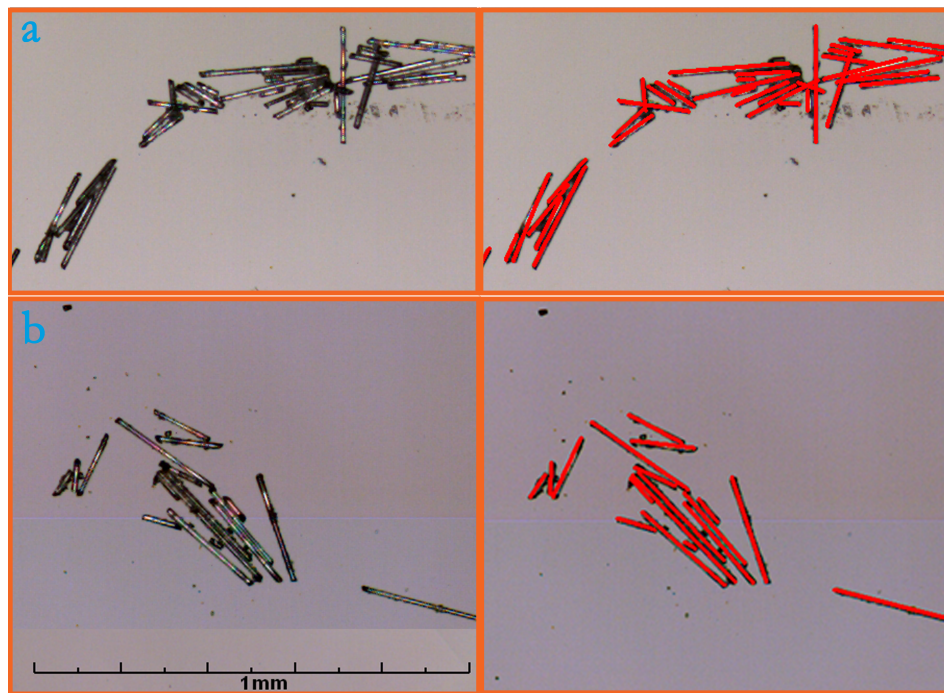


Figure 6.35: Zoomed views of LOM images of samples 2 (a) and 3 (b) containing several fibres, red lines are marks for length measurement

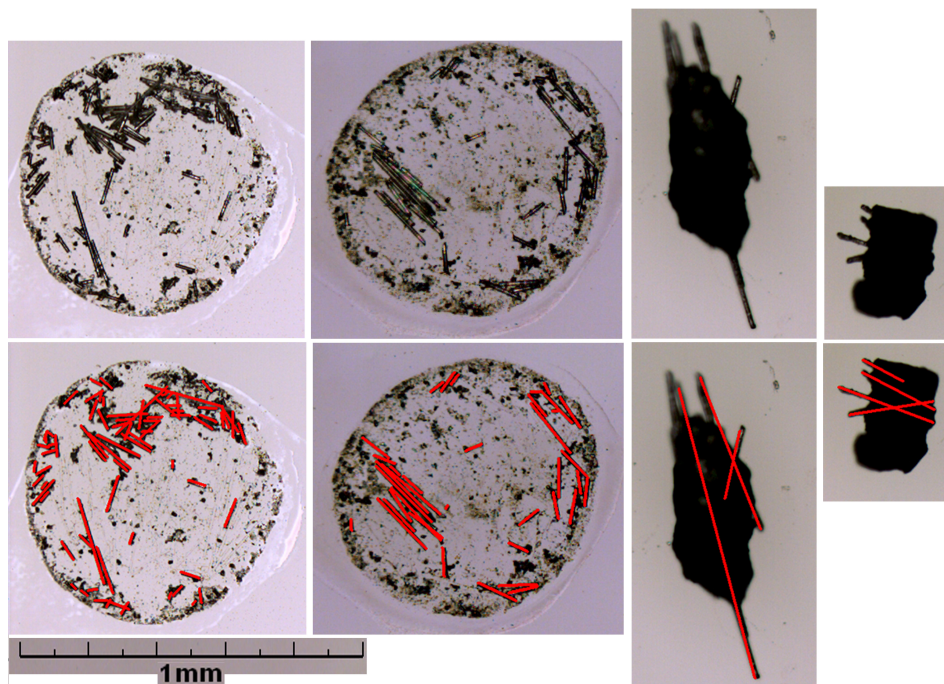


Figure 6.36: Zoomed views of LOM images of 4 special structures of samples 2 and 3.

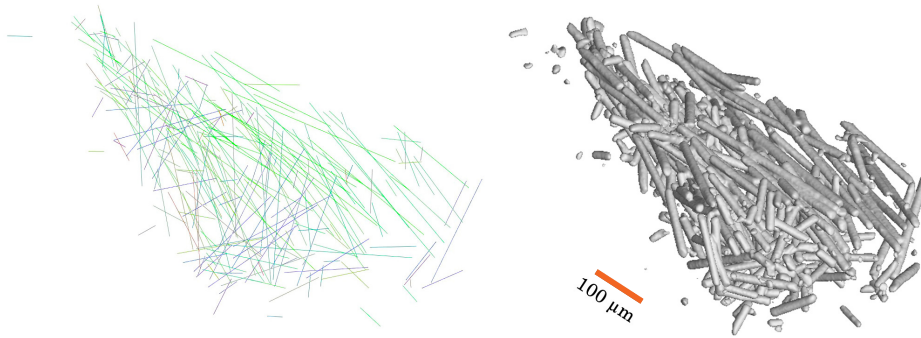


Figure 6.37: Rendered images of CT data analysis result (left) and original grey value image (right) of sample 1 (PP-sGF-30) scanned at 2 μm voxel edge length

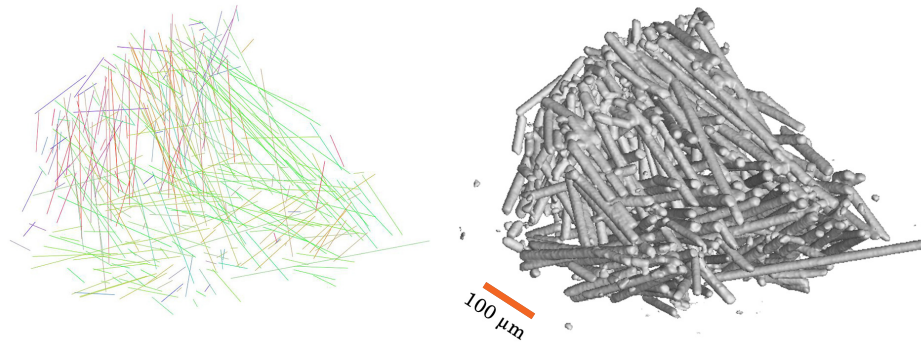


Figure 6.38: Rendered images of CT data analysis result (left) and original grey value image (right) of sample 2 (PP-sGF-30) scanned at 2 μm voxel edge length

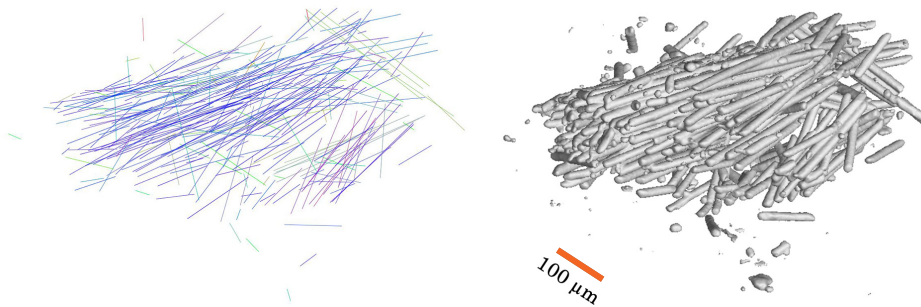


Figure 6.39: Rendered images of CT data analysis result (left) and original grey value image (right) of sample 3 (PP-sGF-30) scanned at 2 μm voxel edge length

The 3D renderings shown in Figure 6.37, 6.38 and 6.39) show original grey values and the extracted fibres with colour coded lines. For all three specimens very small

fragments are visible near the surface which were partly extracted by the software. The visual impression of extraction quality is good.

The deviations of average fibre length between pyrolysis and CT are below 11 % and in average below 10 μm or 8 %. Both analyses lead to very similar length results. Number of fibres is comparable differing by maximal 27 fibres.

Table 6.9: Characteristics of the three small cut-outs from LOM after pyrolysis and CT analyses with deviations from 2 μm Voxel edge length compared to LOM

| Specimen | Method | Average length (μm) | Deviation (μm) | Deviation (%) | Weighted average length (μm) | Deviation (μm) | Deviation (%) | Fibre count |
|-------------------|--------|----------------------------------|-----------------------------|---------------|---|-----------------------------|---------------|-------------|
| 1 | LOM | 113 | | | 174 | | | 214 |
| 1 | CT | 125 | 12.0 | 10.7 | 193 | 19.1 | 11.0 | 222 |
| 2 | LOM | 131 | | | 203 | | | 335 |
| 2 | CT | 144 | 13.1 | 10.0 | 216 | 12.7 | 6.3 | 313 |
| 3 | LOM | 146 | | | 208 | | | 239 |
| 3 | CT | 151 | 4.6 | 3.1 | 209 | 1.2 | 0.6 | 266 |
| Average deviation | | | 9.9 | 7.9 | | 11.0 | 5.9 | |

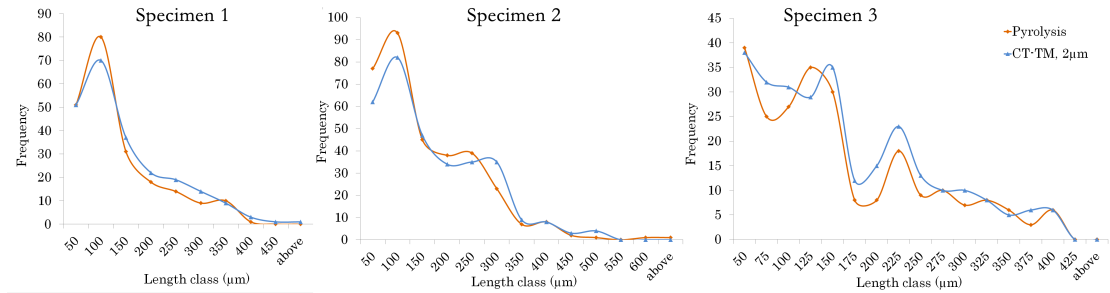


Figure 6.40: Fibre length distributions from pyrolysis and CT for three specimens

6.8 Correction of Voxel edge length

The ball bar was calibrated by the company FEINMESS GmbH & Co. KG (Bad Endbach - Bottenhorn, Deutschland) with the DAkkS accreditation as calibration laboratory D-K-18311-01-00 (previously DKD-K-25901 for dimensional measured variables). The measurement was conducted in April 2012 and yielded the value:

$$3,9796 \text{ mm} \pm 0,0020$$

(Approval number 71562)

Table 6.10 shows results from CT scans with different resolutions. For 2 and 3 μm Voxel edge length a second scan was conducted with corrected object position on scanner Z axis (ZO) after the first scan with nominal ZO, to show the remaining deviation after position correction.

Table 6.10: Results of the ball bar with different resolution

| Voxel edge length nominal (μm) | | Ball distance d (μm) | Voxel edge length corrected (μm) | Object position ZO (mm) | Deviation Ball distance (μm) |
|---|-----------|-----------------------------------|---|-------------------------|---|
| 3 | initial | 3923 | 3,03 | 18 | -56,4 |
| | corrected | 3979 | 3,00 | 17,74 | -0,4 |
| 2 | initial | 3896 | 2,04 | 12 | -83,5 |
| | corrected | 3980 | 2,00 | 11,75 | 0,4 |
| 1 | initial | 3824 | 1,04 | 6 | -156 |
| | corrected | 3974 | 0,99 | 5,76 | -5,9 |

Quantitative fibre characterisation

Applications were selected for applying the developed method of individual fibre characterisation. These examples will show different micro-structure characterisations for different fibre composite materials.

At first the influence of fibre content on micro-structure along the production process will be discussed. The following sub chapters deal with changes of fibre orientation and length along the injection length and along sheet thickness.

A sub chapter about long fibre characterisation shows the specific determination of free fibre length after impact testing for polymer as well as glass fibres. The last chapter shows how the determined fibre characteristics can be used for FE modelling.

The results presented in the following two sub chapters were acquired by Bernhard Plank within his master's thesis [81]. Differences in values may occur due to the fact that the novel approach of Template Matching was used for this thesis which was not available for the master's thesis.

7.1 Impact of fibre content on FOD and FLD

It is well known and documented that increasing fibre content leads to increased mechanical properties but also leads to fibre length shortening because of fibre fibre interaction at compounding and injection moulding [3]. A quantification of this effect is shown in Table 7.1. The features that change are number of fibres and average lengths. Diameter and orientation tensor show only very small changes.

The specimen with highest fibre content shows slightly higher fibre alignment in injection direction, the other results are almost same.

Fibres are damaged during compounding and injection moulding leading to reduction of average length. This reduction is more severe for higher fibre content. Average length

follows an almost linear trend between 10 and 30 wt.%. Fibre length distributions (7.2) show a movement of higher frequency towards shorter fibre length for higher fibre content which results in smaller average length.

Fibre fraction can be determined accurately for 5 wt.%, the deviation to nominal value increases with fraction and is ca. 4 wt.% for the 30 % specimen.

Table 7.1: Result of FCP analysis for 4 specimens with fibre content ranging from 5 to 30 wt.%

| | Unit | PPGF5 | PPGF10 | PPGF20 | PPGF30 |
|---------------------------|-------------------|--------|--------|--------|--------|
| Fibre count | | 12985 | 28681 | 57945 | 109677 |
| Weighted average length | (μm) | 731 | 668 | 572 | 456 |
| Average length | (μm) | 465 | 412 | 356 | 299 |
| Average diameter | (μm) | 11,5 | 11,6 | 12,2 | 12,1 |
| Fibre fraction per volume | (vol.%) | 1,8 | 3,7 | 6,9 | 11,1 |
| Fibre fraction per weight | (wt.%) | 5,0 | 9,6 | 17,3 | 26,0 |
| a_{XX} | | 0,132 | 0,137 | 0,139 | 0,110 |
| a_{YY} | | 0,056 | 0,063 | 0,065 | 0,066 |
| a_{ZZ} | | 0,812 | 0,799 | 0,796 | 0,825 |
| a_{XY} | | -0,013 | -0,020 | -0,016 | -0,014 |
| a_{XZ} | | -0,003 | 0,010 | 0,002 | -0,001 |
| a_{YZ} | | 0,005 | 0,009 | 0,004 | 0,009 |

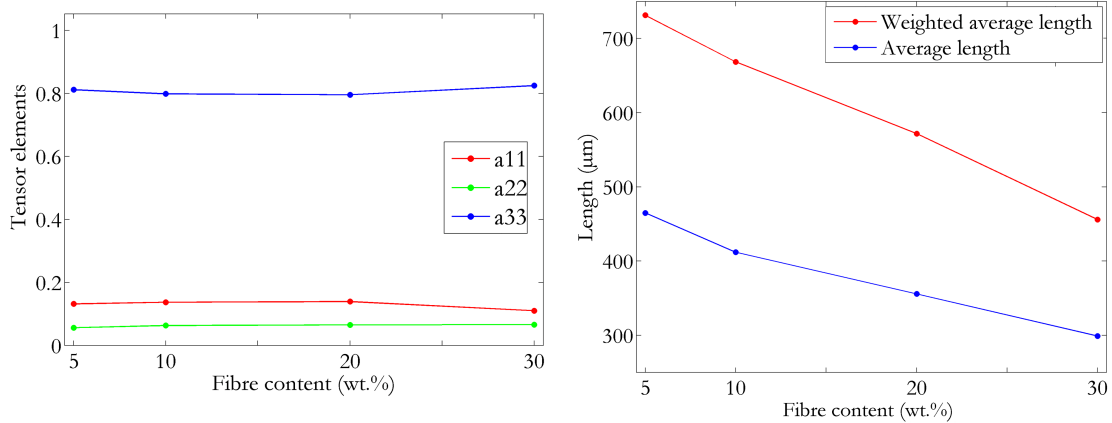


Figure 7.1: Main tensor elements (left) and average fibre length values (right) for different fibre contents for MPS specimens

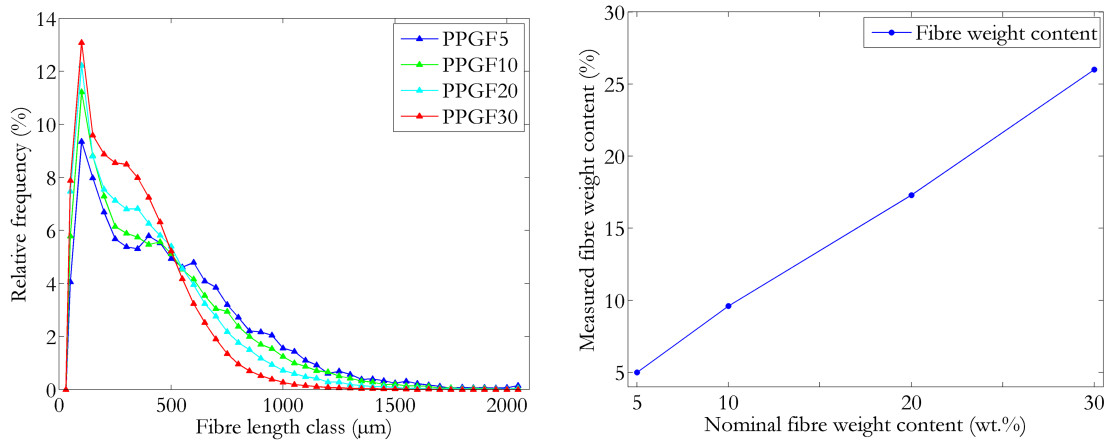


Figure 7.2: Fibre length distributions (left) and fibre weight fraction (right) for different fibre contents and MPS specimens

7.2 Fibre degradation along injection moulding process

At every step of the injection moulding process mechanical and thermal load is applied to the fibres. During compounding fibres undergo shear stress near the screw surface and fibres interact with each other. During injection moulding fibre-fibre interaction occurs too but also shear stress at the gate and near the tool surfaces are applied.

From length distributions shown in Figure 7.3 it is obvious that with higher fibre content these effects are stronger leading to shorter fibres. Starting from initial fibre length of 1.5 mm for all fibres the average fibre length is reduced to values between ca. 25 and 50 % (30 wt.% and 5 wt.%) at compounding. Weighted average length is reduced to values between ca. 40 and 75 %. During injection moulding the reduction of length is less severe for higher fibre contents. Average length is reduced to values between ca. 20 and 30 %. This means an additional reduction of 5 % points for higher content and 20 % points for lower content. Nevertheless the final reduction of average lengths is strongest for highest fibre content.

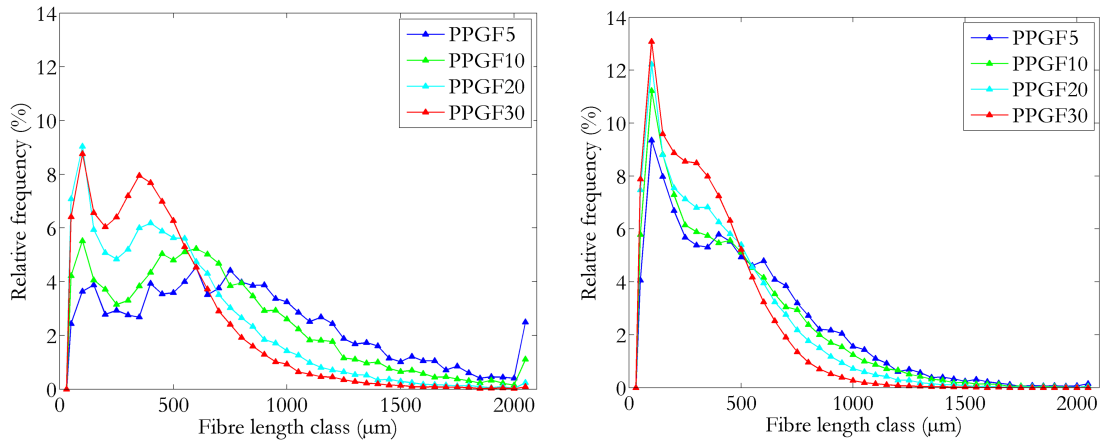


Figure 7.3: Fibre length distribution for different fibre contents. Pellets (left), MPS (right)

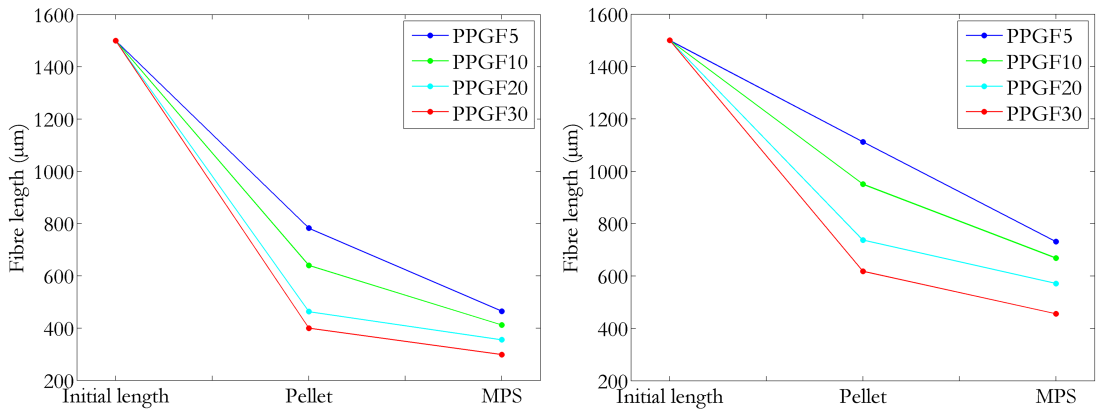


Figure 7.4: Average fibre length (left) and weighted average fibre length (right) from initial length to pellet and MPS for different fibre contents

7.3 Skin-core layered micro-structure

As an example, that should show the capabilities of micro-structural analysis of injection moulded sFRP materials, FOD and FLD were determined on sector specimens. This section will show one specimen at position 1 only. Additional data from all other specimens showing average length and strength of orientation distribution can be found in Appendix C 8.

FOD for position 1 was already shown in chapter 6.6, in this chapter FLD and slice images are shown in addition. As for orientation, the analysed volume was subdivided into 21 regions along sheet thickness to calculate average fibre length for each region.

The overlay of tensor elements and cross sectional CT images (Figure 7.5) shows the variation of orientation over sheet thickness. The quite narrow bands of very strong orientation manifested by high a_{ZZ} or a_{XX} values match very well to the visual impression of the cross sectional image. Information about length is not directly visible because individual fibres are only visible completely when they are aligned parallel to a coordinate axis which hold true only for two regions with highest a_{ZZ} values. Weighted average length shows slightly higher values in the core and lower values where a_{ZZ} is highest.

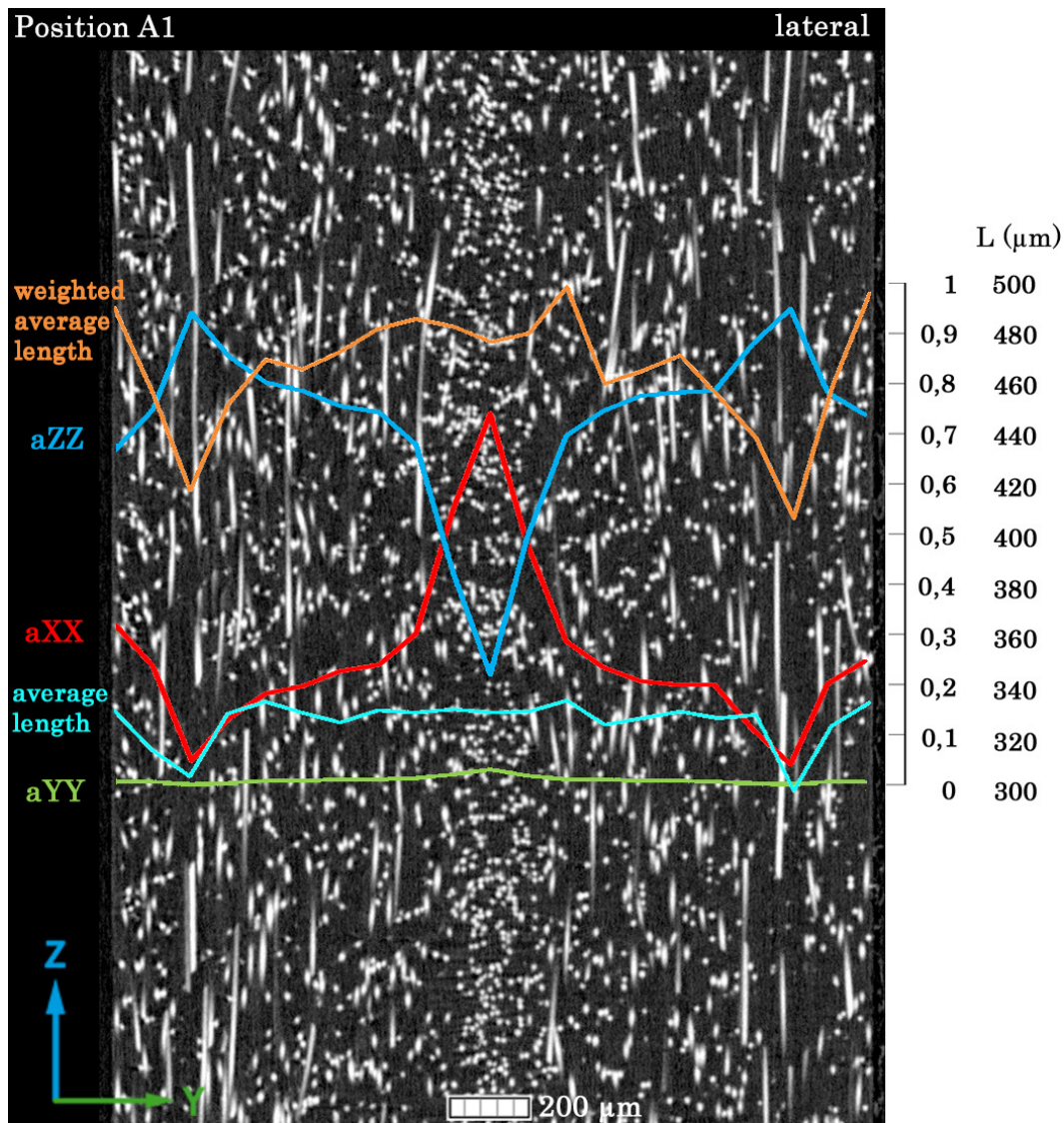


Figure 7.5: CT slice image showing sheet thickness horizontally (Y-axis) of sector position A1 with main tensor elements, average length and weighted average length along thickness overlaid

Average results of three specimens at position 1 are shown in Figure 7.6. Variation between specimens is a bit higher for length determination compared to orientation. The lower length values at regions with strongest orientation can be seen in average length and weighted average length. Increased values in the core region were only detected for weighted average length.

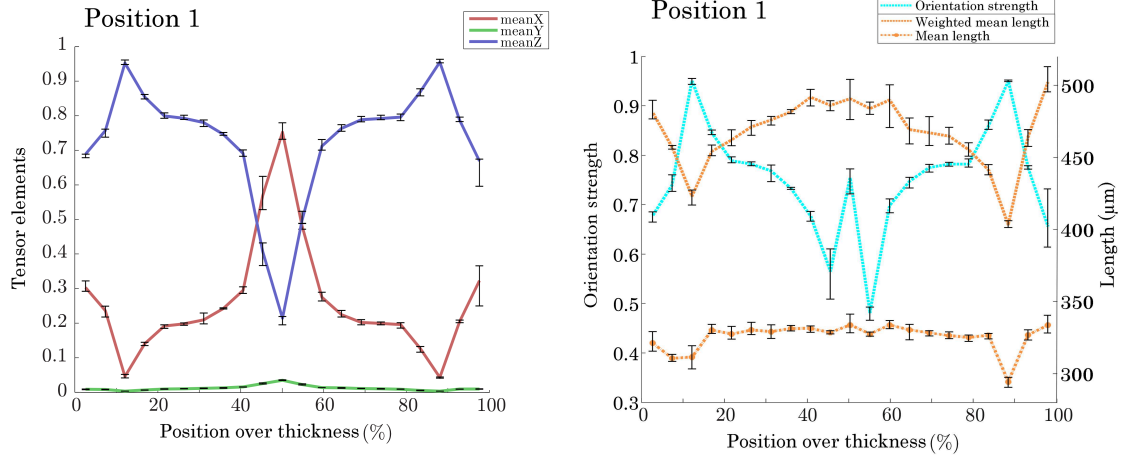


Figure 7.6: Orientation distribution (left) and length distribution (right) over sheet thickness as average of three sector specimens at position 1 together with deviation bars

7.4 Fibre degradation along injection length

For each of 16 positions distributed over half of an A5 sheet, orientation tensor and length were determined. Fibre orientation was determined at 21 positions over sheet thickness. A bigger image of the small individual images should explain the content of the following landscape images (Figure 7.7). It shows results of position 8 alone. The landscape images will not show axes labels since the single images are too small. The same labels shown in the example Figure 7.7 have been applied to every small figure as well. Also the ranges of all axes were chosen same for all positions. Strength of orientation is the biggest tensors eigenvalue which can have values between $\frac{1}{3}$ and 1 which is also the scale of the colour bar. Landscape images showing all 16 positions at once are given in Figure 7.8.

Fibre orientation is shown in three ways: main tensor elements over thickness, ellipsoids for averaged tensors and interpolated coloured information of a_{ZZ} of almost the complete sheet. The ellipsoids were calculated from the average tensor of all fibres and give therefore an impression of main fibre direction as well as fibre orientation distribution. The distribution determines the shape of the ellipsoid and the colour shows the strength of orientation. The tensor component a_{ZZ} is calculated for all 16 positions and interpolated between them on a grid with 0.5 mm spacing in X and Z (Figure 7.9). The same is done for the weighted average length (Figure 7.10).

Orientation and length distribution values are shown along injection direction (Z) and lateral direction (X). Values for positions at different distances for each direction as shown in Figure 7.11 are considered for Figure 7.12. For showing differences in injection direction, three lateral positions (centre, edge and medial in between) were chosen. For lateral direction three longitudinal positions (near gate, centre, far away from the gate) were chosen.

Visualisation of tensor elements as ellipsoids and through thickness values allows to get an overview of fibre orientation distribution across half of the A5 sheet (Figure 7.8). Regions with distinct skin-core layered structure are located in the centre of the complete A5 sheet. The further away from the gate, the broader the core region with altered orientation is spread. The weakest skin-core orientation alternation is seen near the border in lateral and in the middle in longitudinal direction. Since the variation of orientation is also transferred to the shape of the ellipsoids and the strength of orientation, ellipsoids with distinct layered structure are round and blue while weak layered structure leads to needle like ellipsoids with red colour. The direction of ellipsoids principal main axis describes the preferred fibre orientation. Especially along longitudinal direction at medial position the direction is not aligned to injection direction.

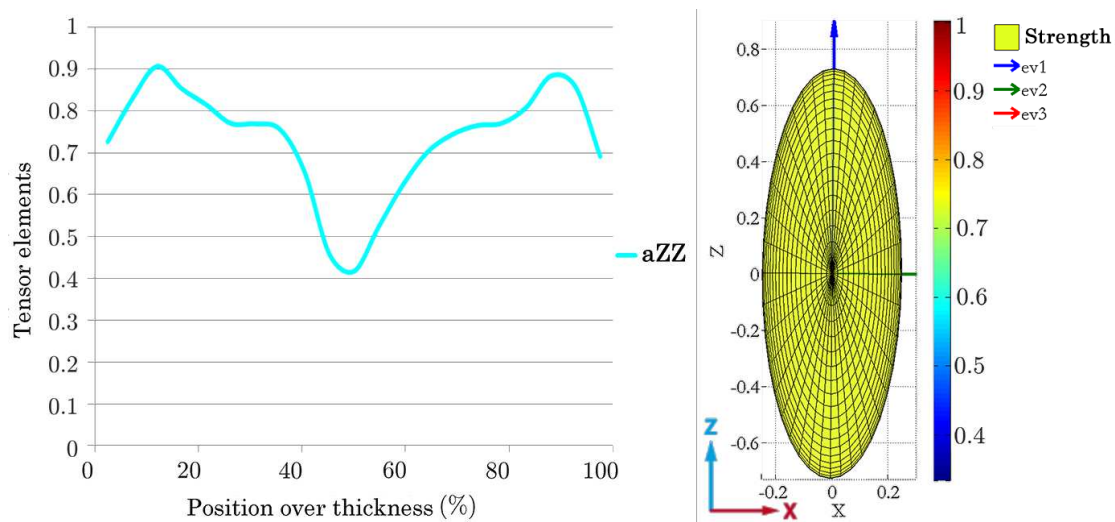


Figure 7.7: Example of how orientation is visualised in the following Figure 7.8. The values of tensor element a_{ZZ} (injection direction, sheet long axis Z) over sheet thickness are shown on the left. For all positions scaling was set same from 0 to 1. An ellipsoid is calculated from the tensor elements with colour coded strength of orientation which is shown on the right. In the following figure the ellipsoid is rotated with respect to the coordinate system as specified by the tensor.

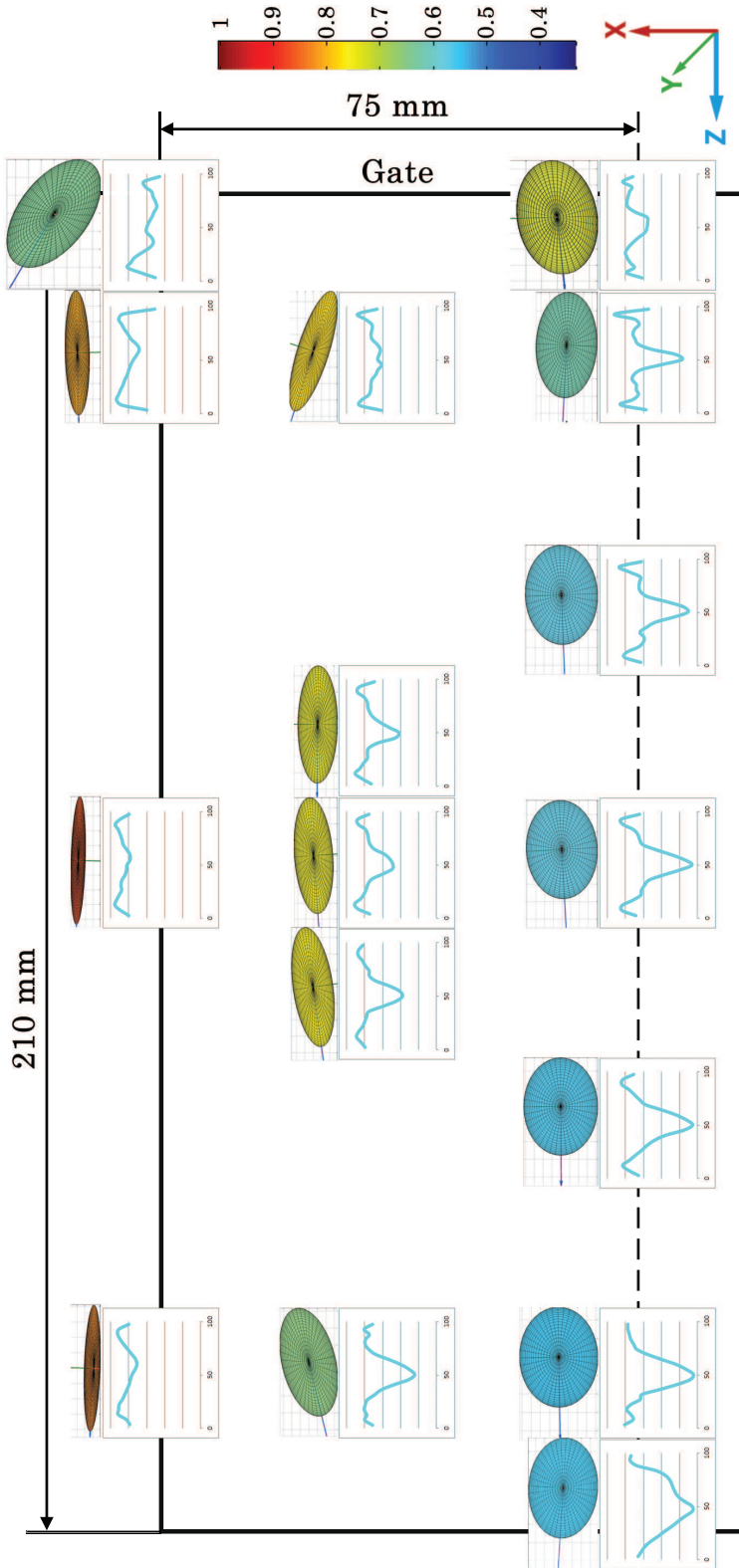


Figure 7.8: Orientation information for 16 positions distributed over half of an A5 sheet. The curves show tensor component a_{ZZ} over sheet thickness as shown in Figure 7.7. The ellipsoids contain information of all data per position. Shape and colour are depending on the strength of orientation. The eigenvector corresponding to the biggest eigenvalue is heading in main orientation direction. Injection direction is Z from right.

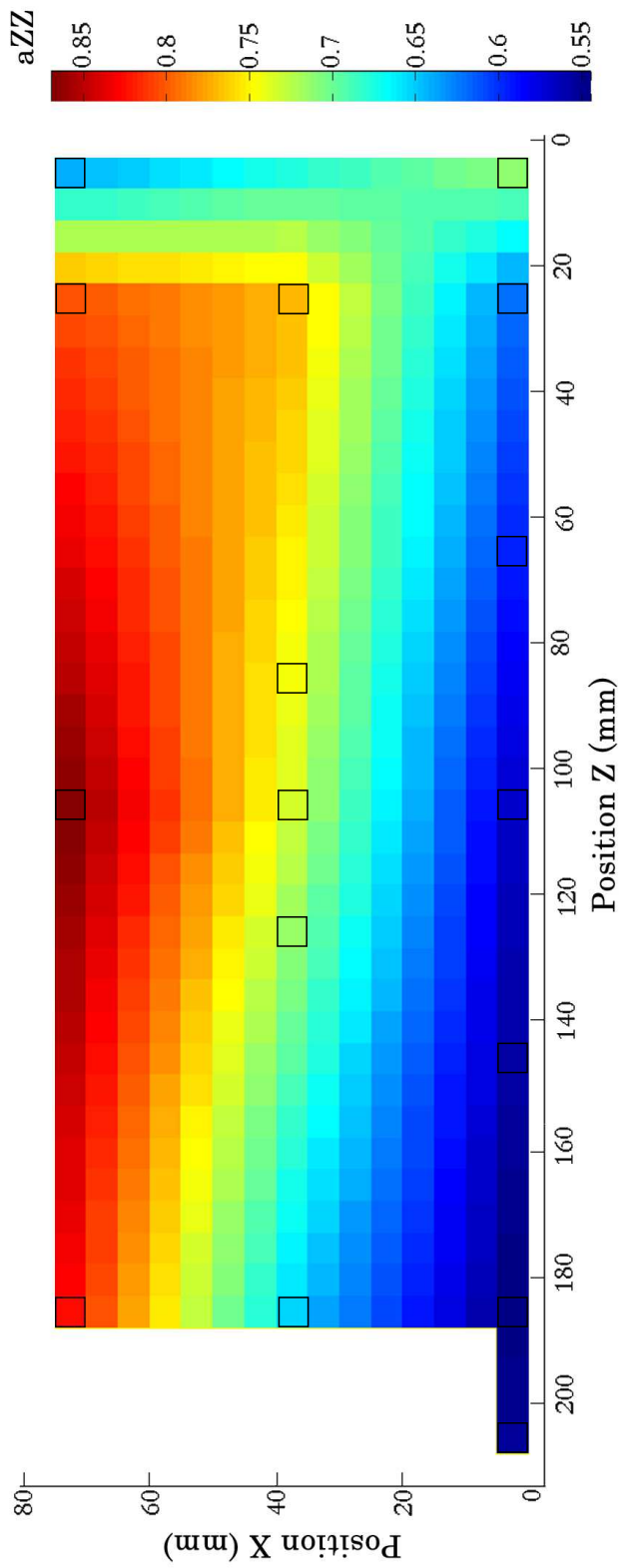


Figure 7.9: Orientation distribution information for 16 positions (black rectangles) distributed over half of an A5 sheet. Values in between scanned positions were linearly interpolated. Tensor component a_{ZZ} is shown colour coded in the range of minimum and maximum value determined. Injection direction is Z from right.

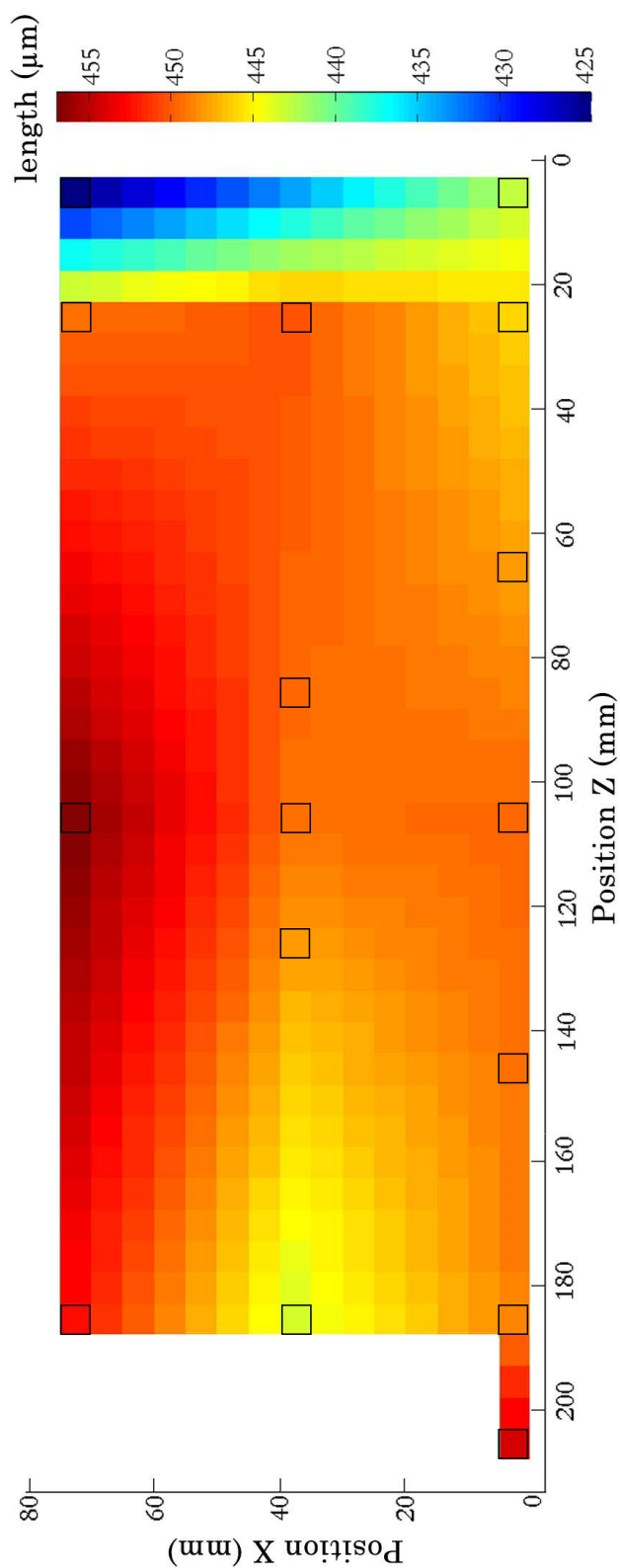


Figure 7.10: Length distribution information for 16 positions (black rectangles) distributed over half of an A5 sheet. Values in between scanned positions were linearly interpolated. Weighted average length l_w is shown colour coded in the range of minimum and maximum value determined. Injection direction is Z from right.

7.4. FIBRE DEGRADATION ALONG INJECTION LENGTH

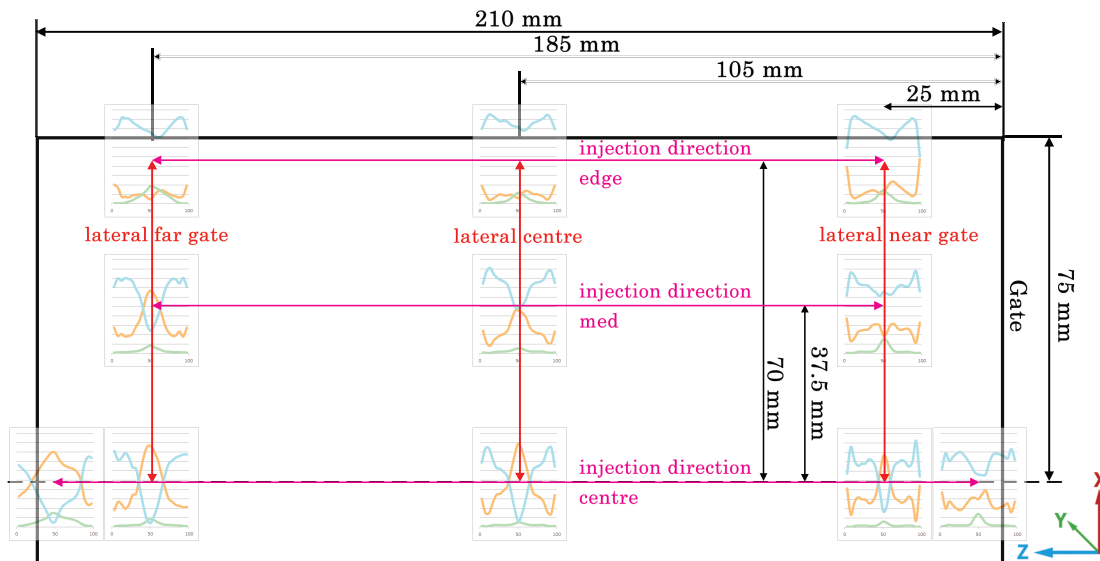


Figure 7.11: Definition of positions for which quantitative values shown in Figure 7.12. For each line 3 positions at different distance are shown except „injection direction centre“ for which 5 positions were analysed. The sheet was injected from the right.

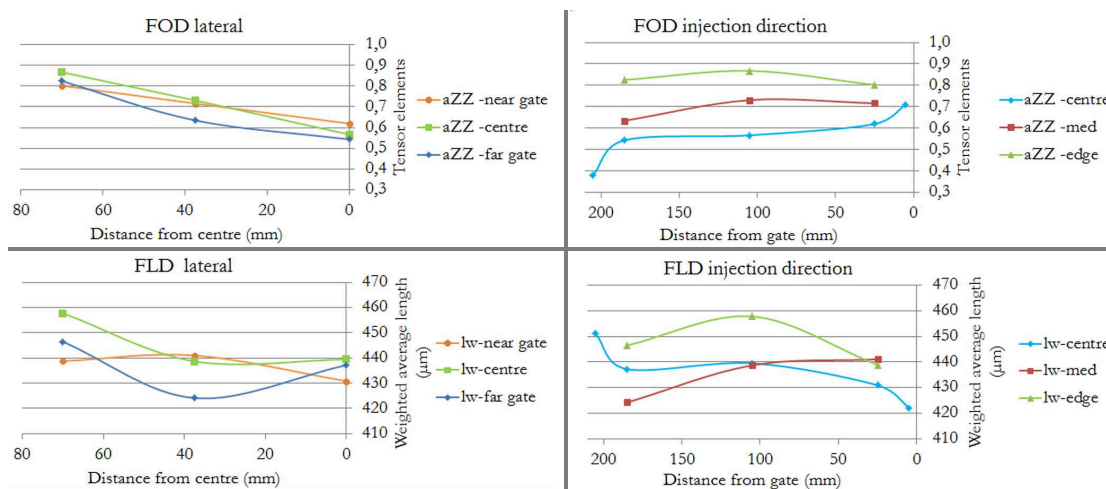


Figure 7.12: Average values of FOD and FLD per position along lateral direction (left) and along injection direction (right). The positions are defined as shown in Figure 7.11. From the tensor only the element a_{ZZ} is shown which is the component in injection direction. The weighted average length l_w is shown for length.

The same information about variation of orientation is shown in Figure 7.9 but the interpolation between scanned positions gives a more complete picture. The very complex orientation distribution near the gate can be conceived easier. The trend of lower orientation in Z- direction further away from the gate and it's spread in lateral

direction is obvious. The position of strongest orientation can be identified easily as the lateral border and longitudinal centre.

Values for tensor component a_{ZZ} and weighted average length can be compared in Figure 7.12. The described differences of orientation along injection direction at centre, medial and edge position can be detected in similar way for weighted average length. The longest fibres can be found at the position of strongest orientation.

7.5 Micro-structure of long fibres

As shown in the figures in Chapter 5 a big difference between long and short fibres is the strong bending. Depending on the type of fibre material the bending can lead to curving but also to building loops and even knots. For polymer and natural fibres this effect was found to be most prominent.

For building models from the determined micro-structure it is necessary to take the curvature into account for both, length and orientation. The length of a curved fibre can be estimated by tracing the fibre and summing up intermediate lengths or by defining splines for which the length can be calculated. The orientation of a curved fibre is per se not defined. For modelling some work was published that addresses this problem. One is the „Poly Inclusion Model“ [101] which takes local curvature into account for setting up a single fibre from several substitutional ellipsoids. The intermediate points that are determined during fibre tracing and saved into a csv-file can be used to calculate local curvature and build up the „Poly Inclusion Model“. In the following subsections the orientation tensor values will not be given because it is calculated from fibre endpoints only and therefore meaningless.

7.5.1 Influence of analysis volume for long GF

A study about the influence of analysis volume was conducted similar as for short fibres in Chapter 6.4 since fibre length and distribution was not known beforehand. A specimen from a 2mm thick sector sheet at position 2 made of PP-IGF-a was cut-out and scanned at 2 μm Voxel edge length. Three scans in vertical direction were put together to build up an total analysis volume of 4 x 1.1 x 11.1 mm^3 . This volume was then split up into sub-volumes to determine the influence of cutting fibres at the borders. 4 sub-volumes were cut-out centred or starting from one end as shown in Figure 7.13. The size was varied from 25 % (2.8 mm), 50 % (5.5 mm), 66 % (7.3 mm), 75 % (8.3 mm) to 100 % (11.1 mm). For all datasets the size in Y direction was ca. half of the sheet thickness.

The cross sectional images reveal a distinct core-shell layered fibre orientation. In every plane curved fibres are visible. Fibre bundles can be found near the surface and at the centre of the sheet. The distribution of remaining fibre bundles is very inhomogeneous. It is obvious that many fibres that are oriented horizontally (perpendicular to injection direction) are cut at the border of the dataset.

Weighted average length of both data series, „centred“ and „from bottom“, show similar trends from 50 % up to total volume (7.14). The absolute difference between the two cut-out methods is significant and it is remarkable that for the „from bottom“ data the maximum length is not at total volume as expected but at 66 %. For the centred data the length also shows a local maximum at 66 % but the length for the total volume is highest. This indicates that not only the size but also the position has a big influence on the determined average length. The conclusion for further analyses on long fibre material is that it is sufficient to scan twice in vertical direction. This leads to an analysis volume of maximal 7.6 mm in height (68 % of 11.1 mm).

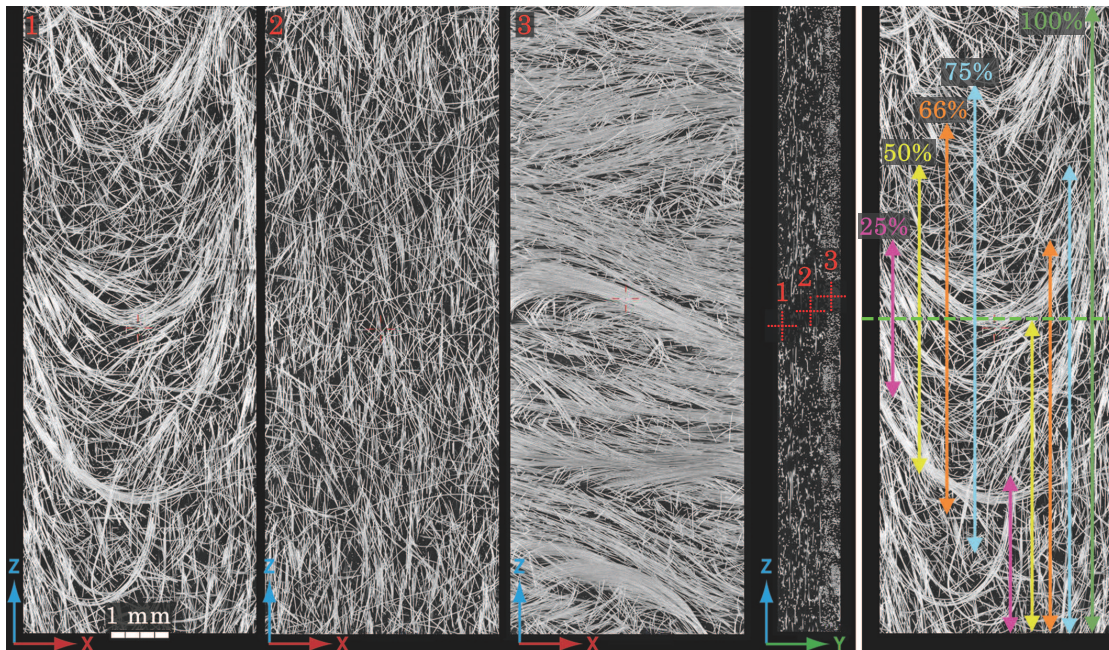


Figure 7.13: CT cross sectional images at three positions over thickness (Y-direction). Position 1 is near the surface, position 3 is near the core of the sheet and position 2 is in between. The right image shows the definition of sub-volumes.

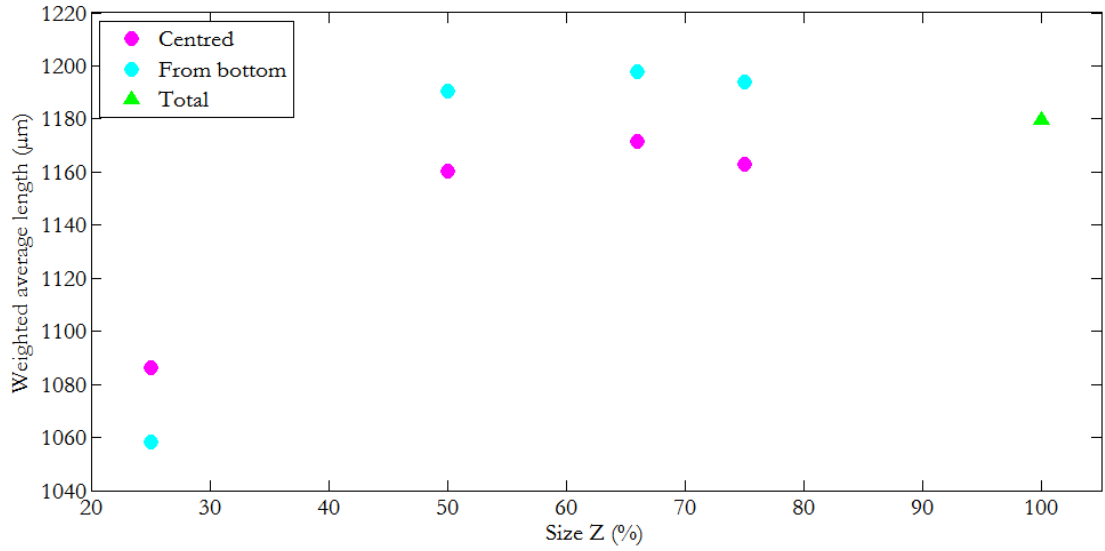


Figure 7.14: Weighted average length for sub-volumes defined by relative size in Z direction. The value for total volume is marked with a green triangle.

7.5.2 Multi purpose test specimens (MPS)

Cut-outs of multi purpose test specimens according to [90], were analysed for the material systems PP-IGF and PP-IPET. Two scans in vertical direction at $3 \mu\text{m}$ Voxel edge length were stitched together to form a scan volume of $5 \times 2 \times 11.4 \text{ mm}^3$ which represents a quarter of the MPS cross section. The length threshold was set to $60 \mu\text{m}$.

Table 7.2: Results of FCP analyses for long fibre specimens from 7 mm pellet length with nominal fibre content of 10 vol.%

| | Unit | PP-IGF | PP-IPET |
|--------------------|-------------------|--------|---------|
| Fibre count | | 30 204 | 10 310 |
| Curved fibre count | | 26 479 | 7922 |
| Curved length | | | |
| Weighted average | (μm) | 3185 | 4379 |
| Average | (μm) | 1506 | 2490 |
| Average diameter | (μm) | 15.4 | 21.2 |
| Fibre fraction | | | |
| per volume | (vol.%) | 8.1 | 8.1 |
| per weight | (wt.%) | 19.7 | 11.8 |

Different number of fibres are included in the same volume. The number of glass fibres is triple the number of PET fibres which can be explained by the different diameters and

average length values. The majority of fibres were classified as curved for both materials. The nominal diameters of 16 and 22 μm were determined accurately. Fibre content was underestimated in the same way as for short fibres (7.2).

Average fibre length for glass is reduced from 7 mm pellet length to 1.5 mm which is a reduction to 21 % of initial length. For PET average length is reduced to 36 %.

Fibre length distributions (7.15) show distinct peaks at bigger length and broader peaks at very small length. The bigger peak is at ca. 7.2 mm for glass and ca. 5.9 mm for PET. The frequency at these peaks is much higher for PET fibres. At small lengths the number of glass fibres is much higher since the shoulder of the peak is much broader. This difference could be explained by the difference of modulus. Glass fibres tend to break and form short pieces which should not happen for PET fibres.

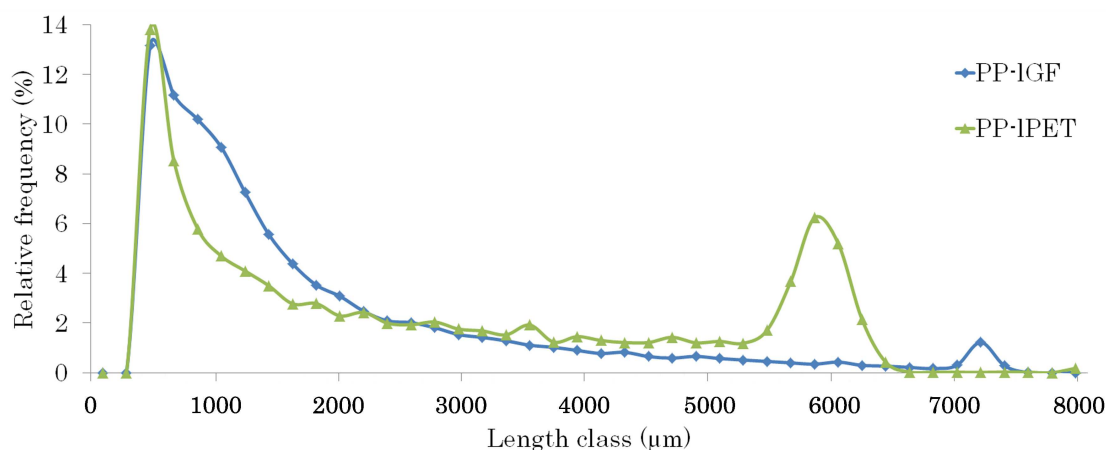


Figure 7.15: Length distribution of PP-IGF and PP-IPET MPS specimens from 7 mm pellet length

7.5.3 Special features of long fibre micro-structure

Since the long fibre materials investigated were not produced by compounding but pultrusion and because of the higher length, some special fibre arrangement can be found in long fibre composites. If the fibres within the bundles are not separated well, the bundle structure can still be present after injection moulding (Figure 7.13). For polymer fibres curvature can be very high leading to knots. The cyan coloured fibre in Figure 7.16 was split into two fibres at the knot. Some fibre bundles and fibres with high curvature are shown in Figure 7.17. The visual impression of fibre distribution is much more inhomogeneous compared to short fibres.

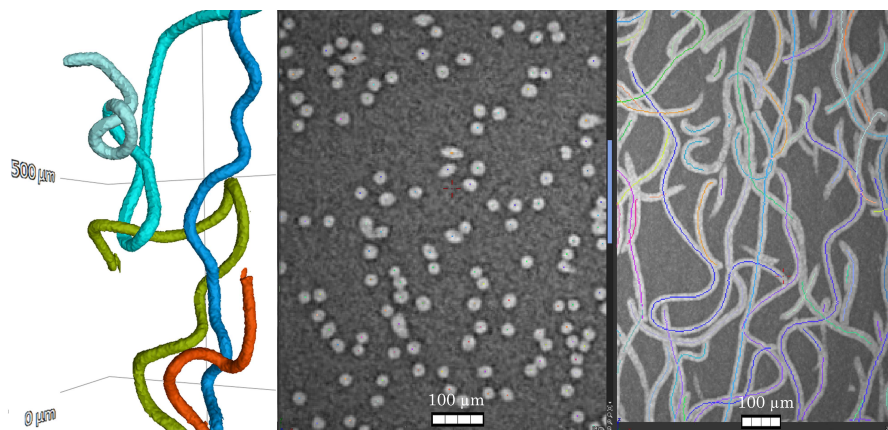


Figure 7.16: 3D rendering of selected long PET fibres extracted and colour coded (left) and cross sectional images with original grey values overlaid with extracted medial axes (right)

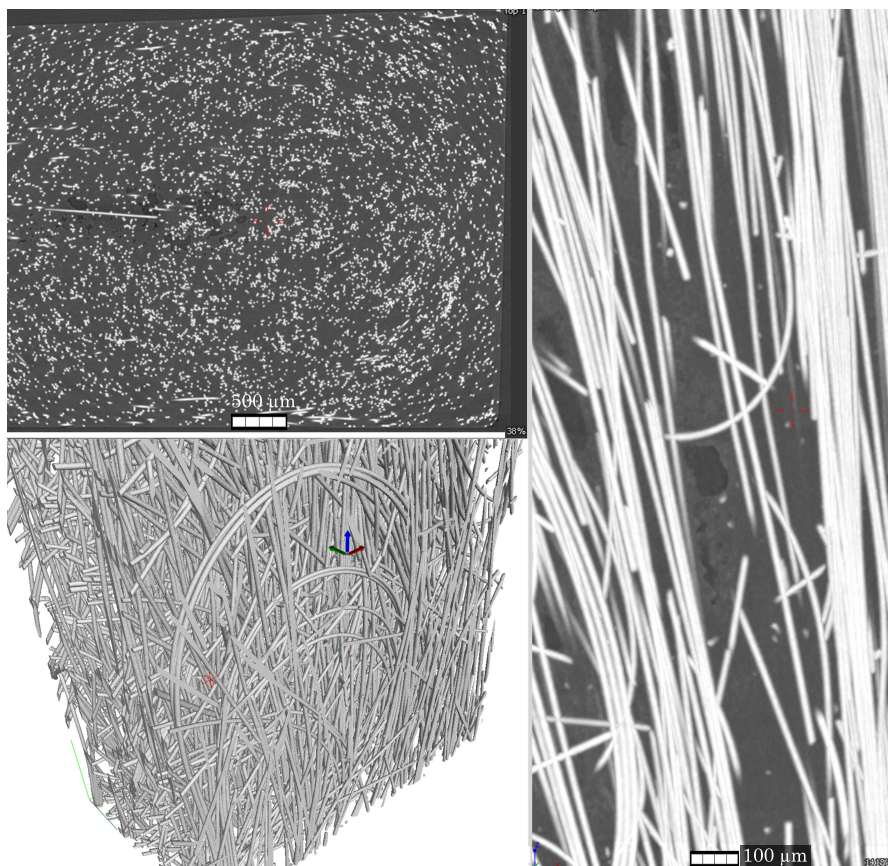


Figure 7.17: 3D rendering and cross sectional images of selected long glass fibres

7.6 Determination of free fibre length

Similar as with microscopy the fracture surface can be analysed by looking at the rendered 3D data. The surfaces shown in Figure 7.18 indicate different fracture mechanisms involved comparing polymer and glass/carbon fibre materials. The ductile polymer fibre materials lead to very straight fracture surface while the brittle materials GF and CF lead to highly structured surfaces. The reason might be the difference of fibre orientation which is visualized in Figure 7.19. The images show information from 200 μm slab thickness in inverted grey values. It is obvious that glass fibres align to the fountain flow which mainly develops in the centre of the specimen. This alignment cannot be seen for PET fibres.

Table 7.3 shows another difference between these groups of fibre materials: the percentage of free curved fibres is much higher for polymer fibres as for GF and CF. GF and CF fibres that are pulled out of the other part of the specimen can align and get straight again which is not possible for polymer fibres.

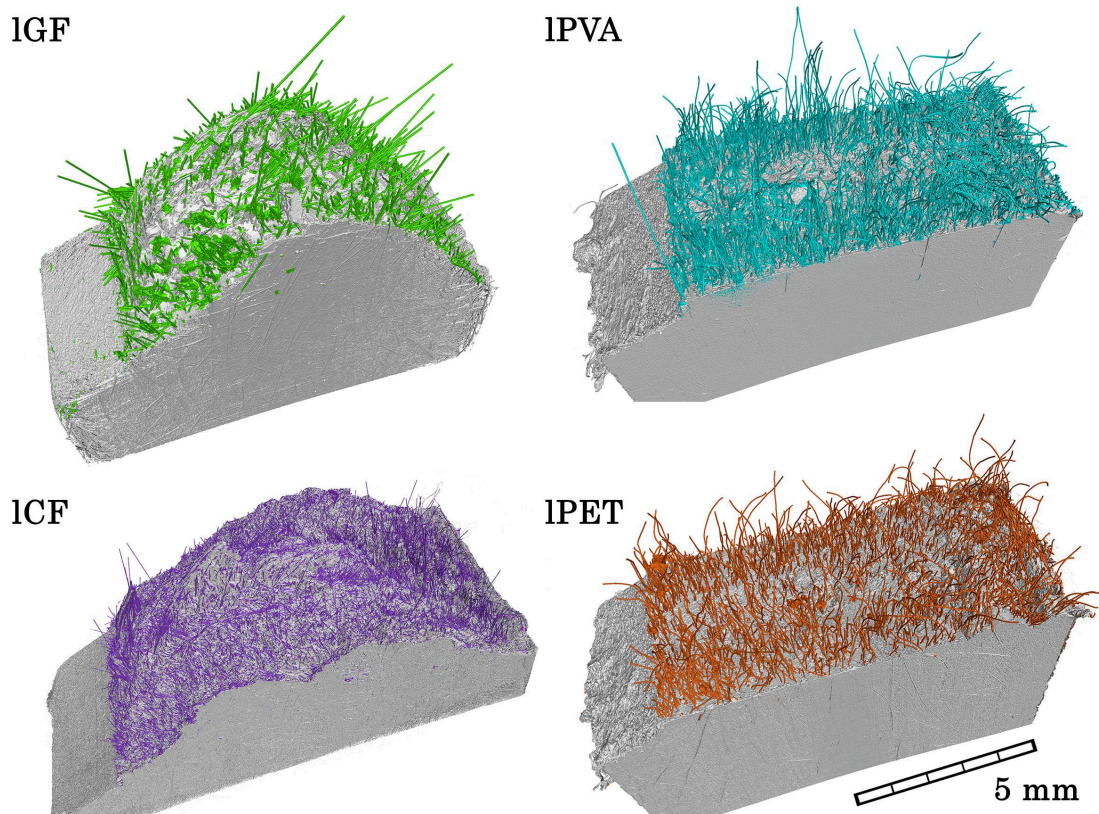


Figure 7.18: 3D renderings of fracture surfaces of notched Charpy test specimens for PP-IGF, PP-ICF, PP-IPVA and PP-IPET and 10 mm pellet length

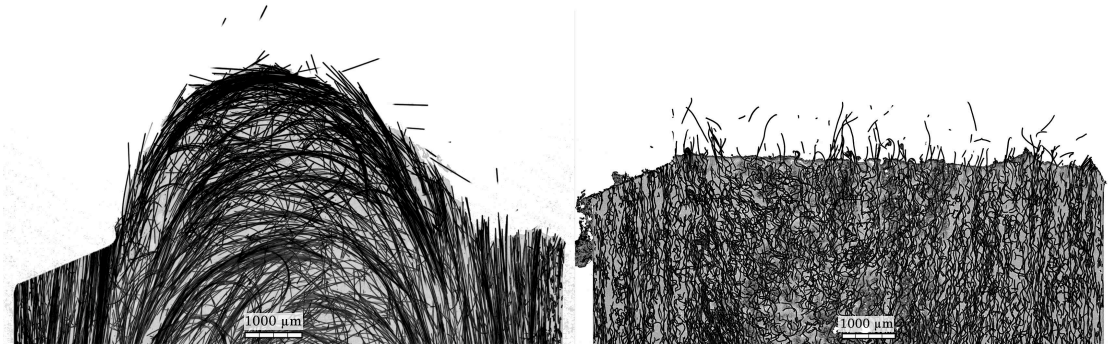


Figure 7.19: Maximum intensity projections from 200 μm slab thickness near specimen centre of fracture surfaces for PP-IGF (left) and PP-IPET (right) and 10 mm pellet length

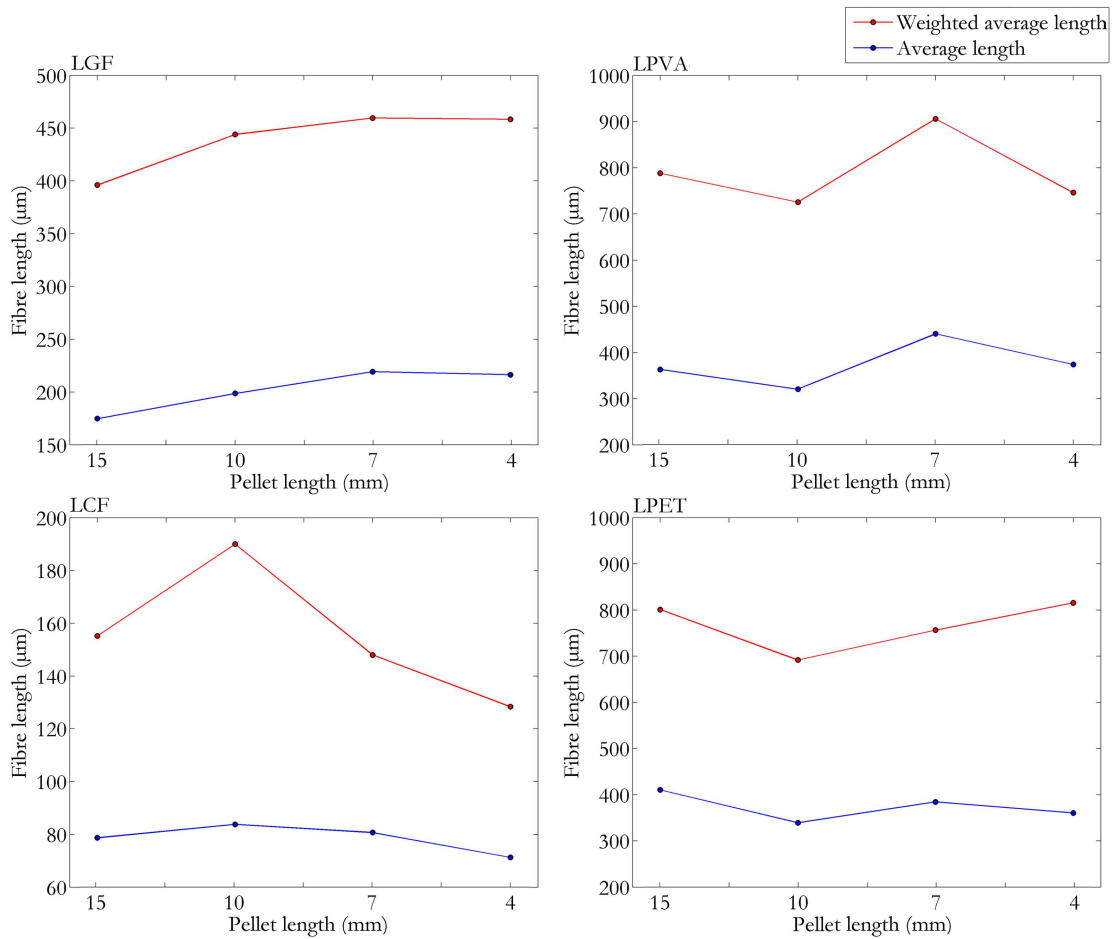


Figure 7.20: Weighted average free fibre length and average free fibre length for PP-IGF, PP-ICF, PP-IPVA and PP-IPET and all 4 pellet lengths each

Free fibre length for PET and PVA are similar and longer than GF and CF. CF show shortest free length. The influence of pellet length on free fibre length is shown in Figure 7.20. For all materials no clear trend can be found which is expected. Free fibre length is only depending on the shear strength of fibre-matrix interface, fibre tensile strength and fibre diameter [10].

Average values for free fibre length of specimens from 4 different pellet lengths for all materials is shown in Table 7.3. Results for each specimen are shown in Appendix D 8.

Table 7.3: Average values of free fibre length for long fibre composites for all four pellet lengths. All given length values are curved lengths.

| Fibre material | | IGF | ICF | IPET | IPVA |
|-------------------------|-------------------|------|--------|------|------|
| Fibre count | | | | | |
| average | | 3616 | 21 983 | 3078 | 5252 |
| σ | | 888 | 2139 | 222 | 843 |
| Curved fibre percentage | | | | | |
| average | (%) | 27.0 | 15.2 | 59.6 | 52.1 |
| σ | (%) | 4.4 | 4.2 | 6.5 | 8.1 |
| Weighted average length | | | | | |
| average | (μm) | 440 | 157 | 766 | 792 |
| σ | (μm) | 29.9 | 23.1 | 55.7 | 80.6 |
| Average length | | | | | |
| average | (μm) | 202 | 79 | 374 | 375 |
| σ | (μm) | 20.4 | 5.3 | 30.7 | 49.6 |
| Average diameter | | | | | |
| average | (μm) | 15.5 | 9.2 | 19.6 | 16.8 |
| σ | (μm) | 0.5 | 0.3 | 0.5 | 0.2 |

7.7 Modelling and virtual tensile testing

This chapter gives a summary of the work presented by Stefan Oberpeilsteiner within his master's thesis [102]. Main emphasis for this thesis is put on chapter 5 which addresses the evaluation of virtual tensile tests by comparison with interrupted in-situ CT experiments.

The goal of the master's thesis was to conduct FE simulations by taking the real microstructure into account and to validate the results with CT experiments. For that purpose, a specimen geometry was designed and specimens produced that allowed for clamping and tensile testing within the CT device. Specimen dimensions and tensile testing device are shown in Figure 7.21. The dimensions were chosen such that the constraints of the tensile testing device were considered and that the cross section in combination with the

tensile strength of the material allowed for breaking the specimens. The model material system was PP-sGF-30a.

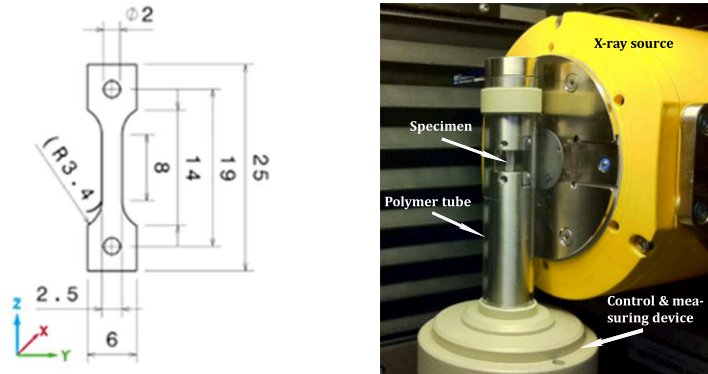


Figure 7.21: Sketch of miniaturized tensile test specimen (left), photo of tensile stage in the CT device in front of the X-ray tube (right)

A mesh of cylinders was generated in Abaqus using the information about the individual fibres from CT analyses. The fibres were modelled assuming cylindrical shape. This assumption holds true for most of the short fibres but some fibres are slightly curved. These fibres cause problems at the step of meshing because they can lead to intersections. A pre-processing step searches for possible intersections and tries to overcome that problem by modifying diameter or length of the fibres. This may lead to small deviations in mechanical properties but is mandatory to achieve a processable cylinder mesh. All fibres are modelled with its determined length and diameter except they had to be changed because of intersections. Because of computational limitations it is possible to mesh only a few hundred fibres. This represents only a part of the investigated specimen. As part of the master's thesis the minimal feasible volume for convergence was investigated and lead to representative volume elements (RVEs) with edge length bigger than 500 μm . The scanned region was therefore split into several RVEs with unique material properties determined using the scanned fibre details. If fibres would be cut at the border of the RVE, the total, uncut fibre length was taken into account and the fibre was embedded also into the other RVE. For the other parts of the specimen that were not scanned, a homogenization approach was implemented taking into account the information of adjacent RVEs. Different colours in Figure 7.22 indicate different regions with unique material properties.

As a result of taking the anisotropic material behaviour into account for the model, von-Mises stress distribution at the surface is inhomogeneous and shows the well known skin-core layered structure as seen in Figure 7.23. The edges of the clamps as well as the radius region introduce high stress levels.

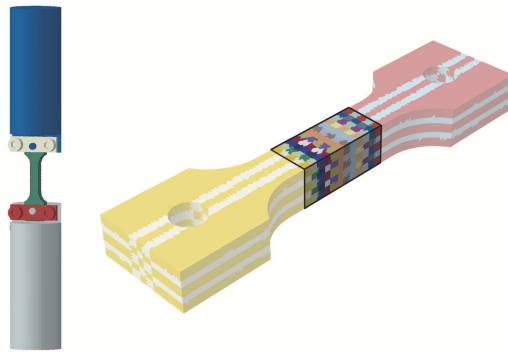


Figure 7.22: Sketch of modelled clamps and specimen (left), sub-regions of specimen that are modelled by RVEs and homogenization (right)

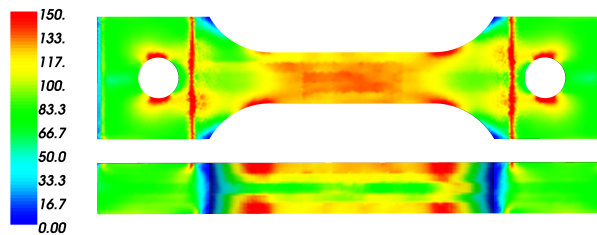


Figure 7.23: Von-Mises stress distribution (MPa) at specimen surface in frontal and lateral view

The interrupted in-situ CT experiment was conducted until final fracture. After the desired force was reached, the position was kept constant while force was dropping due to relaxation effects. The relaxation had also an effect on the elongation at break. Experimentally measured data and corrected strain is shown in Figure 7.24. For the visual evaluation of the FE modelling results a few fibres were selected and taken to generate 3D images. The most important types of defects that could be detected were fibre fracture, fibre pull-out, fibre matrix longitudinal debonding and matrix cracks. Fibre related defects are highlighted in the cross sectional images in Figure 7.25. These four types of defects were defined according to [103].

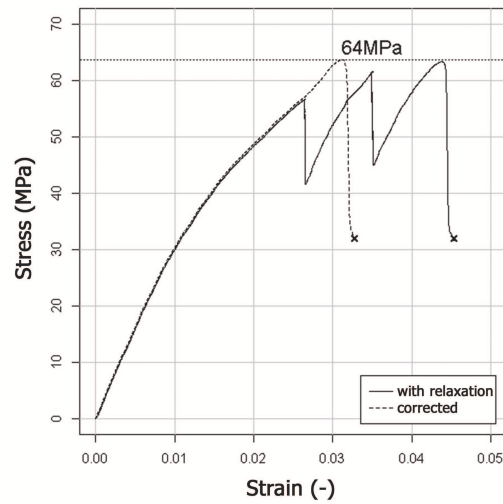


Figure 7.24: Stress-strain curve with interruptions for CT scanning

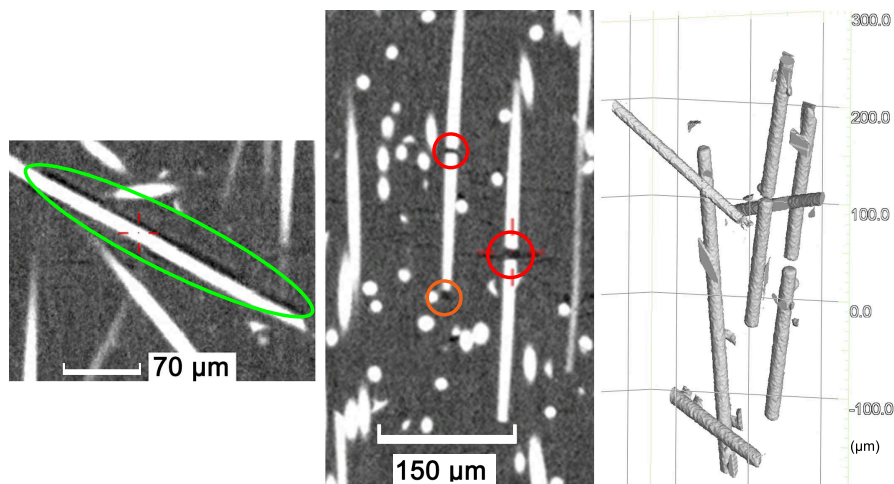


Figure 7.25: CT cross sectional images and 3D rendering of selected fibres with defects at higher load: fibre fracture (ref), fibre pull-out (orange) and fibre-matrix longitudinal debonding (green). The 3D rendered image on the right shows only 6 fibres, all others are hidden for clarity

For the selected seven fibres stress distributions were calculated. Force is applied in vertical direction which leads to high normal stress for vertically aligned and long fibres. Distributions of normal, surface normal and shear stress are shown colour coded in Figure 7.26. Surface normal stress is high at fibre surface of horizontally aligned fibres. At fibre ends shear stress is highest, pointing away from the fibre. Comparing

these stress distributions with the CT image it is obvious that long and well aligned fibres break due to high normal stress whereas fibres aligned perpendicular to loading direction tend to show fibre matrix longitudinal debonding. High shear stress at fibre ends can lead to fibre pull-out which is seen in the cross sectional image in Figure 7.25.

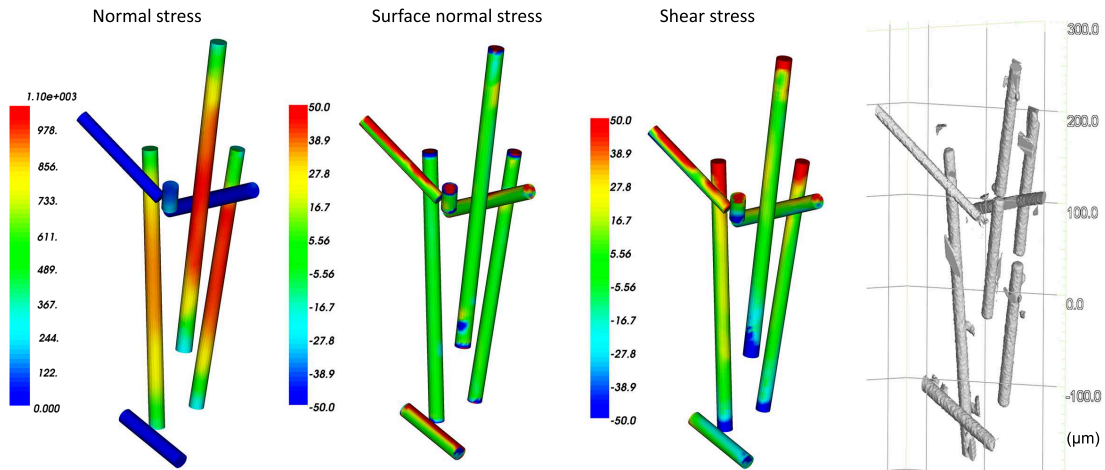
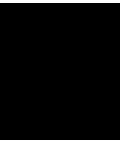


Figure 7.26: Calculated stress levels shown for 7 selected fibres: normal stress in fibre direction, surface normal stress and shear stress at fibre surface. The rendered image at the right shows two fractured fibres



Conclusion

Two software concepts were developed based on published ideas with the goal to characterise every individual fibre accurately. For this purpose CT image quality has to fulfil several needs. Resolution has to be sufficient to be able to separate fibre borders from matrix. Noise level has to be low enough to enable the usage of grey level based algorithms and filters. Artefacts should be minimized, removed or not present at all. Some of the mentioned features can be influenced by the user, some are present inherently.

Both concepts (MAE and TM) are model based concepts since some assumptions for the fibres are made. After the first detailed analyses, the evaluation of these assumptions could be made. It was assumed that the fibres have the same diameter which turned out to be false. Diameter variation is high (Figure 6.15) and leads for both concepts to problems since the representation of thinner fibres is not so good as for thicker fibres. Another assumption was that the fibres are mainly straight which holds true for short fibres with medium fibre content but not for long fibre materials. The parts of the concepts, where novel developments were made, were the separation of medial axes that were falsely connected. For the development of the first concept some representative fibre arrangements were taken into account which were used as model problems to be solved. At the end several other fibre arrangements were found where the approach did not lead to good results. This was especially the case for highly filled materials (>30 wt.%) and long fibre materials. For the development of the second concept these findings were taken into account and the assumptions were updated.

Images presented in chapter 5 show data quality for different fibre composites at different resolutions. Both cross sectional images and histograms indicate that 5 μm Voxel edge length (VS) is not sufficient for quantitative analysis of glass fibres with 12.5 μm diameter (Figures 5.2, 5.1). It is hard to separate fibres by eye and the histogram tends to get very noisy and does not show any peak for glass. For such histograms binarisation algorithms like Otsu would not work properly. Cross sections perpendicular to fibre direction emphasise the said. At 3 μm VS two adjacent fibres can be separated because

grey value between the fibres is only slightly higher than at 1 μm VS (Figures 5.6, 5.7, 5.8). For this material system 2 μm VS leads to ca. 6 Voxel that represent fibre diameter.

The influence of resolution on the quality of fibre characterisation results was investigated by comparisons with standard methods, simulated data and reference data. The final result of the examination of accuracy shown in Figure 6.8 shows the improvement achieved with the second concept. At 1 μm VS all analyses showed the same very high accuracy of $>97\%$. For 2 μm VS only the first concept drops to a value of 94 %. Severe difference were found at 3 μm VS where MAE accuracy drops to 77 % and TM to 88 %. With simulated data, accuracies of 91 % for varying diameters and 95 % for constant diameters were reached. Simulated data with very high data quality and no variation of fibre diameter is the best possible data, therefore 95 % accuracy is the best possible value reachable with the second concept TM. This value will change of course when fibre material, fibre cross sectional shape or fibre content is changed. For the investigated PP-sGF material a resolution of 2 μm VS was chosen as standard value since accuracy is high and analysis volume bigger than with 1 μm VS.

The identification of sources of error shown in Figure 6.5 together with the resulting differences in length compared to the reference (Figure 6.6) lead to the conclusion that fibre splitting is the major cause for differences in length since the average value is smaller for lower accurate results. This information can be used for parameter optimisation since average fibre length could be optimised to the maximum possible. If the only interest of the investigations would be determination of fibre orientation, resolution could be reduced since there was no big change in the orientation tensor values as shown in Figure 6.7.

Comparable with high accuracy also reproducibility was very high, both for FOD and FLD. Since the scans for the reproducibility study were acquired over a period of three years, the result includes, besides software properties, instabilities of the complete CT device.

The comparison of CT analyses with standard, destructive methods showed very good correspondence. The experience of the researcher who did the grinding and LOM analyses for FOD helped to get very good results with the standard method. While statistics and therefore deviations were less for CT analyses, the results of tensor elements over sheet thickness were almost equal. A drawback of the standard method is that only 4 of the 6 unique tensor components can be determined. For FLD pyrolysis results derived from a calibration laboratory were not corresponding with the CT results. Especially the very short fibre fragments were not taken into account for the pyrolysis which lead to higher average length values. Another problem was the very small number of fibres that were analysed compared to CT analyses. A detailed analysis of exactly the same fibres after pyrolysis and with CT revealed some issues for the standard method since it was hard to avoid losing or breaking any fibre. These analyses lead to higher values for CT with deviations of 8 %.

The possibility of determination of FOD and FLD with high accuracy is useful for different applications. If new models for predicting fibre orientation are developed it is

necessary to have valid ground truth. The best possible simulation will take into account FOD, FOD and diameter distribution. For the development of novel materials and the optimization of production parameters the accurate knowledge of micro-structure is useful, too. Optimizing materials and products in terms of light weight and optimized material utilisation is done on a very high level nowadays meaning that the optimization potential is not high. For such high level optimization, highly accurate data is essential.

Standard materials used in industry contain minimal 30 wt.% glass fibres which generates a complex micro-structure. Figure 5.3 gives a clue about increasing complexity. At the moment fibre materials with content up to 60 wt.% are developed and already used for selected parts. For the histogram higher fibre content is good because the fibre peak gets more pronounced. For glass fibre in PP 30 wt.% lead to 13.4 vol.% which means that still the majority of all Voxels represent PP matrix. Cross sectional but also 3D rendered images (Figure 5.4) show the problem of cutting fibres on top and bottom. Also some fibres are cut left and right but these are only a few. The specimen has to be cut always since resolution is depending on specimen size and injection moulded specimens are usually too big for high resolution. The standard resolution of 2 μm VS allows for scanning a volume of 6.5 x 6.5 x 3.8 mm³ at the CT device Nanotom-s with the given specifications using „Virtual Sensor“ mode. This would lead to a data set of 40 GB. With very powerful workstations this data set could be analysed but for this thesis 6 GB was the limit for applying the software concepts. However it was necessary to investigate the influence of cutting fibres in vertical direction. This was done for short and long glass fibre materials since the behaviour was expected to be different. The short fibre material showed stable length values from ca. 3 mm Z dimension while the long fibre material allowed the conclusion of 7.6 mm in Z. Since the very complex micro-structure of long fibre materials which is caused by the presence of fibre bundles, severe fibre bending and big fibre length itself, the influence of sampling volume is much more critical than for short fibres. The problem mentioned in [26] and [28] is still not completely solved by using CT techniques but the determined results indicate that the influence of virtually cut fibres at data edges do not have big influence if above mentioned dimensions are considered. This might be caused by the much higher number of fibres that are analysed and the lower relative fraction thereof.

In Chapter 7 results are discussed where the developed concepts were used to investigate fibre reinforced composite materials.

At the beginning two examples of the injection moulding process of short glass fibres was discussed, the influence of increasing fibre content and processing on micro-structure. For both topics the determination of length distribution is most important because the process itself but also increasing fibre content lead to fibre fracture. For higher filled materials the compounding process has more influence on the final fibre length than the injection process. Orientation distribution is more or less independent from fibre content.

The next example investigated the well known effect of skin-core layered orientation. For this purpose CT analysis brings several advantages because orientation and length

can be determined at once and one can look at the fibre by cross sectional images. The example image Figure 7.5 leads to conclusions about the correlation of FOD and FLD over sheet thickness. The expected shear flow at sheet surface should lead to increased fibre damage and therefore shorter fibres. The opposite effect should take place in the core since the melt flow is a fountain flow leading to lower fibre loading and less damage. These effects can be clearly seen and quantified by applying the developed method. A comprehensive analysis of several positions across half of an injection moulded A5 sheet specimen was conducted. The goal was to characterise micro-structure across the complete specimen. Similar investigations were already presented but without the determination of more than the orientation. Especially the interpolated Figures 7.9 for FOD and 7.10 for FLD give a very good overview about changes in micro-structure.

For long fibre materials the free fibre length after Charpy impact testing was determined. The four materials glass, carbon, PET and PVA showed different fracture surface geometries which could be explained by showing fibre orientation underneath the fracture surface (Figure 7.19). The variation of pellet length showed no significant trend for free fibre length. This is reasonable since free length is only depending on shear strength of matrix, tensile strength of the fibre and fibre diameter. By choosing the proper fibres from all free fibres detected it should be possible to determine the shear strength of the fibre-matrix interface. The question that has to be solved is which fibres should be taken into account. One has to take the orientation and for notched specimens also the position into account.

The last application example shows the usefulness of individual fibre characterisation for modelling. Generation of RVEs allowed to take measured material properties into account and to build up FE meshes of cylinders with measured fibre arrangement. Interrupted tensile tests within the CT device were compared with mechanical simulations of the same specimen. A resolution of 2 μm VS allowed for detecting different types of damage: fibre fracture, fibre pull-out, fibre matrix debonding and matrix cracks. FE simulations helped understanding the reasons why some fibres broke. For some selected fibres the fracture took place at the positions of maximum normal stresses. Fibre pull-out takes place where shear stress at fibre surface is highest which is at the fibre ends.

X-ray computed tomography on laboratory basis can fulfil the needs of comprehensive polymer composite characterisation. Advantages compared to other methods are the very good statistical analysis (>100.000 fibres), the ability to determine 2nd and 4th order orientation tensor completely and the accessibility of features that are difficult to detect otherwise (e.g. free fibre length). Tomography comprises quantification but also imaging which both together can give the big picture of the given task.

Bibliography

- [1] S. Fu, B. Lauke, and Y. Mai, eds., *Science and Engineering of Short Fibre Reinforced Polymer Composites*. Woodhead Publishing Series in Composites Science and Engineering, Woodhead Publishing, 2009.
- [2] K. Meyer, J. Hofmann, and D. Baird, “Prediction of short glass fibre orientation in the filling of an end-gated plaque,” *Composites Part A: Applied Science and Manufacturing*, vol. 62, pp. 77–86, 2014.
- [3] J. L. Thomason, “The influence of fibre length and concentration on the properties of glass fibre reinforced polypropylene: 7. Interface strength and fibre strain in injection moulded long fibre PP at high fibre content,” *Composites Part A: Applied Science and Manufacturing*, vol. 39, pp. 1732–1738, 2008.
- [4] S. Fu, B. Lauke, E. Mäder, C. Yue, and X. Hu, “Tensile properties of short-glass-fiber- and short-carbon-fiber-reinforced polypropylene composites,” *Composites Part A: Applied Science and Manufacturing*, vol. 31, pp. 1117–1125, 2000.
- [5] A. R. Clarke, G. Archenhold, and N. C. Davidson, “A novel technique for determining the 3D spatial distribution of glass fibres in polymer composites,” *Composites Science and Technology*, vol. 55, pp. 75–91, jan 1995.
- [6] C. Eberhardt and A. Clarke, “Fibre-orientation measurements in short-glass-fibre composites. Part I: automated, high-angular-resolution measurement by confocal microscopy,” *Composites Science and Technology*, vol. 61, pp. 1389–1400, aug 2001.
- [7] S. Advani and C. Tucker III, “The use of tensors to describe and predict fiber orientation in short fiber composites,” *Journal of Rheology*, vol. 31, no. 8, pp. 751–784, 1987.
- [8] B. E. Verweyst, C. L. Tucker III, P. H. Foss, and J. F. O. Gara, “Fiber orientation in 3-D injection molded features : prediction and experiment,” *International Polymer Processing*, vol. 14, no. 4, pp. 409–420, 1999.
- [9] ISO 22314:05-2006, *Plastics-Glass-fibre-reinforced products-Determination of fibre length*.

- [10] S. Fu, B. Lauke, and Y. Mai, eds., *Science and Engineering of Short Fibre Reinforced Polymer Composites: 5 - Strength of short fibre reinforced polymers*. Woodhead Publishing Series in Composites Science and Engineering, Woodhead Publishing, 2009.
- [11] M. W. Darlington, P. L. McGinley, and G. R. Smith, "Structure and anisotropy of stiffness in glass fibre-reinforced thermoplastics," *Journal of Materials Science*, vol. 11, pp. 877–886, 05 1976.
- [12] S. Fu, B. Lauke, and Y. Mai, eds., *Science and Engineering of Short Fibre Reinforced Polymer Composites: 3 - Major factors affecting the performance of short fibre reinforced polymers*. Woodhead Publishing Series in Composites Science and Engineering, Woodhead Publishing, 2009.
- [13] M. W. Darlington and P. L. McGinley, "Fibre orientation distribution in short fibre reinforced plastics," *Journal of Materials Science*, vol. 10, pp. 906–910, 1975.
- [14] P. J. Hine, N. Davidson, R. A. Duckett, and I. M. Ward, "Measuring the fibre orientation and modelling the elastic properties of injection-moulded long-glass-fibre-reinforced nylon," *Composites Science and Technology*, vol. 53, pp. 125–131, 1995.
- [15] S. Fakirov and C. Fakirova, "Direct determination of the orientation of short glass fibers in an injection molded poly(ethylene terephthalate) system," *Polymer Composites*, vol. 6, no. 1, pp. 41–46, 1985.
- [16] P. J. Hine, R. A. Duckett, N. Davidson, and A. R. Clarke, "Modelling of the elastic properties of fibre reinforced composites. i: Orientation measurement," *Composites Science and Technology*, vol. 47, no. 1, pp. 65 – 73, 1993.
- [17] B. Mlekusch, "Fibre orientation in short-fibre-reinforced thermoplastics II. Quantitative measurements by image analysis," *Composites Science and Technology*, vol. 59, no. 4, pp. 547–560, 1999.
- [18] K. S. Lee, S. W. Lee, J. R. Youn, T. J. Kang, and K. Chung, "Confocal microscopy measurement of the fiber orientation in short fiber reinforced plastics," *Fibers and polymers*, vol. 2, no. 1, pp. 41–50, 2001.
- [19] J. J. McGrath and J. M. Wille, "Determination of 3d fibre orientation distribution in thermoplastic injection molding," *Composites Science and Technology*, vol. 53, 1995.
- [20] N. C. Davidson, A. R. Clarke, and G. Archenhold, "Large-area, high-resolution image analysis of composite materials," *Journal of Microscopy*, vol. 185, no. 2, pp. 233–242, 1997.

-
- [21] C. Eberhardt, A. Clarke, M. Vincent, T. Giroud, and S. Flouret, "Fibre-orientation measurements in short-glass-fibre composites — II : a quantitative error estimate of the 2D image analysis technique," *Composites Science and Technology*, vol. 61, pp. 1961–1974, 2001.
- [22] A. Clarke and C. Eberhardt, "The representation of reinforcing fibres in composites as 3D space curves," *Composites Science and Technology*, vol. 59, pp. 1227–1237, 1999.
- [23] G. Régnier, D. Dray, E. Jourdain, S. L. Roux, and F. M. Schmidt, "A simplified method to determine the 3d orientation of an injection molded fiber filled polymer," *Polymer Engineering & Science*, vol. 48, no. 11, pp. 2159–2168, 2008.
- [24] G. M. Vélez-García, P. Wapperom, D. G. Baird, A. O. Aning, and V. Kunc, "Unambiguous orientation in short fiber composites over small sampling area in a center-gated disk," *Composites Part A: Applied Science and Manufacturing*, vol. 43, no. 1, pp. 104–113, 2012.
- [25] M. Rohde, A. Ebel, and V. Altstädt, "Injection molding of long fibre reinforced thermoplastic systems: fibre length analysis and impact properties," in *Processings of the Polymer Processing Society 26th Annual Meeting*, 2010.
- [26] S. Goris, T. Back, A. Yanev, D. Brands, D. Drummer, and T. A. Osswald, "A Novel Fiber Length Measurement Technique for Discontinuous Fiber-Reinforced Composites: A Comparative Study with Existing Methods," *Polymer Composites*, vol. 28, pp. 1–13, 2017.
- [27] T. Birr, *Verarbeitung von langglasfaserverstärkten Thermoplasten für Spritzgussanwendungen auf dem Planetwalzenextruder*. PhD thesis, University Berlin, 2015.
- [28] S. Fu, Y. Mai, E. Ching, and R. Li, "Correction of the measurement of fiber length of short fiber reinforced thermoplastics," *Composites Part A: Applied Science and Manufacturing*, vol. 33, pp. 1549–1555, nov 2002.
- [29] G. Zak, M. Haberer, C. B. Park, and B. Benhabib, "Estimation of average fibre length in short- fibre composites by a two-section method," *Composites Science and Technology*, vol. 60, pp. 1763–1772, 2000.
- [30] E. Oestman and S. Persson, "Application of X-Ray Tomography in Non- Destructive Testing of Fibre Reinforced Plastics," *Materials & Design*, vol. 9, no. 3, pp. 142–147, 1988.
- [31] L. Salvo, P. Cloetens, E. Maire, S. Zabler, J. Blandin, J. Buffiere, W. Ludwig, E. Boller, D. Bellet, and C. Jossierond, "X-ray micro-tomography an attractive characterisation technique in materials science," *Nuclear Instruments and Methods in Physics Research Section B: Beam Interactions with Materials and Atoms*, vol. 200, pp. 273–286, jan 2003.

- [32] E. Maire and P. J. Withers, "Quantitative X-ray tomography," *International Materials Reviews*, vol. 59, no. 1, pp. 1–43, 2014.
- [33] S. Stock, "X-ray microtomography of materials," *International Materials Reviews*, vol. 44, no. 4, pp. 141–164, 1999.
- [34] E. N. Landis and D. T. Keane, "X-ray microtomography," *Materials Characterization*, vol. 61, no. 12, pp. 1305–1316, 2010.
- [35] J. P. Kruth, M. Bartscher, S. Carmignato, R. Schmitt, L. De Chiffre, and A. Weckenmann, "Computed tomography for dimensional metrology," *CIRP Annals - Manufacturing Technology*, vol. 60, no. 2, pp. 821–842, 2011.
- [36] K. Schladitz, "Quantitative micro-CT," *Journal of Microscopy*, vol. 243, pp. 111–117, aug 2011.
- [37] T. M. Buzug, ed., *Computed Tomography*. Springer-Verlag Berlin Heidelberg, 1. ed., 2008.
- [38] M. G. R. Sause, ed., *In Situ Monitoring of Fibre-Reinforced Composites*. Springer International Publishing, 1. ed., 2016.
- [39] S. Carmignato, W. Dewulf, and R. Leach, eds., *Industrial X-Ray Computed Tomography*. Springer International Publishing, 1. ed., 2018.
- [40] J. Cazaux, D. Erre, D. Mouze, J. M. Patat, S. Rondot, a. Sasov, P. Trebbia, and a. Zolfaghari, "Recent developments in X-ray projection microscopy and X-ray microtomography applied to materials science," *Le Journal de Physique IV*, vol. 03, no. C7, pp. C7–2099–C7–2104, 1993.
- [41] A. Kantzas and N. Kalogerakis, "Monitoring the fluidization characteristics of polyolefin resins using x-ray Computer Assisted Tomography scanning," *Chemical Engineering Science*, vol. 51, no. 10, pp. 1979–1990, 1996.
- [42] A. Sasov, "Desktop X-ray Micro-CT," in *DGZfP Proceedings of Computerized Tomography for Industrial Applications and Image Processing in Radiology*, pp. 165–168, 1999.
- [43] R. A. Smith, M. J. Paulus, J. M. Branning, and P. J. Phillipss, "X-ray computed tomography on a cellular polysiloxane under compression," *Journal of Cellular Plastics*, vol. 37, no. 3, pp. 231–248, 2001.
- [44] P. Schilling, B. Karedla, a. Tatiparthi, M. Verges, and P. Herrington, "X-ray computed microtomography of internal damage in fiber reinforced polymer matrix composites," *Composites Science and Technology*, vol. 65, pp. 2071–2078, nov 2005.

-
- [45] J. Schell, M. Renggli, G. van Lenthe, R. Müller, and P. Ermanni, “Micro-computed tomography determination of glass fibre reinforced polymer meso-structure,” *Composites Science and Technology*, vol. 66, pp. 2016–2022, 2008.
- [46] F. Awaja, M. Nguyen, S. Zhang, and B. Arhatari, “The investigation of inner structural damage of UV and heat degraded polymer composites using X-ray micro CT,” *Composites Part A: Applied Science and Manufacturing*, vol. 42, pp. 408–418, apr 2011.
- [47] F. Sket, R. Seltzer, J. M. Molina-Aldareguía, C. Gonzalez, and J. Llorca, “Determination of damage micromechanisms and fracture resistance of glass fiber/epoxy cross-ply laminate by means of X-ray computed microtomography,” *Composites Science and Technology*, vol. 72, no. 2, pp. 350–359, 2012.
- [48] Y. Nikishkov, L. Airoldi, and A. Makeev, “Measurement of voids in composites by X-ray Computed Tomography,” *Composites Science and Technology*, vol. 89, pp. 89–97, 2013.
- [49] R. Seltzer, C. González, R. Muñoz, J. Llorca, and T. Blanco-Varela, “X-ray microtomography analysis of the damage micromechanisms in 3D woven composites under low-velocity impact,” *Composites Part A: Applied Science and Manufacturing*, vol. 45, pp. 49–60, 2013.
- [50] T. Le, P. Dumont, L. Orgéas, D. Favier, L. Salvo, and E. Boller, “X-ray phase contrast microtomography for the analysis of the fibrous microstructure of SMC composites,” *Composites Part A: Applied Science and Manufacturing*, vol. 39, pp. 91–103, 2008.
- [51] G. Requena, G. Fiedler, B. Seiser, P. Degischer, M. Dimichiel, and T. Buslaps, “3D-Quantification of the distribution of continuous fibres in unidirectionally reinforced composites,” *Composites Part A: Applied Science and Manufacturing*, vol. 40, pp. 152–163, feb 2009.
- [52] M. W. Czabaj, M. L. Riccio, and W. W. Whitacre, “Numerical reconstruction of graphite/epoxy composite microstructure based on sub-micron resolution X-ray computed tomography,” *Composites Science and Technology*, vol. 105, pp. 174–182, 2014.
- [53] K. Schladitz, A. Büter, M. Godehardt, O. Wirjadi, J. Fleckenstein, T. Gerster, U. Hassler, K. Jaschek, M. Maisl, U. Maisl, S. Mohr, U. Netzelmann, T. Potyra, and M. O. Steinhauser, “Non-destructive characterization of fiber orientation in reinforced SMC as input for simulation based design,” *Composite Structures*, vol. 160, pp. 195–203, 2017.
- [54] R. G. Rinaldi, M. Blacklock, H. Bale, M. R. Begley, and B. N. Cox, “Generating virtual textile composite specimens using statistical data from micro-computed

- tomography: 3D tow representations,” *Journal of the Mechanics and Physics of Solids*, vol. 60, no. 8, pp. 1561–1581, 2012.
- [55] I. Straumit, S. V. Lomov, and M. Wevers, “Quantification of the internal structure and automatic generation of voxel models of textile composites from X-ray computed tomography data,” *Composites Part A: Applied Science and Manufacturing*, vol. 69, pp. 150–158, 2015.
- [56] P. Wright, X. Fu, I. Sinclair, and S. M. Spearing, “Ultra high resolution computed tomography of damage in notched carbon fiber-epoxy composites,” *Journal of Composite Materials*, vol. 42, no. 19, pp. 1993–2002, 2008.
- [57] A. E. Scott, M. Mavrogordato, P. Wright, I. Sinclair, and S. M. Spearing, “In situ fibre fracture measurement in carbon-epoxy laminates using high resolution computed tomography,” *Composites Science and Technology*, vol. 71, no. 12, pp. 1471–1477, 2011.
- [58] Y. Swolfs, H. Morton, A. E. Scott, L. Gorbatikh, P. A. S. Reed, I. Sinclair, S. M. Spearing, and I. Verpoest, “Synchrotron radiation computed tomography for experimental validation of a tensile strength model for unidirectional fibre-reinforced composites,” *Composites Part A: Applied Science and Manufacturing*, vol. 77, pp. 106–113, 2015.
- [59] K. M. Jespersen, J. Zangenberg, T. Lowe, P. J. Withers, and L. P. Mikkelsen, “Fatigue damage assessment of uni-directional non-crimp fabric reinforced polyester composite using X-ray computed tomography,” *Composites Science and Technology*, vol. 136, pp. 94–103, 2016.
- [60] B. Yu, R. Blanc, C. Soutis, and P. J. Withers, “Evolution of damage during the fatigue of 3D woven glass-fibre reinforced composites subjected to tension-tension loading observed by time-lapse X-ray tomography,” *Composites Part A: Applied Science and Manufacturing*, vol. 82, pp. 279–290, 2016.
- [61] E. Rosenberg, N. Brusselle-Dupend, and T. Epsztein, “A mesoscale quantification method of cavitation in semicrystalline polymers using X-ray microtomography,” *Materials Science and Engineering: A*, vol. 528, pp. 6535–6544, aug 2011.
- [62] L. Laiarinandrasana, T. F. Morgeneyer, H. Proudhon, and C. Regrain, “Damage of semicrystalline polyamide 6 assessed by 3D X-ray tomography: From microstructural evolution to constitutive modeling,” *Journal of Polymer Science Part B: Polymer Physics*, vol. 48, pp. 1516–1525, may 2010.
- [63] L. Laiarinandrasana, T. F. Morgeneyer, H. Proudhon, F. N’guyen, and E. Maire, “Effect of Multiaxial Stress State on Morphology and Spatial Distribution of Voids in Deformed Semicrystalline Polymer Assessed by X-ray Tomography,” *Macromolecules*, vol. 45, pp. 4658–4668, jun 2012.

-
- [64] V. Le Saux, Y. Marco, S. Calloch, and P. Charrier, "Evaluation of the fatigue defect population in an elastomer using X-ray computed micro-tomography," *Polymer Engineering & Science*, vol. 51, no. 7, pp. 1253–1263, 2011.
- [65] J. P. James, H. W. Choi, and J. G. Pharoah, "X-ray computed tomography reconstruction and analysis of polymer electrolyte membrane fuel cell porous transport layers," *International Journal of Hydrogen Energy*, vol. 37, no. 23, pp. 18216–18230, 2012.
- [66] D. Tsarouchas and A. Markaki, "Extraction of fibre network architecture by X-ray tomography and prediction of elastic properties using an affine analytical model," *Acta Materialia*, vol. 59, pp. 6989–7002, oct 2011.
- [67] M. De Monte, E. Moosbrugger, and M. Quaresimin, "Influence of temperature and thickness on the off-axis behaviour of short glass fibre reinforced polyamide 6.6 - Cyclic loading," *Composites Part A: Applied Science and Manufacturing*, vol. 41, no. 10, pp. 1368–1379, 2010.
- [68] S. A. Young, "High resolution x-ray tomography of fiber reinforced polymeric composites," Master's thesis, University of Tennessee, Knoxville, US, 2009.
- [69] X. Sun, J. Lasecki, D. Zeng, Y. Gan, X. Su, and J. Tao, "Measurement and quantitative analysis of fiber orientation distribution in long fiber reinforced part by injection molding," *Polymer Testing*, vol. 42, pp. 168–174, 2015.
- [70] T. B. Nguyen Thi, M. Morioka, A. Yokoyama, S. Hamanaka, K. Yamashita, and C. Nonomura, "Measurement of fiber orientation distribution in injection-molded short-glass-fiber composites using X-ray computed tomography," *Journal of Materials Processing Technology*, vol. 219, pp. 1–9, 2015.
- [71] A. Bernasconi, F. Cosmi, and D. Dreossi, "Local anisotropy analysis of injection moulded fibre reinforced polymer composites," *Composites Science and Technology*, vol. 68, pp. 2574–2581, sep 2008.
- [72] F. Cosmi, a. Bernasconi, and N. Sodini, "Phase contrast micro-tomography and morphological analysis of a short carbon fibre reinforced polyamide," *Composites Science and Technology*, vol. 71, pp. 23–30, jan 2011.
- [73] A. Bernasconi, F. Cosmi, and P. Hine, "Analysis of fibre orientation distribution in short fibre reinforced polymers: A comparison between optical and tomographic methods," *Composites Science and Technology*, vol. 72, pp. 2002–2008, nov 2012.
- [74] A. Miettinen, L. H., C. L., G. Chinga-Carrasco, E. K. Gamstedt, and M. Kataja, "A non-destructive X-ray microtomography approach for measuring fibre length in short-fibre composites," *Composites Science and Technology*, vol. 72, no. 15, pp. 1901–1908, 2012.

- [75] E. Di Giuseppe, R. Castellani, S. Dobosz, J. Malvestio, F. Berzin, J. Beaugrand, C. Delisée, B. Vergnes, and T. Budtova, “Reliability evaluation of automated analysis, 2D scanner, and micro-tomography methods for measuring fiber dimensions in polymer-lignocellulosic fiber composites,” *Composites Part A: Applied Science and Manufacturing*, vol. 90, pp. 320–329, 2016.
- [76] P. Pinter, S. Dietrich, B. Bertram, L. Kehrer, P. Elsner, and K. A. Weidenmann, “Comparison and error estimation of 3D fibre orientation analysis of computed tomography image data for fibre reinforced composites,” *NDT and E International*, vol. 95, no. January, pp. 26–35, 2018.
- [77] C. N. Eberhardt and A. R. Clarke, “Automated reconstruction of curvilinear fibres from 3D datasets acquired by X-ray microtomography,” *Journal of Microscopy*, vol. 206, no. 1, pp. 41–53, 2002.
- [78] H. Shen, S. Nutt, and D. Hull, “Direct observation and measurement of fiber architecture in short fiber-polymer composite foam through micro-CT imaging,” *Composites Science and Technology*, vol. 64, pp. 2113–2120, oct 2004.
- [79] M. Teßmann, S. Mohr, S. Gayetskyy, U. Haßler, R. Hanke, and G. Greiner, “Automatic Determination of Fiber-Length Distribution in Composite Material Using 3D CT Data,” *EURASIP Journal on Advances in Signal Processing*, vol. 2010, no. 1, p. 545030, 2010.
- [80] D. Salaberger, K. A. Kannappan, J. Kastner, J. Reussner, and T. Auinger, “Evaluation of Computed Tomography Data from Fibre Reinforced Polymers to Determine Fibre Length Distribution,” *International Polymer Processing*, vol. XXVI, no. 3, pp. 283–291, 2011.
- [81] B. Plank, “Vom Granulat zum Spritzgussbauteil: Einfluss der Spritzgussprozesskette auf die Faserlängenverteilung bestimmt durch Röntgen- Computer-Tomografie,” Master’s thesis, University of Applied Sciences Upper Austria, Campus Wels, 2012.
- [82] T. Köpplmayr, I. Milosavljevic, M. Aigner, R. Hasslacher, B. Plank, D. Salaberger, and J. Miethlinger, “Influence of fiber orientation and length distribution on the rheological characterization of glass- fiber- filled polypropylene,” *Polymer Testing*, vol. 32, pp. 535–544, 2013.
- [83] R. Glöckner, C. Heiliger, and S. Kolling, “A Monte-Carlo algorithm for 3D fibre detection from microcomputer-tomography,” *Composites Science and Technology*, vol. 2016, 2016.
- [84] A. Ayadi, H. Nouri, S. Guessasma, and F. Roger, “Determination of orthotropic properties of glass fibre reinforced thermoplastics using X-ray tomography and multiscale finite element computation,” *Composite Structures*, vol. 136, pp. 635–649, 2016.

- [85] A. Miettinen, A. Ojala, L. Wikström, R. Joffe, B. Madsen, K. Nättinen, and M. Kataja, “Non-destructive automatic determination of aspect ratio and cross-sectional properties of fibres,” *Composites Part A: Applied Science and Manufacturing*, vol. 77, pp. 188–194, 2015.
- [86] A. F. Frangi, W. J. Niessen, K. L. Vincken, and M. A. Viergever, “Multiscale vessel enhancement filtering,” *Lecture Notes in Computer Science*, vol. 1496, pp. 130–137, 1998.
- [87] T. Müller, V. and Böhlke, “Prediction of effective elastic properties of fiber reinforced composites using fiber orientation tensors,” *Composites Science and Technology*, vol. 130, pp. 36–45, 2016.
- [88] “photon cross section data.”
- [89] DIN EN ISO 527-2:06-2012, *Kunststoffe – Bestimmung der Zugeigenschaften – Teil 2: Prüfbedingungen für Form- und Extrusionsmassen*, 06-2012.
- [90] ISO 179-1:06-2010, *Plastics – Determination of Charpy impact properties – Part 1: Non-instrumented impact test*, 06-2010.
- [91] Hamamatsu datasheet, *Flat panel sensor, C7942SK-05, Hamamatsu, Japan*.
- [92] phoenix|x-ray, GE Sensing & Inspection Technologies, *xs|control Version 1.9, Betriebsanleitung*, 2011.
- [93] L. Feldkamp, D. L.C., and K. J.W., “Practical cone-beam algorithm,” *Journal of the Optical Society of America A*, vol. 1, pp. 612–619, 1984.
- [94] L. De Chiffre, S. Carmignato, J.-P. Kruth, R. Schmitt, and A. Weckenmann, “Industrial applications of computed tomography,” *CIRP Annals - Manufacturing Technology*, vol. 63, no. 2, pp. 655–677, 2014.
- [95] N. Otsu, “A threshold selection method from gray-level histograms,” *IEEE Transactions on Systems, Man, and Cybernetics*, vol. 9, no. 1, pp. 62–66, 1979.
- [96] doxygen 1.8.5, *ITK:NormalizedCorrelationImageFilter*. ITK 5.0.0, 2018, (accessed 20.07.2018). https://itk.org/Doxygen/html/classitk_1_1NormalizedCorrelationImageFilter.html.
- [97] doxygen 1.8.5, *ITK:BinaryThinning*. ITK 5.0.0, 2018, (accessed 20.07.2018). https://itk.org/Doxygen/html/classitk_1_1BinaryThinningImageFilter.html.
- [98] P. Kollmannsberger, *Matlab:Skeleton3D*. MathWorks, 2018, (accessed 20.07.2018). <https://www.mathworks.com/matlabcentral/fileexchange/43400-skeleton3d>.
- [99] M. Reiter, M. Erler, C. Kuhn, C. Gusenbauer, and J. Kastner, “SimCT: a simulation tool for X-ray imaging,” in *Proceedings of iCT2016, 6th Conference on Industrial Computed Tomography*, (Wels, Austria), February 2016.

- [100] S. Gleiss, “Analyse der Faserlängenverteilung von kurzglasfaserverstärktem Polypropylen: Ein Methodenvergleich,” Master’s thesis, University of Applied Sciences Upper Austria, Campus Wels, 2013.
- [101] G. Huysmans, I. Verpoest, and P. Van Houtte, “A poly-inclusion approach for the elastic modelling of knitted fabric composites,” *Acta Materialia*, vol. 46, no. 9, pp. 3003–3013, 1998.
- [102] S. Oberpeilsteiner, “Mikromechanische Modellierung kurzfaserverstärkter Materialien mittels CT-basierender RVEs,” Master’s thesis, University of Applied Sciences Upper Austria, Campus Wels, 2013.
- [103] K. Friedrich, ed., *Composite Materials Series, 6: Application of Fracture Mechanics to Composite Materials*. Elsevier, Science Publishers B.V., 1. ed., 1989.

Curriculum Vitae

Name: Dipl. Ing. Dietmar Salaberger
Date of birth: 14.07.1976
Place of birth: Linz, Austria
Marital status: Married
Address: Apfelstrasse 5, 4621 Sipbachzell, Austria

Education:

Diploma in Electrical Engineering / Biomedical Engineering at TU Graz, Austria (2003)

Professional experience:

Research assistant NDT/CT at University of Applied Sciences Upper Austria (2004-2008)

Research project manager NDT/CT of polymer materials at University of Applied Sciences Upper Austria (2008-2018)

Senior Engineer Physical Characterisation at Borealis Polyolefine GmbH (2018 - dato)

List of publications:

- [1] D. Salaberger, K. A. Kannappan, J. Kastner, J. Reussner, and T. Auinger, „Evaluation of Computed Tomography Data from Fibre Reinforced Polymers to Determine Fibre Length Distribution“, *International Polymer Processing*, vol. XXVI, no. 3, pp. 283-291, 2011.
- [2] T. Köpplmayr, I. Milosavljevic, M. Aigner, R. Hasslacher, B. Plank, D. Salaberger, and J. Miethlinger, „Influence of fiber orientation and length distribution on the rheological characterization of glass fiber filled polypropylene“, *Polymer Testing*, vol. 32, pp. 535-544, 2013.
- [3] J. K. Jørgensen, E. Andreassen, and D. Salaberger, „The effect of fiber concentration on fiber orientation in injection molded film gated rectangular plates“, *Polymer Composites*, 2017.
- [4] D. Salaberger, K. A. Kannappan, J. Kastner, J. Reussner, and T. Auinger, „CT data evaluation of fibre reinforced polymers to determine fibre length distribution“

- in Proceedings of PPS26, Polymer Processing Society, (Banff, Canada, Canada), 2010.
- [5] M. Jerabek, M. Reiter, H. Herbst, B. Plank, D. Salaberger, and Z. Major, „Characterization of short fiber reinforced polypropylene composites“, in Proceedings of iCT2012, 4th Conference on Industrial Computed Tomography, (Wels, Austria), pp. 55-58, 2012.
- [6] M. Aigner and D. Salaberger, „The influence of glass fibres on the longational viscosity studied by means of optical coherence tomography and X-ray computed tomography“, in Proceedings of PPS29, Polymer Processing Society, (Nuremberg, Germany), 2013.
- [7] D. Salaberger, S. Gleiss, and J. Kastner, „Comparison of methods to determine fibre length distribution: X-ray CT versus standard method“, in Proceedings of ICSAAM2013, International Conference on Structural Analysis of Advanced Materials, (Kos, Greece), 2013.
- [8] S. Oberpeilsteiner, T. Reiter, and D. Salaberger, „Coupling of in-situ-CT with virtual testing by FEM of short fiber reinforced materials“, in Proceedings of iCT2014, 5th Conference on Industrial Computed Tomography, (Wels, Austria), p. 7, 2014
- [9] M. Jerabek, D. Salaberger, M. Reiter, and Z. Major, „Prediction of fiber orientation in short glass fiber polypropylene composites and the consequences for micromechanical simulations“, in Proceedings of ECCM 17, European Conference on Composite Materials, (Sevilla, Spain), p. 1, 2014.
- [10] D. Salaberger, M. Jerabek, T. Koch, and J. Kastner, „Consideration of accuracy of quantitative X-ray CT analyses for short-glass-fibre-reinforced polymers“, Materials Science Forum, vol. 825, pp. 907-913, 2015.
- [11] H. Zauner, J. Kastner, D. Salaberger, and C. Heinzl, „3D image processing for single fibre characterization by means of XCT“, Acta Stereologica, vol. 1, 2015.
- [12] D. Salaberger, P. Hine, M. Jerabek, and J. Kastner, „Assessment of accuracy of fibre orientation measurement using X-ray computed tomography“, in Proceedings of the 20th International Conference on Composite Materials, (Copenhagen, Denmark), p. 8, 2015.
- [13] S. Kleindel and D. Salaberger and R. Eder and H. Schretter and C. Hochenauer, „Measurement and Numerical Simulation of Void and Warpage in Glass Fiber Reinforced Molded Chunky Parts“, International Polymer Processing, vol.XXX, no. 1, pp 100-112, 2015
- [14] S. Kleindel and D. Salaberger and R. Eder and H. Schretter and C. Hochenauer, „Prediction and Validation of Short Fiber Orientation in a Complex Injection Molded Part with Chunky Geometry“, International Polymer Processing, vol.XXX, no. 3, pp 366-380, 2015

- [15] G. Gsellmann, M. Jerabek, and D. Salaberger, „Comparison of predicted and measured fiber orientations in injection molded parts“, in Proceedings of iCT2016, 6th Conference on Industrial Computed Tomography, (Wels, Austria), 2016.
- [16] D. Salaberger, T.Lummerstorfer, M. Jerabek, and J. Kastner, „Single fibre characterisation of heavily curved polymer fibres using X-ray computed tomography“, in Proceedings of ECCM18 - 18th European Conference on Composite Materials, (Athens, Greece), 2018.

List of supervised diploma/master thesis:

- B. Plank, „Vom Granulat zum Spritzgussbauteil: Einfluss der Spritzgussprozesskette auf die Faserlängenverteilung bestimmt durch Röntgen- Computer-Tomografie“, Master’s thesis, University of Applied Sciences Upper Austria, Campus Wels, 2012
- S. Gleiss, „Analyse der Faserlängenverteilung von kurzglasfaserverstärktem Polypropylen: Ein Methodenvergleich“, Master’s thesis, University of Applied Sciences Upper Austria, Campus Wels, 2013
- S. Oberpeilsteiner, „Mikromechanische Modellierung kurzfaserverstärkter Materialien mittels CT-basierender RVEs“, Diploma thesis, University of Applied Sciences Upper Austria, Campus Wels, 2013.

Appendix A

The Tables in this chapter show average length values and the determined values for length correction for every cut-out, every software method and every Voxel edge length separately. For every cut-out the results are shown in the order: MAE (scan), TM (scan), TM (simulation). The definition of correct fibres is that no virtual breakage, wrong connection or too short fibre ends were found.

One can recognize the smallest deviation from desired value at highest resolution. Differences at the same Voxel edge length between the three cut-outs result from the relatively small number of fibres per data set which promotes statistical differences. The difference of measured and reference average lengths for all fibres is partly smaller than taking only correct fibres into account. This can be caused because of a higher number of wrong connection of fibre segments.

Table A1: Average lengths and length correction values for cut-out *Centre_1* at different Voxel edge length for scans analysed with concept MAE with comparison to reference input values

| Parameter | Scan 1 μm | | Scan 2 μm | | Scan 3 μm | |
|--|----------------------|------|----------------------|-------|----------------------|-------|
| | Input | MAE | Input | MAE | Input | MAE |
| Fibre count | 237 | 237 | 237 | 240 | 237 | 259 |
| Average length (μm) | 202 | 194 | 202 | 189 | 202 | 168 |
| Δ (μm) | | -7.9 | | -12.5 | | -33.4 |
| Fibre count correct | 233 | 233 | 218 | 218 | 185 | 185 |
| Average length only correct fibres (μm) | 202 | 194 | 201 | 192 | 193 | 182 |
| Length correction (μm) | | 7.7 | | 9.0 | | 11.6 |

Table A2: Average lengths and length correction values for cut-out *Centre_1* at different Voxel edge length for scans analysed with concept TM with comparison to reference input values

| Parameter | Scan 1 μm | | Scan 2 μm | | Scan 3 μm | |
|---|----------------------|-------|----------------------|------|----------------------|-------|
| | Input | TM | Input | TM | Input | TM |
| Fibre count | 279 | 274 | 279 | 267 | 279 | 262 |
| Average length (μm) | 202 | 192 | 202 | 192 | 202 | 192 |
| Δ (μm) | | -10.1 | | -9.5 | | -10.4 |
| Fibre count correct | 249 | 249 | 230 | 230 | 199 | 199 |
| Average length only correct fibre (μm) | 206 | 196 | 207 | 196 | 204 | 192 |
| Length correction (μm) | | 9.7 | | 10.6 | | 11.9 |

Table A3: Average lengths and length correction values for cut-out *Centre_1* at different Voxel edge length for simulations analysed with concept TM with comparison to reference input values

| Parameter | SIM 1 μm | | SIM 2 μm | | SIM 3 μm | |
|---|---------------------|--------|---------------------|--------|---------------------|--------|
| | Input | TM-SIM | Input | TM-SIM | Input | TM-SIM |
| Fibre count | 279 | 269 | 279 | 270 | 279 | 279 |
| Average length (μm) | 202 | 195 | 202 | 198 | 202 | 187 |
| Δ (μm) | | -7.4 | | -4.3 | | -14.5 |
| Fibre count correct | 261 | 261 | 267 | 267 | 242 | 242 |
| Average length only correct fibre (μm) | 207.3 | 196 | 206 | 196 | 200 | 189 |
| Length correction (μm) | | 11.3 | | 9.8 | | 11.4 |

Table A4: Average lengths and length correction values for cut-out *Centre_2* at different Voxel edge length for scans analysed with concept MAE with comparison to reference input values

| Parameter | Scan 1 μm | | Scan 2 μm | | Scan 3 μm | |
|--|----------------------|------|----------------------|------|----------------------|------|
| | Input | MAE | Input | MAE | Input | MAE |
| Fibre count | 232 | 226 | 232 | 223 | 232 | 229 |
| Average length (μm) | 192 | 189 | 192 | 189 | 192 | 176 |
| Δ (μm) | | -1.7 | | -1.7 | | -8.3 |
| Fibre count correct | 225 | 225 | 220 | 220 | 177 | 177 |
| Average length only correct fibres (μm) | 196 | 189 | 196 | 187 | 191 | 181 |
| Length correction (μm) | | 7.3 | | 9.3 | | 10.0 |

Table A5: Average lengths and length correction values for cut-out *Centre_2* at different Voxel edge length for scans analysed with concept TM with comparison to reference input values

| Parameter | Scan 1 μm | | Scan 2 μm | | Scan 3 μm | |
|---|----------------------|------|----------------------|-------|----------------------|-------|
| | Input | TM | Input | TM | Input | TM |
| Fibre count | 276 | 267 | 237 | 262 | 237 | 259 |
| Average length (μm) | 194 | 187 | 202 | 186 | 202 | 181 |
| Δ (μm) | | -6.3 | | -15.3 | | -20.8 |
| Fibre count correct | 237 | 237 | 217 | 217 | 180 | 180 |
| Average length only correct fibre (μm) | 202 | 193 | 200 | 189 | 201 | 189 |
| Length correction (μm) | | 9.3 | | 10.7 | | 11.6 |

Table A6: Average lengths and length correction values for cut-out *Centre_2* at different Voxel edge length for simulations analysed with concept TM with comparison to reference input values

| Parameter | SIM 1 μm | | SIM 2 μm | | SIM 3 μm | |
|---|---------------------|--------|---------------------|--------|---------------------|--------|
| | Input | TM-SIM | Input | TM-SIM | Input | TM-SIM |
| Fibre count | 276 | 261 | 276 | 260 | 276 | 263 |
| Average length (μm) | 194 | 191 | 194 | 192 | 194 | 184 |
| Δ (μm) | | -2.2 | | -1.2 | | -9.7 |
| Fibre count correct | 258 | 258 | 258 | 258 | 240 | 240 |
| Average length only correct fibre (μm) | 203 | 192 | 201 | 191 | 201 | 189 |
| Length correction (μm) | | 11.3 | | 9.7 | | 11.3 |

Table A7: Average lengths and length correction values for cut-out *Edge* at different Voxel edge length for scans analysed with concept MAE with comparison to reference input values

| Parameter | Scan 1 μm | | Scan 2 μm | | Scan 3 μm | |
|--|----------------------|------|----------------------|-------|----------------------|-------|
| | Input | MAE | Input | MAE | Input | MAE |
| Fibre count | 223 | 217 | 223 | 222 | 223 | 235 |
| Average length (μm) | 192 | 188 | 192 | 181 | 192 | 166 |
| Δ (μm) | | -4.3 | | -11.3 | | -25.5 |
| Fibre count correct | 215 | 215 | 211 | 211 | 166 | 166 |
| Average length only correct fibres (μm) | 196 | 187 | 191 | 181 | 187 | 176 |
| Length correction (μm) | | 8.7 | | 10.1 | | 10.9 |

Table A8: Average lengths and length correction values for cut-out *Edge* at different Voxel edge length for scans analysed with concept TM with comparison to reference input values

| Parameter | Scan 1 μm | | Scan 2 μm | | Scan 3 μm | |
|---|----------------------|------|----------------------|------|----------------------|-------|
| | Input | TM | Input | TM | Input | TM |
| Fibre count | 250 | 246 | 250 | 244 | 250 | 249 |
| Average length (μm) | 197 | 196 | 197 | 192 | 197 | 183 |
| Δ (μm) | | -1.5 | | -5.1 | | -14.2 |
| Fibre count correct | 212 | 212 | 207 | 207 | 171 | 171 |
| Average length only correct fibre (μm) | 202 | 191 | 202 | 189 | 200 | 187 |
| Length correction (μm) | | 10.7 | | 12.1 | | 12.7 |

Table A9: Average lengths and length correction values for cut-out *Edge* at different Voxel edge length for simulations analysed with concept TM with comparison to reference input values

| Parameter | SIM 1 μm | | SIM 2 μm | | SIM 3 μm | |
|---|---------------------|--------|---------------------|--------|---------------------|--------|
| | Input | TM-SIM | Input | TM-SIM | Input | TM-SIM |
| Fibre count | 250 | 238 | 250 | 238 | 250 | 249 |
| Average length (μm) | 197 | 194 | 197 | 192 | 197 | 181 |
| $ \Delta $ (μm) | | -3.6 | | -5.1 | | -15.7 |
| Fibre count correct | 232 | 232 | 229 | 229 | 213 | 213 |
| Average length only correct fibre (μm) | 204 | 193 | 201 | 191 | 197 | 185 |
| Length correction (μm) | | -11.1 | | -9.8 | | -12.0 |

Appendix B

This chapter contains tables with detailed results for the cut-outs. Each table shows results for one fibre characterisation approach.

Table B1: Average values of three scanned data sets at different Voxel edge length - MAE approach

| Parameter | Input | MAE Scan 1 μm | MAE Scan 2 μm | MAE Scan 3 μm |
|--|-------|-----------------------------|-----------------------------|-----------------------------|
| Fibre count | 230.7 | 226.7 | 227.7 | 241.0 |
| Average length (μm) | 195 | 194 | 194 | 178 |
| Δ (μm) | | -0.8 | -1.7 | -16.9 |
| Δ (%) | | -0.4 | -0.9 | -8.6 |
| Weighted average length (μm) | 268 | 266 | 265 | 255 |
| Δ (μm) | | -1.7 | -2.6 | -13.2 |
| Δ (%) | | -0.6 | -1.0 | -4.9 |
| a_{XX} | 0.130 | 0.127 | 0.127 | 0.130 |
| a_{YY} | 0.009 | 0.008 | 0.009 | 0.011 |
| a_{ZZ} | 0.861 | 0.865 | 0.864 | 0.859 |
| a_{XY} | 0.001 | -0.001 | -0.001 | -0.003 |
| a_{XZ} | 0.010 | -0.071 | -0.067 | -0.064 |
| a_{YZ} | 0.030 | 0.031 | 0.034 | 0.031 |
| Strength of orientation | 0.80 | 0.81 | 0.81 | 0.80 |
| Average diameter (μm) | 12.5 | 12.7 | 12.2 | 12.5 |
| Correct fibre count | 230.7 | 224.3 | 216.0 | 177.3 |
| Accuracy (Extracted fibres) (%) | | 99.0 | 95.0 | 73.7 |
| (Input cylinders) (%) | | 97.2 | 93.7 | 76.9 |
| Separated | | 0.3 | 5.0 | 31.0 |
| Wrong connected | | 2.3 | 4.7 | 14.0 |
| Other problems | | 3.7 | 5.0 | 8.3 |
| \sum wrong fibres | | 6.3 | 14.7 | 53.3 |

Table B2: Average values of three scanned data sets at different Voxel edge length - TM approach

| Parameter | Input | TM Scan 1 μm | TM Scan 2 μm | TM Scan 3 μm |
|--|--------|----------------------------|----------------------------|----------------------------|
| Fibre count | 243.0 | 240.3 | 242.3 | 241.7 |
| Average length (μm) | 195 | 194 | 192 | 188 |
| Δ (μm) | | -2.6 | -4.3 | -8.5 |
| Δ (%) | | -1.3 | -2.2 | -4.3 |
| Weighted average length (μm) | 268 | 268 | 266 | 262 |
| Δ (μm) | | -0.9 | -2.3 | -6.0 |
| Δ (%) | | -0.3 | -0.9 | -2.2 |
| a_{XX} | 0.136 | 0.132 | 0.134 | 0.131 |
| a_{YY} | 0.009 | 0.008 | 0.009 | 0.008 |
| a_{ZZ} | 0.855 | 0.860 | 0.857 | 0.860 |
| a_{XY} | -0.002 | -0.001 | -0.001 | -0.001 |
| a_{XZ} | -0.073 | -0.069 | -0.073 | -0.069 |
| a_{YZ} | 0.030 | 0.031 | 0.030 | 0.030 |
| Strength of orientation | 0.86 | 0.90 | 0.90 | 0.90 |
| Average diameter (μm) | 12.5 | 12.4 | 12.2 | 12.5 |
| Correct fibre count | 243.0 | 236.3 | 236.7 | 212.7 |
| Accuracy (Extracted fibres) (%) | | 98.3 | 97.7 | 88.0 |
| (Input cylinders) (%) | | 97.2 | 97.4 | 87.5 |
| Separated | | 1.7 | 2.3 | 16.3 |
| Wrong connected | | 1.7 | 2.0 | 9.0 |
| Other problems | | 3.3 | 2.0 | 5.0 |
| \sum wrong fibres | | 6.7 | 6.3 | 30.3 |

Table B3: Average values of three simulated data sets at different Voxel edge length - TM approach

| Parameter | Input | TM SIM 1 μm | TM SIM 2 μm | TM SIM 3 μm |
|--|--------|---------------------------|---------------------------|---------------------------|
| Fibre count | 243.0 | 243.0 | 240.0 | 251.3 |
| Average length (μm) | 195 | 194 | 195 | 185 |
| Δ (μm) | | -1.0 | 0.2 | -10.0 |
| Δ (%) | | -0.5 | 0.1 | -5.1 |
| Weighted average length (μm) | 268 | 267 | 268 | 258 |
| Δ (μm) | | -1.2 | -0.8 | -10.4 |
| Δ (%) | | -0.4 | -0.3 | -3.9 |
| a_{XX} | 0.136 | 0.136 | 0.135 | 0.133 |
| a_{YY} | 0.009 | 0.009 | 0.008 | 0.011 |
| a_{ZZ} | 0.855 | 0.855 | 0.857 | 0.858 |
| a_{XY} | -0.002 | -0.002 | -0.002 | -0.003 |
| a_{XZ} | -0.073 | -0.072 | -0.071 | -0.078 |
| a_{YZ} | 0.030 | 0.028 | 0.029 | 0.031 |
| Strength of orientation | 0.86 | 0.90 | 0.90 | 0.90 |
| Average diameter (μm) | 12.5 | 12.7 | 12.5 | 12.3 |
| Correct fibre count | 243.0 | 238.0 | 236.3 | 221.3 |
| Accuracy (Extracted fibres) (%) | | 98.0 | 98.4 | 88.1 |
| (Input cylinders) (%) | | 98.0 | 97.2 | 91.1 |
| Separated | | 2.0 | 0.7 | 14.0 |
| Wrong connected | | 2.7 | 4.7 | 5.7 |
| Other problems | | 0.3 | 1.3 | 2.0 |
| \sum wrong fibres | | 5.0 | 6.7 | 21.7 |

Table B4: Average values of three simulated data sets at different Voxel edge length - TM approach, constant diameter (SIM-CD)

| Parameter | Input | TM SIM-CD 1 μm | TM SIM-CD 2 μm | TM SIM-CD 3 μm |
|--|--------|------------------------------|------------------------------|------------------------------|
| Fibre count | 243.0 | 241.3 | 240.7 | 239.7 |
| Average length (μm) | 195 | 194 | 195 | 194 |
| Δ (μm) | | -0.8 | -0.7 | -0.9 |
| Δ (%) | | -0.4 | -0.4 | -0.4 |
| Weighted average length (μm) | 268 | 268 | 267 | 267 |
| Δ (μm) | | -0.6 | -1.7 | -1.5 |
| Δ (%) | | -0.2 | -0.7 | -0.5 |
| a_{XX} | 0.136 | 0.136 | 0.136 | 0.137 |
| a_{YY} | 0.009 | 0.008 | 0.009 | 0.009 |
| a_{ZZ} | 0.855 | 0.855 | 0.856 | 0.854 |
| a_{XY} | -0.002 | -0.002 | -0.002 | -0.002 |
| a_{XZ} | -0.073 | -0.072 | -0.073 | -0.074 |
| a_{YZ} | 0.030 | 0.029 | 0.031 | 0.029 |
| Strength of orientation | 0.86 | 0.9 | 0.9 | 0.9 |
| Average diameter (μm) | 12.5 | 11.8 | 11.4 | 11.3 |
| Correct fibre count | 243.0 | 238.3 | 237.0 | 230.7 |
| Accuracy (Extracted fibres) (%) | | 98.7 | 98.5 | 96.3 |
| (Input cylinders) (%) | | 98.0 | 97.5 | 94.9 |
| Separated | | 1.0 | 1.7 | 4.7 |
| Wrong connected | | 3.3 | 2.7 | 5.7 |
| Other problems | | 0.3 | 1.7 | 2.0 |
| \sum wrong fibres | | 4.7 | 6.0 | 12.3 |

Appendix C

This chapter shows graphs of strength of orientation and weighted average length for all 4 positions of the sector specimen.

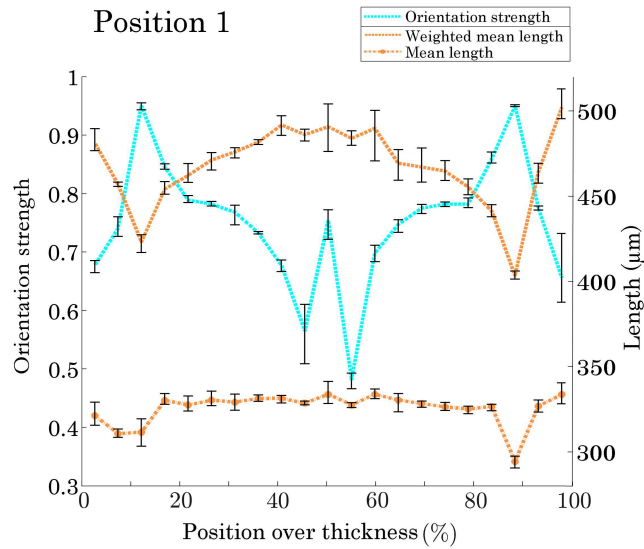


Figure .1: Average length, weighted average length and strength of orientation distribution over sheet thickness. Average values determined from 3 specimens showing min-max bars.

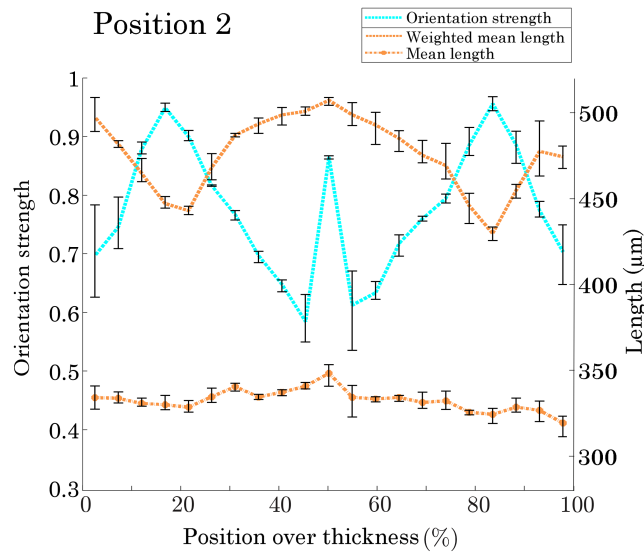


Figure .2: Average length, weighted average length and strength of orientation distribution over sheet thickness. Average values determined from 3 specimens showing min-max bars.

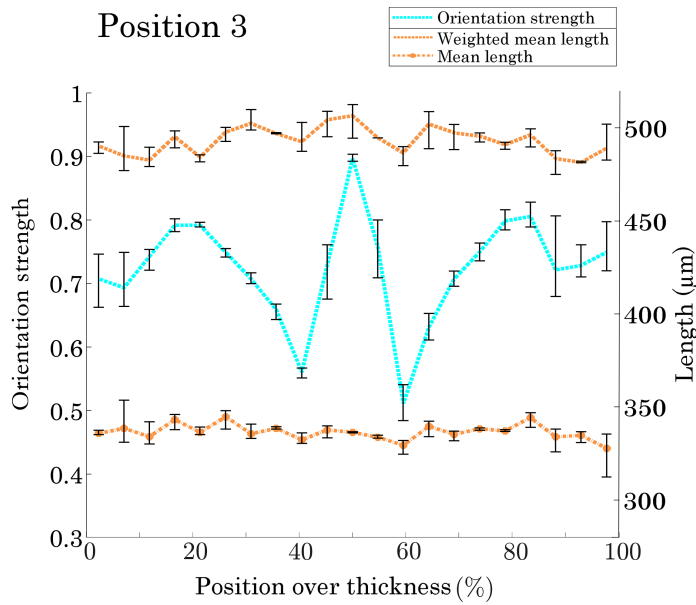


Figure .3: Average length, weighted average length and strength of orientation distribution over sheet thickness. Average values determined from 3 specimens showing min-max bars.

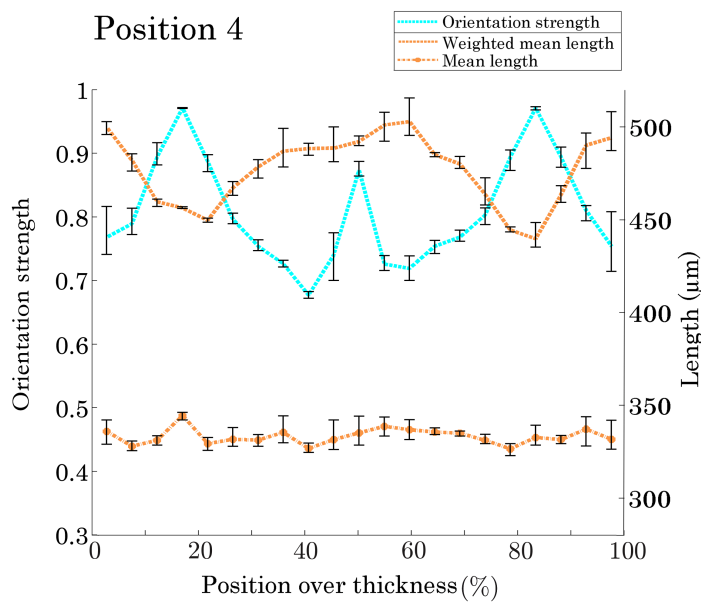


Figure .4: Average length, weighted average length and strength of orientation distribution over sheet thickness. Average values determined from 3 specimens showing min-max bars.

Appendix D

This chapter shows length and diameter for all long fibre materials tested.

Table B5: Results of free fibre length for long fibre composites, glass and carbon fibres

| Fibre material | lGlass | | | | lCarbon | | | |
|---|--------|------|------|------|---------|-------|-------|-------|
| | 15 | 10 | 7 | 4 | 15 | 10 | 7 | 4 |
| Pellet length (mm) | | | | | | | | |
| Fibre count | 4872 | 3574 | 3163 | 2853 | 25168 | 20945 | 20592 | 21226 |
| Curved fibres (%) | 32.7 | 27.9 | 25.0 | 22.3 | 11.9 | 20.3 | 16.9 | 11.5 |
| Weighted average length (μm) | 396 | 444 | 460 | 458 | 155 | 190 | 148 | 136 |
| Average length (μm) | 175 | 199 | 219 | 216 | 79 | 84 | 81 | 76 |
| Maximal length (μm) | 2452 | 2366 | 2838 | 3029 | 1220 | 1643 | 1063 | 1157 |
| Avg. diameter (μm) | 14.8 | 15.3 | 16.1 | 15.6 | 9.2 | 9.6 | 8.9 | 9.2 |

Table B6: Results of free fibre length for long fibre composites, PET and PVA fibres

| Fibre material | IPET | | | | IPVA | | | |
|---|------|------|------|------|------|------|------|------|
| | 15 | 10 | 7 | 4 | 15 | 10 | 7 | 4 |
| Pellet length (mm) | | | | | | | | |
| Fibre count | 2758 | 3188 | 3107 | 3257 | 4348 | 4993 | 6367 | 5299 |
| Curved fibres (%) | 55.0 | 53.3 | 63.4 | 66.7 | 45.6 | 47.3 | 51.9 | 63.4 |
| Weighted average length (μm) | 801 | 692 | 757 | 816 | 788 | 726 | 906 | 746 |
| Average length (μm) | 410 | 339 | 385 | 361 | 363 | 321 | 441 | 374 |
| Maximal length (μm) | 3481 | 2511 | 3490 | 6162 | 2996 | 5601 | 3124 | 3097 |
| Avg. diameter (μm) | 20.3 | 19.5 | 19.6 | 19.1 | 17.1 | 16.9 | 16.6 | 16.6 |

Appendix E

Fibre characterization - definition of results:

Two csv files and one raw file are written at the end of the calculations:

„filename“ is the name of the input CT data.

- „filename“ -FCP.csv: header1 + one line for each fibre with all features
- „filename“ -FCP-curvedfib.csv: header2 + one line for each fibre with intermediate point coordinates
- „filename“ -[TM, MAE]-Rev[X].raw: labelled medial axes data

Header1 contains five rows giving the following information:

- Specimen: „filename“.mhd
- Scan-parameters: CT-device, U, I, Ti, NoI, mode, Voxelsize, X, Y, Z
- Software Revision: X
- FCP-Parameters: variance, error, ROIthreshold, profilepoints, HessianTH, segmentTH, lenghtTH, lengthCorr, CClength, binaryTH, templatefile ¹
- Label, X1, Y1,Z1, X2, Y2, Z2, straightLength, curvedLength, diameter, surfacearea, volume, separated fibre, curved fibre ¹

Header2 contains five rows with row 1-4 same as header 1. Row 5 is giving the following information:

- Label, [X1a, Y1a , Z1a, X1b, Y1b , Z1b, ...] ¹

¹all values in (μm , μm^2 or μm^3)